



**HAL**  
open science

# Apport de la diffraction des rayons X à l'optimisation des propriétés de films minces anisotropes micro-et nano-cristallisés

Magali Noelle Valerie Morales

► **To cite this version:**

Magali Noelle Valerie Morales. Apport de la diffraction des rayons X à l'optimisation des propriétés de films minces anisotropes micro-et nano-cristallisés. Matière Condensée [cond-mat]. Université de Caen, 2007. tel-00332795

**HAL Id: tel-00332795**

**<https://theses.hal.science/tel-00332795>**

Submitted on 21 Oct 2008

**HAL** is a multi-disciplinary open access archive for the deposit and dissemination of scientific research documents, whether they are published or not. The documents may come from teaching and research institutions in France or abroad, or from public or private research centers.

L'archive ouverte pluridisciplinaire **HAL**, est destinée au dépôt et à la diffusion de documents scientifiques de niveau recherche, publiés ou non, émanant des établissements d'enseignement et de recherche français ou étrangers, des laboratoires publics ou privés.



**UNIVERSITE DE CAEN BASSE NORMANDIE**

**U.F.R : Sciences**

**ECOLE DOCTORALE: SIMEM**

# **HABILITATION A DIRIGER DES RECHERCHES**

présentée par

**Magali MORALES**

*Maître de conférences à l'IUFM de Basse Normandie*

*28<sup>ème</sup> section, Milieux Denses et Matériaux*

**Apport de la diffraction des rayons X à l'optimisation  
des propriétés de films minces anisotropes  
micro-et nano-cristallisés**

Soutenue le 19 Octobre 2007

## **Membres du jury**

<b>C. DUBOURDIEU</b> (rapporteur)	Directeur de Recherches CNRS, LMGP-INPG, Grenoble
<b>C. DUFOUR</b>	Professeur, Université de Caen (rapporteur)
<b>R. GUINEBRETIERE</b>	Professeur, ENSCI Limoges (rapporteur)
<b>M. LEVALOIS</b>	Professeur, Université de Caen
<b>J. RICOTE</b>	Chargé de Recherches CSIC, ICMA, Madrid
<b>R. RIZK</b>	Directeur de Recherches CNRS, SIFCOM-ENSICAEN, Caen



## **SOMMAIRE**

### **↳ Curriculum vitae succinct**

*Etat civil* p. 3

*Cursus et diplômes* p. 3

### **↳ Notice individuelle – Recherche**

*Expériences en recherche* p. 7

*Domaines de compétences* p. 7

*Travaux* p. 8

*A - Liste des publications* p. 8

*B - Communications orales* p. 13

*Encadrement d'étudiants* p. 15

*Activités d'intérêt collectif* p. 15

*Organisation de colloques et de formation* p. 16

*Collaborations scientifiques* p. 16

### **↳ Notice individuelle – Enseignement**

*Expériences d'enseignement* p. 19

*Responsabilités pédagogiques* p. 20

### **↳ Synthèse des activités de recherche**

*Introduction générale* p.23

*Chapitre 1 et articles les plus significatifs* p.25

*Chapitre 2 et articles les plus significatifs* p.45

*Conclusion et perspectives* p.83



**CURRICULUM VITAE**

**SUCCINCT**



## CURRICULUM VITAE

### MORALES Magali

Maître de Conférences IUFM de Basse-Normandie

28<sup>ème</sup> section, Milieux Denses et Matériaux

<u>Etat civil</u>	<u>Adresse professionnelle</u>	<u>Adresse personnelle</u>
Née le 27/12/1972	Laboratoire SIFCOM – ENSICAEN	91 rue Jean Moulin
à GAP (Hautes-Alpes).	UMR 6176	14880 Hermanville
<u>Nationalité</u> : Française	6 Bd Maréchal Juin	sur mer
1 enfant	14050 Caen cedex	<u>Tél.</u> : 02-31-96-08-48
	<u>Tél.</u> : 02-31-45-26-58	
	<u>Fax</u> : 02-31-45-26-60	
	<u>e-mail</u> : <a href="mailto:magali.morales@ensicaen.fr">magali.morales@ensicaen.fr</a>	

### CURSUS ET DIPLOMES

- 
- ♦ Septembre 2002 : Maître de conférences de l'IUFM de Basse Normandie ; titularisation le 1<sup>er</sup> septembre 2003.
  - ♦ 2001-02 : Postdoc au Laboratoire de Physique de l'Etat Condensé du Mans (LPEC) - Université du Maine (contrat européen ESQUI).
  - ♦ 2000-01 : ½ A.T.E.R. en 28<sup>ème</sup> section à l'Université J. Fourier (UJF), Grenoble I, rattaché au Laboratoire de Cristallographie (LC), CNRS - Grenoble.
  - ♦ 1999-2000 : ½ A.T.E.R. en 28<sup>ème</sup> section à l'Université du Maine rattaché au Laboratoire de Physique de l'Etat Condensé du Mans (LPEC).
  - ♦ 1996-99 : Thèse en cotutelle au Laboratoire de Cristallographie (LC), CNRS - Grenoble et "L'Instituto de Ciencia de Materiales de Aragon" (ICMA), Zaragoza.

Directeurs de thèse : D. Fruchart & J. Bartolomé.

Sujet : Analyse des couplages magnétiques et de la polarisation magnétique des éléments 3d dans les composés  $\text{RMn}_{12-x}\text{Fe}_x\text{X}$ .



Soutenu le 8 Octobre 1999 à l'UJF, Grenoble I, mention Très Honorable.

- ◆ 1995-96 : D.E.A Science et Structure des Matériaux, UJF Grenoble I, mention AB.
- ◆ 1994-95 : Maîtrise de Physique Recherche, UJF Grenoble I, mention B.
- ◆ 1993-94 : Licence de Physique Recherche, UJF Grenoble I, mention AB.
- ◆ 1990-93 : Classes Préparatoires (Spéciale Physique, Lycée Champollion). Obtention en double inscription du DEUG A Module Concours, mention AB.
- ◆ Juin 1990 : Baccalauréat série C, mention TB, Académie Aix-Marseille.

**NOTICE INDIVIDUELLE -  
RECHERCHE**



## EXPERIENCES EN RECHERCHE

---

- ◆ **stage de maîtrise : (02-09/1995)** - Instituto de Ciencias de Materiales de Barcelona (ICMAB), CSIC, Barcelone. Responsable : A. Fuertes. Sujet : Synthèse et stabilisation des phases tubulaires  $(\text{Bi}_{2,2-x}\text{Pb}_x\text{Cu}_{1,05}\text{O}_z)_n$  ( $\text{Sr}_8\text{Cu}_5\text{O}_{16}$ ) avec  $n$  élevé, isostructurales de la phase  $\text{Sr}(\text{Pb}, \text{Bi})\text{O}_3$ .
- ◆ **stage de DEA (03-06/1996) et thèse en cotutelle (1996-1999)** en continuation du stage de DEA - LC, CNRS, Grenoble et ICMA, Zaragoza (Espagne). Directeurs : D. Fruchart & J. Bartolomé. Sujet : Analyse des couplages magnétiques et de la polarisation magnétique des éléments 3d dans les alliages  $\text{R}(\text{Mn}, \text{Fe})_{12}\text{X}$ .
- ◆ **1/2 ATER : (1999-2000)**–LPEC. Sujet : Etudes de films minces conducteurs ioniques  $\text{La}_{2/3-x}\text{Li}_{3x}\square_{1/3-2x}\text{TiO}_3$  ( $\square$  = lacunes) déposés par pulvérisation magnétron réactive.
- ◆ **1/2 ATER : (2000-01)**–LC. Sujets : **1)** Caractérisations microstructurales par MET de films minces LLTO et de nanoprecipités  $\text{Pd}_{1-x}\text{Ce}_x$  avec  $x < 0.3$ . **2)** Dépôts d'intermétalliques par voie de chimie douce (MOCVD).
- ◆ **Postdoc : (2001-02)**–LPEC. Sujet : Analyse quantitative de texture aux rayons X et analyse combinée texture/structure/contraintes appliquées à des films minces ferroélectriques ((Pb, Ca)TiO<sub>3</sub>, LbNiO<sub>3</sub>, BaTiO<sub>3</sub>...) et conducteurs ioniques LLTO (contrat européen ESQUI).
- ◆ **Enseignant-chercheur au Laboratoire SIFCOM – ENSICAEN : (depuis septembre 2002)**

### Sujets principaux:

- 1) Elaboration et caractérisations structurale et microstructurale de films minces nanostructurés de Si et de SiC déposés par la technique de pulvérisation magnétron radiofréquence (jusqu'en février 2005).
- 2) Elaboration et caractérisation de films minces nanostructurés de  $\text{Cr}^{2+}:\text{ZnSe}$  pour la réalisation de micro-lasers émettant dans l'infra-rouge moyen (depuis février 2005).

## DOMAINES DE COMPETENCE

---

- Elaboration de films minces par pulvérisation cathodique radiofréquence.
- Microscopie électronique à balayage (MEB), en transmission (MET) et haute résolution (HREM) ; analyse EDX.

- Diffraction sur poudre et films minces; Analyses quantitatives de texture : rayons X et neutrons; réflectivité X.
- Analyse chimique de films minces par diffusion Rutherford (RBS) et par réaction nucléaire (NRA).
- Dichroïsme magnétique circulaire des rayons X (XMCD).
- Mesures d'aimantation (techniques classiques de caractérisations magnétiques, susceptibilité alternative...), et magnétiques anisotropes d'échantillons texturés sous champ.

## TRAVAUX

---

### ◆ Publications :

- **Publications dans des revues avec comité de lecture** : 21 articles
- **Publications dans des actes de congrès** : 10 articles

### ◆ Communications :

- **orales** : Congrès internationaux : 8 ; Congrès nationaux : 2  
7 conférences invitées dont 1 en tant qu'orateur
- **par affiches** : Congrès internationaux : 9 ; Congrès nationaux : 3.

### ◆ Séminaires : 5 (2 internes + 3 externes).

## A-Publications

### *Publications dans des revues à comité de lecture*

[1] New perovskite-related phases in the Bi-Pb-Sr-Ca-O system

C. C. Luhrs, **M. Morales**, F. Sapina, D. Beltran-Porter, A. Fuertes.  
Solid State Ionics 101(1997) 1107.

[2] Transition metal distribution in the  $\text{ErMn}_{12-x}\text{Fe}_x$  ( $0 \leq x \leq 8$ ) compounds

M. Artigas, M. Bacmann, D. Fruchart, **M. Morales**, E. Tomey.  
Physica B 234(1997) 155.

[3] Relationship between structural and magnetic properties of  $\text{ErMn}_{12-x}\text{Fe}_x$  compounds.

**M. Morales**, M. Artigas, M. Bacmann, D. Fruchart, P. Wolfers, J.L. Soubeyroux.

Journal of Alloys and Compounds 262(1997) 134.

[4] Comparison of the magnetic properties of the  $\text{ErMn}_{12-x}\text{Fe}_x$  series with their related hydrides and carbides.

**M. Morales**, M. Artigas, M. Bacmann, D. Fruchart, R. Skolozdra, P. Wolfers.

Journal of Magnetism and Magnetic Materials 196 (1999) 703.

[5] Magnetic characteristics of  $\text{ErMn}_{12-x}\text{Fe}_x$  compounds ( $x = 5$  and  $9$ ) determined by X-ray magnetic circular dichroism.

**M. Morales**, M. Bacmann, D. Fruchart, P. Wolfers, Ch. Baudelet, A. Delobbe, G. Krill.

Journal of Alloys and Compounds 317 (2001) 470.

[6] Magnetic properties and interactions in the  $\text{RMn}_{12-x}\text{Fe}_x$  series with  $R = \text{Y, Ho, Er, Nd}$  and  $x \leq 8$ .

**M. Morales**, M. Artigas, M. Bacmann, D. Fruchart, P. Wolfers, B. Ouladiaff.

Physical Review B 64 (2001) 144426.

[7] Impact of hydrogen and carbon insertion on the fundamental characteristics of  $\text{ErMn}_{12-x}\text{Fe}_x$  compounds.

**M. Morales**, M. Bacmann, D. Fruchart, P. Wolfers, B. Ouladiaff.

Journal of Magnetism and Magnetic Materials 236 (2001) 83.

[8] Resistivity of  $\text{RMn}_{12-x}\text{Fe}_x$  alloys

J. Stankiewicz, J. Bartolomé, **M. Morales**, M. Bacmann, D. Fruchart

Journal of Applied Physics 90 (2001) 5632-5636.

[9] Characterisation by EPR analysis of the magnetic phase diagram of  $\text{RFe}_{12-x}\text{M}_x\text{X}_y$  compounds.

M. G. Sheliapina, V. S. Kasperovich, V. S. Baranov, **M. Morales**, P. Wolfers, D. Fruchart.

Journal of Alloys and Compounds 343 (2002) 1-4

[10] Neoformation of Ni phyllosilicate upon Ni uptake on Montmorillonite. A Kinetics study by powder and polarized EXAFS.

R. Dähn, A. M. Scheidegger, A. Manceau, M. Schlegel, B. Baeyens, M. H. Bradbury and **M. Morales**.

Geochimica and Cosmochimica Acta, 66 (2002) 2335-2347.

[11] Characterisations of lanthanum lithium titanate thin films deposited by radio frequency sputtering on [100]-oriented MgO substrates.

**M. Morales**, P. Laffez, D. Chateigner, I. Vickridge.

Thin Solid Films 418 (2002) 119-128.

[12] Texture and magnetocrystalline anisotropy analysis of an oriented ErMn<sub>4</sub>Fe<sub>8</sub>C powder sample.

**M. Morales**, D. Chateigner, D. Fruchart.

Journal of Magnetism and Magnetic Materials 257 (2003) 258-269.

[13] Magnetic properties of RMn<sub>12-x</sub>Fe<sub>x</sub> type compounds: X-ray magnetic circular dichroism study of the ErMn<sub>12-x</sub>Fe<sub>x</sub> series with x=0, 7, 8 and 9.

M. G. Shelyapina, **M. Morales**, M. Bacmann, F. Baudalet, D. Fruchart, C. Giorgetti, E. K. Hlil, G. Krill and P. Wolfers

Journal of Alloys and Compounds 368 (2004) 84-93.

[14] Structural and microstructural characterization of nanocrystalline silicon thin films obtained by radio-frequency magnetron sputtering.

**M. Morales**, Leconte, R. Rizk and D. Chateigner

Journal of Applied Physics 97 (2004) 034307

[15] Structural and optical characterization of InN layers grown by MOCVD.

P. Singh, P. Ruterana, **M. Morales**, F. Gourbilleau, W. Wodjak, J-F. Carlin, M. Ilegems, D. Chateigner.

Superlattices and microstructures 36 (2004) 537-545

[16] Effect of the low temperature buffer and annealing on the properties of InN layers grown by MOVPE

P. Ruterana, **M. Morales**, F. Gourbilleau, P. Singh, M. Drago, T. Schmidtling, U. W. Pohl, W. Richter.

Physica Status Solidi (A), Applied Research 202 (2005) 781-784.

[17] Influence of substrate temperature on growth of nanocrystalline silicon carbide by reactive magnetron sputtering.

H. Colder, R. Rizk, **M. Morales**, P. Marie, J. Vicens.

Journal of Applied Physics 98 (2005) 024313

[18] Study of an internally-oxidized Pd<sub>0.97</sub>Ce<sub>0.03</sub> alloy

V. M. Azambuja, D. S. Dos Santos, L. Pontonnier, **M. Morales**, D. Fruchart

Scripta Materialia 54 (2006) 1779-1783.

[19] Optimization of ZnSe -SiO<sub>2</sub> nanostructures deposited by RF magnetron sputtering: correlations between plasma species and thin film composition, structural and microstructural properties

**M. Morales**, N. Vivet, M. Levalois, J-F. Bardeau

Thin Solid Films 515 (2007) 5314.

[20] Comments on "Bounds to Texture Components in Superposed Crystallographic Textures" by Jacob L. Jones

D. Chateigner, **M. Morales**

Journal of the American Ceramics Society 90 [3] (2007) 1002.

[21] Photoluminescence properties of Cr<sup>2+</sup>:ZnSe films deposited by radio-frequency magnetron co-sputtering.

N. Vivet, **M. Morales**, M. Levalois, J.L. Doualan, R. Moncorgé

Applied Physics Letters 90 (2007) 181915.

### *Publications dans des actes de congrès*

[1] X-ray combined QTA using a CPS applied to a ferroelectric ultrastructure.

**M. Morales**, D. Chateigner, L. Lutterotti, J. Ricote.

Materials Science Forum 408-412 (2002) 113-118.



[2] Texture analysis of ferroelectric thin films on platinised Si-based substrates with a TiO<sub>2</sub> layer.

J. Ricote, **M. Morales**, M. L. Calzada.

Materials Science Forum 408-412 (2002) 1543-1548.

[3] Anisotropic magnetization curves simulation of an easy-plane ferrimagnetic carbide from orientation distribution data.

**M. Morales**, D. Chateigner, D. Fruchart.

Materials Science Forum 408-412 (2002) 1055-1060.

[4] QTA of prismatic calcite layers of some bivalves, a link to trichite ancestrals.

D. Chateigner, **M. Morales**, L. Harper.

Materials Science Forum 408-412 (2002) 1687-1692.

[5] Anisotropic crystallite size analysis of textured nanocrystalline silicon thin films probed by X-ray diffraction.

**M. Morales**, Y. Leconte, R. Rizk, D. Chateigner.

Thin Solid Films 450 (2004) 216-221.

[6] Application of the X-ray combined analysis to the study of lead titanate based ferroelectric thin films.

J. Ricote, D. Chateigner, **M. Morales**, M. L. Calzada and C. Wiemer.

Thin Solid Films 450 (2004) 128-133.

[7] X-ray magnetic circular dichroism study of the of RMn<sub>12-x</sub>Fe<sub>x</sub> with R = Er, Y, Lu

M. G. Shelyapina, **M. Morales**, M. Bacmann, F. Baudelet, D. Fruchart, C. Giorgetti, E. K. Hlil, G. Krill and P. Wolfers

Journal of Alloys and Compounds 383 (2004) 152-156.

[8] Exchange interactions and magneto-crystalline anisotropy in RFe<sub>12-x</sub>M<sub>x</sub> and parent interstitial compounds.

M. Bacmann, F. Baudelet, D. Fruchart, D. Gignoux, E. K. Hlil, G. Krill, **M. Morales**, R. Vert and P. Wolfers

Journal of Alloys and Compounds 383 (2004) 166-172.

[9] Characterization of SiC thin films obtained by reactive magnetron sputtering : IBA, IR and Raman studies.

H. Colder, **M. Morales**, R. Rizk and I. Vickridge  
Materials Science Forum 483-485 (2005) 287-290

[10] Comparative study of structural damage under irradiation in SiC Nanostructured and conventional Ceramics

Y. Leconte, I. Monnet, M. Levalois, **M. Morales**, X. Portier, Y. Lionel, N. Thomé, C. Reynaud  
"Structural and Refractory Materials for Fusion and Fission Technologies", MRS Proceedings (2007) Volume 981E, manuscript n° 0981-JJ06-01

### **B-Conférences : communications orales**

#### *Conférences internationales*

{1} Annual Meeting of the Physical Society of Portugal : Magnetism in Metals, Lisbonne, 20-21 novembre 1997.

"Magnetic properties of novel intermetallic compounds" (**Conf. invitée**).  
D. Fruchart, **M. Morales**, M. Bacmann, P. Wolfers

{2} 13<sup>th</sup> International Conference on Textures of Materials, Seoul (Corée) 26-30 août 2002.

"Texture and magneto-crystalline anisotropy of an oriented ferrimagnetic ErMn<sub>4</sub>Fe<sub>8</sub>C powder sample."

**M. Morales**, D. Chateigner, D. Fruchart.

{3} EMRS 2003, Strasbourg juin 2003

"Application of the x-ray combined analysis to the study of lead titanate based ferroelectric thin films."

J. Ricote, D. Chateigner, **M. Morales**, M.L. Calzada, C. Wiemer, L. Lutterotti

{4} EMRS 2004, Strasbourg juin 2004, Symposium L

"Structural and optical characterization of InGaN layers grown by MOCVD."

P. Singh, **M. Morales**, M. Wodjeck, A. Braud, J.F. Carlin et P. Ruterana.

{5} 2<sup>nd</sup> International conference on Texture and Anisotropy of Polycrystals (ITAP2), 7-9 juil. 2004, Metz.

a) "Combined analysis of oriented oxides and thin films: Bi2223, Ca<sub>3</sub>Co<sub>4</sub>O<sub>9</sub>, PTC and nano-Si". D. Chateigner, E. Guilmeau, R. Funahashi, **M. Morales**, J. Noudem, J. Ricote, L. Lutterotti, B. Ouladdiaf (**Conf. invitée**).

b) "Texture development and anisotropic magnet properties: polymer embedded Er-Mn-Fe easy plane and hot forged Nd-Fe-V and Nd-Fe-B easy c-axis alloys."

D. Chateigner, S. Rivoirard, I. Popa, **M. Morales**, B. Ouladdiaf, D. Fruchart, P. de Rango

{6} 3<sup>rd</sup> Symposium of the International French-Chinese Laboratory for the Applications of Superconductors and Magnetic Materials, 27-29 sept. 2004, Grenoble.

"Combined texture-structure-microstructure-phase analysis of multiphased bulks and thin films using x-ray and neutron diffraction: Ca<sub>3</sub>Co<sub>4</sub>O<sub>9</sub>, PTC and nano-Si."

D. Chateigner, J. Noudem, **M. Morales**, E. Guilmeau, J. Ricote, B. Ouladdiaf, L. Lutterotti (**Conf. invitée**).

{7} MRS Fall Meeting, 27 nov.-1<sup>er</sup> déc. 2006, symposium JJ

"Comparative study of structural damage under irradiation in SiC Nanostructured and conventional Ceramics"

Y. Leconte, I. Monnet, M. Levalois, **M. Morales**, X. Portier, Y. Lionel, N. Thomé, C. Reynaud

{8} The European Conference on Lasers and Electro-Optics and the International Quantum Electronics Conference (CLEO), 17-22 juin 2007, Munich

"Growth and luminescence of Cr<sup>2+</sup>:ZnSe films deposited by radio-frequency magnetron co-sputtering"

N. Vivet, **M. Morales**, M. Levalois, J.L. Doualan, R. Moncorgé (**Conf. Invitée**).

### *Conférences nationales*

{1} Journées Couches Minces Ferroélectriques JCF : Maubeuge, 26-27 novembre 2001.

"Combined X-ray texture-microstructure analysis applied to thin ultrastructures : a case of study on  $Pb_{0.76}Ca_{0.24}TiO_3$ ."

D. Chateigner, **M. Morales**, J. Ricote, L. Lutterotti (**Conf. invitée**).

{2} Association Française de Cristallographie (AFC) 7-10 Juillet 2003, Caen.

"Combinaison d'algorithmes pour la détermination microstructurale et structurale."

D. Chateigner, **M. Morales**, L. Lutterotti (**Conf. invitée**).

## ENCADREMENT D'ETUDIANTS

---

### Encadrements de thèse

♦ **Héloïse Taupin-Colder** : SIFCOM-ENSICAEN, Université de Caen, soutenue le 15 septembre 2005 ; encadrement : 50%

Sujet : Croissance basse température de films minces de carbure de silicium nanocristallin : propriétés et performances d'hétérojonctions SiC/Si.

♦ **Nicolas Vivet** : SIFCOM-ENSICAEN, Université de Caen, débutée en octobre 2005 ; encadrement : 50%

Sujet : Elaboration et caractérisation de films minces nanostructurés de  $Cr^{2+}$ :ZnSe pour la réalisation de microlasers dans l'infrarouge moyen.

### Encadrements de stage de Master Recherche (M2) et de Master 1<sup>ère</sup> année (M1)

♦ **Nicolas Vivet** : stage de M2 de février à juin 2005; Sujet : Elaboration et caractérisation de couches minces composites ZnSe/SiO<sub>2</sub> par pulvérisation magnétron.

♦ **Farid El Yazami** : stage de M2 de février à juin 2004; Sujet : Analyse par spectroscopies de masse et d'émission optique des plasmas réactif utilisés lors du dépôt de couches minces de SiC.

♦ **A. Debout et A. Hard** : stage de M1 d'avril à juin 2003; Sujet : Etude de poudres cristallines par diffraction des rayons X.

## ACTIVITES D'INTERET COLLECTIF

---

♦ Correspondant formation CNRS du laboratoire SIFCOM de septembre 2002 à septembre 2005.

- ◆ Membre de la Commission de Spécialistes 28<sup>ème</sup> section de Caen depuis septembre 2003.
- ◆ Membre du Conseil du laboratoire SIFCOM depuis janvier 2004.

### **ORGANISATION DE COLLOQUES ET DE FORMATIONS**

- 
- ◆ Colloque de l'Association Française de Cristallographie, AFC Caen du 7 au 10 juillet 2003.
  - ◆ Organisation et intervenant dans le cadre de la formation CNRS - Région Basse Normandie "Analyse combinée par diffraction des rayons X et des neutrons" : 22-24 juin 2005
  - ◆ Organisation et intervenant dans le cadre de la formation Nationale CNRS "Analyse combinée par diffraction des rayons X et des neutrons" : 19-23 juin 2006

### **COLLABORATIONS SCIENTIFIQUES**

- 
- ◆ Institut Laue-Langevin (ILL), Grenoble : B. Ouladiaff (D1B, D2B, D20).
  - ◆ Laboratoire Louis Néel, CNRS-Grenoble : D. Gignoux.
  - ◆ Laboratoire de Chimie du Solide Minéral, Université H. Poincaré-Nancy : B. Malaman, G. Le Caer (ENSMN).
  - ◆ Laboratoire de Physique de l'Etat Condensé, Université du Maine : J-M. Grenèche, A. Gibaud, P. Laffez, J.F. Bardeau, A. Bulou.
  - ◆ Groupe de Physique du Solide, Jussieu : I. Vickridge.
  - ◆ Laboratoire de Génie des Matériaux, ISITEM, Nantes : T. Brousse.
  - ◆ Faculty of Physics and Nuclear Techniques, Academy of Mining and Metallurgy – Krakow, Pologne : J. Tobola.
  - ◆ Laboratoire de Géophysique Interne et de Tectonophysique, Grenoble : A. Manceau.
  - ◆ Paul Scherrer Institute, Viligen, Suisse : R. Dähn.
  - ◆ Instituto de Ciencias de Materiales de Madrid, Departamento de materiales ferroelectricos, Espagne : J. Ricote et M. L. Calzada.
  - ◆ Università degli Studi di Trento, Facoltà di Ingegneria, Italie : L. Lutterotti.
  - ◆ Laboratoire de Physicochimie de la Matière Condensée, Université de Montpellier : V. Bornand.
  - ◆ Institut de Chimie de la Matière Condensée de Bordeaux : J.-P. Manaud, M. Maglione.
  - ◆ Laboratoire de Cristallographie et Sciences des Matériaux, Ensicaen : D. Chateigner.

**NOTICE INDIVIDUELLE -  
ENSEIGNEMENT**



## EXPERIENCES D'ENSEIGNEMENT

---

### ↳ IUT Mesures Physiques – Grenoble I (vacations durant ma thèse en co-tutelle avec l'université de Zaragoza, 1996-1999)

- ◆ 56 h ~ TD de Travaux Dirigés (TD) de Mécanique du Solide, Vibrations et Ondes en 2<sup>ème</sup> année.
- ◆ 61 h ~ TD de Travaux Pratiques (TP) d'Electricité en 1<sup>ère</sup> année.

### ↳ Université Joseph Fourier– Grenoble I (1/2 ATER 2000-2001)

- ◆ 72 h ~ TD de TP de Cristallographie en 2<sup>ème</sup> année d'école d'ingénieurs ISTG, Maîtrise Physique et Applications, Maîtrise de Sciences Physiques.
- ◆ 24 h ~ TD de TD de Physique Nucléaire et d'Ondes mécaniques en Deug STSV1.

### ↳ Université du Maine – Le Mans (1/2 ATER 1999-00 et stage postdoctoral 2001-2002)

- ◆ 68 h ~ TD de TD en Deug SV2 et STSV1.
- ◆ 28 h ~ TD de TP en Deug MIAS2 et Licence de Physique.
- ◆ 8 h ~ TD de Cours en DESS Modélisation en Physique et en Mécanique.
- ◆ 10 h ~ TD de TD en DESS Modélisation en Physique et en Mécanique.
- ◆ 12 h ~ TD de TP en Maîtrise de Physique.

### ↳ Université de Caen et IUFM de Basse-Normandie – Caen (depuis septembre 2002)

- ◆ 14 h ~ TD de TD Pré-rentree Deug MIAS et SM 1<sup>ère</sup> année
- ◆ 58.5 h ~ TD de Cours + 39 h ~ TD de Travaux Dirigés de Mécanique en Deug MIAS 1<sup>ère</sup> année
- ◆ 12 h ~ TD de TP et 14 h ~ TD de TD de Physique du Solide en Maîtrise de Physique
- ◆ 20 h ~ TD de TD d'Analyse Structurale des Matériaux en Master 1 de Physique



- ◆ 10 h ~ TD de TD de Cristallographie en Master 1 de Physique
- ◆ 29 h ~ TD de Cours d'Electromagnétisme et d'optique en Licence 1 de Mathématiques
- ◆ 86 h ~ TD de Cours, TD, TP et montages au Capes de Physique.

## **RESPONSABILITES PEDAGOGIQUES**

---

- ◆ Coordinatrice de la préparation au Capes de Physique – Chimie de l'IUFM de Basse Normandie depuis septembre 2004.
- ◆ Co-responsable en 2006 de l'unité de formation et d'innovation (UFI) Sciences et Technologie de l'IUFM de Basse Normandie.

**SYNTHESE DES ACTIVITES**

**DE**

**RECHERCHE**



## *INTRODUCTION GENERALE*

La détermination des corrélations existant entre la structure et la microstructure d'un matériau et ses propriétés physiques est primordiale pour son optimisation et dans ce contexte, les techniques de diffraction de rayons X, neutrons ou électrons sont des outils de choix. De plus, dans un souci de miniaturisation constant, l'élaboration de matériaux sous forme de films minces et leur éventuelle nanostructuration leur confèrent des propriétés physiques particulières souvent améliorées par rapport au matériau massif, ce qui constitue ces dernières années un enjeu stratégique et économique majeur en raison de leur potentiel d'applications énorme.

Dans cet objectif, de nombreuses techniques de dépôt sous vide existent pour l'élaboration de films minces nanostructurés ou non, et elles sont en général séparées en deux grandes catégories avec les techniques de dépôt en phase vapeur chimique (CVD, PECVD, MOCVD...) ou de dépôt physique (évaporation, pulvérisation, ablation laser...). Parmi ces dernières, la technique de pulvérisation magnétron est une des méthodes de dépôt la moins onéreuse, facilement transposable à un niveau industriel et permettant aussi bien de déposer des couches que des multicouches conductrices ou isolantes de bonne qualité cristalline. De plus, la possibilité de l'utilisation d'un gaz réactif tel que l'oxygène ou l'hydrogène est un atout supplémentaire comme nous le verrons dans cette synthèse.

L'élaboration de matériaux polyphasés, massifs ou sous forme de films minces, aux propriétés physiques spécifiques très anisotropes a relancé également ces dernières années un intérêt croissant pour l'analyse texturale, puisque l'anisotropie des propriétés physiques macroscopiques d'un échantillon polycristallin ne peut être observée que si ses cristallites sont préférentiellement orientés. C'est le cas notamment des matériaux magnétiques, conducteurs ioniques, ferro- et piézo-électriques et des matériaux à transparence optique. L'analyse quantitative des orientations préférentielles (QTA) par diffraction des rayons X, méthode d'investigation non destructive, joue donc un rôle essentiel dans l'optimisation de ces propriétés anisotropes pour comprendre les corrélations existant entre les tenseurs microscopiques et les propriétés macroscopiques, ainsi que pour déterminer les modes de croissance (épitaxie) et optimiser les conditions d'élaboration.

De plus, l'ajout des informations de QTA devient indispensable afin de repousser certaines limites dans des techniques de caractérisation structurale basées sur le rayonnement X, par exemple en EXAFS polarisé, et en couplant les analyses de Rietveld et de texture avec

l'analyse dite "combinée" structure/texture/contraintes. En effet, dans un échantillon texturé, si on ne connaît pas exactement sa structure, on ne peut pas en extraire sa texture et vice-versa. De même, la détermination des contraintes dans un échantillon texturé est délicate et une approche par une analyse globale du profil (dite analyse combinée) est souvent nécessaire, encore plus si les échantillons sont polyphasés et de basse symétrie cristalline.

Mes activités de recherche jusqu'à aujourd'hui et présentées ci-après visent à établir lorsque cela est possible les corrélations existant entre la structure et la microstructure, déterminées essentiellement par les techniques de diffraction, et les propriétés physiques de matériaux massifs magnétiques ou sous forme de films minces (conducteurs ioniques, ferroélectriques, à transparence optique) en vue de leur optimisation.

Ces activités se sont orientées suivant deux axes :

- d'une part (Chapitre 1) avec l'analyse quantitative de texture classique et en utilisant principalement la technique de diffraction de rayons X, pour l'optimisation de matériaux massifs intermétalliques ferromagnétiques texturés sous champ magnétique (et étudiés dans le cadre de ma thèse 1996-1999), et de films minces texturés conducteurs ioniques  $(\text{La,Li})\text{TiO}_3$  ou semi-conducteurs d'InN.
- d'autre part (Chapitre 2), avec l'optimisation de films minces texturés en utilisant une approche via l'analyse combinée des spectres de diffraction X. Le recours à une analyse globale du profil pour l'étude des films minces ferroélectriques texturés  $(\text{Pb,Ca})\text{TiO}_3$  et de  $\text{TiC}_x$  et  $\text{TiN}_y$ , a été nécessaire du fait de recouvrements importants de pics inter-phases. Cette approche dans le cadre de l'optimisation de films minces nanostructurés semi-conducteurs de Si, SiC,  $\text{Cr}^{2+}:\text{ZnSe}$  étudiés au Laboratoire SIFCOM, a été motivée par la présence d'orientations préférentielles et de nanocristallites de tailles anisotropes, ainsi que par la nécessité de lever l'ambiguïté sur la structure du SiC (présence de plusieurs polytypes).

Depuis que j'ai rejoint le Laboratoire SIFCOM (septembre 2002), outre des activités ponctuelles de caractérisations structurales par diffraction de rayons X sur des films minces semi-conducteurs texturés de Si et d'InN, mon activité de recherche repose essentiellement sur l'élaboration par pulvérisation magnétron et l'optimisation des propriétés optiques de films texturés de SiC et, depuis février 2005 de films de  $\text{Cr}^{2+}:\text{ZnSe}$ , nouveau sujet de recherche que je développe au laboratoire.

# CHAPITRE 1.

L'analyse quantitative de texture (QTA)

classique par

diffraction des rayons X



La texture rend compte de la diversité des orientations des cristallites à l'intérieur d'un matériau polycristallin et est décrite en utilisant la fonction de distribution des orientations cristallines (FDOC). La FDOC d'une phase représente les différentes orientations des domaines cohérents de diffraction ou cristallites de cette phase et leur distribution. Seule est considérée l'orientation des cristallites d'une même phase, c'est à dire ayant même composition et même structure cristalline. Si  $g$  est l'orientation d'un cristallite à l'intérieur de l'échantillon, alors la fonction  $f(g)$  de distribution des orientations est définie comme étant la fraction volumique  $dV$  des cristallites ayant une orientation comprise entre  $g$  et  $g+dg$ , par unité surfacique :  $\frac{dV(g)}{V} = \frac{1}{8\pi^2} f(g)dg$  (Equ. 1) où :

- ◆  $g$  est définie par les angles d'Euler  $\alpha$ ,  $\beta$  et  $\gamma$  (Figure 1). Les angles  $\alpha$  et  $\beta$  donnent l'orientation de la direction  $[001]^*$  d'un cristallite, dans l'échantillon considéré, auquel est associé le repère de coordonnées  $\{XYZ\}$  ; ces angles sont appelés respectivement azimuth et co-latitude. Le troisième angle  $\gamma$  définit la direction cristallographique  $[010]^*$  (dans le plan  $(\vec{a}, \vec{b})$ )

- ◆  $V$  est le volume de la phase considérée de l'échantillon et irradié par les rayons X

- ◆  $8\pi^2$  normalise la fonction  $f(g)$  dans l'espace des orientations :

$$\int_{\alpha=0}^{2\pi} \int_{\beta=0}^{\pi} \int_{\gamma=0}^{2\pi} f(g)dg = 8\pi^2 \text{ avec l'élément d'orientation } dg = \sin\beta \, d\beta \, d\alpha \, d\gamma.$$

La fonction  $f(g)$  est la description quantitative de la texture du matériau et c'est une fonction de densité de distribution mesurée en m.r.d. (multiple of random distribution). Pour un échantillon non orienté, on a  $f(g)=1$ m.r.d. quel que soit  $g = (\alpha, \beta, \gamma)$ .

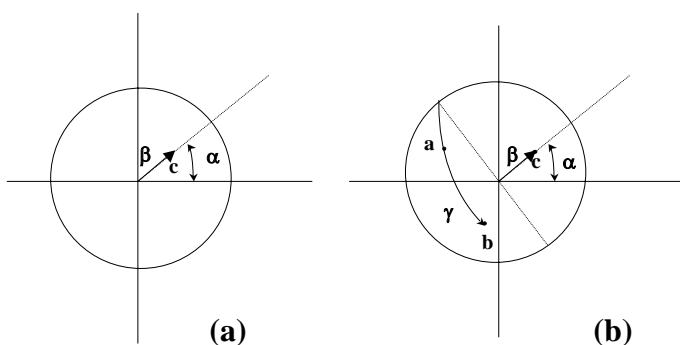


**Figure 1.** (a) Définition des angles sur une figure de pôles et (b) angles d'Euler définissant l'orientation d'un cristal.

Les figures de pôles  $P_{hkl}(\alpha, \beta)$  permettent une représentation aisée des orientations préférentielles des cristaux dans un échantillon polycristallin. Elles représentent la répartition



des normales  $\langle hkl \rangle^*$  aux plans réticulaires  $\{hkl\}$  diffractant pour une orientation  $(\alpha, \beta)$  de l'échantillon. Pour mesurer une figure de pôles  $\{hkl\}$ , on fait varier les angles  $\alpha$  et  $\beta$  afin de couvrir le maximum d'orientations de l'échantillon. Elle représente donc la densité de distribution angulaire des directions cristallines  $\langle hkl \rangle^*$  :

$$\frac{dV(\alpha, \beta)}{V} = \frac{1}{4\pi} P(\alpha, \beta) \sin \beta d\beta d\alpha$$

(Equ. 2) où le facteur  $4\pi$  normalise  $P$  par intégration sur toute la surface de projection :

$$\int_{\alpha=0}^{2\pi} \int_{\beta=0}^{\pi} P_{hkl}(\alpha, \beta) \sin \beta d\beta d\alpha = 4\pi.$$

Pour le tracé d'une figure de pôles, on trace les normales  $\langle hkl \rangle^*$  aux plans  $\{hkl\}$  de l'échantillon ; les intersections de celles-ci avec l'hémisphère supérieur de la sphère des pôles sont les points  $P(\alpha, \beta)$  appelés les pôles des plans réticulaires, associés aux densités de distributions mesurées  $P_{hkl}(\alpha, \beta)$ . La figure de pôles est ensuite obtenue, par exemple, par projection stéréographique de  $P_{hkl}(\alpha, \beta)$  d'une réflexion de Bragg pour une position angulaire  $(\alpha, \beta)$  donnée de l'échantillon (Figure 2).

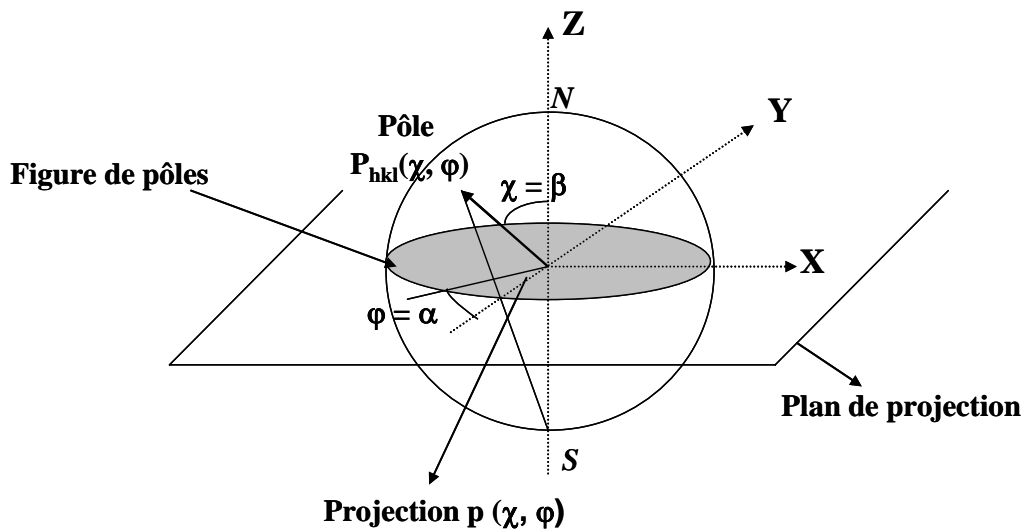


**Figure 2.** Projection stéréographique du pôles  $P_{hkl}(\chi, \varphi)$ ,  $\varphi$  étant conservé par projection.

### 1. Calcul de la fonction de distribution des orientations cristallines (FDOC) : la méthode WIMV

On peut remarquer que les figures de pôles représentent la répartition de directions cristallines (connues par deux angles d'Euler), alors que nous cherchons à connaître les

distributions d'orientations cristallines (connues par trois angles d'Euler, car deux directions doivent être spécifiées pour connaître une orientation). Toutes les informations nécessaires sont néanmoins accessibles, grâce à la mesure de plusieurs figures de pôles  $P_{hkl}(\alpha, \beta)$ . Le problème consiste donc à connaître  $f(g)$  à partir de plusieurs  $P_{hkl}(\alpha, \beta)$ . Ceci peut se faire par inversion de:  $P_{hkl}(\alpha, \beta) = \frac{1}{2\pi} \int_{hkl} f(g) d\tilde{\varphi}$  (Equ. 3) qui se déduit des Equ. 1 et 2 et où  $d\tilde{\varphi}$  est un chemin d'intégration de  $f(g)$  tenant compte de la symétrie cristalline de la phase considérée de l'échantillon.

La méthode choisie pour extraire la fonction des distributions  $f(g)$  à partir des figures de pôles est un affinement numérique utilisant une méthode de type "maximum d'entropie". Ce type d'affinement est appelé affinement "WIMV" (abréviation de Williams, Imhof, Matties et Vinel) utilisé par le logiciel Beartex. La procédure est la suivante : à partir des figures de pôles expérimentales  $P_{hkl}^0(\alpha, \beta)$ , on estime  $f^0(g)$ , qui nous permet de recalculer les mêmes figures de pôles à l'étape 1,  $P_{hkl}^1(\alpha, \beta)$ . Par itérations successives à l'ordre  $n$ , on obtient une bonne évaluation  $f^n(g)$  de  $f(g)$ . La comparaison des figures de pôles expérimentales et calculées permet d'estimer la validité du calcul de la FDOC via des facteurs de fiabilité statistiques.

Il est souvent plus aisé de se donner une idée de la texture à partir des figures de pôles recalculées d'indices simples. Cependant, pour connaître toutes les directions cristallines  $\langle hkl \rangle$  alignées avec une direction macroscopique XYZ de l'échantillon, il est nécessaire de calculer toutes les figures de pôles  $P_{hkl}(\alpha, \beta)$  à partir de la FDOC. Ceci n'est pas réalisable et il est souvent préférable de tracer les figures de pôles inverses XYZ, obtenues également à partir de la FDOC. Dans le cas d'une texture de fibre (les axes cristallins sont aléatoirement répartis autour de la normale aux figures de pôles, c'est à dire autour de l'angle  $\varphi$ ), la figure de pôles inverse tracée pour l'axe de fibre, par exemple la normale au plan d'un film  $\bar{n} = 00Z$ , est suffisante pour avoir une représentation complète de la texture. Pour un système cristallin cubique, toutes les directions du système sont représentées dans un seul secteur cubique, délimité par les directions  $\langle 001 \rangle$ ,  $\langle 110 \rangle$  et  $\langle 111 \rangle$ , les autres secteurs étant symétriques du précédent.

Pour apprécier quantitativement la force de la texture, on calcule l'index de texture  $F^2$ , donné par :  $F^2 = \frac{1}{8\pi^2} \sum_g [F(g)]^2 \Delta g$  où  $\Delta g = \sin\beta\Delta\beta\Delta\alpha\Delta\gamma$  représente l'élément d'orientation expérimental. Il permet de comparer la force de la texture entre différents échantillons de textures similaires : plus la valeur de l'index  $F^2$  est élevée, plus la texture de l'échantillon est

forte. L'index  $F^2$  évolue inversement à l'entropie  $S$  donnée par :  $S = \frac{-1}{8\pi^2} \sum_g f(g) \ln[f(g)]$ . En effet, si l'entropie diminue, le désordre diminue et donc la texture de l'échantillon devient forte.

L'analyse quantitative de texture en fournissant des renseignements au niveau macroscopique à l'échelle de la sonde considérée (typiquement quelques  $(10\mu\text{m})^3$  pour les rayons X et quelques  $\text{cm}^3$  pour les neutrons) permet de mieux comprendre les phénomènes liés à l'anisotropie se produisant à l'échelle macroscopique dans un échantillon orienté.

## 2. Dispositif expérimental de mesure des figures de pôles

Expérimentalement, la FDOC est mesurée sous la forme de plusieurs figures de pôles  $P_{hkl}(\chi, \varphi)$  donnant pour une orientation  $(\chi, \varphi)$  donnée de l'échantillon la répartition des normales  $\langle hkl \rangle^*$  aux plans réticulaires  $\{hkl\}$  diffractant et permettant ainsi une représentation aisée des orientations préférentielles des cristaux dans un polycristal (Figure 3). La mesure des figures de pôles nécessite un dispositif expérimental particulier comprenant un goniomètre quatre cercles (Figure 4) composé d'un goniomètre classique  $\theta$ - $2\theta$  et d'un cercle d'Euler possédant les rotations  $\chi$  et  $\varphi$  permettant d'explorer toutes les directions de l'espace.

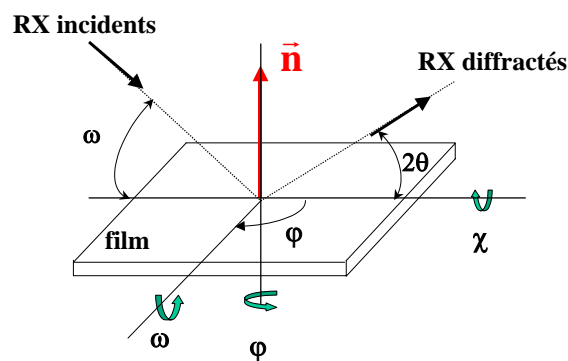


**Figure 3.** Définition des différents angles par rapport à la surface du film mince étudié.

L'acquisition des pics de diffraction s'effectue à l'aide d'un détecteur courbe à localisation de position (CPS) permettant l'enregistrement de toutes les figures de pôles simultanément sur un domaine angulaire de  $120^\circ$  en  $2\theta$  (évitant ainsi des temps de comptage rédhibitoires) avec une résolution de  $0.03^\circ$  dans notre configuration. Les figures de pôle

$P_{hkl}(\chi, \varphi)$  ont été mesurées en faisant varier par pas de  $5^\circ$  l'angle de tilt du goniomètre,  $\chi$ , de  $0$  à  $45^\circ$  et l'angle azimuthal,  $\varphi$ , entre  $0$  et  $360^\circ$  sous un angle d'incidence  $\omega$  donné.

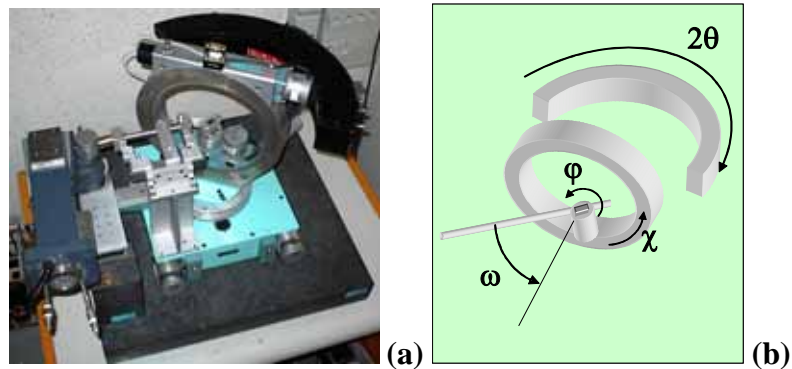


**Figure 4.** (a) Vue du goniomètre quatre cercles du Laboratoire CRISMAT (Ensicaen) utilisé pour la QTA et (b) représentation schématique avec les différents angles de mesure  $\omega$ ,  $2\theta$ ,  $\chi$  et  $\varphi$ .

### 3. Applications

Cette analyse quantitative de texture classique, en utilisant la technique de diffraction de rayons X, a permis d'optimiser des matériaux massifs intermétalliques ferromagnétiques texturés sous champ magnétique et des films minces conducteurs ioniques ou semi-conducteurs.

En effet, l'analyse des orientations préférentielles par diffraction X sur une poudre orientée permet d'associer à température ambiante une direction macroscopique d'aimantation à un type de direction cristalline particulière. Afin d'analyser les propriétés fondamentales d'anisotropie magnétocristalline des matériaux composites ferromagnétiques étudiés lors de ma thèse, ces derniers ont été texturés sous champ magnétique. De plus, à partir des résultats affinés de la fonction de distribution des orientations cristallines, il a été possible de simuler les courbes d'aimantation anisotropes  $M(H)$  obtenues expérimentalement (ATER 1999-2000, Le Mans).

L'analyse quantitative de texture couplée aux analyses par microscopie électronique en transmission a permis également :

- de déterminer les conditions optimales de dépôt des films minces conducteurs ioniques  $(La, Li)TiO_3$  élaborés par pulvérisation magnétron (ATER 1999-2000, Le Mans)

- d'établir les relations existant entre la structure/microstructure et les propriétés de photoluminescence de films d'InN élaborés par MOPVE (collaboration Laboratoire SIFCOM, thèse P. Singh).

### **3.1. Détermination des propriétés magnétiques anisotropes d'un échantillon massif ferromagnétique $\text{ErMn}_4\text{Fe}_8\text{C}$ et simulation des courbes d'aimantation $M(H)$ : Laboratoire de Cristallographie – Grenoble , Doctorat (1996-1999).**

Depuis quelques décennies, un intérêt particulier a été porté à l'étude des composés intermétalliques à base de métaux de terre rare (R) et de métaux de transition 3d (M) où le magnétisme localisé des éléments R se combine à celui des éléments de transition beaucoup moins localisé. Un certain nombre de ces composés tels que  $\text{RCO}_5$ ,  $\text{R}_2\text{Fe}_{14}\text{B}$ ,  $\text{R}_2\text{Fe}_{17}\text{N}$ ... présentent des propriétés d'aimants permanents exceptionnelles (température de Curie bien au-dessus de l'ambiante, aimantation élevée, anisotropie magnétocristalline axiale très forte...) et sont largement utilisés à des fins d'applications technologiques.

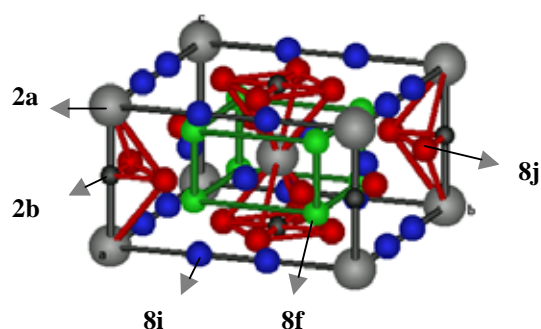
Les composés intermétalliques de structure type  $\text{ThMn}_{12}$  peuvent être stabilisés en remplaçant le thorium par un métal de terre rare R :  $\text{RM}_{12}$ . Avec le fer seul ( $M = \text{Fe}$ ), ce type de formule est instable ; cependant, cette structure peut être stabilisée par substitution partielle des atomes de fer par des métaux de transition 3d (Ti, V, Cr...) dont le manganèse, 4d (Mo, Nb) ou 5d (W, Re, Ta) ayant une densité d'électrons de valence moindre. Certains composés  $\text{RM}_{12}$  sont susceptibles de présenter des propriétés d'aimants permanents (par exemple le composé interstitiel  $\text{PrFe}_{10,5}\text{V}_{1,5}\text{N}$ ) mais ce n'est pas l'optimisation des composés  $\text{RMn}_{12-x}\text{Fe}_x$  dans l'objectif de leur application qui a retenu notre attention au début de ma thèse. En effet, afin de mieux comprendre la nature des interactions magnétiques dans ce type de composés, nous avons entrepris l'étude fondamentale des caractéristiques structurales et magnétiques des séries  $\text{RMn}_{12-x}\text{Fe}_x$  où nous avons choisi comme élément R une terre rare magnétique lourde telle que Er (coefficient de Stevens  $\alpha_j > 0$ ) et Ho ( $\alpha_j < 0$ ), une terre rare magnétique légère telle que Nd ( $\alpha_j < 0$ ) ainsi que l'élément non magnétique Y. Dans les composés  $\text{RMn}_{12-x}\text{Fe}_x$ , la compétition Mn/Fe sur le plan des interactions magnétiques devrait conduire à des comportements magnétiques complexes que nous nous sommes proposés d'étudier. Comme avec l'insertion d'éléments légers tels que  $X = \text{H}, \text{C}$  ou  $\text{N}$ , on induit généralement une augmentation substantielle des caractéristiques magnétiques (échange, anisotropie...), nous nous sommes intéressés dans un second temps aux composés interstitiels  $\text{ErMn}_{12-x}\text{Fe}_x\text{X}$  dans

le but de comprendre les modifications structurales et magnétiques induites par la présence de l'interstitiel X.

Cette étude des diverses séries de matériaux  $\text{RMn}_{12-x}\text{Fe}_x\text{X}$  a été menée en utilisant parallèlement trois types de caractérisation :

- ♦ caractérisation à l'échelle atomique (études structurales et magnétiques) par diffraction neutronique.
- ♦ caractérisation magnétique à l'état massif avec des mesures d'aimantation, de susceptibilité alternative (ac), de résistivité...
- ♦ caractérisation spectroscopique atomique (dichroïsme magnétique des rayons X).

L'affinement de la structure nucléaire de ces composés a été la démarche préalable à l'interprétation de leurs configurations magnétiques. Tous les composés étudiés sont isotypes de la structure  $\text{ThMn}_{12}$  (Figure 5).



*L'atome R occupe le site 2a et les atomes M (Mn, Fe) se répartissent sur les 3 sites 8i, 8j et 8f. Le site 2b est connu pour sa faculté d'insertion des éléments légers H, C ou N.*

**Figure 5.** Structure  $\text{RM}_{12}$   
(groupe d'espace  $I4/mmm$ ).

En ce qui concerne leurs propriétés structurales, les études par DN ont permis de préciser :

- ♦ l'importance des facteurs stériques contrôlant l'évolution des paramètres de maille.
- ♦ le schéma d'occupation des différents sites de la structure.
- ♦ les effets de l'insertion de H et C sur les sous-réseaux 3d(Mn, Fe).

L'ensemble des techniques de caractérisation magnétique macroscopique et microscopique a permis une détermination très précise des diagrammes de phases magnétiques des composés  $\text{RMn}_{12-x}\text{Fe}_x\text{X}$  avec l'existence de deux températures d'ordre  $T_N$  et  $T_C$  caractéristiques respectivement d'un ordre antiferromagnétique (AF) et ferromagnétique

(F). Dans les composés  $\text{RMn}_{12-x}\text{Fe}_x$ , une grande variété de configurations magnétiques complexes pour les sous-réseaux de métal de transition en fonction de  $x$  a été observée à  $T = 2\text{K}$  auxquelles vient se superposer une structure F des moments des atomes de terre rare. Cette étude par DN et XMCD a également permis de préciser la nature des couplages R-(Mn, Fe) et Mn-Fe en fonction de  $x$  dans ces composés.

L'insertion d'éléments légers tels que H et C dans la matrice métallique des composés de la série  $\text{ErMn}_{12-x}\text{Fe}_x$  provoque l'évolution du comportement de ces séries de ferro-faible vers ferro-fort avec une modification importante de l'anisotropie magnétocristalline (notamment avec  $X = \text{C}$ ) et la disparition des phénomènes de frustrations magnétiques.

Afin de sonder les propriétés ferromagnétiques potentiellement applicables, il est intéressant de connaître le comportement des poudres du point de vue de l'anisotropie d'orientation et sur le plan coercitivité. Par ailleurs, la qualité d'orientation d'une poudre mélangée à une résine détermine aussi la possibilité d'analyser les propriétés fondamentales d'anisotropie magnétocristalline à partir d'un échantillon composite. C'est pourquoi nous avons orienté le composé ferromagnétique  $\text{ErMn}_4\text{Fe}_8\text{C}$  ( $T_{\text{Curie}} = 450\text{K}$ ) sous forme de poudre et mélangé à une résine époxy, par solidification de ce mélange cylindrique sous l'application d'un champ magnétique de texturation  $H_{\text{ext}} = 0,5\text{T}$ .

L'analyse QTA montre que dans cet échantillon les plans  $\{001\}$  sont préférentiellement alignés perpendiculairement à l'axe du cylindre (normale au plan des figures), avec une densité d'orientation de 3,9 m.r.d. au maximum de la distribution (Figure 6). Une deuxième composante est visible, avec les plans  $\{001\}$  parallèles à cet axe (renforts autour de 1 m.r.d. sur l'équateur de la figure de pôles  $\{001\}$ ).

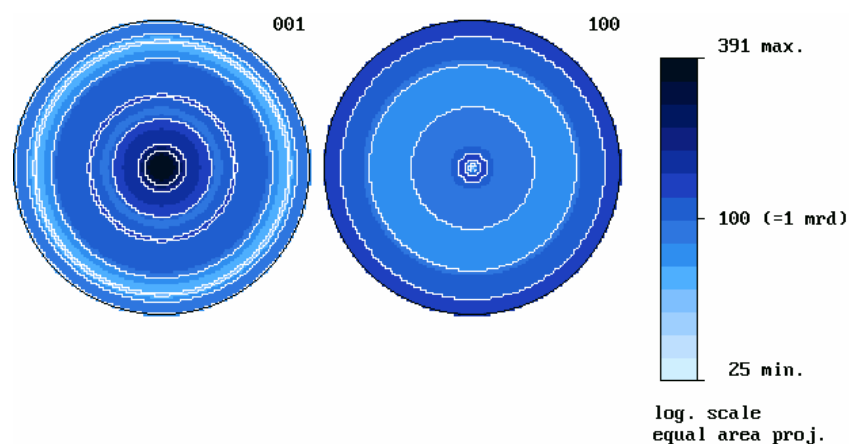


**Figure 6.** Figures de pôles recalculées d'indices simples  $\{001\}$  et  $\{100\}$ .

Les courbes d'aimantation mesurées sur cet échantillon montrent que la direction de facile aimantation de ce système est située dans le plan de base  $(\vec{a}, \vec{b})$  en accord avec le modèle de structure magnétique déterminé par diffraction neutronique lors de ma thèse.

La force de la texture, révélée par l'index de texture  $F^2$  de  $1.3 \text{ m.r.d.}^2$ , est représentative d'une texture relativement faible, cependant, cette faible orientation ( $\approx 4$  fois celle de la poudre libre) suffit à l'obtention de comportements magnétiques anisotropes avec des champs d'anisotropie (champs nécessaires pour amener l'aimantation parallèle au champ appliqué selon la direction de difficile aimantation) pouvant aller jusqu'à 7 T.

En utilisant les résultats affinés de la fonction de distribution des orientations, il a été de plus possible de simuler les courbes d'aimantation anisotropes  $M(H)$  obtenues expérimentalement en utilisant les résultats affinés de la fonction de distribution des orientations cristallines (ATER Le Mans 1999-2000).

Il apparaît dans cette étude que le rôle des éléments interstitiels dans ces matériaux magnétiques prend un caractère déterminant quant aux propriétés fondamentales notamment en ce qui concerne les forces d'échange. De plus, l'augmentation substantielle des caractéristiques magnétiques telles que l'aimantation, l'anisotropie, la température de Curie ..., induites par la présence de l'interstitiel dans les composés riches en fer, ouvre des perspectives pour la réalisation à partir de ces composés de nouveaux aimants permanents.



### 3.2. Films minces conducteurs ioniques (La, Li)TiO<sub>3</sub> : Laboratoire LPEC – Le Mans , ATER (1999-2000)

Depuis quelques années un intérêt scientifique et industriel grandissant est observé pour la recherche de piles à ions lithium afin d'obtenir des systèmes plus légers à haute densité énergétique tout en satisfaisant des critères de sécurité donnés. Les performances globales de ces piles sont conditionnées non seulement par la qualité des électrodes mais aussi par le choix de l'électrolyte qui doit posséder une bonne conductivité ionique et une faible conductivité électronique. Aux matériaux connus de longue date et susceptibles d'être utilisés comme électrolyte (les LISICON, les NASICON...) se sont rajoutés récemment des oxydes à base de terre rare riches en lithium  $\text{La}_{2/3-x}\text{Li}_{3x}\square_{1/3-2x}\text{TiO}_3$  (notés LLTO et où  $\square$  = lacunes) de structure dérivée perovskite  $\text{ABO}_3$  (Groupe d'espace  $\text{P4/mmm}$ ). Ces composés de structure chimique non stœchiométrique présentent une conductivité ionique élevée (maximale pour  $x \approx 0,11$ ) proche de celle des électrolytes liquides usuels ( $\approx 10^{-3} \text{ S.cm}^{-1}$ ) et induite par la mobilité des ions  $\text{Li}^+$  via les sites vacants de la structure LLTO (Figure 7).

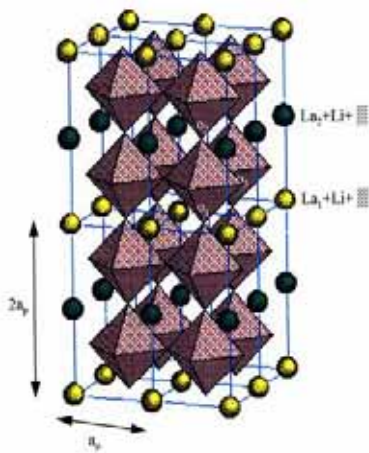


**Figure 7.** Structure quadratique LLTO.

Des cibles de composition de départ  $\text{La}_{0.57}\text{Li}_{0.33}\square_{0.11}\text{TiO}_3$  ( $x \approx 0,11$  correspond au maximum de conductivité ionique dans le massif) ont été élaborées par voie céramique. Un contrôle standard de la pureté de ces cibles a été effectué par diffraction X.

Des dépôts ont été réalisés sur substrats monocristallins  $[100]\text{-Si}$  et  $[100]\text{-MgO}$  à différentes températures de substrat ( $650^\circ\text{C} \leq T_d \leq 800^\circ\text{C}$ ) et pression partielle d'oxygène  $p(\text{O}_2)$  allant de  $9 \cdot 10^{-4}$  à  $7 \cdot 10^{-2}$  mbar. Après le dépôt, les films sont recuits durant une heure in situ en maintenant la température constante à  $T_d$  et sous flux d'oxygène à  $p(\text{O}_2)$  constante.

Les dépôts sur silicium apparaissent par diffraction X toujours amorphes ou très mal cristallisés et sur les spectres Raman, aucun des 3 modes  $E_g$  caractéristiques de la poudre de

LLTO et prédits par la théorie des groupes (de fréquences de vibration 139.7, 236.0 et 523.1  $\text{cm}^{-1}$ ) n'a été observé. Sur ce type de substrat, il semble donc que la diffusion du lithium dans le silicium ne permette pas de stabiliser la phase LLTO.

Les dépôts sur les substrats MgO monocristallins sont beaucoup plus prometteurs. La composition chimique (concentrations en La et Ti) et l'épaisseur de ces films ( $\sim 3000\text{\AA}$ ) a été contrôlée par analyse RBS. La présence de lithium dans ces films a été vérifiée et quantifiée par réaction nucléaire (réaction  $\text{Li}(p, \alpha)$ ).

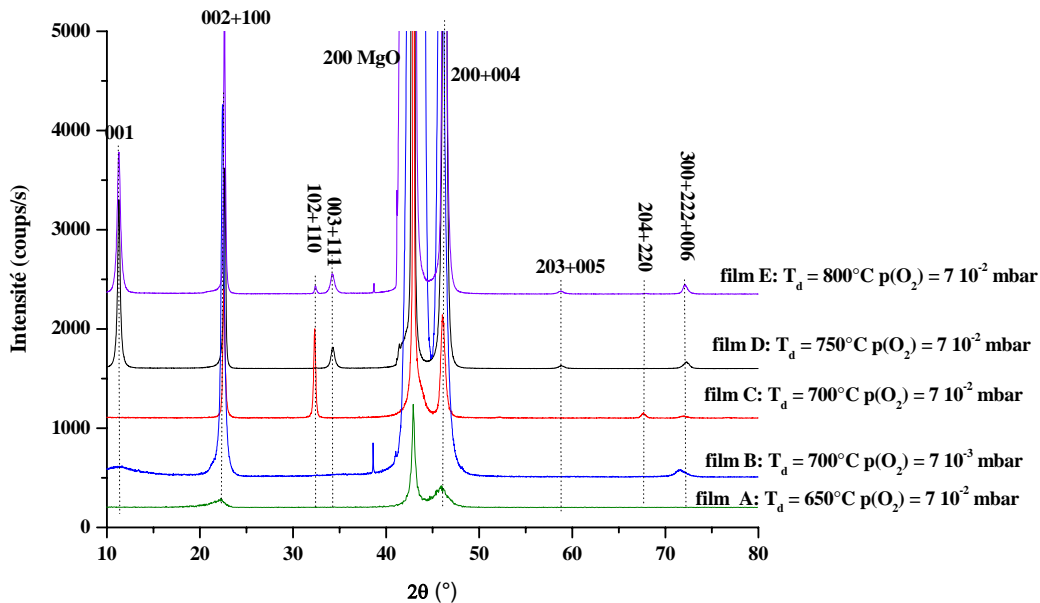


**Figure 8.** Diagrammes RX  $\theta$ - $2\theta$  des films LLTO déposés à différentes  $T_d$  et  $p(\text{O}_2)$  et indexés dans la structure quadratique LLTO (film E).

Quelle que soit  $T_d$ , les diagrammes de diffraction X des films minces (Figure 8) présentent des orientations préférentielles et s'indexent soit dans une maille cubique ( $a = 3,92 \text{\AA}$ ) soit dans la maille quadratique LLTO ( $a_p \approx 3,89 \text{\AA}$ ,  $c_p \approx 7,8 \text{\AA}$ ). En effet, pour les films B, D et E, la présence des raies  $00\ell$  avec  $\ell$  impair impose sans ambiguïté le doublement de l'axe  $\bar{c}$  de la structure LLTO alors que pour le film C, la non observation de ces réflexions peut être due soit à une forte incorporation du lithium dans ces films soit à une texture particulière.

Pour le film A, la seule observation des raies  $h00$  suggère que ce film présente une texture soit avec les axes  $\bar{a}$  parallèles à la normale au plan du film dans un système cubique, soit avec les axes  $\bar{a}$  et  $\bar{c}$  parallèles à la normale au plan du film dans un système quadratique. Afin de lever cette ambiguïté avec la détermination du rapport  $c/a$  pour les films A et C, des scans en  $\chi$  ont été réalisés en faisant varier l'angle  $\chi$  dans le domaine  $40 - 50^\circ$  avec  $\Delta\chi = 0.1^\circ$ ,

domaine centré approximativement autour de l'angle de  $45^\circ$  que fait la raie 102 du LLTO avec l'axe  $\bar{a}$  ou  $\bar{c}$  de la structure LLTO (Figure 9 (a)). Ces scans en  $\chi$  montrent que cette contribution 102 est plutôt centrée autour d'un angle supérieur à  $45^\circ$  (Figure 9 (b)) à relier à un rapport  $c/a$  dans ces films différent de 1. Ces films ont donc bien la structure quadratique LLTO.

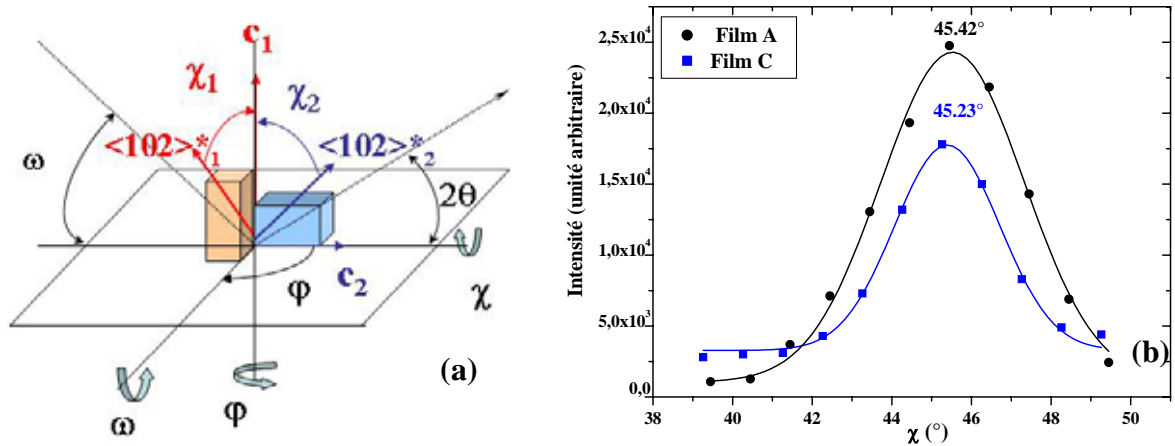


**Figure 9.** (a) Représentation schématique des cristallites de structure quadratique orientés avec  $\bar{a}$  ou  $\bar{c}$  parallèle à la normale au plan du film (b) Scans en  $\chi$  du pôle  $\{102\}$  pour le film A et C.

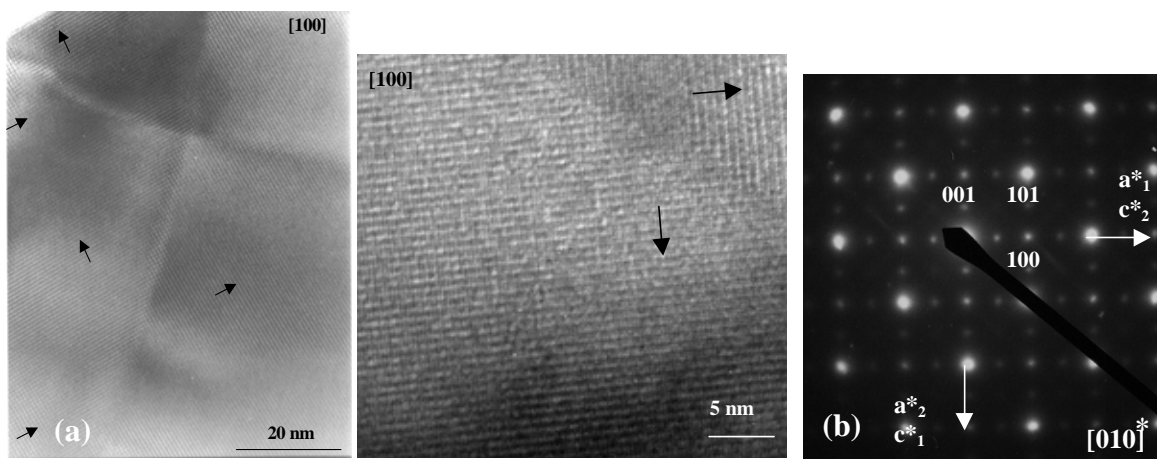


**Figure 10.** (a) Images HRMET de LLTO ( $x \approx 0.08$ ) montrant des microdomaines orientés à  $90^\circ$  (les flèches indiquent les directions  $\langle 001 \rangle$ ). (b) Diagramme correspondant de diffraction électronique mettant en évidence une pseudo-maille cubique de paramètres  $a_p$ . Les indices de Miller sont donnés dans la maille quadratique LLTO ( $a_p$ ,  $c \approx 2a_p$ ).

L'indexation en maille quadratique de ces films a de plus été confirmée par MET (Figure 10) bien que les diagrammes de diffraction électronique peuvent toujours s'indexer dans une pseudo-maille cubique (de paramètre  $a \approx a_p$ ) du fait de la présence de microdomaines orientés à  $90^\circ$ .

Les analyses de texture ont été réalisées sur les films B, C et D. Le même type de texture a été observé pour les films B et D (Figure 11 (a)). Trois orientations préférentielles avec les plans  $\{001\}$ ,  $\{100\}$  et  $\{111\}$  parallèles au plan de l'échantillon, sont présentes avec une très forte texture (jusqu'à 95 fois celle d'une poudre libre au maximum de l'orientation). La majorité des plans  $\{001\}$  sont préférentiellement alignés parallèlement à la surface des films B et D. Pour le film C, la composante majoritaire de texture précédente est également observée avec cependant un maximum d'orientation plus faible (48 m.r.d) alors que la composante d'orientation  $\{111\}$  est remplacée par une composante où les plans  $\{102\}$  et  $\{110\}$  sont parallèles à la surface du film (Figure 11 (b)). L'absence des réflexions  $00\ell$  dans les diagrammes RX du film C est donc due sans aucune ambiguïté à un taux de lithium incorporé dans ce film beaucoup plus important que dans les autres dépôts.

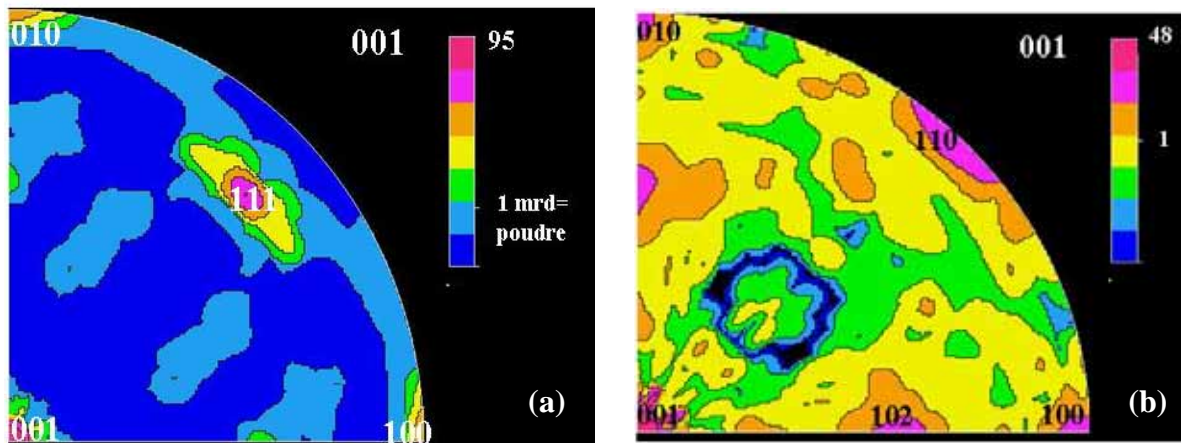


**Figure 11.** Figures de pôles inverses 001 pour les films (a) B et D et (b) pour le film C

Contrairement aux substrats Si, la présence de MgO stabilise donc fortement la structure des films LLTO par des relations d'épitaxies suivantes pour les composantes mineures de texture:



(111)-LLTO // (001)-MgO; [135]\*-LLTO // [100]-MgO; [ $\bar{1}\bar{3}5$ ]-LLTO // [010]-MgO

En ce qui concerne leurs propriétés physiques, les mesures d'impédances complexes en fonction de la température ont permis de déterminer pour le film C riche en lithium des valeurs d'énergie d'activation (0,33 eV) et de conductivité électronique ( $\sigma \approx 10^{-9} \text{ S.cm}^{-1}$ ) du même ordre de grandeur que celles obtenues dans les matériaux massifs.

### 3.3. Films minces d'InN déposés par épitaxie en phase vapeur (MOPVE) : Laboratoire SIFCOM - Thèse de P. Singh (soutenue le 7 Décembre 2005)

Les semi-conducteurs à base de composés nitrurés (GaN, AlN, InN) et leurs alliages sont l'objet depuis une dizaine d'années de recherches intensives afin de maîtriser l'élaboration de composants et de déterminer leurs propriétés optiques. La connaissance des propriétés physiques de ces hétérostructures III-V (décalage de bandes, énergie de bande interdite, gradualité des interfaces, présence de champs électriques internes...) est indispensable pour la conception de composants optoélectroniques fiables et performants tels que les diodes électroluminescentes, lasers et détecteurs... Parmi ces semiconducteurs, InN est le moins connu des nitrures, et ce très probablement en raison des difficultés rencontrées lors de sa croissance (température de dissociation faible, vitesse de croissance très lente, manque de substrats adaptés en maille...). Cependant, récemment il a été mis en évidence que l'utilisation des techniques de dépôt telles que l'épitaxie par jet moléculaire (MBE) et par MOCVD (MOPVE) permettait de déposer des films d'InN de bonne qualité cristalline, films qui présentent de plus de fortes potentialités d'application dans le domaine de la photonique et des énergies renouvelables (cellules solaires).

Les films d'InN étudiés en vue de leur optimisation dans le cadre de la thèse de P. Singh, ont été déposés par MOPVE à des températures  $T_{\text{dépôt}}$  variant entre 400 et 650°C sur des substrats tels que [001]-Al<sub>2</sub>O<sub>3</sub>/GaN (échantillons A50, A52, A53 et A60) ou [001]-Al<sub>2</sub>O<sub>3</sub>. La détermination des relations d'épitaxie et des distributions d'orientations cristallines dans ces films a été réalisée par des analyses de QTA par diffraction de rayons X (( $\chi$ ,  $\varphi$ ) scans avec  $\Delta\chi = \Delta\varphi = 0.5^\circ$  et/ou  $0.1^\circ$ ).

Les films résultants sont très texturés avec une composante de texture <001> parallèle à la normale aux films. Cette analyse par QTA a permis de déterminer les relations d'hétéro-épitaxie suivantes, qui ont été confirmées localement par microscopie électronique à haute résolution :

$$[001] \text{ Al}_2\text{O}_3 // [001] \text{ GaN} // [001] \text{ InN} \text{ ou } [001] \text{ Al}_2\text{O}_3 // [001] \text{ InN} \\ [1\bar{1}20]_{\text{Al}_2\text{O}_3} // [10\bar{1}0]_{\text{InN, GaN}} \text{ et } [10\bar{1}0]_{\text{Al}_2\text{O}_3} // [1\bar{1}20]_{\text{InN, GaN}} .$$

Ces analyses de texture ont également mis en évidence des distributions angulaires très fines en  $\chi$  et en  $\varphi$  et il apparaît sans ambiguïté que l'introduction d'une couche de GaN sur le

substrat de saphir augmente la qualité cristalline des films d'InN :  $\Delta\phi$  décroît de  $1.19^\circ$  à  $0.72^\circ$  pour la raie 103 de InN suite à l'introduction du GaN pour des films élaborés avec  $T_{\text{dépôt}} = 475^\circ\text{C}$ . Ceci est de plus corrélé à l'augmentation de l'intensité du signal de photoluminescence dans ces films.

Lorsque  $T_{\text{dépôt}}$  augmente de  $400^\circ\text{C}$  à  $550^\circ\text{C}$ , la qualité cristalline des films est améliorée alors que pour  $T_{\text{dépôt}} = 650^\circ\text{C}$  on observe une dispersion  $\Delta\phi$  5 fois plus importante (Tableau 1). Cette valeur de  $\Delta\phi$  élevée est caractéristique de la présence de domaines pivotés autour de la direction  $\langle 002 \rangle$ , domaines qui sont à l'origine de fautes d'empilement et de défauts dans le film. A cette température, on commence à observer une dissociation de l'InN ainsi que la présence d'agrégats d'In, et cette diminution de la qualité cristalline des films se traduit par une dégradation de leurs propriétés électriques et optiques.

La mise en évidence des corrélations existant entre propriétés structurales et physiques de ces films a permis de déterminer leur condition optimale de dépôt correspondant à  $T_{\text{dépôt}} = 550^\circ\text{C}$ .

	Raies 103 d'InN				Raies 103 de GaN				Raies 104 d'Al <sub>2</sub> O <sub>3</sub>			
$\chi_{\max}$ (°)	31.839	31.66	32	31.85	32.13	32.019	32.12	31.98	-	-	-	-
$\Delta\chi$ (°)	0.77	0.78	0.77	1.2	0.63	0.665	0.66	0.65	-	-	-	-
$\varphi_{\max}$ (°)	17.62	17.79	17.92	17.69	17.59	18.12	17.86	18.02	47.271	47.64	48.147	48.3
$\Delta\varphi$ (°)	0.72	0.365	0.395	1.70	0.24	0.24	0.25	0.25	0.15	0.16	0.16	0.15
Films	A60	A53	A50	A52	A60	A53	A50	A52	A60	A53	A50	A52
T <sub>dépôt</sub>	475°C	500°C	550°C	650°C	475°C	500°C	550°C	650°C	475°C	500°C	550°C	650°C

**Tableau 1.** Evolution en fonction de T<sub>dépôt</sub> des distributions angulaires en  $\chi$  et  $\varphi$  des films d'InN déposés sur substrats Al<sub>2</sub>O<sub>3</sub>/GaN.





**PUBLICATIONS DU**

**CHAPITRE 1**





ELSEVIER

Available online at [www.sciencedirect.com](http://www.sciencedirect.com)

SCIENCE @ DIRECT®

Journal of Magnetism and Magnetic Materials 257 (2003) 258–269

Journal of  
magnetism  
and  
magnetic  
materials

[www.elsevier.com/locate/jmmm](http://www.elsevier.com/locate/jmmm)

# Texture and magneto-crystalline anisotropy analysis of an oriented $\text{ErMn}_4\text{Fe}_8\text{C}$ powder sample

M. Morales<sup>a,\*</sup>, D. Chateigner<sup>b</sup>, D. Fruchart<sup>c</sup>

<sup>a</sup>Laboratoire d'Etude et de Recherche sur les Matériaux, ISMRA, 6 Boulevard Maréchal Juin, 14050 Caen Cedex, France

<sup>b</sup>Laboratoire de Cristallographie et Sciences des Matériaux, ISMRA, 6 Boulevard Maréchal Juin, 14050 Caen Cedex, France

<sup>c</sup>Laboratoire de Cristallographie, CNRS, BP166, 38042 Grenoble Cedex 09, France

Received 28 February 2002; received in revised form 4 September 2002

## Abstract

Powder samples of the ternary carbide  $\text{ErMn}_4\text{Fe}_8\text{C}_{x-1}$  were oriented under a low magnetic field  $H \sim 0.5$  T. Analysis of the crystal texture of the samples confirms that the compound is of easy-plane type, in agreement with magnetization measurements and neutron diffraction experiments performed elsewhere. Both the latter techniques have revealed that the magnetic arrangement is rather complicated, as supported by competing contributions to magneto-crystalline anisotropy. However, assuming a reasonably simple expression for the magneto-crystalline anisotropy valid at high temperature only, the texture analysis, performed at 300 K, has allowed simulation of the magnetization versus field curve for this planar ferrimagnetic structure. A comparison with the experimental magnetization curve reveals the onset of a first-order magnetization process taking place under an applied field up to 1.8 T.

© 2002 Elsevier Science B.V. All rights reserved.

PACS: 75.30.Gw; 71.20.Lp; 61.10.Yh; 75.60.-d

Keywords: 4f–3d Intermetallics; Interstitial compounds; X-ray quantitative texture analysis; Magnetic anisotropy; Magnetization curves

## 1. Introduction

Most of the iron-rich intermetallic compounds of rare-earth elements (R) and 3d transition metals (M) are characterized by the existence of interstitial sites suited for the insertion of elements such as H, C or N. Thanks to the insertion of light elements in compounds having the  $\text{ThMn}_{12}$  structure type, most of their fundamental char-

acteristics, such as the 3d magnetization, the Curie temperature  $T_C$  and the magneto-crystalline anisotropy, are modified [1]. Previous studies on the insertion of H and C atoms in the  $\text{ErMn}_{12-x}\text{Fe}_x$  compounds ( $x \leq 9$ ) have revealed large modifications of the magnetic properties induced by the interstitial atoms; firstly a marked increase of  $T_C$  (e.g.  $\text{ErMn}_4\text{Fe}_8\text{C}_{x-1}$ ,  $\Delta T_C/T_C = 85\%$ ) and secondly a drastic change from easy-axis to easy-plane behavior with the insertion of C [2,3].

In order to optimize extrinsic anisotropic properties, a lot of effort has been devoted in the last decade to the development of texturing

\*Corresponding author. Tel.: +33-2-31-45-25-02; fax: +33-2-31-45-26-60.

E-mail address: [magali.morales@ismra.fr](mailto:magali.morales@ismra.fr) (M. Morales).

processes. As the ability for magnetic moments to be aligned along the main crystal axis (easy-axis materials) is of fundamental importance for hard magnetic properties, many studies have been devoted to the characterization of the magneto-crystalline anisotropy via magnetization curves, e.g. in intermetallic compounds [4,5]. These analyses generally concentrate on the estimation of the crystallite distribution and the intrinsic magnetic properties (crystalline anisotropy constants  $K_1$ ,  $K_2$ , sample polarization, etc.) from the magnetization curves, using differently defined orientation or misalignment parameters in easy-axis ferromagnetic compounds [4,5]. Since many parameters influence the magnetization curves, it seems relevant to measure them independently as much as possible. Besides, such orientation distribution factors are accessible for any crystalline material using diffraction measurements, and can be estimated using quantitative texture analysis (QTA) [6,7].

The aim of this paper is to simulate at  $T = 300$  K the magnetization curve of the oriented easy-plane ferrimagnetic  $\text{ErMn}_4\text{Fe}_8\text{C}$  sample [2,8] using the texture parameters (degree of orientation of the sample) determined by X-ray QTA analysis and assuming a reasonably simple expression for the magneto-crystalline anisotropy at high temperature.

## 2. Experimental

The starting compound  $\text{ErMn}_4\text{Fe}_8$  was prepared by induction melting of the metal constituents in a water-cooled copper crucible under a purified argon atmosphere. For the synthesis of the ferrimagnetic  $\text{ErMn}_4\text{Fe}_8\text{C}$  carbide, finely crushed powder of the starting compound was mixed with an excess amount of anthracene (by 10%) [8]. The mixed powders compacted into pellets, were sealed under vacuum in quartz tubes and annealed at  $T = 623$ – $673$  K during 4 days. Above 623 K, the anthracene decomposition provides elemental carbon, making possible the formation of ternary carbides [9]. A home-made thermomagnetic torque was used to determine the change in  $T_C$  upon carburization from 200 to 370 K, respectively, for

the starting compound and the carbon charged compound [8]. In order to determine the macroscopic easy magnetization direction (EMD) and to estimate the magnetic anisotropy, two differently aligned samples were prepared by polymerization of a resin-powder mixture under an applied magnetic field,  $H_{\text{text}}$ , of 0.5 T. Both samples were 4 mm diameter and 5 mm long cylinders. Sample A was solidified with  $H_{\text{text}}$  applied parallel to the  $z$ -axis of the cylinder (Fig. 1, right column), while Sample B was rotated (10 rd/min) around its  $z$ -axis during polymerization [10] with  $H_{\text{text}}$  applied perpendicular to it (Fig. 1, left column).

Room temperature X-ray diffraction patterns were recorded in the Bragg–Brentano geometry ( $\theta$ – $2\theta$  scans) on the two samples, with the scattering vector  $\mathbf{S}(\mathbf{q})$ , aligned parallel to the  $z$ -axis for both samples (Fig. 1). The EMD was then determined by a qualitative interpretation of the preferred orientation of the two samples, by comparing relative intensities of the diffraction peaks with those of the free powder.

X-ray QTA was performed on Sample B using a Huber 4-circles diffractometer and the INEL curved position sensitive detector, which spans a  $120^\circ$  range in  $2\theta$ , for the simultaneous acquisition of several pole figures [11]. These measurements

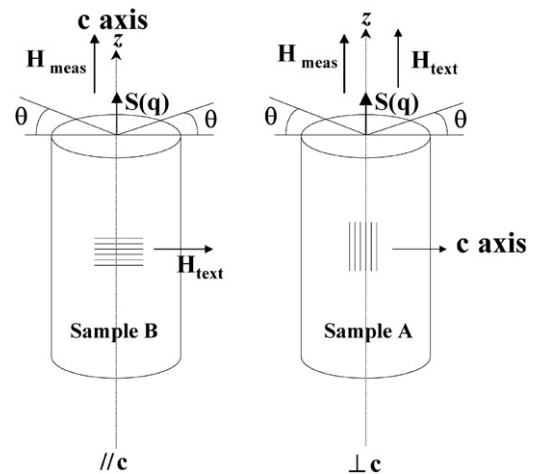


Fig. 1. Traditional technique (right column) and rotation alignment procedure (left column) used for the alignment of samples A and B, respectively. The geometry of X-ray diffraction measurements ( $\mathbf{S}(\mathbf{q})$ ) and the configurations for the magnetization measurements ( $H_{\text{meas}}$ ) are also shown.

were made in order to determine the possibility to orient the magnetization axes under a relatively low magnetic field, and to determine the quantitative distribution of the  $c$ -axes used later in the anisotropic magnetization curve simulation.

Magnetization measurements were carried out on the free powder and on the aligned samples using an automated extraction magnetometer, in the 2–300 K temperature range. Measurements were performed for the oriented powders with an applied magnetic field,  $H_{\text{meas}}$ , parallel and perpendicular to  $H_{\text{text}}$  for Samples A and B, respectively (Fig. 1).

Neutron diffraction experiments were performed at  $T = 300$  K on the  $\text{ErMn}_4\text{Fe}_8\text{C}$  random powder using the D1B diffractometer ( $\lambda = 2.522 \text{ \AA}$ ) of the ILL high-flux reactor in order to determine the microscopic magnetic properties.

### 3. Results and discussion

#### 3.1. X-ray diffraction analysis

Classical X-ray diffraction diagrams recorded on the faces perpendicular to the  $z$ -axis of the samples and showing the  $\{220\}$  and  $\{002\}$  diffraction lines are presented in Fig. 2. The inset of this figure shows the full diffraction pattern of Sample B, which exhibits peak ratios different from those of a random powder, indicating the existence of a texture. However, all the lines are visible, revealing a relatively low texture strength. Looking at specific peaks, for instance those associated with the  $\{220\}$  and  $\{002\}$  families of planes, allows a first qualitative estimate of the texture. The patterns measured with  $\mathbf{S}(\mathbf{q})$  parallel (Sample A) and perpendicular (Sample B) to  $H_{\text{text}}$  exhibit different  $\{220\}/\{002\}$  intensity ratios,

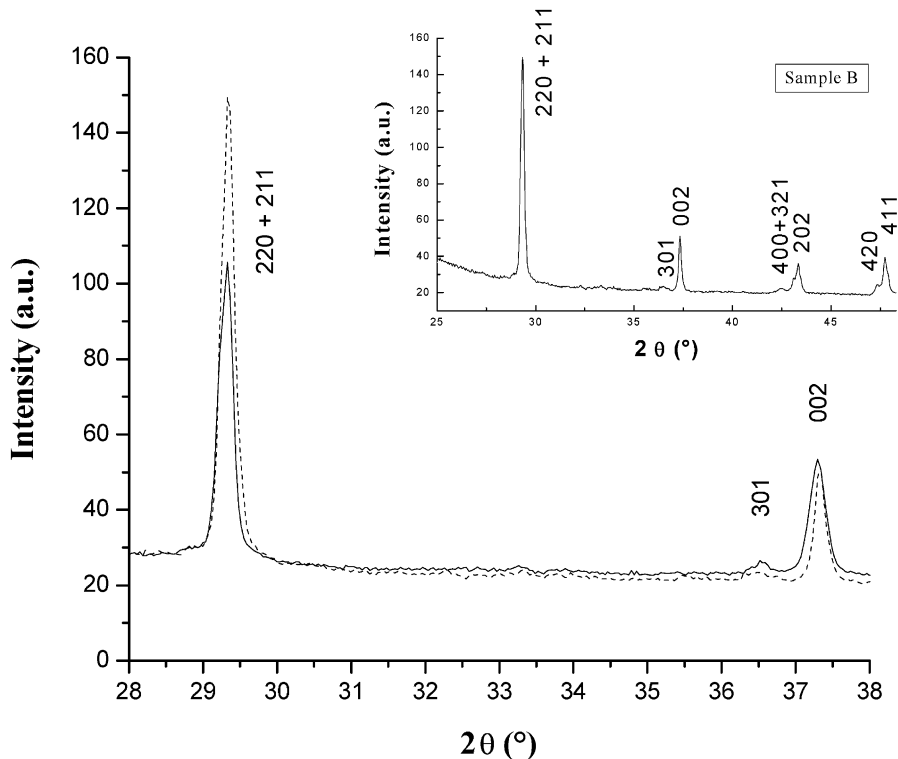


Fig. 2. X-ray diffraction pattern of the oriented  $\text{ErMn}_4\text{Fe}_8\text{C}$  compound with  $H_{\text{text}}$  parallel (Sample A, dotted line) and perpendicular (Sample B, full line) to the cylinder axis. The inset shows the full diffraction pattern of Sample B.

with favored  $\{220\}$  reflections when  $H_{\text{text}}$  is applied parallel to  $\mathbf{z}$  (Sample A), and favored  $\{002\}$  reflections for  $H_{\text{text}}$  perpendicular to  $\mathbf{z}$ . This indicates that the mean EMD is located in the basal plane of the structure.

### 3.2. Quantitative texture analysis (QTA)

Quantitative texture analysis was performed on Sample B (oriented carbide with  $H_{\text{text}}$  perpendicular to the  $z$ -axis). We firstly verified that no significant change in the diffracted lines occurred when rotating the sample around the azimuth  $\varphi$  axis of the diffractometer, aligned parallel to  $\mathbf{z}$ . Pole figures were then measured by scanning the tilt angle of the goniometer,  $\chi$ , between  $0^\circ$  and  $70^\circ$  [11]. For the refinement of the orientation distribution function (ODF), we used the  $\{321/400/202\}$  and  $\{420/411\}$  groups of reflections, thus covering a large distribution of orientations. The experimental normalized pole figures (left column of Fig. 3(a)) determine the distribution of the normal to the  $\{hkl\}$  planes,  $\langle hkl \rangle^*$ . These pole figures are representative of a so-called “fibre texture”, with crystalline axes randomly distributed around their normal ( $z$ -axis). The ODF refined using the Williams–Imhof–Matthies–Vinel (WIMV) method allows the recalculation of the experimental pole figures (Fig. 3(a), right column) [6]. A good reproduction of the experimental pole figures is obtained and this recalculation allows the completion of the blind and non-measured zones (appearing in white on the experimental pole figures) [11]. The average reliability factor [7] calculated on the  $\{321/400/202\}$  and  $\{420/411\}$  pole figures is only 1.2% and attests for the quality of the ODF refinement. Calculation of the low indices  $\{001\}$  and  $\{100\}$  pole figures allows a simpler texture visualization (Fig. 3(b)). The  $\{001\}$  planes are preferentially aligned perpendicular to the cylinder  $z$ -axis (normal of the figure plane) with a maximum orientation density about 3.9 times that of a random powder (measured in mrd units: multiple of a random distribution), showing a relatively low texture strength. A second orientation is observed with the  $\{001\}$  planes parallel to this axis (reinforcements observed around 1 mrd on the equator of

the  $\{001\}$  pole figure). The minimum orientation density of 0.5 mrd indicates that 50% of the sample volume is randomly oriented.

From the point of view of the magnetic anisotropy, it is important to check if  $\{hkl\}$  planes align with their normals along  $\mathbf{z}$ , which would be difficult to evidence on the recalculated pole figures of Fig. 3(b). This can be directly checked by looking at the inverse pole figure calculated for the  $z$ -direction (Fig. 4). In this figure we have represented the Miller indices of the components having planes parallel to  $\mathbf{z}$  and a maximum value larger than 1 mrd. One can retrieve the previously described  $\{001\}$  major and the  $\{100\}$  minor components, and also two other minor ones:  $\{221\}$  and  $\{201\}$ .

The texture strength is quantified with the texture index  $F^2$  equal to  $1.3 \text{ mrd}^2$ . The degree of “texture disorder” is given by calculating the entropy  $S$  found to be equal to  $-0.13$ . The values of the  $F^2$  and  $S$  indicate a relatively weak texture [4] but this orientation (4 times the free powder) would be sufficient to induce a large anisotropy of the magnetic behavior.

### 3.3. Magnetization measurements

In order to determine the magnetic properties associated with anisotropy, magnetization measurements  $M(H)$  in the 2–300 K temperature range have been performed on the oriented  $\text{ErMn}_4\text{Fe}_8\text{C}$  samples. The magnetic field used for these measurements,  $H_{\text{meas}}$ , was applied parallel and perpendicular to the  $c$ -axis for Samples B and A, respectively (Fig. 1) in order to determine the EMD. The notations  $M_{\parallel}$  and  $M_{\perp}$  correspond to the magnetization curves measured, respectively, on Sample B with  $\mathbf{H}_{\text{meas}} \parallel \mathbf{z}$  (parallel to the mean  $\mathbf{c}$ -axis direction) and on Sample A with  $\mathbf{H}_{\text{meas}} \perp \mathbf{z}$  (perpendicular to the mean  $\mathbf{c}$ -axis direction).

Whatever the temperature (Fig. 5), the EMD corresponds to the magnetization measurements performed on Sample B ( $H_{\text{meas}} \perp H_{\text{text}}$ ), i.e. to the basal planes ( $\mathbf{a}$ ,  $\mathbf{b}$ ) of the structure, revealing the absence of spin reorientation transition (SRT) contrary to what was observed in the parent  $\text{RFe}_{10.5}\text{Mo}_{1.5}\text{X}$  compounds ( $X = \text{H}, \text{C}$ ) [12]. Differences are observed in the  $M(H)$  curves between

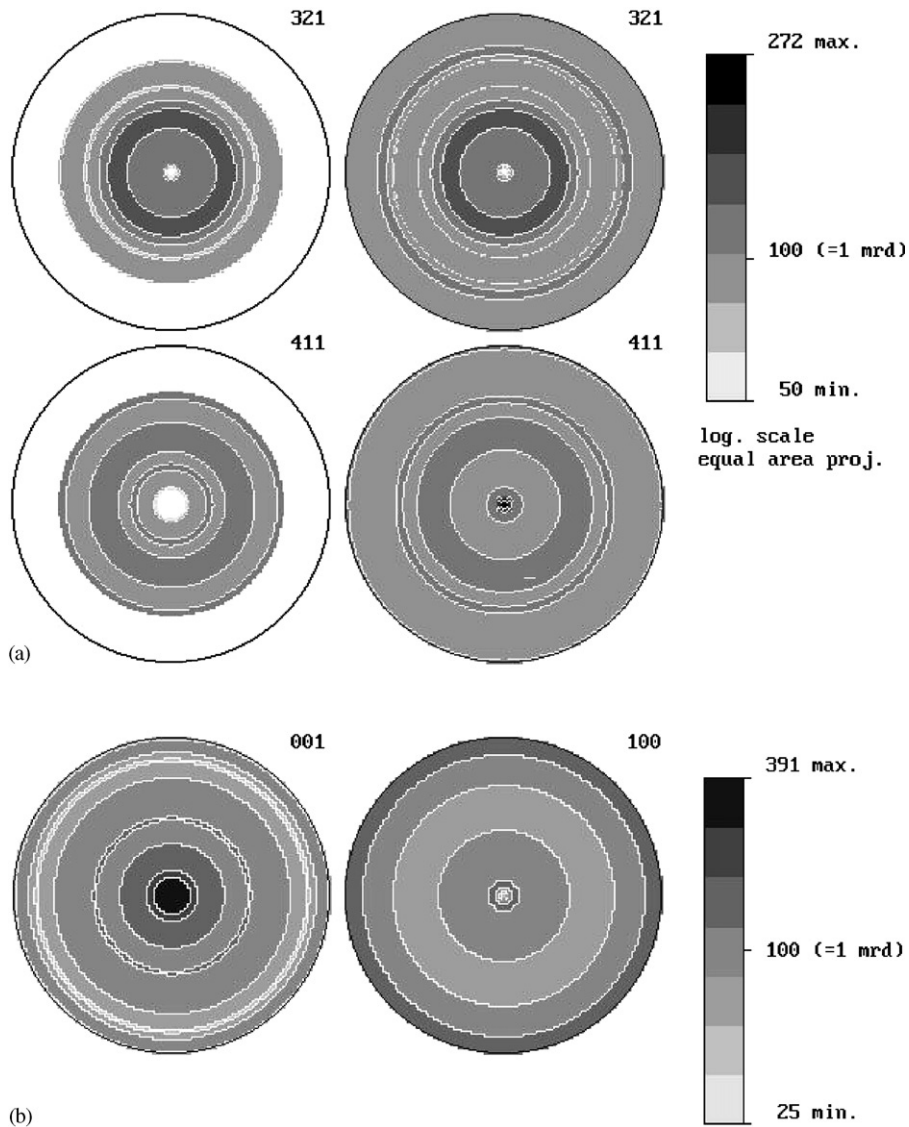


Fig. 3. (a) Experimental normalized  $\{321/400/202\}$  and  $\{420/411\}$  overlapped pole figures of Sample B (left column) and recalculated ones (right column) from the ODF. (b) Low-indices  $\{001\}$  and  $\{100\}$  recalculated pole figures. Logarithmic density scale, equal area projection.

the low and the room temperature ranges as seen in Fig. 5. From these curves, the anisotropy field  $H_A$  was determined as the junction point for which the applied field makes  $M_{\parallel} = M_{\perp}$ . Its thermal variation shows a maximum of 9 T close to 80 K (Fig. 6). In the  $RT_{12}$  structure type compounds, the magneto-crystalline anisotropy results from

the competition between the rare-earth R and  $3d(T)$  sublattices anisotropy. The latter dominates at high temperatures and could give rise to SRT if the former was dominating at low temperature, but it is not the case here [1]. Furthermore, it clearly appears that at lower temperatures (e.g. 4 K) the junction point is more complex than a



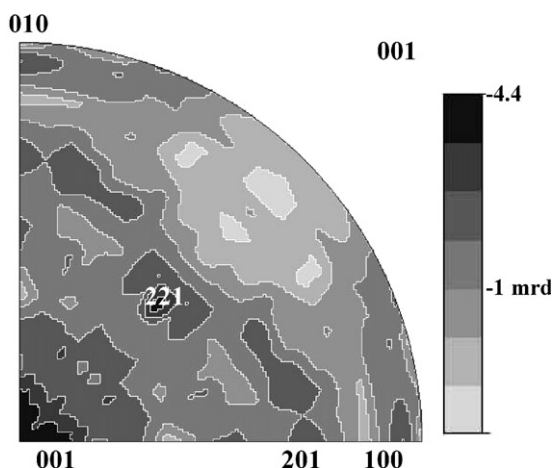


Fig. 4. Inverse pole figure calculated for the  $z$ -direction of Sample B, showing the low-density levels of the secondary components of the texture, significant of their low volume ratio. Logarithmic density scale, equal area projection.

simple anisotropy field  $H_A$  (Fig. 5), with the occurrence of a first-order magnetization process (FOMP) induced by the field, as already observed elsewhere in parent compounds [12,13,14].

The area in-between  $M_{\parallel}$  and  $M_{\perp}$  curves was used for a first estimate of the magneto-crystalline anisotropy energy  $W_A$  (Fig. 6). It markedly increases with temperature with a maximum close to 100 K and then exhibits a normal decrease going to  $T_C = 370$  K. The relative difference observed at a temperature lower than 125 K between  $H_A$  and  $W_A$  should result from more complicated anisotropy contributions, e.g. from rare-earth crystal electrical field (CEF) with possibly higher order terms [14].

### 3.4. Neutron diffraction

Neutron diffraction experiments performed at 300 K on the free  $\text{ErMn}_4\text{Fe}_8\text{C}$  powder allow the determination of the magnetic structure (Fig. 7) [2,3]. In agreement with the magnetization measurements and texture analysis, the collinear ferrimagnetic structure lies within the basal plane (a, b). This ferrimagnetic arrangement belongs to the  $E_g$  irreducible representation of the  $I4/mmm$  space group [2,3] and has been yet observed in the parent compounds  $\text{RFe}_{12-x}\text{Mo}_x\text{X}$  ( $X = \text{H}, \text{C}, \text{N}$ )

[11]. The antiferromagnetic coupling scheme between Er and the 3d sites of the  $\text{ThMn}_{12}$  structure takes place in agreement with the Campbell theory for heavy rare-earth atoms [15]. Since the 8j and 8f sites are preferentially occupied by iron atoms, no ordered ferromagnetic moment was found at room temperature on the 8i sites (preferentially occupied by manganese atoms). The carbon atoms are located in the 2b site of the  $\text{ThMn}_{12}$  structure type [2] in between the 2a positions of the Er atoms. The direct C–Er bonds strongly modify the CEF coefficients of the rare-earth atoms, which, in principle, give the largest contributions to the magneto-crystalline anisotropy [12,14]. This transformation from the easy-axis magnetic behavior of  $\text{ErMn}_4\text{Fe}_8$  to the easy-plane magnetic behavior of  $\text{ErMn}_4\text{Fe}_8\text{C}$  [2] fully agrees with the empirical rules determined for the parent  $\text{RFe}_{12-x}\text{Mo}_x\text{X}$  ( $X = \text{H}, \text{C}, \text{N}$ ) series [11]. Indeed, for the present case where the second-order Stevens factor  $\alpha_J$  is positive [16], the C (or N) insertion markedly reduces the easy-axis character supported by the R atoms, and even transforms it into an easy-plane one [12]. The refined values of the ferromagnetic moments for each crystallographic site, determined using the general least-squares Material eXecutive Diffraction program (MXD) [17], are at  $T = 300$  K (in  $\mu_B/\text{f.u.}$ ):  $\mu_{8i} = 0$ ,  $\mu_{8j} = -0.8(1)$ ,  $\mu_{8f} = -1.3(1)$  and  $\mu_{\text{Er}} = +1.7(1)$ . They correspond to a reliability factor of 2.4% [17].

### 3.5. Numerical simulation of the $M(H)$ curves at $T = 300$ K

The magnetization  $M(H_{\text{meas}})$  in an applied magnetic field  $H_{\text{meas}}$  can be expressed by

$$M(H_{\text{meas}}) = M_S \cos(\theta_0 - \theta), \quad (1)$$

where  $M_S$  is the saturation magnetization,  $\theta$  is the angle between the  $c$ -axis of the crystal and the magnetization direction, and  $\theta_0$  the angle between  $H_{\text{meas}}$  and the  $c$ -axis of the crystallites (Fig. 8). At room temperature, the high-order anisotropy constants  $K_2, K_3, \dots$  are negligible in the  $\text{ThMn}_{12}$  structure type compounds [13,14,18]. Although the exchange forces between the 3d(Mn, Fe) and Er sublattices are strong, the collinear magnetic arrangement of the  $\text{ErMn}_4\text{Fe}_8\text{C}$  compound can

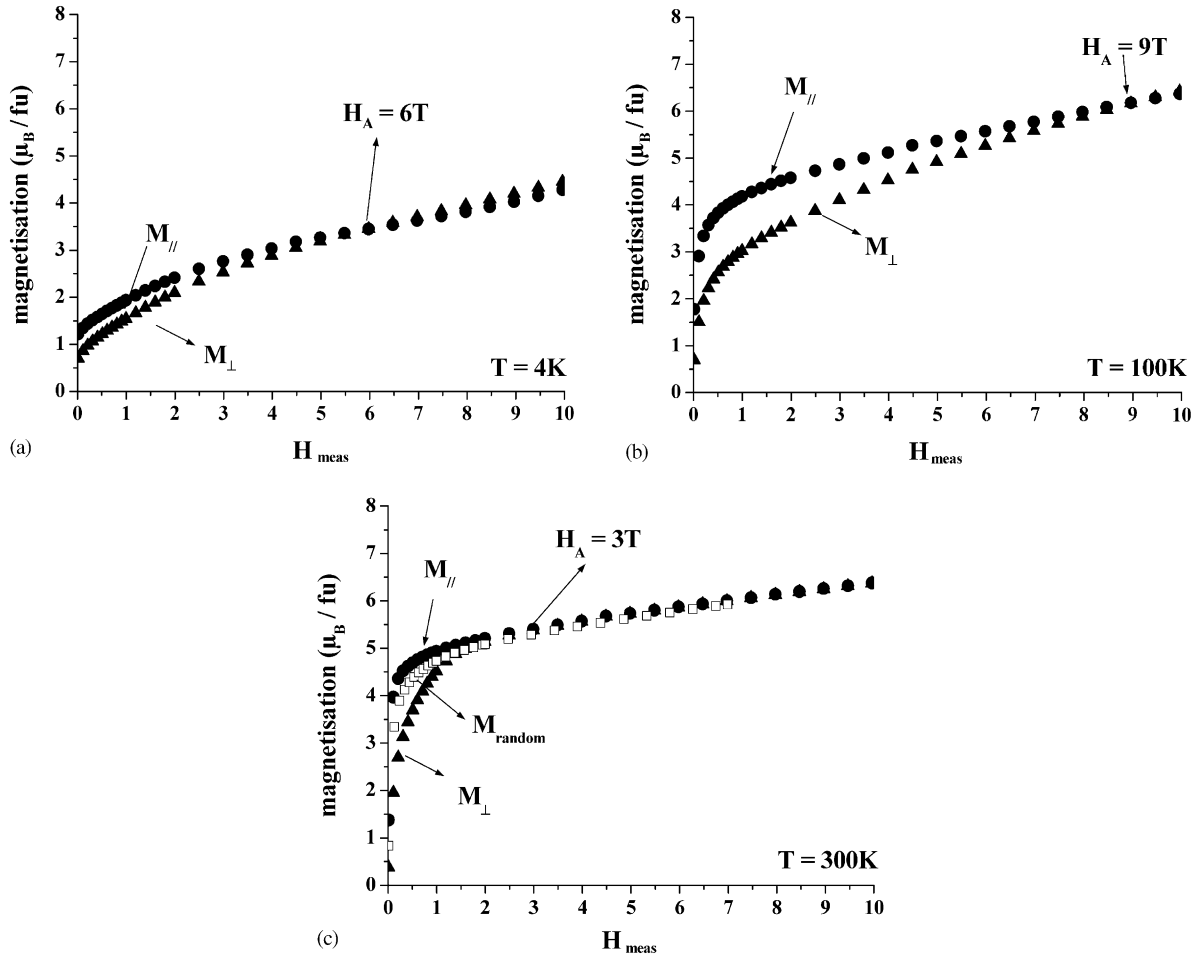


Fig. 5. Thermal behaviour of  $M_{\parallel}$  (i.e. Sample B,  $\mathbf{H}_{\text{meas}} \parallel \mathbf{c}$ ) and  $M_{\perp}$  (i.e. Sample A,  $\mathbf{H}_{\text{meas}} \perp \mathbf{c}$ ) magnetization curves of the  $\text{ErMn}_4\text{Fe}_8\text{C}$  oriented compounds at (a)  $T = 4\text{K}$ , (b)  $T = 100\text{K}$  and at (c)  $T = 300\text{K}$ . For  $T = 300\text{K}$ , the signal measured on the free powder  $M_{\text{random}}$  is also represented.

be considered as quasi-rigid for the  $H_{\text{meas}}$  not too large. Consequently, considering that the 3d and Er sublattices rotate in the same way with  $H_{\text{meas}}$ , the energy of the sample in an applied magnetic field can be expressed at  $T = 300\text{K}$  by

$$E(H_{\text{meas}}) = K_1 \sin^2 \theta - HM_S \cos(\theta_0 - \theta), \quad (2)$$

where  $K_1$  is the first-order phenomenological anisotropy constant [14]. In this equation, the first term,  $K_1 \sin^2 \theta$ , represents the anisotropy energy and the second,  $-HM_S \cos(\theta_0 - \theta)$ , the Zeeman energy. Here, this assumption appears relevant at high temperature only, since at low temperatures a

more complex magnetic behavior occurs [2]. Under the equilibrium condition we have

$$\frac{dE}{d\theta} = 0 \quad (3)$$

which gives from Eq. (2)

$$H_{\text{meas}} = \frac{2K_1 \sin \theta \cos \theta}{M_S \sin(\theta_0 - \theta)}. \quad (4)$$

With an anisotropy field  $H_A = 2K_1/M_S$  [14], the equilibrium condition becomes

$$\frac{H_{\text{meas}}}{H_A} = \frac{\sin \theta \cos \theta}{\sin(\theta_0 - \theta)}. \quad (5)$$

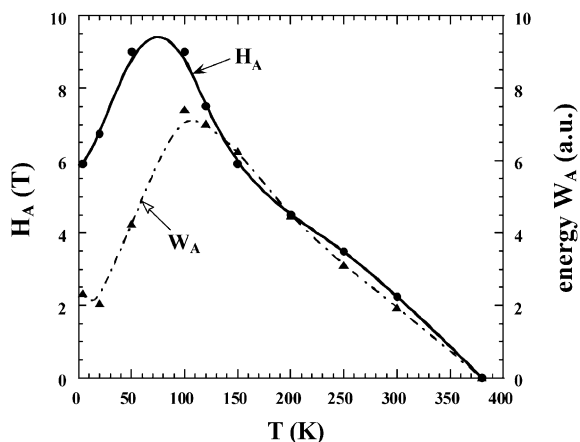


Fig. 6. Thermal behavior of the anisotropy field  $H_A$  (—) and magnetocrystalline anisotropy energy  $W_A$  (· · ·) deduced from the anisotropic magnetization measurements.

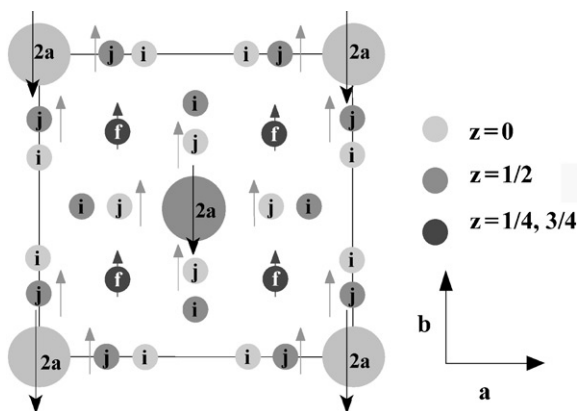


Fig. 7. Ferrimagnetic structure of the  $\text{ErMn}_4\text{Fe}_8\text{C}$  in the basal plane (a, b) at  $T = 300\text{ K}$  deduced from neutron diffraction experiments.

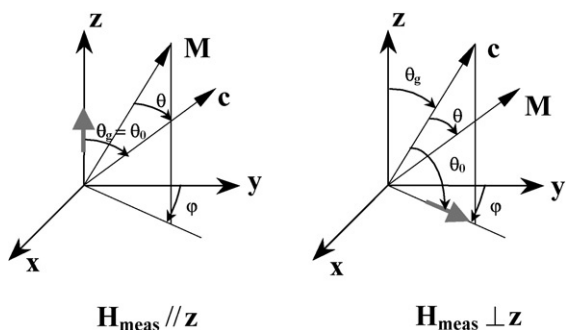


Fig. 8. The two configurations (a)  $H_{\text{meas}} \parallel c$  and (b)  $H_{\text{meas}} \perp c$  used for the measurement of the magnetization curves.

As magnetization curves in  $\text{ErMn}_4\text{Fe}_8\text{C}$  are not saturated for a  $H_{\text{meas}}$  of 10 T, we evaluate the saturation magnetization  $M_S$  using a polynomial extrapolation [19]. Thus, under strong applied fields, there is no more domain wall displacement and the global magnetization variation is only due to the coherent rotation of the magnetic moments:

$$\frac{M}{H_{\text{meas}}} = \chi_0 - \frac{M_S}{H_{\text{meas}}} - \frac{AM_S}{H_{\text{meas}}^2} - \frac{BM_S}{H_{\text{meas}}^3}, \quad (6)$$

where  $\chi_0$  is the initial magnetic susceptibility and  $A$  and  $B$  are coefficients to be determined. The fit of  $M_{\parallel}/H_{\text{meas}} = f(1/H)$  for the Sample B curve at  $T = 300\text{ K}$  gives  $M_S = 6.37 \mu_B/\text{f.u.}$

The studied sample can be represented by crystallites which have their crystallographic  $c$ -axes distributed uniformly around the  $z$ -axis, the texture direction [20]. The angular distribution of the magnetic moments, linked to the basal planes of the tetragonal structure, can be described by the probability function  $F(\theta_g, \varphi)$  of finding the  $c$ -axis in a direction given by the  $\theta_g$  and  $\varphi$  angles (Fig. 8). The  $\theta_g$  angle measures the deviation of the  $c$ -axis from the  $z$ -axis (equivalent to the polar angle of the pole figures), and the angle  $\varphi$  refers to the projection of  $c$  in the  $(x, y)$  plane (azimuth of the pole figures). In fact the probability function is strongly correlated to the pole figures as measured by X-ray diffraction. Depending on the crystallite distribution function, a normalization procedure must be applied to the probability function  $F(\theta_g, \varphi)$  [21]:

$$\int_{\theta_g=0}^{\pi/2} \int_{\varphi=0}^{2\pi} F(\theta_g, \varphi) \sin \theta_g d\theta_g d\varphi = 1. \quad (7)$$

Considering that the  $z$ -direction is a revolution axis of symmetry (axially symmetric texture), one can write  $F(\theta_g, \varphi) = G(\theta_g) \times H(\varphi)$ , where  $H(\varphi)$  is a constant and  $G(\theta_g)$  is the radial behavior of the textured volume distribution. Then the normalization condition (Eq. (7)) becomes

$$2\pi \int_{\theta_g=0}^{\pi/2} G(\theta_g) \sin \theta_g d\theta_g = 1. \quad (8)$$

For a random distribution (isotropic sample),  $G(\theta_g)$  is a constant which is equal to  $1/2\pi$ . For a textured sample, this distribution reflects, to a certain extent, the crystallite distribution function,

if the magnetic moments are linked to specific crystal axes, as revealed by neutron diffraction for the  $\text{ErMn}_4\text{Fe}_8\text{C}$  compound.

In Sample B,  $H_{\text{meas}}$  is parallel to the texturation direction  $\mathbf{z}$ , which is perpendicular to the mean direction of the EMD. Then  $\theta_g = \theta_0$  and the  $z$ -component of the magnetization is given by (Fig. 8):

$$M_z = \frac{M_{\parallel}}{M_S} = 2\pi \int_0^{\pi/2} G(\theta_g) \sin \theta_g \cos(\theta_g - \theta) d\theta_g, \quad (9)$$

where  $\theta$  is calculated from Eq. (4) for every value of  $H_{\text{meas}}$  and  $\theta_g$ .

The ODF refined from the texture experiments allows the calculation of the normalized pole figures  $P_{\mathbf{h}}(\mathbf{y})$  which determine quantitatively the distribution of the directions  $\langle hkl \rangle^*$  to the crystallographic planes  $\{hkl\}$ . The pole figure definition is given by [7]

$$\frac{dV}{V} = \frac{1}{4\pi} P_{\mathbf{h}}(\mathbf{y}) d\mathbf{y} \quad (10)$$

with  $\mathbf{h} = \langle hkl \rangle^*$ ,  $\mathbf{y} = (\theta_g, \varphi)$  and  $d\mathbf{y} = \sin \theta_g d\theta_g d\varphi$ .

Here  $V$  is the irradiated volume of the sample and  $dV$  is the volume of crystallites having orientation between  $\mathbf{y}$  and  $\mathbf{y}+d\mathbf{y}$ . The normalization condition for the pole figures is

$$\int_{\phi=0}^{2\pi} \int_{\theta_g=0}^{\pi/2} P_{\mathbf{h}}(\mathbf{y}) d\mathbf{y} = 4\pi. \quad (11)$$

The radial  $\{001\}$  pole profile  $G(\theta_g)$  determined by texture analysis is represented in Fig. 9. The variations observed at high  $\theta_g$  angles are due to the existence of the minor components of texture described in the inverse pole figure (Fig. 4). From this figure, we estimate the total volume ratio associated with the three minor components to be no more than 5% in total. Since each of the minor component peaks at different  $\theta_g$  values contribute with a low volume ratio to the magnetization, they can be interpreted by an average distribution. For a rotation-aligned sample, the  $\{001\}$  pole profile can be described by a Gaussian or a Lorentzian distribution about the  $z$ -axis [10]. The best fit of the  $\{001\}$  distribution (Fig. 9) was found for a Pseudo-Voigt (PV) shape of the distribution (mean

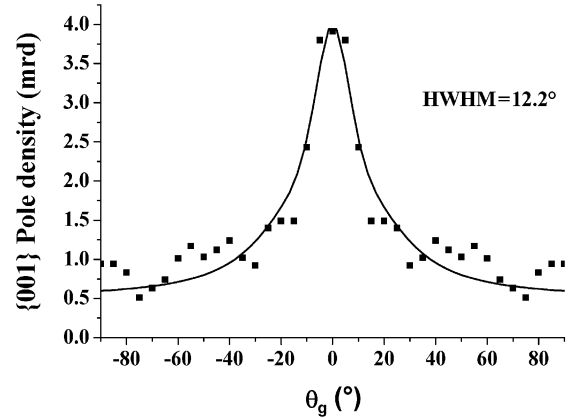


Fig. 9. PV fit of the  $\{001\}$  distribution density deduced from texture analysis. The randomly oriented background is 0.5 mrd, and the fit accounts for the main and the minor contributions.

weighted value of a Gaussian and Lorentzian distribution) with a half-width at half-maximum (HWHM) of  $12.2^\circ$  and a randomly distributed part of the volume,  $\rho_0 = 0.5$  mrd (minimum of the distribution). From the definition of the pole figures,  $\rho_0$  is directly the random volume ratio. Then, the contribution of the random part to the magnetization is the classical random magnetic signal,  $M_{\text{random}}$ , measured on free powder, times the volume ratio associated with this random component. So, the contribution to the magnetization of the textured part is in our case:

$$G(\theta_g) = (1 - \rho_0) \text{PV}(\theta_g). \quad (12)$$

Then Eq. (9) becomes

$$M_z = \frac{M_{\parallel}}{M_S} = 2\pi \int_0^{\pi/2} (1 - \rho_0) \text{PV}(\theta_g) \sin \theta_g \cos(\theta_g - \theta) d\theta_g + \rho_0 \frac{M_{\text{random}}}{M_S} \quad (13)$$

or finally

$$M_z = \frac{M_{\parallel}}{M_S} = 0.5 \frac{M_{\text{random}}}{M_S} + 0.5 \times 2\pi \int_0^{\pi/2} \text{PV}(\theta_g) \sin \theta_g \cos(\theta_g - \theta) d\theta_g. \quad (14)$$

Using this formalism, we have simulated the experimental magnetic curves  $M_{\parallel}/M_S$  at  $T = 300$  K. The fit of the  $M_{\parallel}/M_S$  curves is shown in Fig. 10(a). A good reproduction of the experimental curve is obtained for low values of  $H_{\text{meas}}/H_A$  ratio (i.e.  $H_{\text{meas}} < 1.8$  T) as shown in Fig. 10(b). This model does not take into account the rotation of the various magnetic moments for higher applied magnetic fields, which tend progressively to be aligned along the applied magnetic field.

The most important feature of the present approach is that the angular distribution of the moments is accounted for as a measured para-

meter. A fit of the anisotropic magnetization curves could be done (with an unknown distribution used to fit the same distribution shape), by using three more parameters in the fit ( $\rho_0$ , half-width, Gaussian to Lorentzian ratio). In such a case, it seems difficult to dissociate the texture from the magnetic effects, because the system becomes strongly under-determined, and the fitting procedure leads to unphysical parameters. However, using the present methodology, the texture effect is independently well identified, and the difference between measured and simulated magnetization curves can be associated with pure magnetic effects only.

Also, because the texture is relatively weak, any peculiar shape of the second or higher-order derivative of magnetization versus magnetic field cannot be revealed [9]. The authors of Ref. [9] conclude that it is impossible to measure low texture using magnetization curves, particularly in the case of easy-plane materials. This means that the magnetization curves cannot determine complex textures, as that measured in the present work. Similarly, the methods developed by Searle et al. and Elk and Hermann [21,22] represent clear quantitative determination of the magnetic texture. However, these methods do not apply for complex textures since only one parameter ( $\alpha_n$  in the original works) represents more than two characteristic features of the distributions, e.g. the half-width and the random background  $\rho_0$ . In our analysis, the random texture background deduced from a quantitative texture analysis was effectively subtracted. If not, attributing only one parameter to the texture effect yields an unrealistic over-estimation of its amplitude [23].

Furthermore, another aspect of the QTA analysis should be mentioned. The way used to refine the ODF can introduce uncontrolled artifacts. Some authors [5] tried to make use of the generalized harmonic formalism in order to fit magnetization curves. It has been shown long ago that this formalism intrinsically underdetermines the ODF, creates non-physical negative density values (regrouped as “ghost phenomena”), and are not correctable in a physically understandable way [24]. Again in this case any magnetic effect in the magnetization curves is at least partially masked.

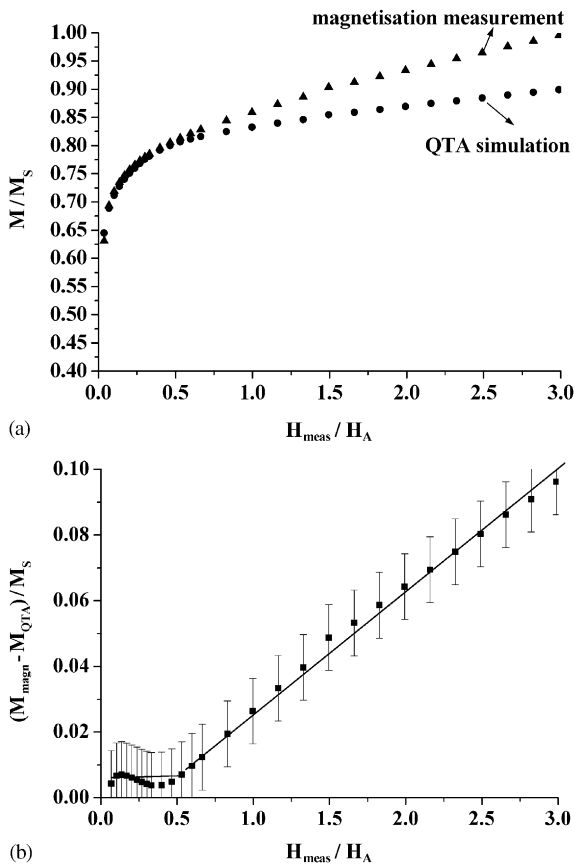


Fig. 10. (a) Comparison for Sample B of measured  $M_{\parallel}/M_S$  ratio and simulated ( $M_{\text{texture}}/M_S$ ) one and their difference (b). The line fit is only a guide for the eye and the constant error bars for this difference have been estimated to 0.01 to take into account the errors introduced by the instrument characteristics.

On the contrary, the WIMV approach corrects for the ghosts intrinsically.

### 3.6. Contribution to the magneto-crystalline analysis

The  $\text{ErMn}_4\text{Fe}_8\text{C}$  compound exhibits an unusual magnetic structure supported by a rather complicated magneto-crystalline anisotropic behavior. In order to better understand the role of the different contributions to the magneto-crystalline anisotropy, high magnetic field measurements have to be undertaken, in particular at low temperature, where the erbium CEF terms are maximized. However, the present crystal analysis of a textured sample (under 0.5 T) reveals that even at 300 K, under the assumption of a simple expression for the magneto-crystalline energy ( $W = K_1 \sin^2 \theta$ , Eq. (2)), a FOMP takes place under an applied magnetic field of about 1.8 T as seen in Fig. 10 (b). A direct analysis of the magnetization curves recorded at room temperature ( $M_{\parallel}$  and  $M_S$ ) cannot provide such a clear-cut result. Due to the low value of the magnetic field used to install the texture, even if the latter is far from complete, this texture was developed without any significant modification of the fundamental state of the magnetic structure (zero field state). The FOMP results from the application of a magnetic field out of the easy plane of magnetization [14]. The corresponding torque created on the different sublattices (R, 3d) is far more efficient to induce relative spin reorientation, than when the field is applied parallel to the easy plane. This reveals highly competing contributions between both the magneto-crystalline anisotropy terms and within the different exchange forces acting between the different sublattices. The antagonist parameters to be considered are not only acting between the global 3d terms on one side and the 4f terms on the other side. Furthermore, competitions between terms relative to the iron-rich and manganese-rich sites must be accounted. Note that in the  $\text{RMn}_{12-x}\text{Fe}_x$  series, a planar non-collinear anti-ferromagnetic structure, rather weak 3d moments and exchange forces characterize the manganese-rich side whereas an easy  $c$ -axis ferromagnetic structure, larger 3d moments and higher exchange

forces characterize the iron-rich side [25]. Recent X-ray magnetic circular dichroism (XMCD) analyses of the 3d element absorption edges allow us to assert local atomic pictures of the Fe and Mn magnetism [26]. A drastic weakening of the axial character of the erbium CEF terms in the  $\text{RT}_{12}$  series is realized by insertion of C atoms as first neighbors along the fourfold axis of the structure, once again superimposing a balance effect in the magneto-crystalline anisotropy energy [27,28].

## 4. Conclusion

This texture analysis performed at 300 K on samples aligned under a moderate field of 0.5 T allows us:

- to confirm that the  $\text{ErMn}_4\text{Fe}_8\text{C}$  carbide is easy plane accordingly with neutron diffraction analysis;
- to simulate the magnetization curve versus field under the assumption of a simple expression to describe the magneto-crystalline anisotropy;
- to evidence a first-order magnetization process ( $T = 300 \text{ K}$ ,  $H \approx 1.8 \text{ T}$ ) that should result in the competition between different contributions to the magneto-crystalline anisotropy energy.

To our knowledge, it is the first time that an experimental determination of the texture is taken into account for the magnetization curve calculation of an easy-plane ferrimagnetic structure. The formalism developed here can be extended to any other texture type, even those exhibiting several texture components. In order to complete the magneto-crystalline anisotropy analysis, the texture measurements must be extended at low temperatures using both X-ray (crystallographic texture) and neutron (magnetic texture) techniques. This will enable us to account for higher anisotropy constants ( $K_2, \dots$ ) that have been neglected here reasonably in Eq. (2). These terms must be considered for a better description of the FOMP which are enhanced in carbides in comparison to the parent compounds  $\text{RT}_{12}$  [28].

## References

- [1] D. Fruchart, J.L. Soubeyroux, O. Isnard, S. Miraglia, E. Tomey, *J. Alloys Compounds* 219 (1995) 16.
- [2] M. Morales, M. Bacmann, D. Fruchart, P. Wolfers, *J. Magn. Magn. Mater.* 236 (2001) 83.
- [3] M. Morales, M. Bacmann, P. Wolfers, D. Fruchart, B. Ouladdiaf, *Phys. Rev. B* 64 (2001) 144426.
- [4] B.A. Legrand, D. Chateigner, R. Perrier de la Bathie, R. Tournier, *J. Magn. Magn. Mater.* 173 (1997) 20.
- [5] T. Walker, S. Wirth, D. Schläfer, N. Mattern, K.-H. Müller, A. Handstein, *Mikrochim. Acta* 125 (1997) 355.
- [6] S. Matthies, G.W. Vinel, *Phys. Stat. Sol. B* 112 (1982) K111.
- [7] H.-R. Wenk, S. Matthies, J. Donovan, D. Chateigner, *J. Appl. Crystallogr.* 31 (1998) 262.
- [8] M. Morales, M. Bacmann, D. Fruchart, P. Wolfers, *J. Magn. Magn. Mater.* 196–197 (1999) 703.
- [9] R. Vert, M. Bououdina, D. Fruchart, D. Gignoux, *J. Alloys Compounds* 287 (1999) 38.
- [10] W. Qun, Z. Zhi-gang, L. Wei, X.K. Sun, Y.C. Chuang, *J. Magn. Magn. Mater.* 109 (1992) 59.
- [11] H. Pillière, D. Chateigner, Program INEL/LPEC, 1999.
- [12] E. Tomey, M. Bacmann, D. Fruchart, D. Gignoux, J.L. Soubeyroux, *J. Alloys Compounds* 262–263 (1997) 194.
- [13] R. Vert, Ph.D. Thesis, Université J. Fourier, Grenoble, France, 1999.
- [14] H.S. Li, J.M.D. Coey, in: K.H.J. Buschow (Ed.), *Handbook of Magnetic Materials*, Vol. 6, North-Holland, Amsterdam, 1991, pp. 1–83.
- [15] J.A. Campbell, *J. Phys. F: Met. Phys.* 2 (1972) L47.
- [16] N.T. Hutching, *Solid State Phys.* 16 (1964) 227.
- [17] P. Wolfers, *J. Appl. Crystallogr.* 23 (1990) 554.
- [18] B.P. Hu, H.S. Li, J.M.D. Coey, *J. Phys.: Condens. Matter* 1 (1989) 755.
- [19] P. Weiss, R. Forrer, *Ann. Phys.* 12 (1929) 279.
- [20] P. Tenaud, Ph.D. Thesis, Université J. Fourier, Grenoble, France, 1988.
- [21] C.W. Searle, V. Davis, R.D. Hutchens, *J. Appl. Phys.* 53 (1982) 2395.
- [22] K. Elk, R. Hermann, *J. Magn. Magn. Mater.* 138 (1993) 138.
- [23] A. Yan, W. Zhang, H.-W. Zhang, B. Shen, *J. Magn. Magn. Mater.* 210 (2000) L10.
- [24] S. Matthies, *Phys. Stat. Sol. B* 92 (1979) 135.
- [25] M. Morales, Ph.D. Thesis, Université J. Fourier, Grenoble, France, 1999.
- [26] M. Morales, M. Bacmann, D. Fruchart, P. Wolfers, Ch. Baudelet, A. Delobbe, G. Krill, *J. Alloys Compounds* 317 (2001) 470.
- [27] D.P.F. Hurley, J.M.D. Coey, *J. Phys.: Condens. Matter* 4 (1992) 5573.
- [28] H. Fujii, H. Sun, in: K.H.J. Buschow (Ed.), *Handbook of Magnetic Materials*, Vol. 9, North-Holland, Amsterdam, 1991, pp. 356–363.

# Characterisation of lanthanum lithium titanate thin films deposited by radio frequency sputtering on [100]-oriented MgO substrates

M. Morales<sup>a,\*</sup>, P. Laffez<sup>a</sup>, D. Chateigner<sup>b</sup>, I. Vickridge<sup>c</sup>

<sup>a</sup>Laboratoire de Physique de l'Etat Condensé, Université du Maine, Avenue O. Messiaen, 72085 Le Mans Cedex, France

<sup>b</sup>Laboratoire de Cristallographie et Sciences des Matériaux (CRISMAT-ISMRA), 6 Boulevard Maréchal Juin 14050 Caen Cedex, France

<sup>c</sup>Groupe de Physique des Solides, Universités Paris VI et VII, 2 Place Jussieu, 75251 Paris Cedex 05, France

Received 14 March 2002; received in revised form 19 June 2002; accepted 21 June 2002

## Abstract

Highly textured and insulating  $\text{Li}_z\text{La}_{2/3\pm y}\text{TiO}_{3-\delta}$  ( $\delta \leq 1$ ) thin films with structurally incorporated lithium, have been deposited for the first time onto MgO[100] substrates by radio frequency magnetron sputtering in an Ar/O<sub>2</sub> mixture. The chemical compositions of the films have been determined by Rutherford backscattering spectrometry and nuclear reaction analysis. The influence of the deposition conditions on the composition, the structure and the microstructure of the films have been analysed by X-ray diffraction, X-ray quantitative texture analysis and transmission electron microscopy, and their hetero-epitaxial growth modes are described.

© 2002 Elsevier Science B.V. All rights reserved.

**Keywords:** Oxides; Epitaxy; Sputtering; Insulators

## 1. Introduction

In the last few decades, considerable attention has been focused on rechargeable power sources as lithium ion batteries because of their high energy density and good cell performances, in which the choice of fast lithium ion conducting solids as electrolytes is crucial [1–5]. The lithium ion oxides  $\text{Li}_{3-x}\text{La}_{2/3-x}\text{TiO}_{3-2x}$  (LLTO), which crystallises in a perovskite derived structure [6,7], are very promising electrolyte materials due to their high ionic conductivity values at room temperature (approx.  $10^{-3}$  S/cm for the composition  $x \approx 0.11$ ) and an electrochemical window larger than 4 V [8,9]. The mechanisms of the ionic conductivity of the LLTO phase have been intensively investigated in the last years. Notably, the relatively higher ionic conductivity values reported in the literature for these phases have been correlated to the high mobility of the Li-ions through the vacant sites of the LLTO structure [10–13].

Then, their ionic conductivity has been evidenced anisotropic, and strongly correlated to the anisotropy of the structure, i.e. the distribution of the La ions in the double perovskite [14].

In the context of using films of the LLTO phases for the micro- and nano-technologies, operational miniaturisation of devices is needed. This implies a considerable research effort on micro-batteries used as power sources for smart cards or CMOS memories. Micro-batteries using LLTO compounds have already been elaborated in the form of sintered pellets with  $\text{LiCoO}_2$  and  $\text{Li}_4\text{Ti}_5\text{O}_{12}$  thin films as cathodes and anodes, respectively [15]. Such devices exhibit good performances (2 V developed voltage, stability with cycling, high current densities of  $40 \mu\text{A}/\text{cm}^2$ , etc.) despite a high level of micro-structural defects and a large thickness (600  $\mu\text{m}$ ) of the LLTO electrolyte. Thin film technology allows the manufacturing of solid-state micro-batteries with thin electrolytes and large electrochemically active interfaces. Attempts to deposit  $\text{Li}_z\text{La}_{2/3+y}\text{TiO}_{3-\delta}$  thin films by laser ablation were shown recently to be very promising [16]. However, if this technique is appropriate

\*Corresponding author. Tel.: +33-2-4383-3268; fax: +33-2-4383-3518.

E-mail address: magali.morales@univ-lemans.fr (M. Morales).



Table 1

Cell parameters, composition and mean crystallite sizes of the studied thin films deduced from RBS, NRA, XRD and EDX analyses

	Deposition conditions		Cell parameters		$c/2a$	$V$ ( $\text{\AA}^3$ )	La/Ti (RBS)	La/Ti (EDX)	Li content $z$ (NRA)	$\text{Li}_z\text{La}_{2/3\pm y}\text{TiO}_{3-\delta}$	Mean crystallite size ( $\text{\AA}$ )
	$T$ ( $^\circ\text{C}$ )	$P_{\text{O}_2}$ (mbar)	$a$ ( $\text{\AA}$ )	$c$ ( $\text{\AA}$ )							
A	650	$7.3 \times 10^{-2}$	3.91 (4)	7.90 (4)	1.010	120.776	0.83 (2)	0.89 (3)	0.02 (1)	$z=0.02, y^+ \approx 0.17$ (3)	236
B	700	$7.8 \times 10^{-3}$	3.883 (7)	7.80 (3)	1.004	117.605	0.54 (2)	0.60 (3)	0.98 <sup>a</sup> (1)	$z \leq 0.46, y^- \approx 0.13$ (3) <sup>a</sup>	271
C	700	$7.3 \times 10^{-2}$	3.885 (2)	7.817 (2)	1.006	117.996	0.74 (6)	0.70 (7)	1 <sup>a</sup> (1)	$z \leq 0.24, y^+ \approx 0.04$ (7) <sup>a</sup>	511
D	750	$7.3 \times 10^{-2}$	3.89 (2)	7.856 (9)	$\approx 1.01$	118.878	0.88 (6)	0.86 (7)	0.10 (1)	$z=0.10, y^+ \approx 0.21$ (7)	559
E	800	$7.3 \times 10^{-2}$	3.889 (3)	7.888 (2)	1.014	119.300	0.72 (2)	0.75 (2)	0.02 (1)	$z=0.02, y^+ \approx 0.05$ (2)	682

<sup>a</sup> As all the XRD patterns have been indexed in a tetragonal cell in agreement with TEM and QTA analyses and as a pure LLTO solid solution is obtained for the compositional range  $0.04 < x < 0.5$  according to the literature, a Li-rich impurity not visible in the XRD patterns must be present in the  $\text{Li}_z\text{La}_{2/3\pm y}\text{TiO}_{3-\delta}$  films.

The  $-$  and  $+$  exponents of  $y$  correspond, respectively, to the compositions  $\text{Li}_z\text{La}_{2/3-y}\text{TiO}_{3-\delta}$  (LLTO) and  $\text{Li}_z\text{La}_{2/3+y}\text{TiO}_{3-\delta}$ . Numbers in parentheses represent errors on the last digit.

for fundamental purposes, its use on an industrial scale is still under progress for such materials. This led us to deposit LLTO thin films by radio frequency sputtering, a well-established technique in industrial processing. For the first time, we show in this work that the stabilisation of the  $\text{Li}_z\text{La}_{2/3\pm y}\text{TiO}_{3-\delta}$  [6,17] thin films can be achieved using single target deposition process. Temperature, oxygen pressure and the nature of the substrate should strongly influence the film structure and composition. Thus, we try to optimise the deposition conditions in order to obtain thin films with structural parameters leading to the highest conductivity values. Films were grown on polycrystalline platinum, Si[100] and MgO[100] single crystals. The crystallinity, texture, composition and microstructure of these films have been determined by X-ray diffraction, transmission electron microscopy and nuclear analyses, and the influence of the deposition conditions on these properties is discussed.

## 2. Experimental

LLTO targets of composition  $x \approx 0.11$  corresponding to the highest bulk ionic conductivity were synthesised by classical solid-state reaction according to the process reported in Fourquet et al. [6]. Stoichiometric mixtures of  $\text{Li}_2\text{CO}_3$ ,  $\text{La}_2\text{O}_3$ ,  $\text{TiO}_2$  heated in air at  $800^\circ\text{C}$  for 4 h were fired at  $1150^\circ\text{C}$  for 12 h. The resulting powders were then pressed into pellets and sintered again twice in air at  $1150^\circ\text{C}$  for 12 h.

Thin films were sputtered on polycrystalline platinum and Si[100] and MgO[100] single crystal substrates ( $5 \times 10$  mm). Reactive sputtering was carried out in a mixture of argon and oxygen atmosphere. The oxygen partial pressure,  $P_{\text{O}_2}$ , was varied between  $9.6 \times 10^{-4}$  and  $7.3 \times 10^{-2}$  mbar and the substrate temperature,  $T$ , was adjusted between 25 and  $800^\circ\text{C}$  in order to determine the optimal deposition conditions. The sputtering conditions were the following: power density  $7 \text{ W/cm}^2$  at

$13.56 \text{ MHz}$  and target–substrate distance of 40 mm. After sputtering, the thin films were kept for 1 h at their growing temperature and oxygen pressure. Then heating system and oxygen flux were turned off and the films cooled down. Five representative films ( $\approx 3000 \text{ \AA}$  thick) grown by varying the deposition conditions described in Table 1 were chosen for this paper.

Both initial targets and thin films have been characterised by X-ray diffraction (XRD) in the Bragg–Brentano geometry using  $\text{CuK}\alpha$  radiation (X-Pert Philips diffractometer). The diagrams were recorded over the angular range  $10^\circ < 2\theta < 80^\circ$  with a step of  $0.02^\circ$ .

As the XRD patterns of the corresponding thin films exhibited preferential orientations, X-ray quantitative texture analysis (QTA) was performed on these films. We used a Huber 4-circles diffractometer and the INEL curved position sensitive detector, which spans a  $120^\circ$  range in  $2\theta$ , allowing the simultaneous acquisition of several pole figures [18]. Pole figures were measured by scanning the tilt angle of the goniometer,  $\chi$ , in the range  $0$ – $60^\circ$  and the azimuthal angle,  $\varphi$ , in the range  $0$ – $360^\circ$ , both using a  $5^\circ$  step. The integrated intensities are treated and corrected for absorption, volume variations and delocalisation effects [19]. In the direct integration approach of peaks that we are using, the defocusing effect is automatically corrected [20]. Pole figures are normalised into distribution densities that are expressed as multiples of a random distribution (m.r.d.). From several of these pole figures, we refined the orientation distribution function (ODF) using the WIMV method [21]. The ODF allows then the recalculation of the experimental pole figures and the completion of the blind and non-measured zones (appearing in white on the experimental pole figures). The calculation of the low Miller-indices pole figures allows simpler texture visualisation. All data reduction and calculations were operated using the Goman, Pofint [22] and Beartex [23] packages.

The composition of the sputtered films onto MgO substrates was determined by Nuclear Reaction Analysis (NRA) and Rutherford Backscattering Spectrometry (RBS) at the Van de Graaff accelerator of the Groupe de Physique des Solides, Jussieu (University of Paris VI, France). RBS Spectra were acquired with a 2 MeV incident beam of  $^4\text{He}$  ions for 5  $\mu\text{C}$  of incident charge. The detector was placed at  $165^\circ$ , and the solid angle was determined using a Bi-implanted silicon reference sample. Clear signals from Ti and La are obtained, allowing absolute determination of atomic area densities of these two elements and in addition, the ratio of La and Ti is obtained directly from the peak areas and the Rutherford cross-section, without need of reference. Since the films are deposited on an oxygen-containing substrate, it is not possible to use NRA to determine the oxygen content. However, an approximate idea can be obtained from the RBS spectra. We fitted these spectra using the RUMP simulation program [24] and varied the assumed oxygen composition to obtain the best fit. This is not very accurate, since the stopping power of the film may be different from that used in RUMP, calculated from the semi-empirical Ziegler–Biersack–Littmarck elemental values and Bragg's rule [24]. We estimate that the oxygen content of the film is determined to within approximately 30% using this method. Further measurements in progress are necessary before a more precise comment can be made on this point.

The lithium content of the films was determined using a 1 MeV incident beam of protons to induce the  $^7\text{Li}(p, \alpha)$  nuclear reaction, which has a cross-section varying slowly with energy in this range. The alpha particles were detected with a 300 mm<sup>2</sup> detector placed at  $150^\circ$ , which was protected from elastically scattered protons by a 19  $\mu\text{m}$  Mylar film. Lithium area density was determined by comparison of peak areas with that obtained from a 15  $\mu\text{g}/\text{cm}^2$  LiF reference film on Mylar backing obtained from MicroMatter Inc. At the low beam current densities employed of 20 nA/mm<sup>2</sup> for the films and 2 nA/mm<sup>2</sup> for the reference, we confirmed that the alpha particle yields were stable up to three times the incident dose used.

Specimens for Transmission Electron Microscopy (TEM) observations were prepared by scraping off the thin films in ethanol using a diamond knife. A drop of the suspension was deposited and dried onto a carbon coated copper grid. TEM study of the scraped samples was performed in a 200 kV side entry JEOL 2010 Transmission Electron Microscope (tilt  $\pm 30^\circ$ ). Conventional bright field images and selected area electron diffraction (SAED) were used for the microstructure study. For comparison with RBS results, the La and Ti contents of the deposited material were determined by Energy Dispersive X-ray analysis (EDX) using a KEV-EX and a LINK EDX Spectrometer coupled with a

SEM Hitachi microscope and the 200 kV TEM microscope.

### 3. Results and discussion

#### 3.1. X-Ray diffraction

The LLTO bulk compounds have been assumed to have in the compositional range  $0.04 < x < 0.167$  a tetragonal structure (P4/mmm) derived from a perovskite-type structure  $\text{ABO}_3$  [6]. Complementary studies have pointed out in these compounds the existence of a phase transition from tetragonal to orthorhombic (Pmmm) when the Li content decreased below  $x=0.06$ , but with a weak orthorhombic distortion [7]. Recent neutron diffraction studies performed on the LLTO compound with the highest Li-substitution level,  $\text{Li}_{0.5}\text{La}_{0.5}\text{TiO}_3$ , have revealed that firstly this compound have a rhombohedral perovskite structure ( $R\bar{3}c$ ) with Li-ions not located at the A-sites of the perovskite as suggested previously [6], and secondly that the LLTO solid solution does extend up to values of  $x=0.167$  [10].

A typical XRD pattern of the LLTO targets is shown in Fig. 1a. A pure phase was found having the LLTO tetragonal structure [6] (space group P4/mmm) with unit cell parameters refined using the MAUD program [25] and deriving from that of the  $\text{ABO}_3$  perovskite:  $a = a_p = 3.874(3)$  Å and  $c = 7.746(2)$  Å  $\approx 2a_p$ .

The stabilisation of the LLTO phase was only observed for thin films grown onto MgO[100] substrates (cubic system with  $a=4.21$  Å). Whatever the deposition conditions, the obtained films are transparent and insulators ( $R \approx 10^{12}$  Ω) in contrast to those observed for thin films grown by laser ablation where  $\text{Li}_z\text{La}_{2/3+y}\text{TiO}_3$  insulator films are obtained only for oxygen pressures  $P_{\text{O}_2} > 0.05$  mbar [16]. The oxygen pressure and the substrate temperature have an important effect on the crystallinity of the grown thin films and on their resulting X-ray patterns.

Fig. 1b shows the typical diffraction pattern measured on films grown at temperature  $T \leq 650$  °C whatever the partial oxygen pressure (illustrated as sample A) and on films deposited at  $T \geq 700$  °C with  $P_{\text{O}_2} = 9.6 \times 10^{-4}$  mbar. The corresponding  $\theta$ - $2\theta$  XRD pattern of sample A exhibits diffraction lines that are not well crystallised. This XRD pattern can be indexed in an apparent cubic crystalline system. The asymmetry and the width of these diffraction lines can be related to composition variations in these films, with cell parameters a comprised between 3.89 and 4.07 Å, and/or to the poor crystallisation of the film. It is a hard task to dissociate between crystal structure symmetry, cell parameter dispersions and axis orientations in such pseudo-symmetric films. The exclusive presence of the ( $h00$ ) lines in the XRD pattern suggests a texture for this film with the  $a$ -

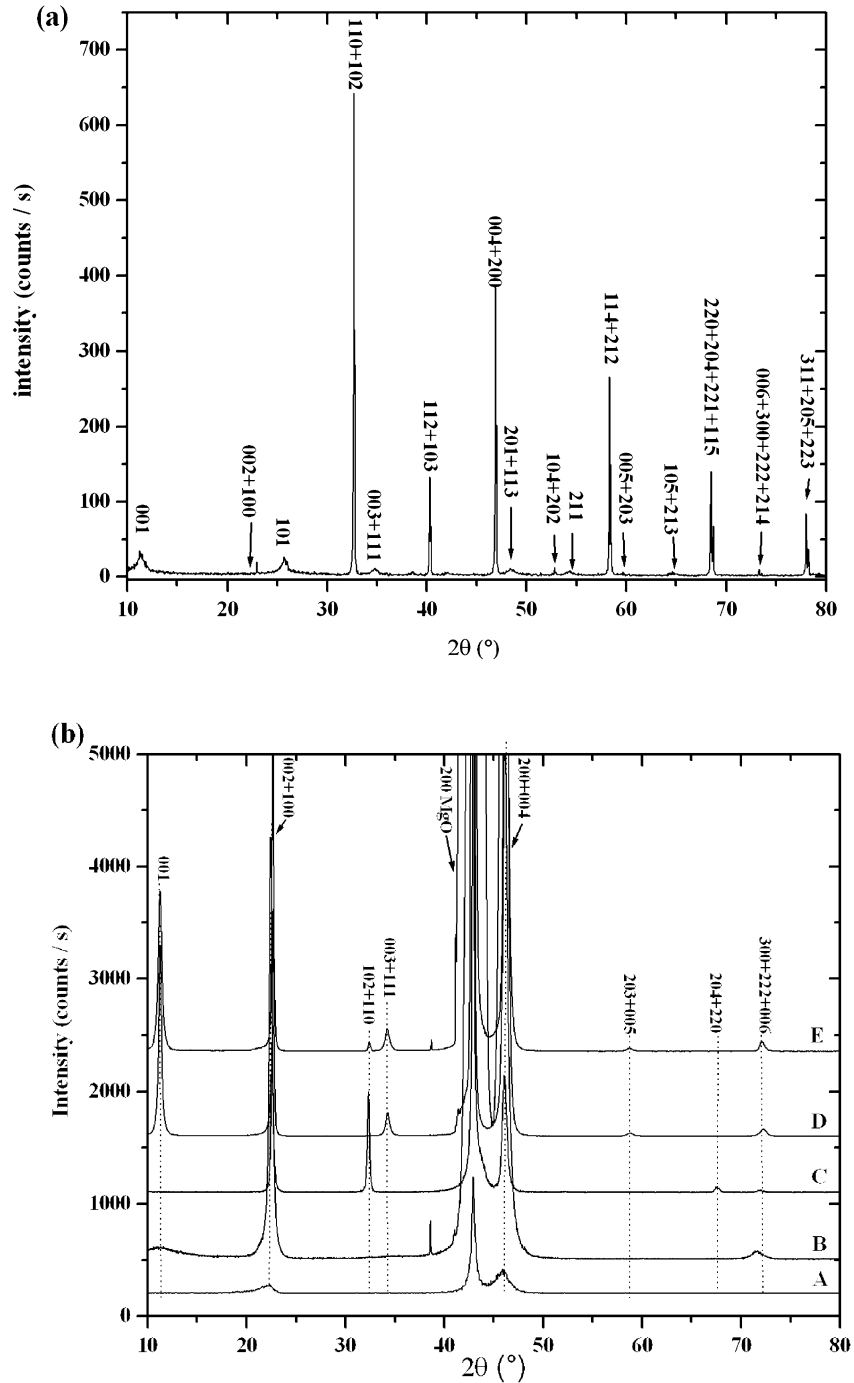


Fig. 1. XRD patterns of (a) the LLTO target and (b) the corresponding thin films synthesised for different temperatures and partial oxygen pressure showing preferential orientations. The small peak at  $2\theta = 39^\circ$  is only a  $\lambda/2$  contribution from the substrate.

axis parallel to the normal of the film in a cubic system or an  $a$ -axis or  $c$ -axis orientation in a tetragonal system. In order to determine the averaged  $c/a$  ratio of this sample, we measured a  $\chi$ -scan using an angular step of  $1^\circ$ , for the maximum of the 102 reflection of LLTO (tetragonal system). Since this line is located approximately  $45^\circ$  from the  $a$ - or  $c$ -axis, we operated this scan in the  $40$ – $50^\circ$  range (Fig. 2). We clearly observe a shift

of the contribution towards values higher than  $45^\circ$  and centred on  $45.42^\circ$  for the maximum of the dispersion. This is indicative of an average  $c/2a$  ratio different from 1, and proves that the film is mainly tetragonal. Obviously, the width of the dispersion extends to more than  $7^\circ$ , including also the  $45^\circ$  position, and we cannot exclude completely the presence of a very minor cubic phase. Simple crystallography links the  $c/a$  ratio to the

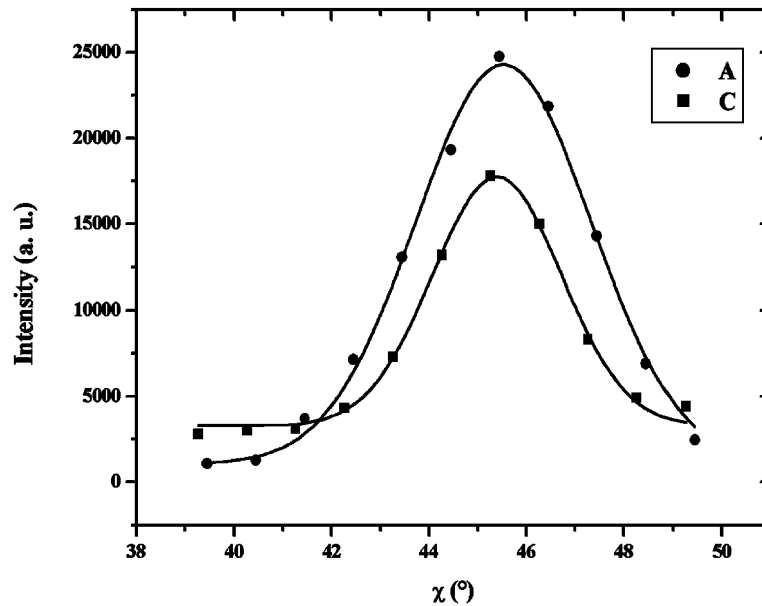


Fig. 2.  $\chi$ -Scans of the {102} poles for samples A (circles) and sample C (squares), corrected from the delocalisation, and showing the tetragonal crystalline system of these samples. The same counting time has been used for both films. The interpolating lines are only guides for eyes.

observed  $\chi$  angle of the dispersion. According to the literature [6,17], in the insulating  $\text{Li}_z\text{La}_{2/3\pm y}\text{TiO}_{3-\delta}$  systems we can suppose that generally  $c > 2a$  and then  $\tan \chi = c/2a$  for  $c$ -axis oriented parallel to the normal of the film plane, from which we obtain a  $c/2a$  ratio of 1.01. The dispersion of the  $\chi$  distribution can then be interpreted by a dispersion of  $c/a$  ratios, which is coherent with the extent of the Bragg peaks of Fig. 1b.

The diffraction patterns corresponding to the insulating films B, C, D and E grown at  $T \geq 700$  °C and  $P_{\text{O}_2} > 9.6 \times 10^{-4}$  mbar are shown in Fig. 1b. These XRD patterns exhibit only narrow peaks and are characteristic of fully crystallised films. They can all be indexed in a tetragonal structure in the P4/mmm space group. No evidence of impurities was observed in such patterns. Their corresponding cell parameters, determined using both classical XRD and texture data, are given in Table 1. The presence of the  $(00\ell)$  reflections with  $\ell$  odd in films B, D and E imposes the doubling of the  $c$ -axis of the LLTO phase [6]. These  $(00\ell)$  reflections are not observed in the XRD pattern of sample C. This could be attributed either to a strong Li incorporation in the LLTO structure [6,7] or to a peculiar texture with no  $\{00\ell\}$  planes parallel to the film plane. Fig. 1b shows that film C exhibits at least two texture components, with  $\{102/110\}$  and with  $\{100/001\}$  planes parallel to the film plane. But a quantitative texture analysis is required to check whether or not some  $\{001\}$  planes are aligned with the film plane or if the strong Li incorporation makes  $\{00\ell\}$  planes with odd  $\ell$ 's extinct [6,7]. Any cubic phase for LLTO in this film is excluded by its 102  $\chi$ -scan (Fig. 2), which is neatly centred on  $\chi =$

45.23°. Fig. 2 also shows the better crystallinity of sample C: the FWHM of the dispersion being approximately half that of sample A. The mean isotropic crystallite sizes of the thin films given in Table 1 have been estimated using the Laue–Scherrer formula. With the increase of the deposition temperature, and for a given temperature with an increase of the partial oxygen pressure, the crystallite size increases showing a better film crystallinity. The crystallite sizes do not extend over the whole film thickness. It can be linked either to some variation in compositions or to a local evolution of the texture (from the interface to the outer surface) and/or stresses in the films.

### 3.2. Quantitative texture analysis

Pole figures were measured and QTA operated on samples B, C and D. We observed the same texture for samples B and D, on which we concentrate now. The experimental and recalculated normalised pole figures of sample D are shown successively on Fig. 3a. A good reproduction of the experimental pole figures is obtained using the wmv program. The average reliability factor of the refinement is of only  $RP_1 = 57\%$  for the levels above 1 m.r.d. that attests for the quality of the ODF refinement for such strong textures. An estimate of the strength of this texture is given by the calculation of the so-called texture index [26] and of the texture entropy [27] which reach the values  $F^2 = 209$  m.r.d.<sup>2</sup> and  $S = -2.6$ , respectively. The texture index increases with the texture strength while the texture entropy (which measures the degree of disorder of the orientation) decreases

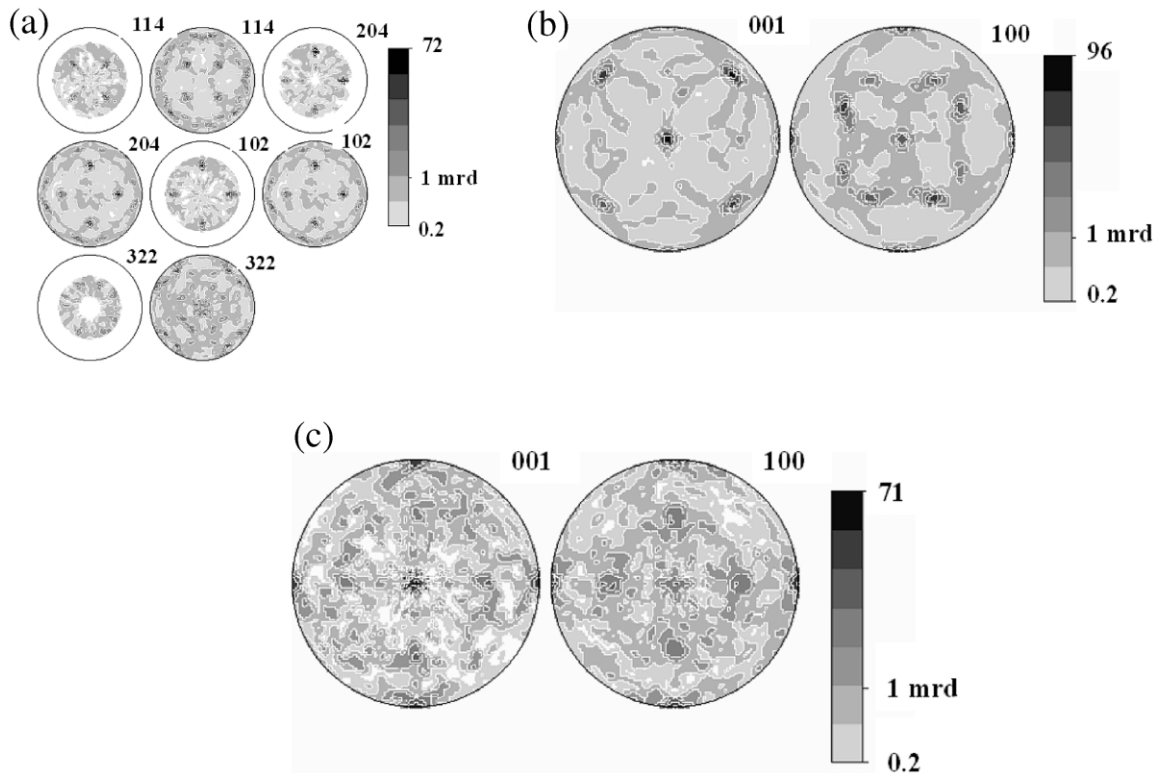


Fig. 3. (a) Experimental and recalculated normalised pole figures of sample D. (b) Recalculated low indices {001} and {100} pole figures for sample D. (c) Same for sample C. Values on the logarithmic scale bar are in m.r.d., equal area projections. Miller indices are shown for each pole figure. The minimum density levels have been fixed to 0.2 m.r.d. for clarity.

for strong textures. The  $F^2$  values obtained in our films are larger than the ones obtained on simpler systems [28] and can be related in our films to a relatively low number of hetero-epitaxial relationships, synonymous of a higher crystallite organisation. Calculation of the low indices {001} and {100} pole figures allows a simpler texture visualisation (Fig. 3b). The {001} planes are preferentially aligned parallel to the film surface (pole figure plane), as seen by the strong pole in the centre of the {001} pole figure. This corresponds to a major texture component, with a maximum orientation density of 96 m.r.d. Two minor orientation components are visible, one with {001} planes perpendicular to the film surface (small reinforcements observed on the equator of the {001} pole figure) and the other with {111} planes parallel to the film surface (four poles located around  $\chi = 70^\circ$ ). For sample C, the orientation distribution function was refined with a reliability factor of  $RP_1 = 33\%$ . The calculation of the low indices {001} and {100} pole figures (Fig. 3c) shows three orientation components, the major one being the same as in samples D and B, but with a somehow lower texture strength ( $F = 105 \text{ m.r.d.}^2$ ,  $S = -2.8$ , maximum on the {001} pole figure, 71 m.r.d.). The {111} minor orientation component of sample D has been replaced by a component with {102} and {110} planes parallel to the film plane

(four poles located at  $\chi = 45^\circ$  in the {001} and {100} pole figures, respectively) coherently with the diagrams of Fig. 1b. The reduction of the main component in this film compared to sample D is due to the relatively larger volume represented by the secondary components, in particular with {100} planes aligned with the film ({001} reinforcements on the equator are enhanced in sample C compared to D). Consequently, the non-observation of the {00 $\ell$ } reflection in the  $\theta$ -2 $\theta$  XRD pattern of sample C must be attributed without ambiguity to a higher lithium content [6,7] incorporated in the LLTO film structure, than that incorporated in samples A, D and E.

### 3.3. Composition analysis

A typical RBS spectrum and its simulation are represented in Fig. 4. The La and Ti contents of the films deduced from RBS are given in Table 1 where they are compared to those determined by the EDX analysis. The RBS values are averaged over the film thicknesses, although the RBS spectra do show evidence of compositional variations as a function of depth. The La/Ti ratios are in good agreement with those determined by EDX (Table 1). For samples C and D, the RBS spectra

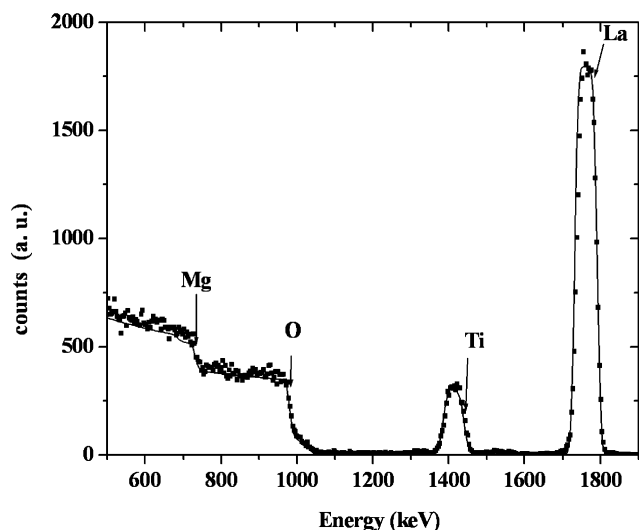


Fig. 4. Experimental Rutherford backscattering spectrum (square symbols) for sample A and its simulation (solid line) with the La/Ti ratio done in Table 1.

show clearly a diffusion of the lanthanum in the MgO substrate.

Whatever the deposition conditions, NRA shows that the Li ions are incorporated in the films (Table 1) in contrast to growth by laser ablation where the lithium is only incorporated for films grown for pressure  $P_{O_2} > 5 \times 10^{-2}$  mbar [16]. We can give a composition  $Li_zLa_{2/3+y}TiO_{3-\delta}$  of such film according to the literature [6,17] (with  $2/3 \pm y + z \leq 1$  if we consider that the Li ions are located on the A-site of the double-perovskite LLTO) and where  $\delta$  is introduced to take into account the imprecision of the oxygen composition.

Since no impurity is visible from the diffraction patterns, the high Li content of films B and C ( $z > 0.5$ , higher limit of the pure perovskite solid solution LLTO, see Fourquet et al. [6] and Kawai and Kuwano [29]) suggests either the presence of an amount of a Li-rich impurity (e.g.  $Li_2O$ ) not visible in our XRD patterns or that the solid solution LLTO can extend up to values of  $z = 0.5$  as suggested in Alonso et al. [10]. For a given oxygen pressure ( $P_{O_2} = 7.3 \times 10^{-2}$  mbar), according to the variation of the intensity of the  $(00\ell)$  reflections with odd  $\ell$  indices, the Li content  $x$  increases dramatically between 650 and 700 °C. Then the Li content decreases due to the evaporation of the Li species when the substrate temperatures increase up to 800 °C. The refined  $a$ -cell parameters in the films are, respectively, approximately 3.88–3.91 Å as compared with the bulk materials LLTO ( $a \approx 3.874$  Å) [6] and  $La_{2/3+x}TiO_{3-\delta}$  ( $3.88 \text{ \AA} < a < 3.90 \text{ \AA}$ ) [17]. The lower unit cell volumes determined by X-ray analyses correspond to the thin films grown at  $T = 700$  °C, namely B and C, which exhibit the higher lithium contents.

In thin films with composition  $Li_zLa_{2/3+y}TiO_{3-\delta}$ , the titanium cannot be fully oxidised to the +4 state [17]. However, as all the studied thin films are insulators, this suggests that the oxidation state of titanium,  $\alpha$ , is in majority +4 ( $\alpha \approx 3.7$  according to Kim et al. [17]). From electro-neutrality rules for samples A and D, we find  $\alpha \approx 3.5$ , and according to Kim et al. [17] and MacEachern et al. [30] a metallic behaviour would be expected in these films. As they are insulators and as the evolution of the unit cell volumes are mostly correlated to the largest ions  $La^{3+}$  content of the structure, this suggests that the number of La atoms incorporated in the  $Li_zLa_{2/3+y}TiO_{3-\delta}$  phase is lower than those expected from Table 1. The La site occupancy in these films will be determined with a better accuracy using a new recent methodology for the analysis of X-ray diffraction data for highly textured thin films, the so-called combined analysis [25] that allows obtaining simultaneously reliable results of texture, structure and microstructural parameters, and will be described in a forthcoming paper.

### 3.4. Microstructural studies

Electron diffraction studies were performed in order to determine the microstructure of the studied thin films, which is closely related to their physical properties. Fig. 5 is a typical SAED pattern along the  $[100]^*$  zone axis. It shows the single-phase nature of the selected area. Such pattern can be indexed in a first step using an apparent ideal cubic perovskite cell ( $a \approx a_p \approx 3.88$  Å). According to a previous study in the bulk LLTO materials [6], this pattern is more likely the superposition of two domains at 90°, with tetragonal cells  $a \approx a_p$  and  $c \approx 2a_p$ . No limiting reflections are evidenced which confirm the P4/mmm space group. The corresponding  $[100]$  HREM image (Fig. 6) exhibits domains oriented

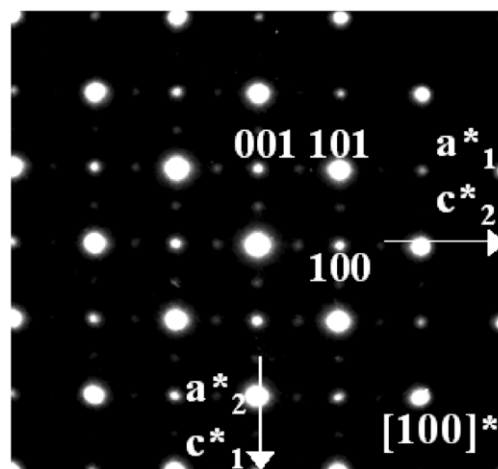


Fig. 5. Typical SAED pattern along the  $[100]^*$  zone axis, indexed on the basis of the tetragonal LLTO cell.

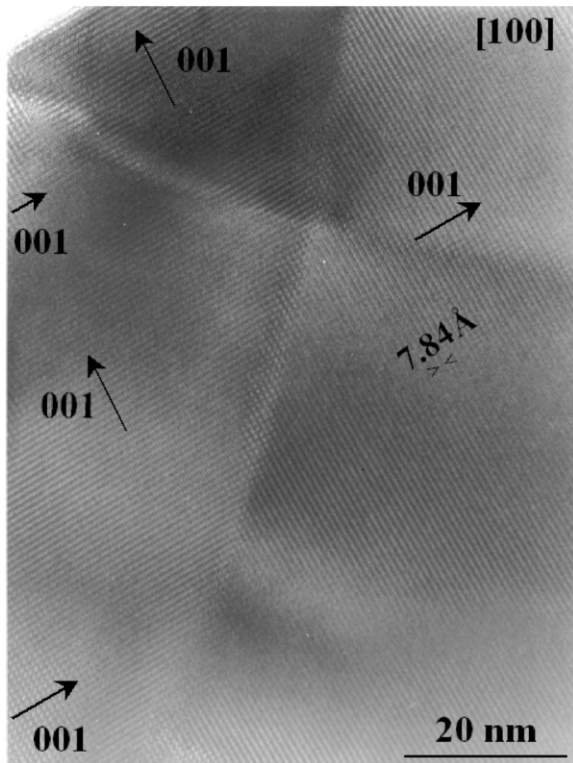


Fig. 6.  $\langle 100 \rangle$  HREM image showing  $90^\circ$  oriented domains and their corresponding Fourier transforms that give the resultant diffraction pattern of Fig. 5.

at  $90^\circ$  with two possible orientations of the  $c$ -axis. The corresponding Fourier transform of these domains (insert of Fig. 6) confirms the two possible orientations of the  $c$ -axis and the periodicity along the  $a$ -axis. A coherent interface between these domains along the  $(110)_p$  directions is evidenced (Fig. 7). This microstructure with different orientations of the  $c$ -axis in the plane of the films is favoured by  $c/2a$  ratios close to 1 (Table 1) and is consistent with the four-fold symmetry of the pole figures. In majority, all the obtained images (Fig. 7) show large domains with very few defects (dislocations, twinning, etc.) in general observed in perovskite thin films.

Fig. 8 shows a SAED pattern along the  $[1\bar{1}0]^*$  zone axis evidenced for example in sample D and that confirms the doubling of the  $c$ -axis of the cubic perovskite cell, characteristic of the LLTO tetragonal cell. In this pattern, extra spots sometime appear at the position  $(1/2, 1/2, \ell)$  with  $\ell$  odd and suggest also a doubling of the unit cell along the diagonal of the perovskite, giving a local tetragonal  $\sqrt{2}a_p \times \sqrt{2}a_p \times c \approx 2a_p$  unit cell yet proposed by Várez et al. [31] and called 'diagonal perovskite'. This SAED pattern can be explained by the superposition of two ED patterns indexed in two tetragonal cells: the LLTO cell and a body-centred (I) diag-

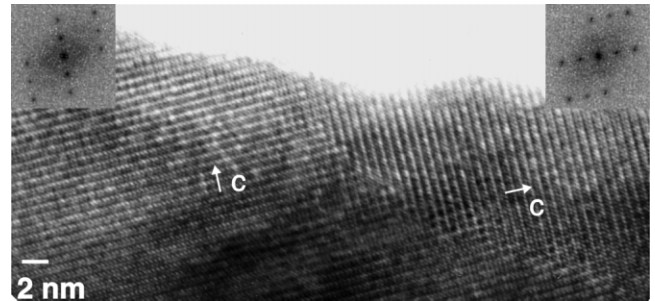


Fig. 7.  $\langle 100 \rangle$  Low resolution image showing coherent interfaces between the domains along  $\langle 110 \rangle$ .

onal perovskite cell. In the corresponding  $[1\bar{1}0]$  HREM image (Fig. 9), three areas labelled I, II and III were selected for Fourier transform. The corresponding Fourier transform patterns confirm the presence of small areas (areas I and II) with a local body-centred tetragonal diagonal perovskite unit cell (extra spot at the  $(1/2, 1/2, \ell = 2n + 1)$  positions). The presence of different ED patterns in our samples suggests local variations, minor in volume, in the ordering of the La and Li atoms [31,32]. Complementary detailed studies are in progress and will be reported elsewhere.

### 3.5. Growth schemes of LLTO on $(100)$ -MgO

Electron microscopy and QTA results point out that the growth of LLTO films deposited on  $(100)$  oriented MgO single crystals is governed by hetero-epitaxial relationships. The main orientation component corresponds to the relation:

$$(001)\text{-LLTO} // (001)\text{-MgO}; [100]\text{-LLTO} // [100]\text{-MgO}$$

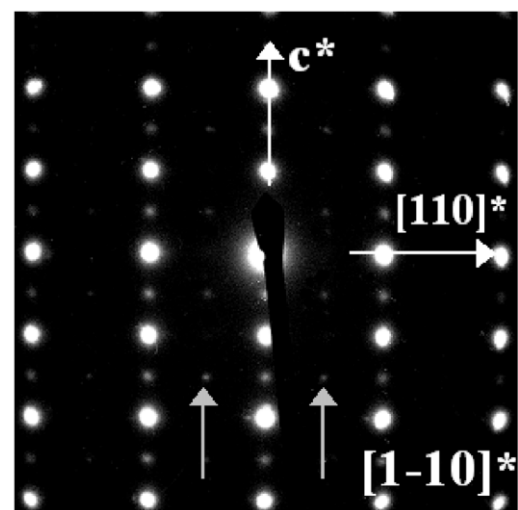


Fig. 8. SAED pattern of sample B along the  $[1\bar{1}0]^*$  zone axis indexed on the basis of the tetragonal LLTO cell. Grey arrows show extra  $(1/2, 1/2, \ell = 2n + 1)$  reflections that are sometimes observed.

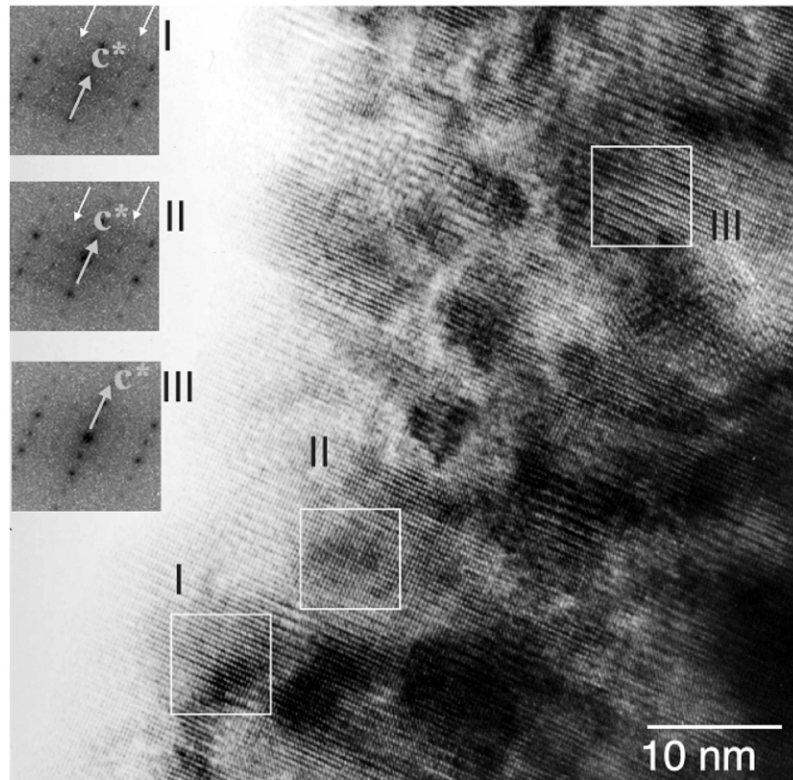


Fig. 9.  $\langle 110 \rangle$  HREM image of sample B and Fourier transforms of different areas showing the combination (areas I and II) or not (area III) of the tetragonal LLTO cell and of the body-centred diagonal perovskite cell  $\sqrt{2}a_p \times \sqrt{2}a_p \times 2a_p$ .

This relation may be surprising since it corresponds to a lattice mismatch of approximately 8%. However, such orientations on MgO have been observed in similar perovskite systems such as high  $T_c$  superconductors and are explained by a continuous adaptation of the film cell through the thickness, via oxygen non-stoichiometry [33]. This could also be the case in LLTO films, though more investigation is necessary to establish it.

The minor texture components are stabilised with the hetero-epitaxial relationships:

(100)-LLTO// (001)-MgO; [100]-LLTO//[100]-MgO;  
[001]-LLTO//[010]-MgO

(102)-LLTO// (001)-MgO; [010]-LLTO//[100]-MgO,  
[10-2]\*-LLTO//[010]-MgO

(111)-LLTO// (001)-MgO; [135]\*-LLTO//[100]-MgO,  
[-1-35]\*-LLTO//[010]-MgO

The first relation is realised with the same averaged mismatch as previously because of the pseudo-symmetry of the structure. The relative amounts of crystallites in the corresponding relationships will then be governed by the real  $c/a$  ratio of the film, and the temperature and oxygen pressure conditions during deposition. The two latter relations are accomplished with higher Miller

indices and will consequently, correspond to the creation of larger interface energies from the coincidence site lattice theory point of view. It looks coherent to find them in a lesser degree in our system.

#### 4. Conclusion

For the first time, we showed that highly textured  $\text{Li}_z\text{La}_{2/3\pm y}\text{TiO}_{3-\delta}$  insulating thin films with Li incorporated in the structure could be synthesised by reactive sputtering onto MgO[100] substrate. Several texture components are generally achieved, which depend on the composition of the films and their deposition conditions, the main texture component being always the simple axis relationship of hetero-epitaxy. Temperatures deposition at approximately 700 °C with oxygen partial pressure greater than  $9.6 \times 10^{-4}$  mbar lead to films with highest lithium contents and La/Ti ratios that give in the bulk LLTO materials the highest ionic conductivity values. These prototype depositions are very promising but as the aim of this work is to obtain thin films that can be used directly as electrolytes in micro-batteries, further depositions on conducting substrates (Ti, MgO/Pt, Si/SiO<sub>2</sub>/TiO<sub>2</sub>/Pt) are also in progress. This work



will be completed in a forthcoming paper with electrochemical measurements.

### Acknowledgments

We want to thank O. Bonkhe, H. Duroy (Laboratoire des Fluorures, Le Mans, France) and T. Brousse (Ecole Polytechnique de Nantes, France) for helpful discussions.

### References

- [1] J.B. Bates, N.J. Dudney, G.R. Gruzalski, R.A. Zuhr, A. Choudhury, C.F. Luck, J.D. Robertson, *J. Power Sources* 43/44 (1993) 103.
- [2] P. Fragnaud, D.M. Schleich, *Sens. Actuat. A* 51 (1995) 21.
- [3] P. Birke, W.F. Chu, W. Weppner, *Solid State Ionics* 93 (1997) 1.
- [4] P. Birke, W. Weppner, *Electrochim. Acta* 42 (1997) 3375.
- [5] C.H. Chen, Ph.D. Thesis, Delft University of Technology, The Netherlands, 1998.
- [6] J.L. Fourquet, H. Duroy, M.P. Crosnier-Lopez, *J. Solid State Chem.* 127 (1996) 283.
- [7] J. Ibarra, A. Várez, C. León, J. Santamaría, L.M. Torrez-Martínez, J. Sanz, *Solid State Ionics* 134 (2000) 219.
- [8] J. Emery, J.Y. Buzaré, O. Bohnke, J.L. Fourquet, *Solid State Ionics* 99 (1997) 41.
- [9] Y. Harada, T. Ishigaki, H. Kawai, J. Kuwano, *Solid State Ionics* 108 (1998) 407.
- [10] J.A. Alonso, J. Sanz, J. Santamaría, C. León, A. Várez, M.T. Fernandez-Díaz, *Angew. Chem. Int.* 39 (3) (2000) 619.
- [11] A.K. Ivanov-Schitz, V.V. Kireev, N.G. Chaban, *Solid State Ionics* 136/137 (2000) 501.
- [12] C.W. Ban, G.M. Choi, *Solid State Ionics* 140 (2001) 285.
- [13] J. Emery, O. Bonkhe, J.L. Fourquet, J.Y. Buzaré, P. Florian, D. Massiot, *C.R. Acad. Sci. II-C* 4 (2001) 845.
- [14] Y. Inaguma, J. Yu, T. Katsumata, M. Itoh, *J. Ceram. Soc. Jpn.* 105 (1997) 548.
- [15] T. Brousse, P. Fragnaud, R. Marchand, D.M. Schleich, O. Bonkhe, K. West, *J. Power Sources* 68 (1997) 412.
- [16] M. Morcrette, A. Gutiérrez-Llorente, A. Laurent, J. Perrière, P. Barboux, J.P. Boilot, O. Raymond, T. Brousse, *Appl. Phys. A* 67 (1998) 425.
- [17] I.S. Kim, T. Nakamura, Y. Inaguma, M. Itoh, *J. Solid State Chem.* 113 (1994) 281.
- [18] J. Ricote, D. Chateigner, L. Pardo, M. Alguero, J. Mendiola, M.L. Clazada, *Ferroelectrics* 241 (2000) 167.
- [19] J.J. Heizmann, C. Laruelle, *J. Appl. Crystallogr.* 19 (1986) 467.
- [20] J. Ricote, D. Chateigner, *Bol. Soc. Española Céram. Vidrio* 38 (1999) 587.
- [21] S. Matthies, G.W. Vinel, *Phys. Status Solidi B* 112 (1982) K111.
- [22] GOMAN, INEL France SA Licence 1997; POFINT, 'Pole figure interpretation', CNRS-INEL France SA Licence 2002.
- [23] H.-R. Wenk, S. Matthies, J. Donovan, D. Chateigner, *J. Appl. Crystallogr.* 31 (1998) 262.
- [24] L.R. Doolittle, *Nucl. Instrum. Methods B* 9 (1985) 344.
- [25] L. Lutterotti, H.-R. Wenk, S. Matthies, in: J.A. Szipunar (Ed.), *Textures of Materials, 2*, NRC Research Press, Ottawa, 1999, pp. 1599–1604.
- [26] H.-J. Bunge, C. Esling, in: H.-J. Bunge, C. Esling (Eds.), *Quantitative Texture Analysis*, DGM, Germany, 1982.
- [27] S. Matthies, G.W. Vinel, K. Helming, *Standard Distributions in Texture Analysis, 1*, Akademie-Verlag, Berlin, 1987, p. 449.
- [28] D. Chateigner, B. Erler, *Mater. Sci. Eng. B* 45 (1997) 152.
- [29] H. Kawai, J. Kuwano, *J. Electrochem. Soc.* 141 (1994) L78.
- [30] M.J. MacEachern, H. Dabkowska, J.D. Garrett, G. Amow, W. Gong, G. Liu, J.E. Greedan, *Chem. Mater.* 6 (1994) 2092.
- [31] A. Várez, F. García-Alvarado, E. Morá, M.A. Alario-Franco, *J. Solid State Chem.* 118 (1995) 78.
- [32] H.-T. Chung, D.-S. Cheong, *Solid State Ionics* 120 (1999) 197.
- [33] D. Chateigner, Ph.D. Thesis, Grenoble University, France, 1994.



ELSEVIER

Superlattices and Microstructures 36 (2004) 537–545

---

---

Superlattices  
and Microstructures

---

---

[www.elsevier.com/locate/superlattices](http://www.elsevier.com/locate/superlattices)

# Structural and optical characterisation of InN layers grown by MOCVD

P. Singh<sup>a,\*</sup>, P. Ruterana<sup>a</sup>, M. Morales<sup>a</sup>, F. Goubilleau<sup>a</sup>,  
M. Wojdak<sup>b</sup>, J.F. Carlin<sup>c</sup>, M. Ilegems<sup>c</sup>, D. Chateigner<sup>d</sup>

<sup>a</sup>*SIFCOM, UMR 6176 CNRS-ENSICAEN, Université de Caen, 6 Bd du Maréchal Juin, 14050 Caen Cedex, France*

<sup>b</sup>*CIRIL, UMR 6637 CNRS-ENSICAEN, Université de Caen, 6 Bd du Maréchal Juin, 14050 Caen Cedex, France*

<sup>c</sup>*IPEQ, Ecole Polytechnique Fédérale de Lausanne, CH-1015 Lausanne, Switzerland*

<sup>d</sup>*CRISMAT, UMR 6508 CNRS-ENSICAEN, 6 Bd Maréchal Juin, 14050 Caen, France*

---

## Abstract

In the following, we report investigations of the dependencies of the structural, optical and electrical characteristics of InN thin films grown by MOCVD on the growth temperature. The layer thicknesses range from 70 to 400 nm. Their carrier concentrations range from  $7 \times 10^{18}$  to  $4 \times 10^{19} \text{ cm}^{-3}$ . Hall mobility values from 150 to 1300  $\text{cm}^2/\text{V/s}$  were determined in these films. The variation of the growth temperature and V/III ratio brought about different growth modes and rates. Using TEM, in addition to measuring layer thickness, we also determined the growth mode along with the structural quality of the InN layers. The surface roughness was obtained from AFM measurements. The layer crystalline quality was also investigated by means of X-ray diffraction in the rocking mode. Photoluminescence measurements performed at room temperature and at 7 K gave emission at around 0.7 eV.

© 2004 Elsevier Ltd. All rights reserved.

---

## 1. Introduction

InN is seen as a material which will be suitable for use in fabricating LEDs, LDs and ultrahigh frequency transistors [1]. It is part of the nitride semiconductor family along with

---

\* Corresponding author.

E-mail address: [protima.singh@ismra.fr](mailto:protima.singh@ismra.fr) (P. Singh).

Table 1  
MOCVD growth conditions of the InN samples

Sample	Growth temperature (°C)	V/III ratio	GT (h)	NH <sub>3</sub> flow (sccm)	In flow (sccm)	Aspect
A50	550	13 000	3.5	3000	50	Black/brown
A52	650	6 500	1.25	3000	100	Black/brown
A53	500	6 500	2	3000	100	Metallic brown
A65	575	3 300	–	3000	200	Black brown/In drops
A69	450	3 300	1.5	3000	200	Metal In drops
A70	450	6 500	1.5	6000	200	Metallic yellow

AlN, GaN and their alloys. InN exhibits the smallest effective mass and the highest electron drift velocity as compared to the rest of the nitride family [2]. However, its growth is more difficult to achieve than that of AlN and GaN due to the weak bonding of In and N [3]. Nevertheless, over the past two years, using MBE and MOCVD as growth techniques has greatly improved the quality of InN films and recent reports on the band gap show that it could be as small as 0.65 eV [4].

## 2. Experimental

The InN layers investigated were grown on a (0001) sapphire substrate followed by a 500 to 1000 nm thick GaN template. The growth temperature was varied from 475 to 650 °C while the V/III ratio ranged from 13 000 to 3300 (Table 1). Since the growth temperature is one of the dominant factors as regards the quality of these films, we tried to correlate it with a number of measurements starting with the surface roughness obtained from AFM over area scans of 5 μm × 5 μm and down to 1 μm × 1 μm. The PL measurements were carried out on all the samples using a Sa:Ti laser at low temperature (7 K) and at room temperature, the pump power used was 500 mW and the excitation wavelength was 781 nm. We also carried out TEM analysis on our JEOL 2010 analytical microscope operated at 200 kV. X-ray diffraction investigation was performed by recording the (0002) rocking curves and exploring the reciprocal lattice from 0° to 60° and 0° to 360° using  $\psi$  and  $\chi$  scans, respectively. This was done to investigate the epitaxial relationships of the layers and to measure the half-width half-maxima of the main out-of-plane peaks.

## 3. Results

### 3.1. Surface roughness investigation by AFM

Fig. 1 shows typical topological (area of 5 μm × 5 μm) and phase images (area of 1.5 μm × 1.5 μm) from AFM measurements for the three samples grown at 650 °C (A52), 575 °C (A65), 450 °C (A70). The sample A52 at this micron scale (Fig. 1(a)) has a surface structure with large separated peaks. The phase image (Fig. 1(d)) of this sample for a smaller scan area shows mostly four-sided grains of various shapes. A65 (Fig. 1(b)) has peaks which are pointed too, but they seem to be almost joined, indicating a continuous

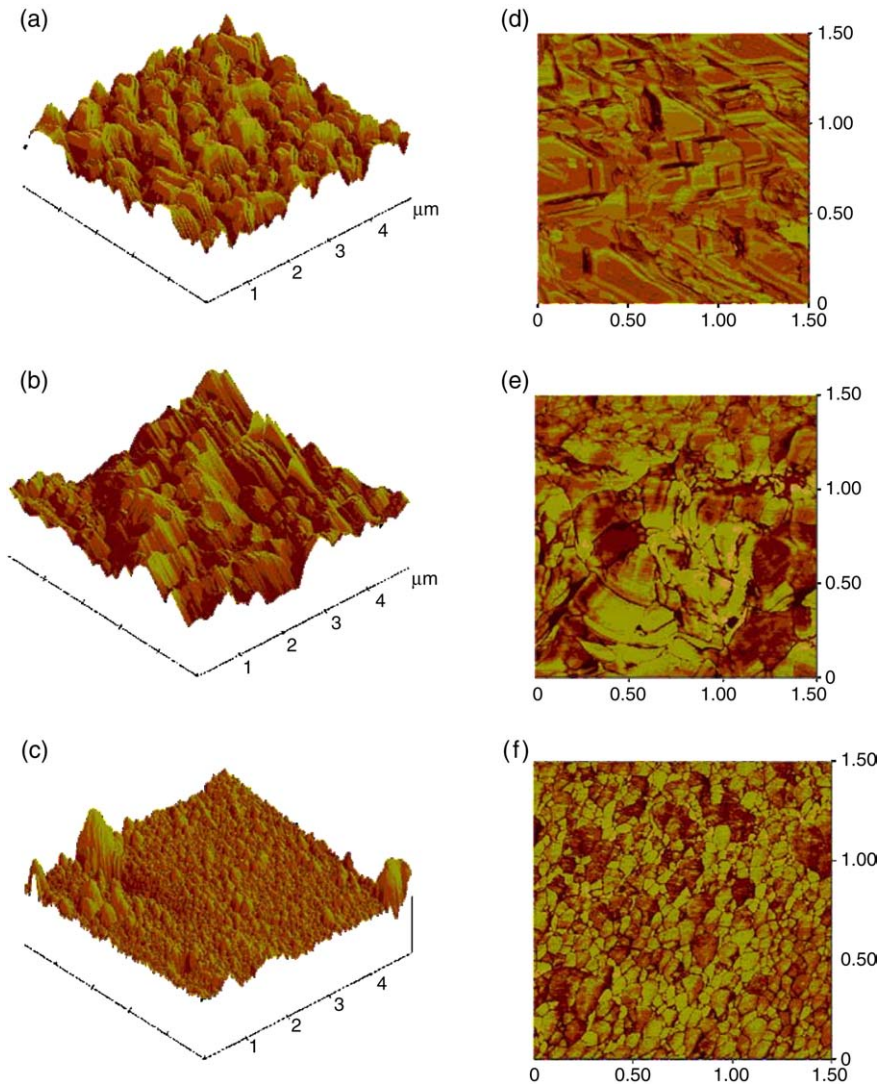


Fig. 1. AFM ((a), (b), (c)) topological images and ((d), (e), (f)) phase images of samples A52, A65, A70 respectively.

layer below. Its phase image (Fig. 1(e)) shows grains that are curved and fit into their neighbours. It is also observed that the grains are larger compared to those of A52. For A70 (Fig. 1(c)), the small peaks have rounded off slopes that almost touch each other, hinting at the presence of a continuous layer. In its phase image (Fig. 1(f)) there are tiny grains which form clusters. This sample had the smallest grains among the three presented here.

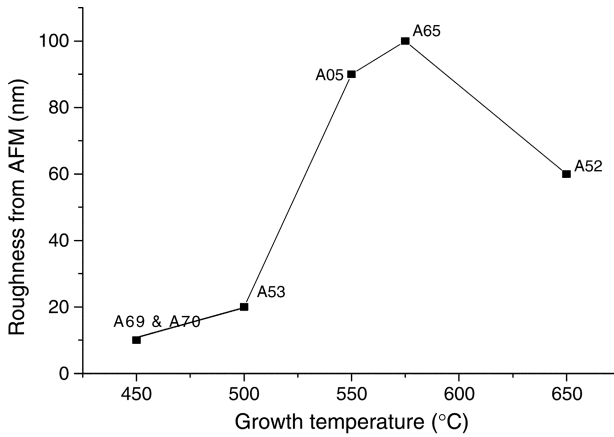


Fig. 2. Roughness obtained from AFM studies as a function of growth temperature.

In Fig. 2, the roughness is plotted versus the growth temperature for the samples investigated. A69 and A70 grown at the same growth temperature of 450 °C have the same roughness. From 450 to 500 °C the roughness increases by only 10 nm. However, from 500 to 550 °C it jumps by 65 nm in a temperature span of 50 °C. From 550 to 575 °C the roughness increases by 15 nm. Finally, the roughness falls by 40 nm from 575 to 650 °C or when close to the InN dissociation temperature.

### 3.2. Layer quality and thickness determination by TEM

Although all the samples shown in Table 1 have been observed by TEM, we concentrate on three samples out of which two were discussed above in relation to AFM measurements. Fig. 3 shows bright field images of the three samples. A52 (Fig. 3(a)) has pointed and sharp peaks, but, towards the interface, the islands are coalesced. This morphology is in agreement with the above AFM images where we also find sharp peaks which are separated. A50 (Fig. 3(b)) grown at 550 °C has almost coalesced islands with flat tops; this probably indicates that we may be close to the growth conditions from which the growth of a coalescence layer can be initiated. A70 (Fig. 3(c)) exhibits pointed peaks but it appears more continuous than A52. If we compare the morphology of the three samples we find that for A52 and A70 have the same V/III ratio, their layers are similar and A70 is more continuous than A52. The layer discontinuity for A52 is attributed to the higher temperature of 650 °C (dissociation temperature for InN) giving a higher growth rate of 0.29  $\mu$ /h in comparison to 0.05  $\mu$ /h for A70.

As a general trend the growth rate increases with the growth temperature (Fig. 4). In our case the In flow was reduced by half every 50 °C rise in temperature from 450 to 550 °C; nevertheless, there was an increase in the growth rate and at a growth temperature of 650 °C for A52 a growth rate as high as 0.29  $\mu$ /h is obtained. Adachi et al. report that the growth rate of InN increased with increasing temperature from 450 to 550 °C, even when the V/III ratio was constant and saturated, when the TMI flow was increased, as excess of In does not form InN bonds limited by NH<sub>3</sub> decomposition or due to the deficiency of

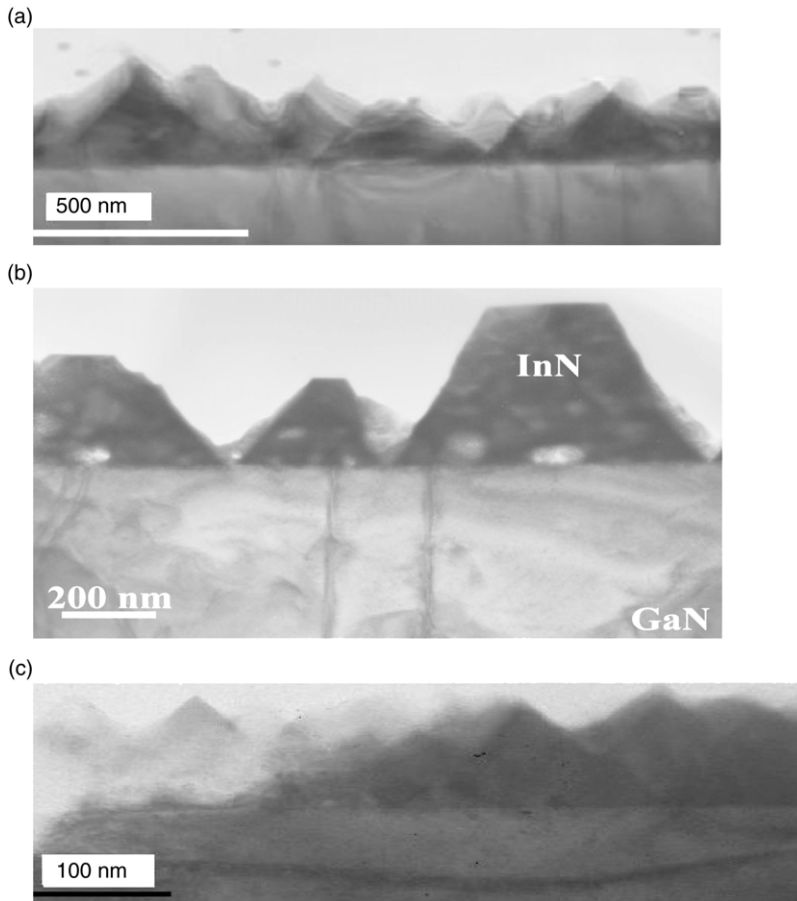


Fig. 3. TEM images of (a) A52, (b) A50, (c) A70.

active nitrogen [5]. At 630–650 °C the growth rate is directly proportional to the V/III ratio due to enhanced decomposition of  $\text{NH}_3$  and a growth rate as high as 0.8  $\mu/\text{h}$  is obtained at 650 °C [5].

### 3.3. X-ray diffraction analysis

X-ray diffraction analysis was performed by recording the (0002) rocking curves in order to obtain mosaicity of the growth along the (0001) axis. By exploring the reciprocal lattice from 0 to 60° and 0 to 360°, i.e. using  $\psi$  and  $\chi$  scans, we confirmed the following epitaxial relationships:  $[11\bar{2}0]_{\text{Sapphire}} \parallel [10\bar{1}0]_{\text{InN\&GaN}}$ ,  $[10\bar{1}0]_{\text{Sapphire}} \parallel [11\bar{2}0]_{\text{InN\&GaN}}$  in agreement with TEM diffraction analysis. The above technique was used also to measure the out-of-plane half-widths at half-maxima (HWHM)  $\Delta\phi$  of the main InN peaks, thus enabling us to study the crystalline quality of the InN grains (Table 2). Fig. 5 is a plot of  $\Delta\phi$  versus the growth temperature. A50 and A53 have almost the same value of

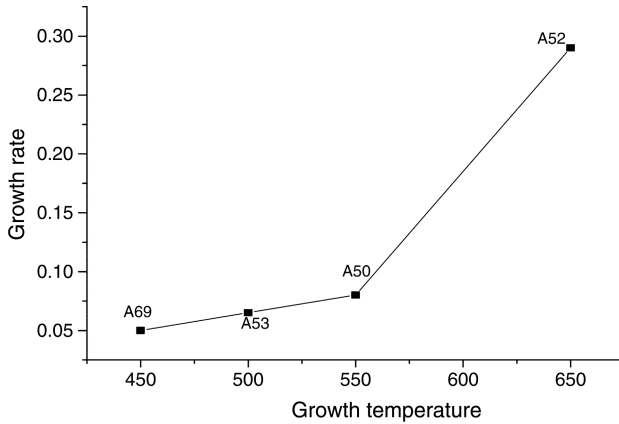


Fig. 4. Growth rate as a function of growth temperature.

Table 2

Asymmetrical 103 and 104 peak positions and half-widths at half-maxima

	103 InN		103 GaN				104 Al <sub>2</sub> O <sub>3</sub>		
$\chi_{\max}$ (°)	32	31.85	31.66	32.12	31.98	32.019	–	–	–
$\Delta\chi$ (°)	0.77	1.2	0.78	0.66	0.65	0.665	–	–	–
$\varphi_{\max}$ (°)	17.92	17.69	17.79	17.86	18.02	18.12	48.147	48.3	47.64
$\Delta\varphi$ (°)	0.395	1.70	0.365	0.25	0.25	0.24	0.16	0.15	0.16
Films	A50	A52	A53	A50	A52	A53	A50	A52	A53

HWHM. However, for A52 it increases by 1.4°. Nanishi et al. reported that a large HWHM is due to the presence of tilted domains along the (0002) direction. These tilted domains give rise to stacking faults and dislocations which are known to degrade the electrical and optical properties of the films. We have taken into account the fact that this sample was grown at a temperature of 650 °C which is the dissociation temperature for InN. This implies that there are In aggregates which degrade the crystalline quality of these films [5].

### 3.4. Photoluminescence

PL measurements were made on all the samples at 7 K and room temperature. Samples A65, A69 and A70 showed no luminescence at all. Among the three samples the minimum and maximum PL emission peaks were centred at 0.68 eV at 7 K and at 0.78 eV for room temperature measurements. The PL spectra for these samples are shown below in Fig. 6a. We find that A52 has the smallest PL band gap; in principle we should have A50 giving the smallest PL band gap because of its good crystalline structure and high mobility. However it does have the most intense signal. A53 and A52 have a PL intensity less than A50 (Fig. 6a). In addition to that, the PL intensity decreases as the crystalline quality decreases. A plot of PL intensity at 7 K and at room temperature versus growth temperature is shown

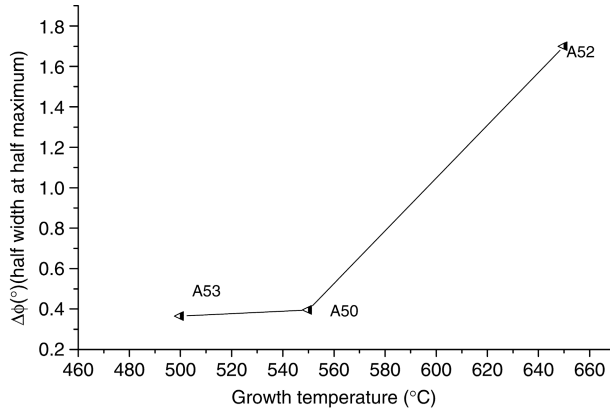


Fig. 5. HWHM ( $\Delta\phi$ ) as a function of growth temperature.

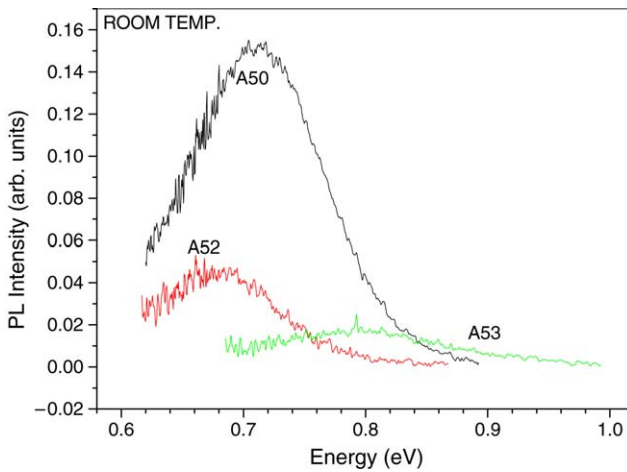


Fig. 6a. Photoluminescence spectra of the samples at room temperature.

in Fig. 6b. It can be noted that the peak position shifts to higher energy with increasing growth temperature [6].

Fig. 6c is the plot of band gap versus carrier concentration. A50 which gives the most intense signal has the lowest carrier concentration (along with A52) due to its rather good crystalline quality, which comes from it being prepared at high temperature (below the InN dissociation temperature) with a high V/III ratio—whereas A53 which has the least intense signal has also the highest carrier concentration due to its lower growth temperature and lower V/III ratio indicating poorer crystalline quality. A52 having the smallest PL band gap gave the least intense signal even though it had the same carrier concentration as A50.



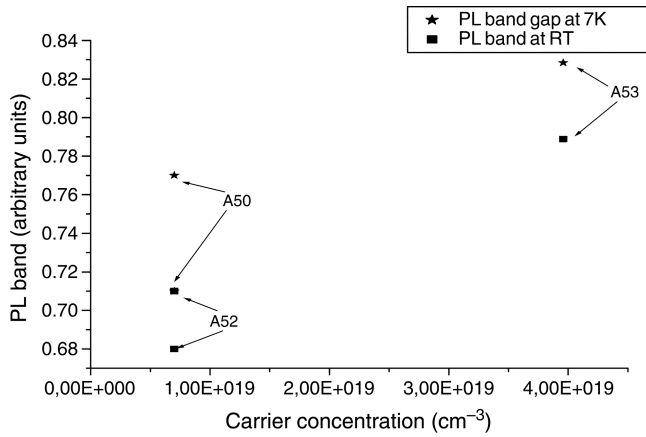


Fig. 6b. PL band gaps of the samples obtained at room temperature and at 7 K as a function of growth temperature.

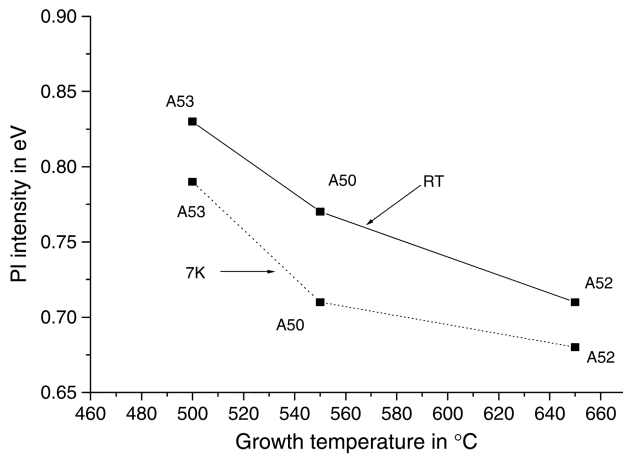


Fig. 6c. PL peak position as a function of carrier concentration.

### 3.5. Hall mobility

Fig. 7 is a plot of Hall mobility versus growth temperature. A50 exhibits the highest hall mobility of 1300 cm<sup>2</sup>/V/s which is higher than that of A53. High V/III ratio or low In flow used during the growth along with temperature rise have been reported to significantly improve the electrical properties due to the filling up of nitrogen vacancies [7]. Moreover, as shown above, it is of good crystalline quality and has a low carrier concentration. A52 on the other hand had a small Hall mobility and as seen from the above this is due to its low crystalline quality (dissociation of the InN bond).

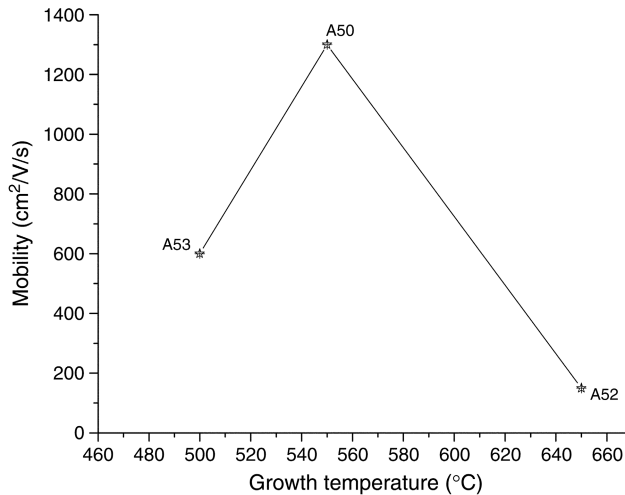


Fig. 7. Hall mobility as a function of growth temperature.

#### 4. Conclusion

We have studied MOCVD samples prepared below the InN dissociation temperature (450–575 °C) and at the InN dissociation temperature 650 °C. On the other hand, A52 prepared at the InN dissociation temperature (650 °C), even though it had a lower roughness, the same carrier concentration as A50 and a smaller PL band gap, had a very small PL signal and Hall mobility which is an indication of its poor crystalline quality. In this case thermal decomposition of the InN layer governs the electrical properties [8]. Among the samples grown below the dissociation temperature, A50 which was grown at 550 °C had the best optical and electrical properties with flat topped islands. This can probably be attributed to its optimum growth temperature and V/III ratio which improved its Hall mobility.

#### References

- [1] S.C. Jain, M. Willander, J. Narayan, R.V. Overstraeten, *J. Appl. Phys.* 87 (2000) 965.
- [2] A.G. Bhuiyan, A. Hashimoto, A. Yamamoto, *J. Appl. Phys.* 94 (2003) 2779.
- [3] V.Yu. Davydov, A.A. Klochikhin, R.P. Seisyan, V.V. Emstev, S.V. Ivanov, F. Bechstedt, J. Furthmüller, H. Harima, A.V. Mudryi, J. Aderhold, O. Semchinova, J. Graul, *Phys. Status Solidi b* 229 (2002) R1.
- [4] M. Adachi, Y. Murakami, A. Hashimoto, A. Yamamoto, *Proceedings of the International Workshop on Nitride Semiconductors, IWN'2000, Nagoya, Japan, September 24–27, IPAP Conference Series, vol. 1, 2000, p. 339.*
- [5] A. Koukitsu, T. Taki, N. Takahashi, H. Seki, *J. Cryst. Growth* 197 (1999) 99.
- [6] Y. Nanishi, Y. Saito, T. Yamaguchi, F. Matsuda, T. Araki, H. Naoi, A. Suzuki, H. Harima, T. Miyajima, *Mater. Res. Soc. Symp.* 798 (2004) Y12.1.1.
- [7] A. Yamamoto, Y. Murakami, K. Koide, M. Adachi, A. Hashimoto, *Phys. Status Solidi b* 228 (2001) 5.
- [8] V. Davydov, A. Khlochikin, S. Ivanov, J. Aderhold, A. Yamamoto, *Nitride semiconductors*, in: P. Ruterana, M. Albrecht, J. Neugebauer (Eds.), *Hand Book on Materials and Devices*, 2003, p. 274.



## Effects of the low temperature buffer and annealing on the properties of InN layers grown by MOVPE

P. Ruterana<sup>\*1</sup>, M. Morales<sup>1</sup>, F. Gourbilleau<sup>1</sup>, P. Singh<sup>1</sup>, M. Drago<sup>2</sup>, T. Schmidtling<sup>2</sup>, U. W. Pohl<sup>2</sup>, and W. Richter<sup>2</sup>

<sup>1</sup> Laboratoire Structures des Interfaces et Fonctionnalité des Couches Minces (SIFCOM), UMR 6176 CNRS-ENSICAEN, 6, Boulevard du Maréchal Juin, 14050 Caen Cedex, France

<sup>2</sup> Technische Universität Berlin, IFP, PN6-1, Hardenbergstr. 36, 10623 Berlin, Germany

Received 12 July 2004, revised 10 February 2004, accepted 22 February 2005

Published online 4 April 2005

**PACS** 61.10.Nz, 68.37.Lp, 68.37.Ps, 68.55.Jk, 81.05.Ea, 81.15.Kh

InN thin films grown by MOVPE with a thickness of about 100 nm are investigated. Growth was carried out in either two or three steps: deposition of a low temperature nucleation layer at 400 °C and subsequent growth of a thicker InN layer at 530 °C, or use of a GaN buffer layer which was annealed at 1050 °C prior to deposition of the low temperature InN buffer layer. The structural evolution of the layers during a 20 min annealing step at 540 °C under nitrogen was investigated using AFM and XRD. We analyzed the orientation distribution function of the layers by XRD reciprocal space maps applying  $\psi$  and  $\chi$  scans. The results show that the crystalline layer quality is improved by use of a GaN buffer, as also assessed from higher photoluminescence intensity.

© 2005 WILEY-VCH Verlag GmbH & Co. KGaA, Weinheim

### 1 Introduction

Nitride semiconductors (AlN, GaN, InN and their alloys) have great potential for use in optical, high-power, and high frequency electronic devices. Among these nitrides, InN has the smallest effective mass and the highest electron drift velocity [1]. Hence, InN is a promising material for the channel layers in high-speed and high frequency electronic devices. However, difficulties in growing high quality InN layers have hindered both the understanding of material properties and applications. During the past two years, the development of growth techniques especially in MBE has significantly improved the quality of InN films, attaining Hall mobilities beyond 1000 cm<sup>2</sup>/Vs and residual carrier concentrations in the 10<sup>18</sup>/cm<sup>3</sup> range at room temperature [2]. In these high quality InN films, a narrow bandgap (<0.7 eV) has been reported [3]. In a recent report, Shubina et al. have claimed that the narrow band gap of InN may be due to the presence of In nanoclusters, where pure InN would have a large band gap [4]. These results are in contrast to other recent reports on highest purity available InN layers grown by MBE or MOVPE. Thus it is interesting to carry out a structural analysis to verify if such clusters are effectively present in good quality InN layers. In this work we investigate InN thin films grown by MOVPE having a thickness of 100 nm. Growth was carried out in two steps at 400 °C for the buffer layer and at 530 °C for the epilayer. Layers were grown either directly on top of sapphire as well as on top of a thin GaN buffer layer. We also have carried out an annealing step at a slightly increased temperature of 540 °C under nitrogen ambient for 20 min. We investigated the structural evolution on the layers during these treatments using

\* Corresponding author: e-mail: pierre.ruterana@ensicaen.fr

AFM and XRD. The results are correlated with a TEM analysis of the local epitaxial relationships, layer thickness and defects, and with photoluminescence properties.

## 2 Experimental

We have studied three InN layers using XRD, AFM, TEM, PL and absorption. Samples were grown in a horizontal MOVPE reactor. Ammonia and trimethylindium were used as precursors. During growth nitrogen was used as carrier gas, the total flux was 4 sl/min and the reactor pressure was 100 mbar. Sample S1 was grown with a 3-step procedure as follows: 1. sapphire nitridation, 2. nucleation layer growth, 3. epitaxial layer growth. The nucleation layer (10–15 nm thick) was grown at 400 °C with a V/III ratio of  $6 \times 10^4$  and an ammonia supply of 1 sl/min. The epitaxial layer (80–90 nm thick) was grown at 530 °C, V/III ratio  $3 \times 10^4$  and an ammonia supply of 3 sl/min. Sample S2 was grown in the same run together with S1, but was annealed afterwards at 540 °C for 20 minutes in nitrogen gas atmosphere. Sample S3 was grown in the same manner but on a thin low temperature GaN buffer (40 nm) which was deposited at 550 °C on sapphire and annealed at 1050 °C for 5 minutes [5]. The imaginary part of the pseudo dielectric function  $\langle \epsilon_{im} \rangle$  was measured by spectroscopic ellipsometry (SE) and compared for both samples S1 and S2. The spectra of the annealed sample S2 shows a damping of the Fabry–Pérot interference structures and increased amplitude of the higher electronic transitions [5], the latter indicating a decreased surface roughness on a nm scale. We have carried out AFM scans in order to examine the layer surface morphology in addition to optical and SE microscopic observations. X-ray diffraction was studied by recording the (0002) rocking curves and exploring the reciprocal lattice from 0 to 60° and 0 to 360°  $\Psi$  and  $\chi$  scans. PL measurements were carried out on all the samples at 10 K and at room temperature using a Kr laser with 200 mW excitation density and 647 nm excitation wavelength.

## 3 Results

XRD rocking curves of the InN (103) reflection did not show a clear trend: the measured full width at half maximum is 1.19, 1.61 and 1.55 degree for samples S1, S2 and S3, respectively. The same tendencies are clearly noticed in AFM observations on a  $\mu\text{m}$  scale, see Fig. 1. Sample S3 appears to have a more granular morphology than samples S1 and S2. However, it should be noted that the surface of S2 is smoother. This finding is in agreement with the optical and SE observations, which indicated that we have less In droplets than on S1.

In the TEM analysis, the three samples presented rather different morphologies and characteristic features, as shown in the typical bright field micrographs Figs. 2 and 3. In many areas S1 exhibits a typical polycrystalline layer which may be induced by the growth interruption and a possible In enrichment. Sample S2 (Fig. 3a) generally showed flat areas, in agreement with AFM data, and no polycrystalline areas have been observed.

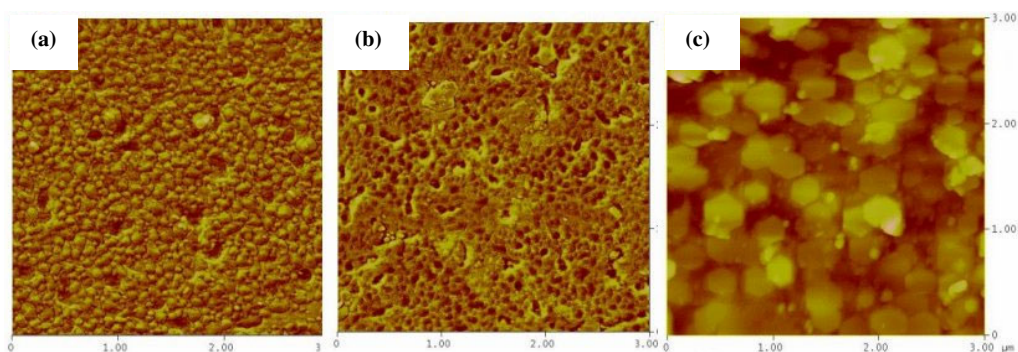


**Fig. 1** (online colour at: [www.pss-a.com](http://www.pss-a.com))  $3 \times 3 \mu\text{m}$  AFM micrographs of InN samples S1 (a), S2 (b) and S3 (c).

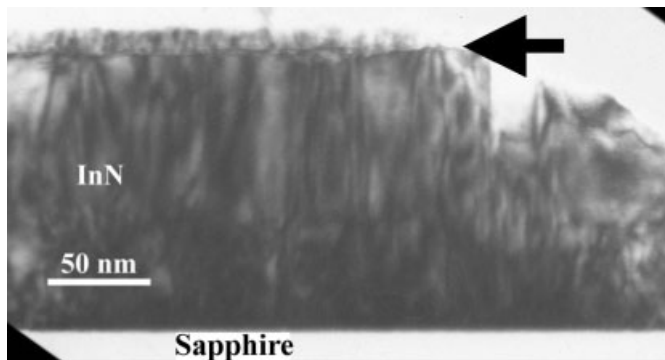


**Fig. 2** Bright field transmission electron micrograph of sample S1, exhibiting a polycrystalline surface layer (arrow).

The most interesting observations come from sample S3 shown in Fig. 3b. The three layers are clearly visible on top of the sapphire substrate. At this scale, we mostly are imaging one of the islands shown in the AFM image Fig. 1c. The GaN buffer layer, which was annealed at 1050 °C, is rough. The first InN layer grown at 400 °C is not continuous, but has a good crystallinity. The thicker InN layer grown on top at 530 °C is well crystallized, with a large number of threading dislocations. The very uniform contrast of this layer indicates that it is pure InN with a homogeneous wurtzite structure. At this scale and down

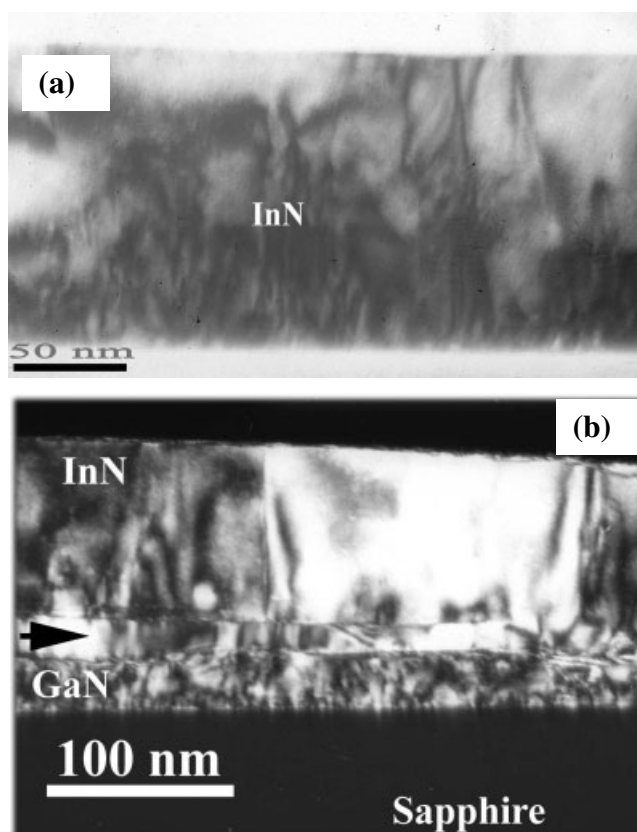


**Fig. 3** Bright field images of samples S2 (a) and S3 (b), the low temperature InN buffer layer is marked by an arrow.

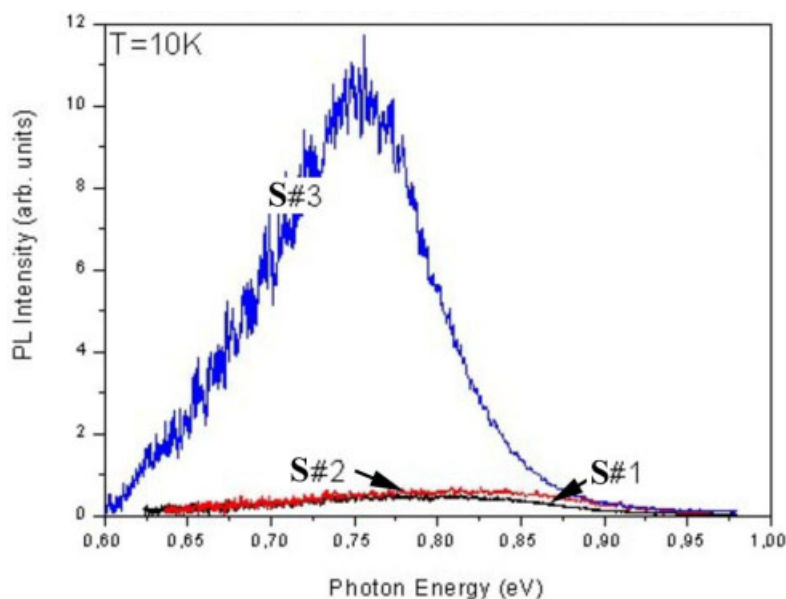


**Fig. 4** (online colour at: [www.pss-a.com](http://www.pss-a.com)) PL emission of samples S1, S2 and S3 at 10 K.

to a subnanometric scale, no In inclusions have been found. The good crystalline quality of sample S3 is in good agreement with optical measurements shown in Fig. 4. The near band-edge PL is centered at 0.75 eV, the intensity of the PL peaks exceeds that of samples S1 and S2 by more than a factor of 10.

#### 4 Summary

Structural properties of differently prepared InN epitaxial layers were studied, namely layers directly grown on sapphire with a low temperature InN nucleation layer, and layers deposited on an annealed GaN layer. TEM images show that the quality of the samples depends critically on the growth procedure. The best layer is grown on top of a high temperature annealed GaN buffer, after deposition of a thin low temperature InN layer. Layers deposited at lowest temperature show a polycrystalline, In-rich surface layer. This surface layer disappears after annealing at 540 °C. The highest PL intensity of the near band-edge emission at 0.75 eV is observed for the layer grown on top of the GaN buffer. Therefore, it is not obvious that any clustering of In takes place in the films, and the increase in the PL intensity at 0.75 eV cannot be correlated with the presence of metallic In nanocrystals.

#### References

- [1] A. G. Bhuiyan, A. Hashimoto, and A. Yamamoto *J. Appl. Phys.* **94**, 2779 (2003).
- [2] V. Yu. Davydov, A. A. Klochikhin, R. P. Seisyan, V. V. Emtsev, S. V. Ivanov, F. Bechstedt, J. Furthmüller, H. Harima, A. V. Mudryi, J. Aderhold, O. Semchinova, and J. Graul, *phys. stat. sol. (b)* **229**(3), R1–R3 (2002).
- [3] Y. Nanishi, Y. Saito, T. Yamaguchi, F. Matsuda, T. Araki, H. Naoi, A. Suzuki, H. Harima, and T. Miyajima, *Mater. Res. Soc. Symp. Proc.* **798**, Y12.1 (2003).
- [4] T. V. Shubina, S. V. Ivanov, V. N. Jmerik, D. D. Solnyshkov, V. A. Vekshin, P. S. Kop'ev, A. Vasson, J. Leymarie, A. Kavokin, H. Amano, K. Shimono, A. Kasic, and B. Monemar, *Phys. Rev. Lett.* **92**, 117407 (2004).
- [5] M. Drago, T. Schmidtling, C. Werner, M. Pristovsek, U. W. Pohl, and W. Richter, *J. Cryst. Growth* **272**, 87 (2004).

## **CHAPITRE 2.**

**Analyse combinée**

**Structure/Texture/Microstructure/**

**Contraintes**

**par diffraction des rayons X**





## 1. Problématique

Afin de déterminer la structure et la microstructure d'un échantillon, il faut pouvoir comparer les intensités mesurées par diffraction X aux intensités calculées théoriquement pour une géométrie instrumentale donnée. Dans cet objectif, on peut utiliser la méthode dite de Rietveld, méthode d'affinement des diagrammes de diffraction par moindres carrés. Pour cela il faut établir un modèle pour les intensités observées qui tienne compte de la structure des phases en présence, de leur microstructure, et d'un certain nombre de corrections (géométriques, d'absorption, facteur de Lorentz-polarisation, facteur d'échelle ...) liées à la configuration de l'instrument. En outre, lorsque l'échantillon est texturé, il faut introduire un modèle supplémentaire pour tenir compte de la FDOC, également à mesurer et à affiner. L'analyse par diffraction des rayonnements est confrontée de plus au fait que les échantillons élaborés sont de plus en plus complexes: hétérostructures minces ou massives, multiphasées avec parfois des recouvrements importants de pic interphase et/ou de basse symétrie cristalline.

Les préoccupations actuelles en ce qui concerne l'analyse par diffraction peuvent être décrites sur la base de cinq dilemmes illustrés ci-après à partir d'un exemple type, celui d'un film mince cristallisé dans une phase pseudo - symétrique avec de nombreux recouvrements de pics interphase. Ce film étant texturé soit involontairement, soit pour lui conférer une anisotropie importante visant à obtenir des propriétés accrues, une analyse QTA est donc indispensable.

Cependant, lorsqu'un échantillon est texturé, si on ne connaît pas exactement sa structure et sa microstructure, on ne peut pas en extraire sa texture (c'est à dire la FDOC) et vice-versa (dilemme n°1).

L'anisotropie est souvent induite facilement par dépôt sur substrat monocristallin et par jeux d'hétéro-épitaxies, qui induisent à leur tour des contraintes résiduelles dans les films. Les pics de diffraction sont alors décalés par rapport à leur position d'origine ce qui fausse d'une part la détermination de la structure et d'autre part l'analyse de texture puisque la position de ces pics change lors des rotations en  $\chi$  et  $\varphi$ , indispensables aux scans de texture. Il devient alors nécessaire d'analyser les contraintes résiduelles pour connaître à la fois texture et structure. Cependant, des domaines orientés différemment ne perçoivent pas de la même façon l'effet des contraintes et il existe également une influence de la texture sur ces contraintes résiduelles (dilemme n°2).

L'inconvénient supplémentaire d'analyser des structures minces est qu'il existe des variations de volume et d'absorption du rayonnement X lors des rotations nécessaires à l'acquisition des données. Ces variations doivent donc être corrigées pour affiner la structure, mais ceci implique une connaissance correcte des épaisseurs des couches puisque des variations d'intensité de pics peuvent être interprétées via des positions atomiques différentes. Or la connaissance des épaisseurs est parfois délicate. Par exemple, des méthodes d'ellipsométrie peuvent ne pas convenir si le film est opaque. Dans le cas de couches suffisamment fines et peu rugueuses, des mesures de réflectivité X permettent en principe de connaître l'épaisseur avec une très bonne précision; il faut cependant être sûr de la densité électronique du matériau, donc de la structure (dilemme n°3).

Dans certains cas, le matériau sera composé de plusieurs phases texturées avec des recouvrements importants de pics inter-phase. L'analyse quantitative de la proportion de chaque phase se fera alors par déconvolution, mais devra prendre en compte les orientations préférentielles et évidemment la structure (dilemme n°4). Ce dilemme est également valide lorsqu'il s'agit d'estimer un pourcentage volumique de phase cristalline dans un matériau mal cristallisé.

Enfin, l'interprétation de toutes ces méthodes de caractérisations restera de plus dépendante des effets microstructuraux éventuellement présents dans le matériau, tels que les tailles de cristallites (isotropes ou anisotropes), les défauts cristallins (ponctuels, linéaires, planaires ou volumiques...), les variations de compositions et les micro-déformations, qui à leur tour seront déterminés avec précision si les autres paramètres sont connus (dilemme n°5).

## **2. Analyse combinée (programme MAUD) et calibration instrumentale**

On voit donc que la clé de voûte des problèmes décrits au paragraphe précédent est l'existence désirée ou non d'orientations préférentielles dans le matériau. Il faut donc pouvoir *in fine* incorporer tous les paramètres accessibles aux rayonnements (X ou neutrons) dans une méthodologie globale de caractérisation dénommée "analyse combinée". Jusqu'à présent aucun programme de traitement des données de rayons X sur films minces ne permettait de résoudre à la fois la structure, la microstructure (dosage de phases cristallines ou amorphes, tailles des cristallites isotropes ou anisotropes, microdéformations, fautes d'empilements ...) et la texture.

Cette approche par une analyse globale du profil ne peut être développée que grâce à une collaboration étroite entre les spécialistes du domaine des films minces et ceux de la

programmation moderne (Java). Le contrat européen ESQUI (X-ray Expert System for Electronic Films QUality Improvements) auquel j'ai participé dans le cadre de mon séjour postdoctoral au Mans (09/2001 - 08/2002) avait pour objectif le développement de cette nouvelle méthodologie de caractérisation aux rayons X (dite "analyse combinée") qui inclut la détermination de la structure, de la texture et de la microstructure, en particulier de films minces pour l'industrie micro- et opto-électronique. Pour cela, le programme développé MAUD (Material Analysis Using Diffraction) par Luca Lutterotti, couple la méthode WIMV pour résoudre la fonction de distribution des orientations cristallines (FDOC) à l'analyse de Rietveld pour extraire les paramètres structuraux et microstructuraux (taille de cristallite, déformation, dosage de phases cristallines ou amorphes...) de matériaux polycristallins, et ce de façon globale. Dans le programme MAUD, les formalismes suivants ont été implémentés :

- WIMV (ou E-WIMV), harmonique sphérique et maximum d'entropie : analyse quantitative de texture
- Rietveld : analyse de structure, phase, microstructure
- Warren-Averbach (Fourier) : micro-déplacements et tailles de cristallites
- Popa : détermination des tailles de cristallites anisotropes, fonction de distribution des contraintes
- Le Bail : extraction des intensités des pics de diffraction
- Matriciel : épaisseurs et rugosités en réflectivité spéculaire
- DWBA : profils de densité électronique par réflectivité
- $\text{Sin}^2\psi$  : contraintes résiduelles
- Layering : pour les épaisseurs de couches simples ou de multicouches

L'épaisseur du film ou des multicouches est un paramètre supplémentaire de l'échantillon qu'il est possible d'affiner en utilisant MAUD.

Tous ces formalismes sont implémentés de façon à pouvoir les faire jouer les uns sur les autres par l'intermédiaire d'un affinement global, selon une méthode des moindres carrés ou par un algorithme génétique... Par exemple, le premier cycle du programme MAUD permet d'extraire par la méthode de Le Bail les intensités intégrées, intensités corrigées des effets d'absorption et de volume et qui vont être ensuite utilisées dans un premier affinement de la FDOC par la méthode WIMV (ou E-WIMV pour les fortes textures). La FDOC ainsi obtenue est alors réinjectée dans l'affinement Rietveld et les nouveaux paramètres structuraux

et microstructuraux ainsi affinés sont utilisés pour un nouveau cycle WIMV (ou E-WIMV) afin d'obtenir la nouvelle FDOC, et ainsi de suite (Figure 1).

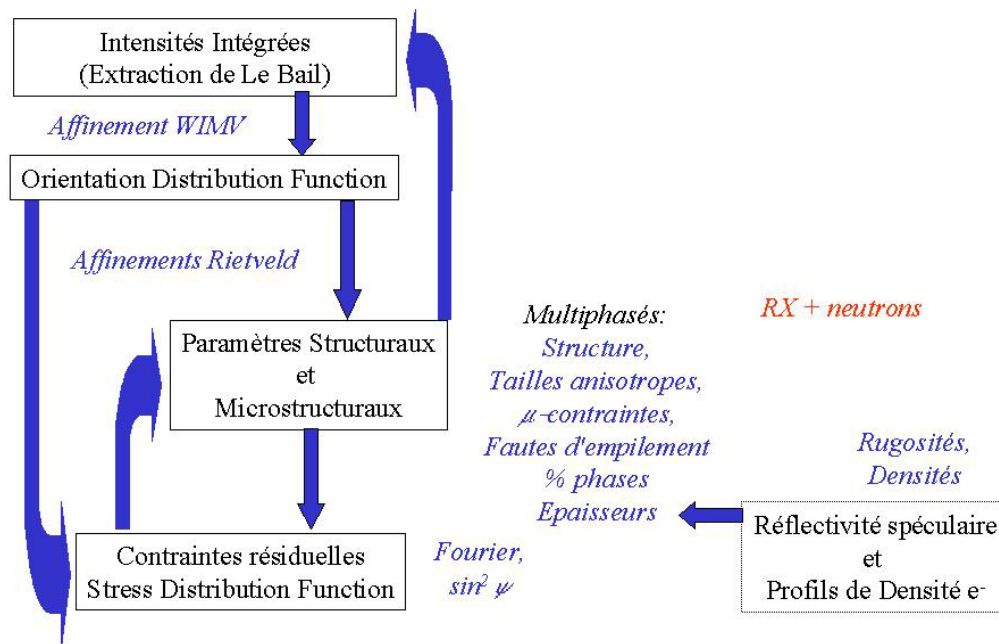


**Figure 1.** Principe de l'analyse combinée de la texture/structure/microstructure/pourcentages de phases/contraintes résiduelles dans le programme MAUD.

La méthode WIMV nécessite que les FDOC puissent se décrire en un nombre fini de cellules réparties sur une grille régulière et auxquelles sont associées des valeurs discrètes de FDOC. Quand le calcul avec la méthode WIMV est couplé avec la méthode de Rietveld dans le programme MAUD, cela exige deux étapes additionnelles:

- l'extraction des figures de pôles ou du poids de la texture
- et l'interpolation des figures de pôles pour affiner une grille régulière ( $5^\circ \times 5^\circ$  par exemple) non accessible directement par la mesure en configuration asymétrique  $\omega - 2\theta$  avec  $\omega \neq \theta$ .

Cette interpolation se traduit par un effet de moyenne au niveau de l'index de texture  $F^2$ , ce qui peut conduire à des valeurs de  $F^2$  artificiellement trop faibles notamment lorsque le film est très texturé. C'est pourquoi, pour les films très texturés, la méthode WIMV a été prolongée via l'approche E-WIMV ("Entropy modified WIMV") qui peut quant à elle être employée avec n'importe quelle grille de mesure. De plus, elle fournit via un algorithme de

maximisation d'entropie une pondération des différentes réflexions calculée de façon analogue aux facteurs de poids de l'analyse de Rietveld.

La comparaison des diagrammes X expérimentaux et calculés pour différentes positions ( $\chi$ ,  $\varphi$ ) dans le programme MAUD et la valeur des différents facteurs de reliabilité pour l'affinement Rietveld  $R_w$ ,  $R_{exp}$  and  $R_B$  permettent d'évaluer la qualité de l'affinement :

$$R_B = \frac{\sum_k |I_k - I_{ck}|}{\sum_k I_k}$$

$$R_w = \left( \frac{\sum_i w_i (y_i - y_{ci})^2}{\sum_i w_i (y_{ci})^2} \right)^{1/2}$$

$$R_{exp} = \left( \frac{N - P}{\sum_i w_i (y_i)^2} \right)^{1/2}$$

où  $I_k$  et  $I_{ck}$  sont respectivement les intensités observées et calculées de la  $k^{\text{ème}}$  réflexion de Bragg,  $y_i$  et  $y_{ci}$  sont le nombre de coups observés et calculés à l' $i^{\text{ème}}$  pas,  $w_i$  est  $y_i^{-1}$ ,  $N$  est le nombre de  $y_i$  et  $P$  le nombre de paramètres affinés.

En vue d'une détermination quantitative des paramètres importants de l'échantillon, il est de plus nécessaire de connaître la contribution instrumentale au profil des raies de diffraction du goniomètre quatre cercles utilisé (et présenté précédemment dans l'analyse classique de texture). En effet, les diagrammes mesurés résultent de la convolution de la contribution instrumentale (fonction de résolution du diffractomètre) avec la contribution de l'échantillon (de structure, texture et microstructure à déterminer). La détermination de la fonction de résolution instrumentale est réalisée par une cartographie de l'espace du diffractomètre en utilisant une poudre étalon de  $LaB_6$  (commercialisée par le National Institut of Standart and Technology) composée de cristallites de taille identique et de forme isotrope (2  $\mu m$  en moyenne), poudre supposée parfaite n'engendrant aucun élargissement de raies dans nos conditions de résolution.

### 3. Applications

Nous allons maintenant illustrer l'utilisation de cette nouvelle technique d'analyse combinée de la texture/structure/microstructure/contraintes sur plusieurs exemples.

Les deux premiers portent sur l'étude par diffraction X en vue de leur optimisation de films minces ferroélectriques  $(\text{Pb,Ca})\text{TiO}_3$  déposés sur des substrats multicouches Pt/TiO<sub>2</sub>/SiO<sub>2</sub>/[100]-Si et des films minces de TiC<sub>x</sub> et TiN<sub>y</sub> déposés sur substrats de tungstène. Dans ces films, l'analyse combinée des spectres de diffraction X a été indispensable du fait de recouvrements importants de pics inter-phase.

Les trois autres exemples concernent des films minces nano- ou micro-cristallisés élaborés au laboratoire SIFCOM par pulvérisation magnétron radiofréquence (Si, SiC, Cr<sup>2+</sup>:ZnSe). L'utilisation de l'analyse combinée a permis de déterminer pour la première fois notamment des tailles anisotropes de cristallites dans ces films texturés. La détermination des corrélations existant entre la composition du plasma, celle des films déposés, leur structure et leur microstructure a permis ainsi de cerner les conditions optimales de dépôt via une meilleure compréhension de leurs propriétés optiques.

### **3.1. Films minces $\text{Pb}_{1-x}\text{Ca}_x\text{TiO}_3$ (PTC) : Collaboration avec J. Ricote, M. L. Calzada -ICMM-CSIC Madrid, partenaire européen du contrat ESQUI.**

Les propriétés remarquables des oxydes ferroélectriques de type pérovskite  $\text{ABO}_3$  tels que BaTiO<sub>3</sub>, PbTiO<sub>3</sub>,... rendent ces matériaux très intéressants pour des applications technologiques telles que la réalisation de mémoires ferroélectriques non-volatiles (FeRAM) et de diodes optiques grâce à leur polarisation rémanente et leur champ coercitif, mais aussi pour la réalisation de transducteurs, d'actuateurs et de détecteurs infrarouges grâce à leur comportement piézo- et pyro-électrique respectivement. Même si la plupart de ces applications industrielles utilisent plutôt ces matériaux sous forme céramique, l'un des défis actuels du fait des exigences croissantes de miniaturisation des dispositifs, est la synthèse de ces matériaux sous forme de couches minces ou d'hétérostructures. Dans le cadre de la réalisation de FeRAM ou de microsystèmes électromécaniques (MEMS), il s'est avéré que le dépôt des films minces de PbTiO<sub>3</sub> non dopé est très difficile. En effet, dans ce matériau ferroélectrique le rapport de distorsion  $c/a$  de la structure quadratique est très élevé et est à l'origine de contraintes internes très importantes lorsqu'on passe en dessous de la température de Curie, ce qui provoque la détérioration du film. Par contre, avec la substitution des cations  $\text{Pb}^{2+}$  par  $\text{Ca}^{2+}$ ,  $\text{Sm}^{2+}$  ou  $\text{La}^{3+}$  on obtient une structure avec un rapport  $c/a$  plus faible, les contraintes sont alors relaxées en partie avec la formation de domaines à 90° et on observe une nette amélioration des propriétés ainsi qu'une meilleure stabilité mécanique des films.

C'est pourquoi, ces dernières années un regain d'intérêt a été consacré au dépôt de films minces  $\text{Pb}_{1-x}\text{Ca}_x\text{TiO}_3$  (PTC).

Dans l'objectif d'optimiser leurs propriétés ferroélectriques, la texture de films minces de PTC obtenus par voie sol-gel et déposés sur des substrats multicouches Pt/TiO<sub>2</sub>/SiO<sub>2</sub>/[001]-Si, la couche TiO<sub>2</sub> servant de couche d'anti-diffusion, a été étudiée. La texture des films de PTC ne peut être en général déterminée par une analyse quantitative de texture "classique" du fait du recouvrement important d'un grand nombre de pics du film ferroélectrique PTC avec ceux du substrat de Pt (Figure 2). De plus, le PTC présente une pseudo-symétrie cubique pérovskite rendant difficile la séparation des contributions 100 et 001, indispensable à l'optimisation des propriétés de ces films ferroélectriques (Figure 2).

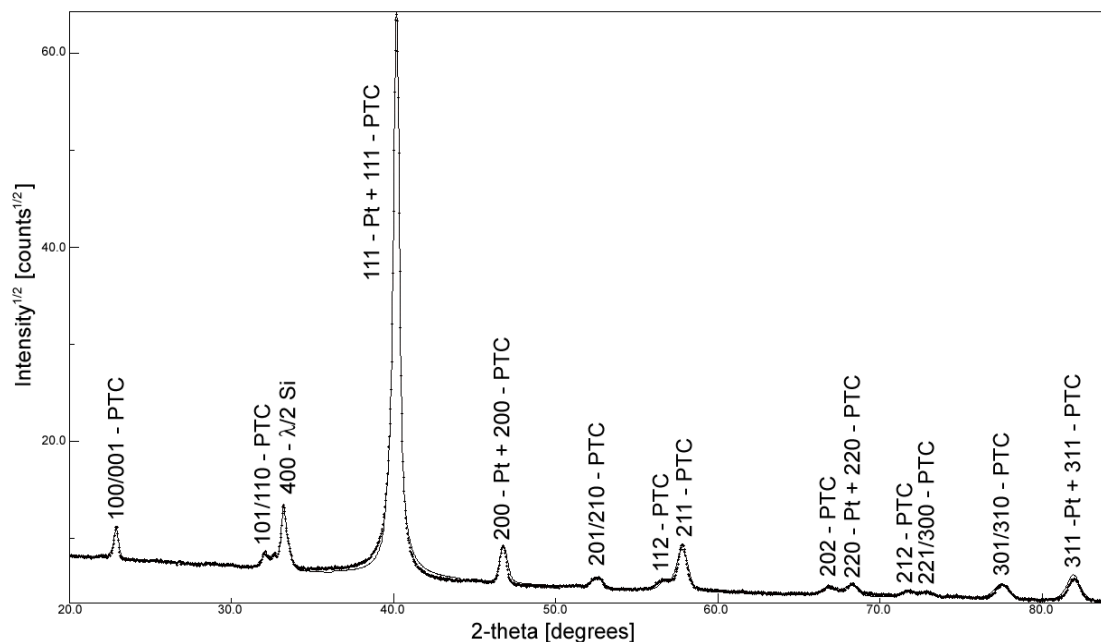


**Figure 2.** Diagramme RX typique d'un film de PTC.

L'analyse "combinée" a permis une détermination quantitative de la texture du film PTC et de l'électrode Pt en affinant simultanément la structure, les épaisseurs des différentes couches, les tailles de cristallites et les micro-déformations et ce avec d'excellents facteurs de reliabilité (Figure 3). On obtient des facteurs de reliabilité  $R_{wp}$  et  $R_B$  de 5% et de 6% pour l'affinement de la texture en utilisant le modèle E-WIMV, et des facteurs  $R_{wp}$  et  $R_B$  de 13% et 12% pour l'affinement de Rietveld, respectivement.



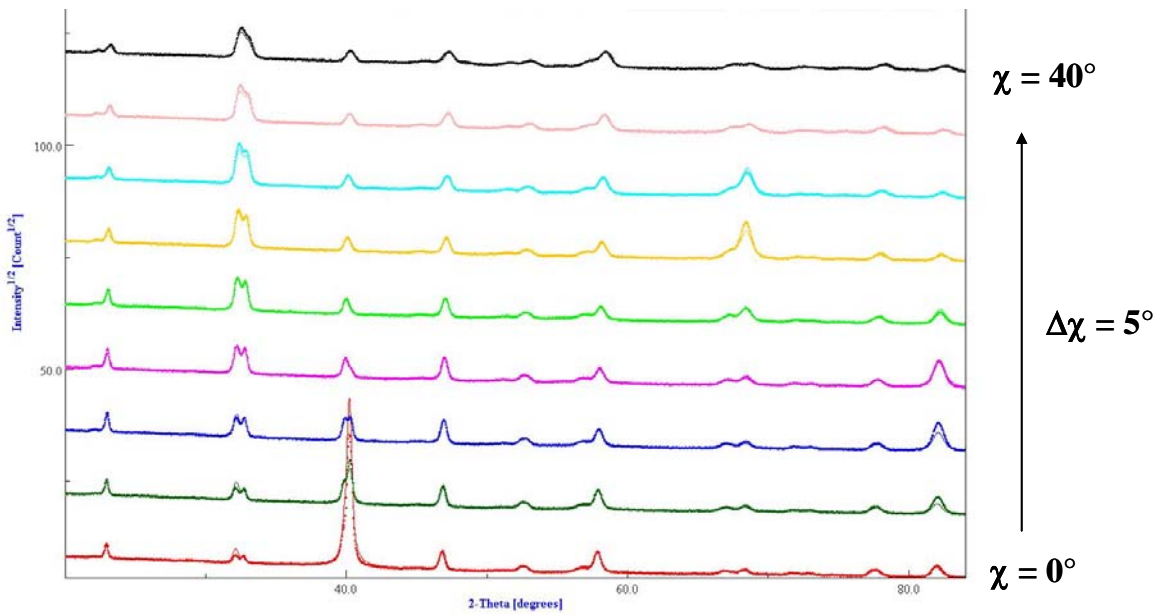


**Figure 3.** Diagrammes X en configuration asymétrique  $\omega$ - $2\theta$  expérimentaux (points) et affinés (traits pleins) pour différentes orientation en  $\chi$  d'un film de PTC.

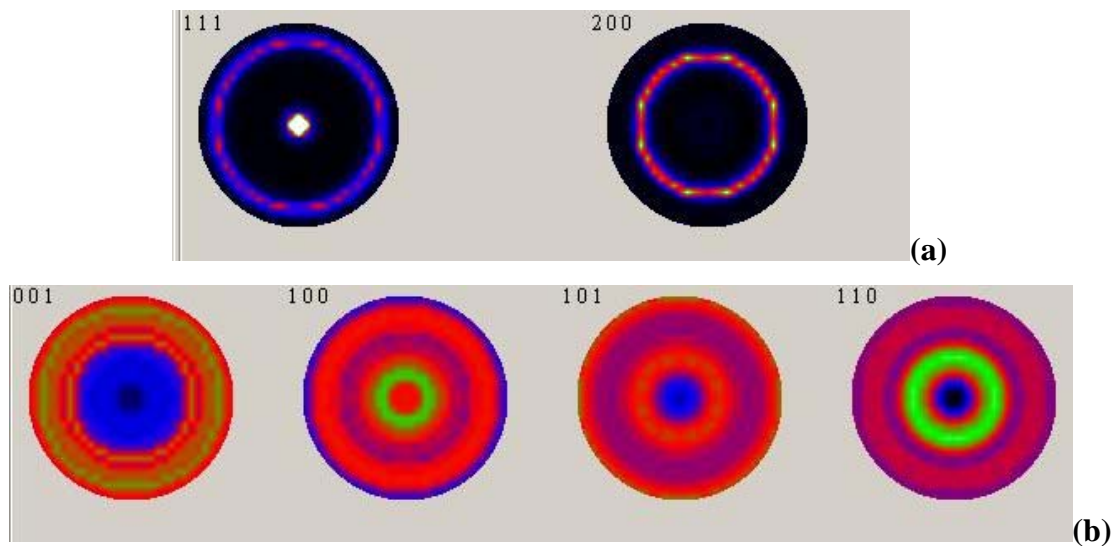


**Figure 4.** (a) Figures de pôles recalculées  $\{111\}$  et  $\{200\}$  pour l'électrode de Pt (avec un maximum et un minimum de densité d'orientation respectivement de 10 et de 0 m.r.d.) (b) Figures de pôles recalculées  $\{001\}$ ,  $\{100\}$ ,  $\{101\}$ ,  $\{110\}$  et  $\{111\}$  pour le film de PTC (maximum et minimum de densité d'orientation respectivement de 2.1 et 0.15 m.r.d.).

L'utilisation du modèle E-WIMV pour l'analyse de la texture s'est avérée plus appropriée dans ce cas étant donné la très forte texture du substrat de Pt (10 m.r.d), substrat orienté avec les plans {111} parallèles à la surface du film (Figure 4 (a)). Les films de PTC présentent des composantes multiples de texture de fibre. Les composantes majoritaires de texture correspondent à des directions  $\langle 100 \rangle^*$  et  $\langle 111 \rangle^*$  perpendiculaires à la surface du film (Figure 4 (b)). La direction de polarisation  $\langle 001 \rangle^*$  étant principalement observée dans le plan du film, cette orientation est préjudiciable pour les futures applications.

<b>Film</b>	<b>Paramètres de maille (Å)</b>	<b>Epaisseur (Å)</b>	<b>Taille isotrope des cristallites (Å)</b>	<b>Micro-déformations (rms)</b>
<b>Pt</b>	3.9108 (1)	457 (3)	458 (3)	0.0032 (1)
<b>PTC</b>	a = 3.9156 (1) c = 4.0497 (6)	2525 (13)	390 (7)	0.0067 (1)

<b>Sites du PTC</b>	<b>Occupation des sites</b>	<b>Coordonnées</b>		
		<b>x</b>	<b>y</b>	<b>z</b>
Pb	0.76	0	0	0
Ca	0.24	0	0	0
Ti	1	0.5	0.5	0.477 (2)
O <sub>1</sub>	1	0.5	0.5	0.060 (2)
O <sub>2</sub>	1	0	0.5	0.631 (1)

**Tableau 1.** Propriétés structurales du film de PTC et de l'électrode de Pt correspondant à l'affinement de la Figure 3.

Cependant, étant donné que 15% des axes  $\vec{c}$  du film ne sont pas orientés dans le plan du film (minimum de densité d'orientation de 0.15 m.r.d), quelques propriétés de polarisation relativement faibles sont obtenues. Alors que le film de Pt apparaît parfaitement cristallisé avec des tailles de cristallites qui s'étendent sur toute l'épaisseur du film et de faibles valeurs de micro-déformations, le film de PTC présente en comparaison des valeurs de micro-déformations doubles avec des tailles de cristallites autour de 39 nm (Tableau 1).

### **3.2. Films minces de $TiC_x$ et de $TiN_y$ déposés sur substrat W: Collaboration J. P. Manaud, J. Montes de Oca Valero - ICMCB Bordeaux.**

La performance des matériaux vis à vis d'une sollicitation particulière est souvent améliorée par un traitement de surface sous forme de couches minces qui, en évitant la formation de fissures ou en déviant ces fissures à l'interface, permet d'améliorer la résistance du matériau considéré. Dans le but de concevoir un matériau susceptible de protéger des dispositifs métalliques à base de tungstène (W) vis à vis d'un liquide agressif tel que l'uranium, le dépôt de revêtements protecteurs pour le W sous forme de couche mince a donc été envisagé dans le cadre de la thèse de Javier Montès de Oca Valero (ICMCB, Bordeaux). Dans cet objectif, le revêtement choisi doit présenter une bonne adhérence au substrat de W, montrer une bonne stabilité thermodynamique vis à vis du W mais aussi de l'uranium liquide, être réfractaire et résister aux chocs thermiques, ainsi que posséder une bonne résistance à l'érosion et être étanche. C'est pourquoi, deux candidats potentiels ont été retenus avec le carbure (TiC) et le nitrure de Titane (TiN) et comme technique d'élaboration le dépôt chimique en phase vapeur (CVD) à haute température (1000°C). Cependant, on s'attend du fait de cette haute température d'élaboration à avoir une fissuration importante des films lors du refroidissement à cause de la relaxation des contraintes résiduelles. De plus, il a été mis en évidence dans la littérature que les performances et les propriétés de dureté des films monocristallins de TiC et de TiN élaborés par les techniques de dépôt en phase vapeur (CVD et PVD) sont fortement corrélées avec la présence d'orientations préférentielles. C'est pourquoi, afin d'établir les corrélations entre la microstructure et le comportement de ces revêtements à la fissuration, une étude systématique de la texture des films a été réalisée par diffraction des rayons X.

Il a été mis en évidence dans cette thèse qu'un contrôle de la microstructure des différents revêtements et de leur état de contraintes résiduelles peut être obtenu en faisant varier la dilution  $\alpha$  du précurseur titane. Une détermination quantitative de la texture des films  $TiC_x$  et de  $TiN_y$  et du substrat W a été obtenue soit par une analyse de texture classique soit via l'utilisation de l'analyse combinée lorsqu'on observe des recouvrements importants de pics inter-phase. Dans ces films une très forte corrélation entre l'orientation du substrat W et celle des films déposés existe. En effet, les films de  $TiC_x$  et de  $TiN_y$  déposés par CVD présentent une orientation préférentielle avec les plans  $\{110\}$  parallèles à la surface du substrat W lui-même orienté avec les plans  $\{110\}$  parallèles à la surface de l'échantillon. Cependant quelles

que soient les conditions de dépôt la fissuration des films de  $\text{TiN}_y$  n'a pas pu être évitée et ces films n'ont donc pas pu être retenus comme revêtements protecteurs du W. Pour les films de  $\text{TiC}_x$ , on observe des forces de texture plus faibles lorsque l'épaisseur du film augmente (Figure 5). De plus, l'augmentation de  $\alpha$  s'accompagne d'une réduction de la taille des grains entraînant un accroissement de la résistance à la fissuration de ces films et ce grâce à une meilleure accommodation des contraintes internes. La diminution de la force de texture est donc corrélée aux modifications de résistances mécaniques des films.

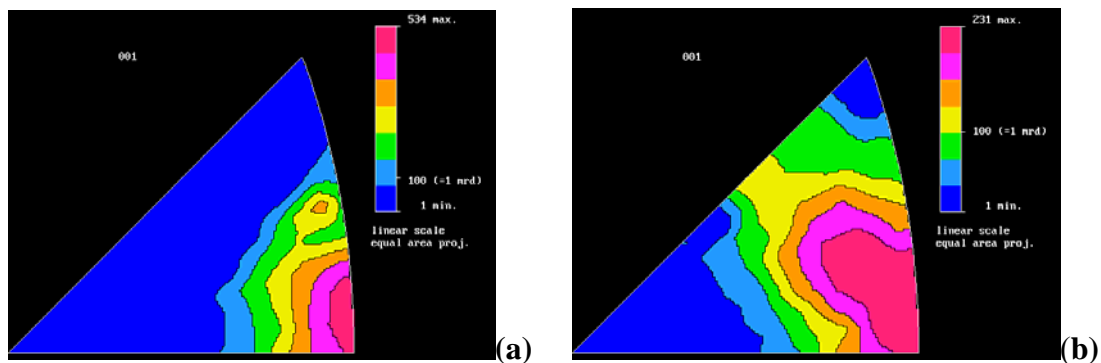


**Figure 5.** Figures de pôles inverses 001 pour des films de TiC de différentes épaisseurs: (a) 10  $\mu\text{m}$  et (b) 30  $\mu\text{m}$ .

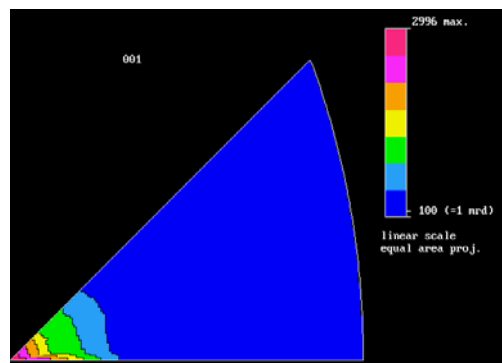


**Figure 6.** Figure de pôles inverse 001 d'un film de Ti déposé sur substrat de W et d'épaisseur  $e = 4744$  (1) nm, affinée avec le programme MAUD.

Suivant les conditions de dépôt on peut obtenir des films uniquement constitués de Ti pur ( $x = y = 0$ ). L'analyse combinée des spectres X correspondants révèle une forte texture de fibre pour ces films de Ti (30 m.r.d.) avec la direction  $\langle 001 \rangle^*$  inclinée de  $5^\circ$  par rapport à la normale de l'échantillon (Figure 6) avec un substrat de W orienté selon  $\langle 001 \rangle$ .

Cette étude est en accord avec ce qui a déjà été observé dans la littérature, à savoir qu'en général lors de la croissance de films minces de matériaux possédant une structure cubique à faces centrées ( $TiC_x$  ou  $TiN_y$ ) ou hexagonale compacte (Ti), la croissance du film a lieu avec les plans les plus compacts parallèles à la surface du substrat, c'est à dire respectivement les plans  $\{111\}$  et  $\{001\}$ , afin de minimiser au maximum les énergies de surface.

### **3.3. Films minces nanostructurés de Si élaborés par un procédé basse température : Laboratoire SIFCOM – thèse Y. Leconte (soutenu le 4 juillet 2003)**

Dans le domaine de l'industrie microélectronique, le silicium est le matériau incontournable. Sous forme de couches minces, le silicium est très utilisé pour la réalisation de composants tels que des transistors, des hétérojonctions ou encore des cellules solaires, et est très étudié dans un souci d'intégration à grande échelle et de miniaturisation croissant. De plus, il a été mis en évidence récemment que les films minces de silicium nanocristallisés sont dotés de propriétés photoniques prometteuses. Dans le cadre de l'élaboration de ces structures, la réduction de la température d'élaboration à des valeurs ne dépassant pas  $200^\circ\text{C}$  et permettant l'utilisation de substrats de faibles coûts comme les verres, constitue l'un des principaux challenges pour la microélectronique.

Dans cet objectif, l'utilisation de la technique de pulvérisation magnétron réactive, dans le cadre de la thèse de Yann Leconte (octobre 1999 à juillet 2003) a permis une approche nouvelle. En effet, grâce à la présence d'hydrogène dans le plasma, la croissance de silicium nanocristallisé sous forme de couches minces a été rendue possible à de faibles températures de dépôt et avec des vitesses de croissance assez rapides. Mais cette vitesse de croissance élevée peut se faire au détriment de la qualité cristalline du film de Si. Dans l'objectif d'obtenir des films minces de qualité pour les applications visées, différents paramètres de dépôt régissant la production et la distribution des radicaux hydrures dans le plasma (pression des gaz précurseurs (Ar et  $H_2$ ), puissance radiofréquence ( $P_{RF}$ ) et distance substrat-cible  $d$ ) ont été optimisés. Nous avons cherché plus particulièrement à étudier l'effet de la distance  $d$  sur la qualité cristalline des couches déposées sur substrat verre  $a\text{-SiO}_2$  (films A à F avec respectivement  $d = 4, 6, 7, 8, 10$  et  $12$  cm) et sur substrat monocristallin  $[100]\text{-Si}$  (films B' et F' avec respectivement  $d = 6$  et  $12$  cm). Pour cela, nous avons couplé un certain nombre de techniques de caractérisation structurale telles que la diffraction et la réflectivité des rayons X,

les spectroscopies infrarouge et Raman, les microscopies à force atomique et électronique en transmission haute résolution. Les propriétés structurales et microstructurales des films ont de plus été corrélées avec leurs propriétés optiques (indice de réfraction et gap dit de Tauc).

Lorsque le plasma est riche en hydrogène (80%) et pour une pression totale de  $10^{-1}$  Torr, la croissance d'une couche de silicium nanostructurée a été obtenue à des températures de dépôt aussi basses que  $200^{\circ}\text{C}$ . Cependant, la réalisation de tels dépôts avec des vitesses de croissance élevées se répercute sur la qualité cristalline et la rugosité de surface des films. En effet, les valeurs de rugosité de surface des films déterminées par AFM ou par affinement des spectres de réflectivité X (XRR) sont relativement élevées (de 4 à 8 nm) mais sont cependant beaucoup plus faibles que celles obtenues lors du dépôt de films de Si par PECVD à  $220^{\circ}\text{C}$ . L'affinement des spectres XRR montre de plus que les films de Si déposés sont constitués par 2 couches, comme cela a été également observé par MET, avec une couche fine en surface (de 10 à 17 nm) présentant une très forte porosité pouvant atteindre 40% pour les faibles valeurs de  $d$ .

Les spectres de diffraction X comparés à ceux d'une poudre de silicium mesurée dans les mêmes conditions démontrent que les films présentent des orientations préférentielles et des tailles de cristallites anisotropes. Une analyse combinée de la texture/structure/microstructure en utilisant le programme MAUD a donc été nécessaire. Quels que soient les substrats utilisés, les films étudiés présentent une texture de fibre c'est à dire que les intensités mesurées ne varient qu'en fonction de l'angle de tilt  $\chi$  du goniomètre (les axes cristallins sont aléatoirement répartis autour de la normale aux films).

Les diagrammes expérimentaux à différents angles  $\chi$  sont représentés sur la Figure 7 pour le film D ( $d = 8$  cm). On constate sur cette figure l'excellent accord entre les intensités observées et celles calculées, avec un facteur de fiabilité pour l'affinement aussi faible que 5.5%. Cette approche par une analyse globale du profil nous a permis de déterminer le paramètre de maille  $a$ , les tailles anisotropes des cristallites, l'épaisseur ainsi que la texture des films minces de silicium. Les épaisseurs des films déterminées par cette analyse, excepté pour les films déposés avec  $d$  faible ( $d \leq 7$  cm), sont en excellent accord avec celles mesurées par profilométrie. Les faibles valeurs d'épaisseur des films déposés avec  $d \leq 7$  cm obtenues par l'affinement des spectres de diffraction X proviennent vraisemblablement de la porosité très importante de ces derniers comme cela a été vu par XRR et sur les images MET.

En ce qui concerne la texture de ce film, nous avons utilisé la FDOC extraite par le programme MAUD pour recalculer les figures de pôles observées et ainsi apprécier leur cohérence avec les figures expérimentales (Figure 8). Nous obtenons des facteurs de reliabilité de 1.4 % entre figures de pôles expérimentales et recalculées, attestant de la très bonne reliabilité du calcul de la FDOC.

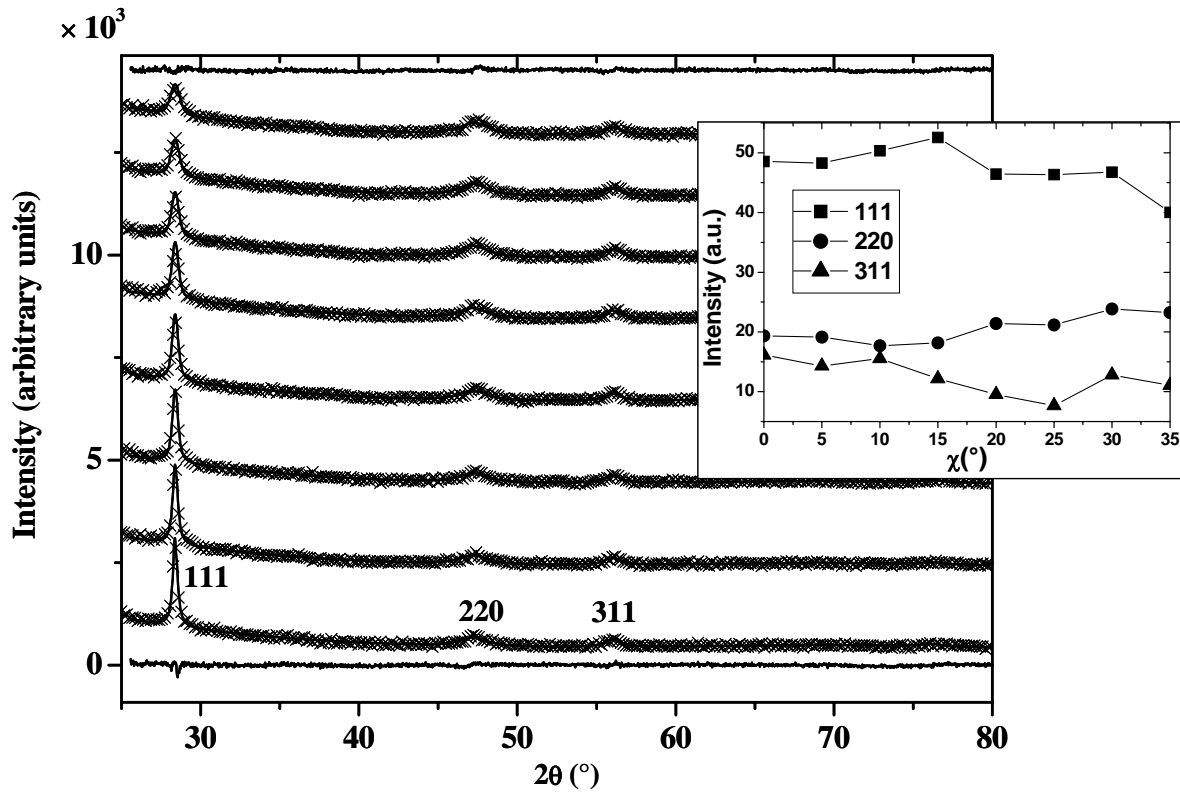


**Figure 7.** Diagrammes de rayons X mesurés (croix) sur le film D ( $d = 8$  cm) à différentes positions en  $\chi$  ( $\chi = 0^\circ$  en bas et  $35^\circ$  en haut,  $\Delta\chi = 5^\circ$ ) et diagrammes simulés avec le programme MAUD (ligne continue). Les diagrammes supérieurs et inférieurs représentent la différence entre les spectres mesurés et calculés respectivement pour  $\chi = 35$  et  $0^\circ$ . En encart, évolution en fonction de  $\chi$  des intensités intégrées des raies 111, 220 et 311 mettant en évidence la présence d'une texture.

Les figures de pôles d'indices simples (Figure 9), recalculées elles aussi à partir de la FDOC en utilisant le programme Beartex montrent que pour le film F, les plans  $\{311\}$  sont préférentiellement alignés avec le plan du film avec une densité d'orientation maximum de 1.48 m.r.d. Deux autres composantes sont visibles avec les plans  $\{110\}$  préférentiellement alignés avec le plan du film et les plans  $\{001\}$  inclinés de  $5^\circ$  par rapport à la surface du film.

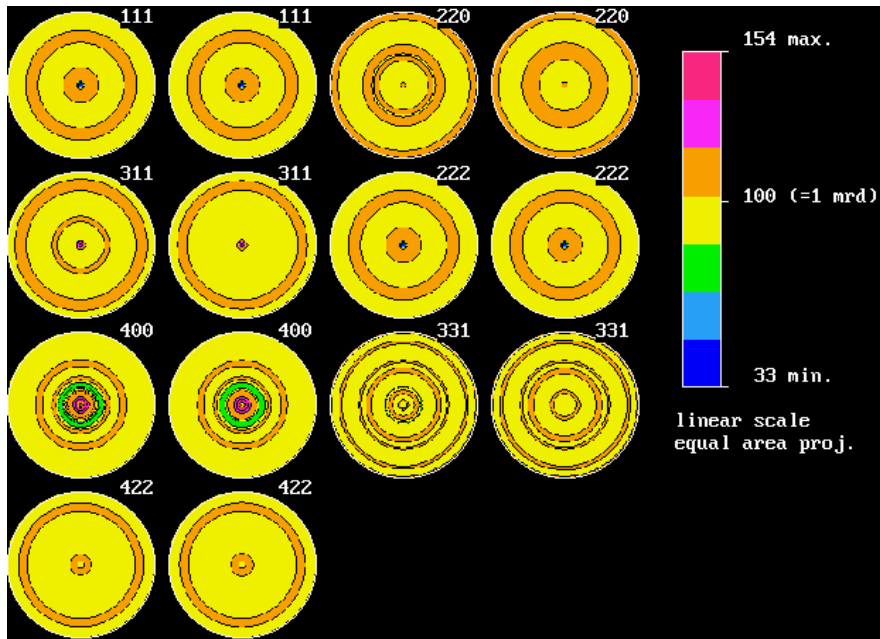


**Figure 8.** Figures de pôles normalisées expérimentales et recalculées à partir de la FDOC pour le film F (substrat a-SiO<sub>2</sub> et d = 12 cm).

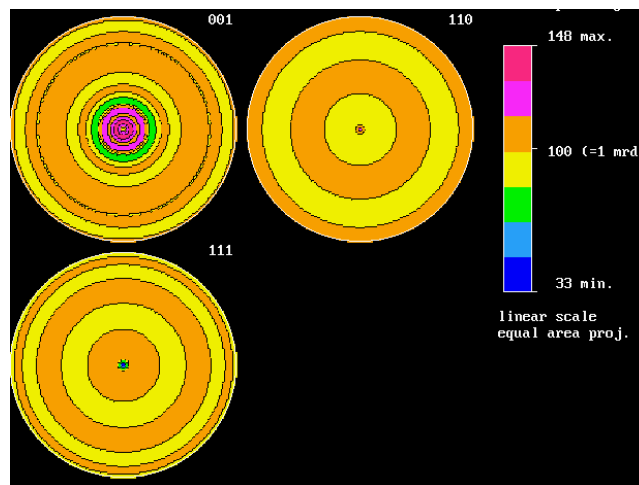


**Figure 9.** Figures de pôles recalculées d'indices simples pour le film F (d = 12 cm).

Quels que soient le substrat utilisé et la distance d, plusieurs orientations préférentielles ont été mises en évidence avec des maxima de densité d'orientation de 2 ou 3 m.r.d. et une tendance marquée à avoir des textures plus faibles pour les films déposés sur les substrats a-SiO<sub>2</sub>. Les valeurs de l'index de texture F<sup>2</sup> sont représentatives d'une texture



relativement faible avec des valeurs minimales de l'ODF relativement élevées de 0.4 à 0.82 m.r.d. démontrant que 40 à 82% du volume du film n'est pas orienté.

Une représentation globale de toutes ces composantes de texture est illustrée par les figures de pôles inverses 001 calculées pour la normale au film  $\vec{n}$  (Figure 10). Sur cette figure, on observe une très nette dépendance des composantes de texture avec  $d$  pour les films déposés sur a-SiO<sub>2</sub> (films A à F) alors que la force de cette texture  $F^2$  n'est quasiment pas affectée. La distance  $d$  la plus proche ( $d = 4$  cm, film A) favorise une orientation avec les directions  $\langle 110 \rangle$  alignées avec  $\vec{n}$  mais des orientations mineures sont également observées avec les directions  $\langle 100 \rangle$  et  $\langle 124 \rangle$  des cristallites selon  $\vec{n}$ . Cette composante de texture  $\langle 110 \rangle$  est défavorisée par l'augmentation de  $d$  qui favorise progressivement une composante  $\langle hh\ell \rangle$  de texture avec  $\ell > 2$ . Ceci s'accompagne d'un léger tilt de la composante  $\langle 100 \rangle$  et de l'apparition d'une composante de texture relativement large et centrée autour de  $\langle 221 \rangle$ . Cette dernière composante, avec l'augmentation de  $d$ , a tendance à progressivement se rapprocher d'une composante d'orientation  $\langle 111 \rangle$ , mais en ne l'atteignant jamais.

Pour les films déposés sur les substrats [100]-Si, la composante d'orientation  $\langle 100 \rangle$  est fortement favorisée avec toujours une texture de fibre (et non une hétéro-épitaxie). Cette texture de fibre observée dans les films nanocristallisés de Si est responsable de la croissance colonnaire visible par MET (Figure 11) des grains de Si, croissance favorisée par un mécanisme de cristallisation induit par les espèces hydrures SiH<sub>2</sub>.

Quel que soit le substrat utilisé ( $d = 6$  et  $12$  cm), une composante de texture de fibre  $\langle 111 \rangle$  est donc observée avec un axe de fibre légèrement décalé par rapport à la normale aux films et ce bien que les nanocristallites de Si présentent une taille anisotrope allongée selon la direction  $\langle 111 \rangle$ . En effet, la forme des cristallites de Si est ellipsoïdale (Figure 12), allongée selon la direction  $\langle 111 \rangle$  (avec une taille d'environ 9 nm) et quasiment isotrope (environ 3 à 5 nm) dans les directions perpendiculaires. Les observations MET en vue plane de ces couches ont de plus démontré que ces cristallites agglomérés en colonne sont entourés de Si amorphe.

Quel que soit le film, le volume de la fraction cristalline de nos films est supérieure à 60% ce qui explique pourquoi la fraction de Si amorphe des films n'est pas visible sur les spectres RX, et ce même pour les films déposés sur substrat [100]-Si.

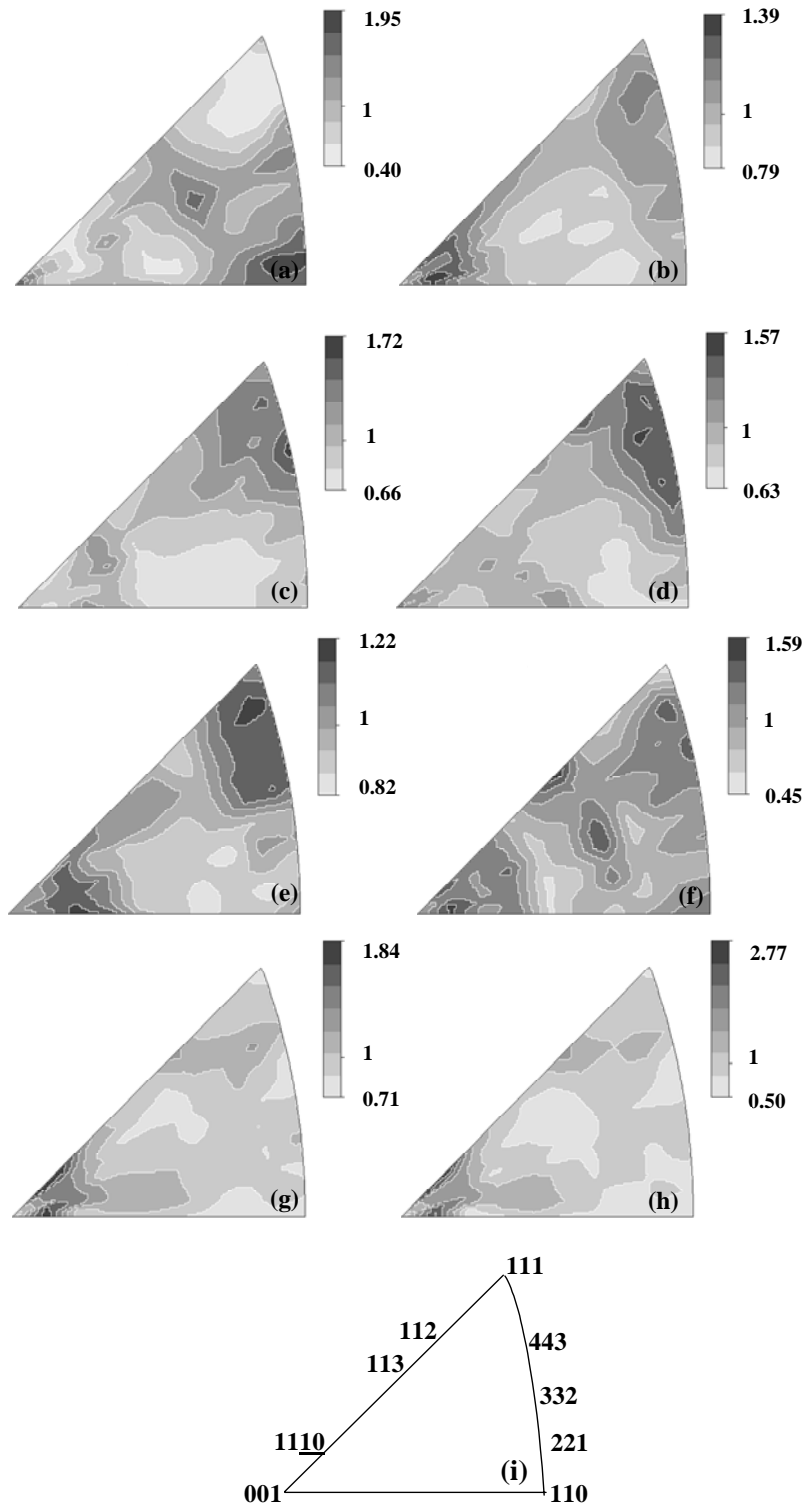


**Figure 10.** (a) – (f) Figures de pôles inverses 001 pour les films A à F déposés sur substrat a-SiO<sub>2</sub> avec respectivement  $4 \leq d \leq 12$  cm et sur substrat [100]-Si avec (g)  $d = 6$  cm et (h)  $d = 12$  cm (films B' et F' respectivement) et (i) localisation de leurs pôles via leurs indices de Miller dans le secteur cubique.

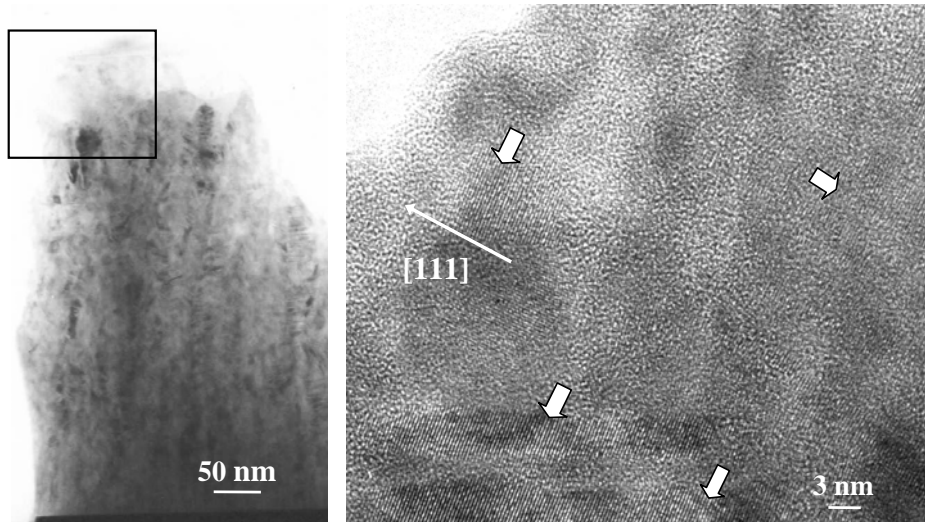


**Figure 11.** Image MET typique du film B de Si ( $d = 6 \text{ cm}$ ) dont l'aire délimitée, agrandie sur la figure de droite, met en évidence la présence de nanograins de Si anisotropes (signalés par une flèche blanche) dans une matrice amorphe.

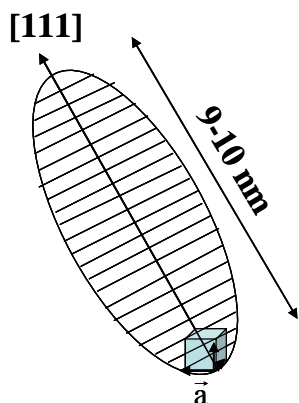


**Figure 12.** Représentation schématique des nanograins de Si de forme ellipsoïdale.

Les propriétés optiques des films avec les valeurs des indices de réfraction et du gap dit de Tauc (valeurs correspondant à l'extrapolation de la courbe  $\sqrt{\alpha(E) \cdot E} = f(E)$  pour  $\alpha = 0$ ) sont étroitement corrélées avec ces propriétés microstructurales et particulièrement avec la taille des nanocrystallites et la présence importante de porosité.

En conclusion, cette étude a permis d'optimiser les paramètres de dépôt permettant d'obtenir des films de Si denses et nanocrystallisés à  $200^\circ\text{C}$  avec des rugosités de surface et des porosités les plus faibles possibles pour des applications en microélectronique, telle que la fabrication de transistors en films minces. La forte rugosité de certains films pourrait aussi être mise à profit pour réaliser des capteurs, tels que des détecteurs de fuite d'hydrogène.

### **3.4. Films minces nanostructurés de SiC élaborés par pulvérisation réactive magnétron radiofréquence: Laboratoire SIFCOM – thèse H. Taupin-Colder (soutenue le 15 septembre 2005)**

Le silicium massif, bien qu'il soit le matériau incontournable pour la réalisation de composants non émetteurs de lumière dans le domaine de la microélectronique, présente des limitations d'utilisation lorsque la température de fonctionnement est supérieure à 200°C ou que l'environnement devient plus ou moins sévère. C'est pourquoi, un regain d'intérêt a été observé ces dernières années pour les semi-conducteurs à "grand gap" comme solution alternative au Si. Parmi ceux-ci, le carbure de silicium (SiC) peut être utilisé dans des conditions extrêmes de températures, d'agressivité chimique ou de fortes irradiations, pour des applications dans le domaine de l'automobile, de l'aéronautique, de l'aérospatiale... De plus, le SiC peut être aisément déposé sous forme de couches minces de bonne qualité cristalline et avec un faible coût. Des travaux précurseurs au Laboratoire SIFCOM (thèse de S. Kerdilès) ont démontré que des couches hydrogénées de SiC nanocristallisées (nc-SiC :H) de bonne qualité pouvaient être déposées par la technique de pulvérisation magnétron réactive en utilisant un plasma 100% hydrogéné et à des températures n'excédant pas 600°C. Les dispositifs (hétérojonction nc-SiC/Si) réalisés à une température de traitement de 600°C à partir de ces films présentent des performances satisfaisantes.

Dans le cadre de la thèse d'Héloïse Taupin-Colder (octobre 2002 - septembre 2005), nous avons cherché à réaliser une hétérojonction nc-SiC/Si avec une température de traitement ne dépassant pas 300°C, présentant des performances comparables voire supérieures à celles obtenues précédemment, tout en augmentant la vitesse de croissance en vue d'une éventuelle transposition industrielle. Dans cet objectif, une attention particulière a été portée à la détermination des corrélations entre d'une part la composition et les propriétés structurales de ces films, et d'autre part leurs propriétés physiques (optiques et électriques). En particulier, l'influence de la température de dépôt  $T_d$  sur la structure, la composition, la morphologie des films nanostructurés de SiC a été étudiée.

L'introduction de 20% d'argon dans le plasma hydrogéné s'est avérée suffisante pour augmenter d'un facteur quatre la vitesse de croissance des films nc-SiC :H, sans diminuer pour autant leur qualité cristalline. En effet, les corrélations établies entre la composition du plasma et celle des films de SiC (stage de Master Recherche de F. El Yazami) déterminées respectivement par spectroscopie d'émission optique in-situ et par spectroscopies RBS et

infrarouge ont mis en évidence le rôle clé que joue l'hydrogène dans les mécanismes de cristallisation du SiC : les radicaux hydrures de silicium et de carbone sont très réactifs, souvent instables, et on observe un phénomène de compétition entre l'adhérence de ces espèces hydrures pour la croissance du SiC et l'attaque du dépôt par ces dernières. L'ajout d'argon dans le plasma modère cette forte réactivité en restreignant notamment le phénomène de gravure du dépôt et permet ainsi d'augmenter le rendement de pulvérisation.

Un changement essentiel dans la nature des échantillons a été mis en évidence lorsque  $T_d$  varie de 200 à 600°C : à  $T_d = 200^\circ\text{C}$  les films sont constitués essentiellement de SiC amorphe et sont riches en silicium et hydrogène avec une fraction cristalline  $f_c$  de SiC de 2.5% (déterminée par spectroscopie d'absorption infrarouge) ; à plus haute température, le silicium amorphe hydrogéné et le carbone sous forme graphite laissent la place à la formation de nanograins de SiC ( $f_c = 80\%$ ) avec une composition quasi-stoechiométrique. La dilution de l'hydrogène par l'argon dans le plasma est donc un choix judicieux puisque les films minces de nc-SiC :H présentent un degré de cristallisation plus important.

On distingue nettement pour  $T_d > 200^\circ\text{C}$  sur les spectres de diffraction X des films de SiC trois pics de diffraction qui peuvent être indexés dans la maille cubique du 3C-SiC (groupe d'espace  $F\bar{4}3m$ ) et dont les intensités relatives diffèrent de celles d'une poudre aléatoire de SiC (encart Figure 13). Comme dans le cas des films nanostructurés de Si, ces couches présentent une texture de fibre autour de la normale  $\vec{n}$  au plan de l'échantillon. Bien que la phase cubique soit probablement le seul polytype de SiC présent dans nos films, la largeur importante des pics de diffraction (Figure 13), révélatrice de la présence de nanocristaux, ne permet pas d'exclure a priori la présence d'autres polytypes du SiC (le polytype hexagonal 6H-SiC étant le plus répandu). En particulier on observe un épaulement à  $2\theta \approx 35^\circ$  qui ne peut s'indexer avec une raie du polytype 3C-SiC (Figure 13).

Ces pics de diffraction présentent de plus en fonction de  $hkl$  des largeurs à mi-hauteur variables et caractéristiques d'une anisotropie de taille. La présence d'une orientation préférentielle et la détermination de la taille anisotrope des nanocristallites ainsi que la nécessité de lever l'ambiguïté sur les polytypes, impliquent l'utilisation d'une analyse globale du profil de ces spectres de diffraction. Une première analyse en utilisant du 3C-SiC texturé comme phase unique dans l'affinement des spectres de rayons X et en adoptant le modèle de Popa pour déterminer les tailles anisotropes des cristallites, n'a pas permis de reproduire de façon satisfaisante les spectres expérimentaux. Cette inadéquation entre les spectres expérimentaux et ceux calculés est d'autant plus marquée que la température  $T_d$  est faible.

Une phase supplémentaire a donc été introduite avec le polytype 6H-SiC et la proportion de 3C-SiC et 6H-SiC est un nouveau paramètre qui est pris en compte dans l'affinement des spectres X.

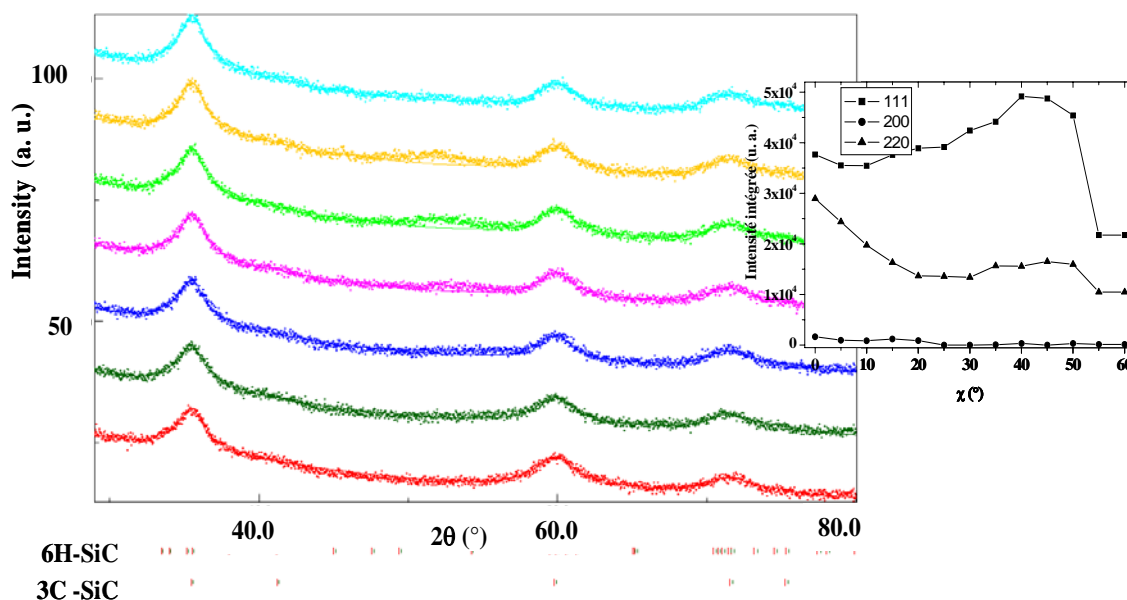


**Figure 13.** Diagrammes de diffraction expérimentaux (en pointillés) et affinés (trait plein) à différentes positions en  $\chi$  pour un film élaboré à  $T_d = 600^\circ\text{C}$  ( $\chi = 0^\circ$  en bas et  $35^\circ$  en haut,  $\Delta\chi = 5^\circ$ ). En encart, évolution en fonction de  $\chi$  des intensités intégrées des raies 111, 200 et 220 (indexées dans la maille SiC cubique) mettant en évidence la présence d'une texture.

$T_d$ ( $^\circ\text{C}$ )	$a_{3\text{C-SiC}}$ ( $\text{\AA}$ )	Proportion de 6H-SiC (%)	Tailles anisotropes selon les directions cristallographiques ( $\text{\AA}$ )			
			[111]	[200]	[220]	[311]
300	4.385 (3)	70 (1)	28 (1)	12 (2)	13 (2)	15 (1)
400	4.38 (1)	66 (1)	34 (2)	12 (1)	16 (2)	15 (2)
500	4.375 (2)	52 (1)	44 (1)	14 (1)	15 (1)	20 (1)
600	4.378 (4)	33 (2)	49 (2)	17 (1)	18 (1)	22 (2)

**Tableau 2.** Principaux paramètres structuraux et microstructuraux affinés du 3C-SiC.

Avec ces paramètres, un excellent accord entre les spectres expérimentaux et ceux calculés (Figure 13) a été trouvé comme l'attestent également les faibles valeurs des facteurs de reliabilité ( $< 5.2\%$ ). Les principaux paramètres structuraux affinés du 3C-SiC sont

regroupés dans le Tableau 2. Quelle que soit  $T_d$ , le paramètre de maille  $a$  de la structure du 3C-SiC est affiné autour de 4.38 Å tandis que les paramètres de maille  $a$  et  $c$  du 6H-SiC sont affinés autour de 3.0 et 15.25 Å respectivement. Ces valeurs de  $a$  supérieures à celles du 3C-SiC massif (4.36 Å) correspondent à un accroissement d'environ 0.7%. Ce dernier ne peut être imputé à la présence de contraintes résiduelles dans nos films, comme cela était le cas pour des films de SiC déposés à 900°C par LPCVD, puisque aucun déplacement des pics de diffraction n'a été observé lorsque l'angle  $\chi$  varie. Cette différence pourrait être due à un phénomène de relaxation dans nos matériaux du fait de la présence d'hydrogène dans le plasma.

La forme des cristallites de 3C-SiC est ellipsoïdale, allongée selon la direction [111] et quasiment isotrope dans les directions perpendiculaires (Tableau 2). Rappelons que cette forme a déjà été observée lors du dépôt de silicium nanocristallin en utilisant la même technique de dépôt. Lorsque  $T_d$  croît de 300 à 600°C, la taille des cristallites selon la direction  $\langle 111 \rangle$  double quasiment (augmentation de 3 à 5 nm) avec des tailles dans les directions perpendiculaires qui restent quasiment constantes aux environs de 1.5 nm. Ceci s'accompagne également d'une décroissance de la proportion de 6H-SiC de 70 à 33% dans nos films. D'après la littérature, la présence de 6H-SiC à des températures aussi basses est inattendue, laissant supposer qu'elle doit résulter de l'existence de fautes d'empilement dans 3C-SiC qui n'ont pas pu être modélisées dans le programme MAUD. La taille isotrope des cristallites de 6H-SiC (autour de 5.6 nm) est quasiment indépendante de  $T_d$ .

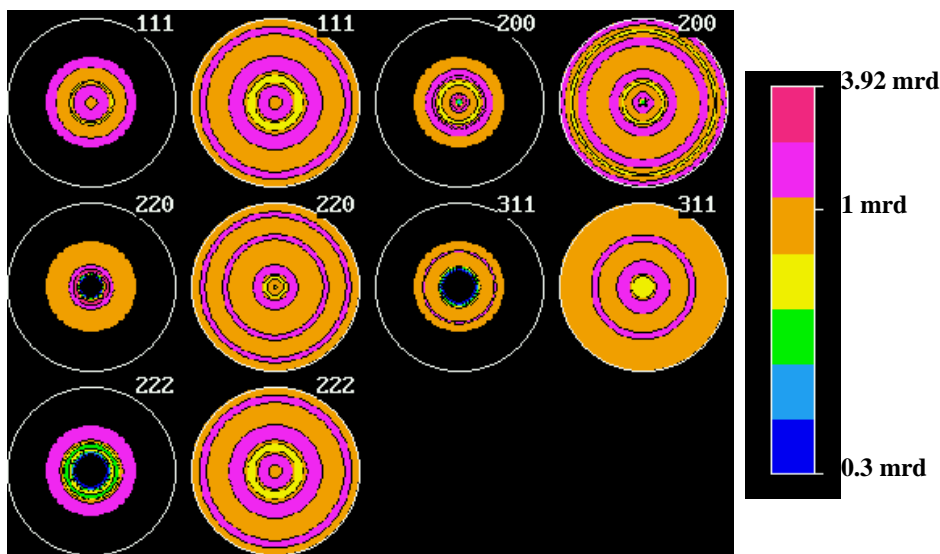


**Figure 14.** Figures de pôles expérimentales et recalculées pour un film élaboré à  $T_d = 600^\circ\text{C}$ .

En ce qui concerne la texture de nos films un excellent accord entre les figures de pôles expérimentales et celles recalculées est observé (Figure 14) avec des facteurs de reliabilité de 1.4%. Les figures de pôles recalculées pour les indices simples  $\{001\}$ ,  $\{102\}$ ,  $\{111\}$ ,  $\{100\}$  (Figure 15) montrent que l'axe d'allongement des cristallites ne correspond pas forcément à l'axe de développement de la texture, comme cela a déjà été observé lors de la croissance de nc-Si. Plusieurs composantes de texture sont présentes dans les films de SiC : en majorité les plans  $\{102\}$  sont préférentiellement alignés perpendiculairement à  $\vec{n}$  avec une densité d'orientation au maximum de 3.92 m.r.d.; deux autres composantes sont visibles avec les plans  $\{11\ell\}$  préférentiellement alignés perpendiculairement à  $\vec{n}$ .

Pour des films déposés à  $T_d = 300^\circ\text{C}$ , la valeur minimale de la FDOC de 0.7 m.r.d. indique que 70% du volume du film n'est pas orienté, et lorsque  $T_d$  croît de  $300^\circ\text{C}$  à  $600^\circ\text{C}$ , cette dernière passe à 0.3 m.r.d. montrant que l'augmentation de la température de dépôt favorise la croissance des cristallites selon des orientations préférentielles dans nos films.

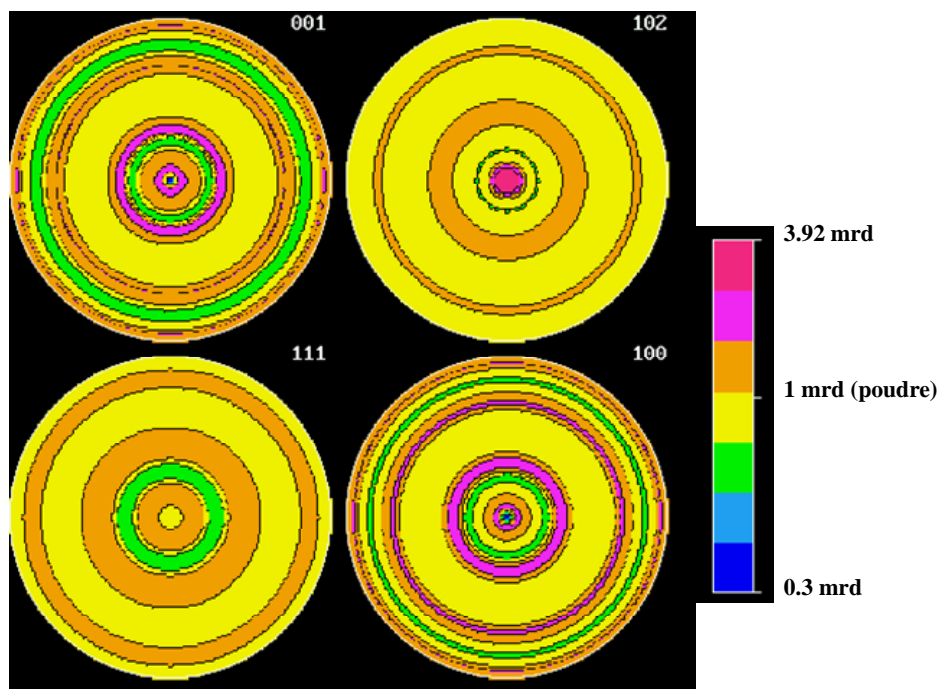


**Figure 15.** Figures de pôles d'indices simples recalculées.

Pour les films de SiC déposés par CVD, cette valeur minimale de la FDOC n'exécède pas 0.48 m.r.d. quelles que soient la température de dépôt ( $> 100^\circ\text{C}$ ). De plus, ces films déposés sur substrats de  $[100]$ -Si présentent une orientation préférentielle avec les plans



{100} ou {111} des cristallites perpendiculaires à  $\vec{n}$  alors que nos films présentent une croissance préférentielle avec les plans {111} des cristallites inclinés d'un angle  $\alpha$  de  $39^\circ$  par rapport à  $\vec{n}$  (Figure 16).

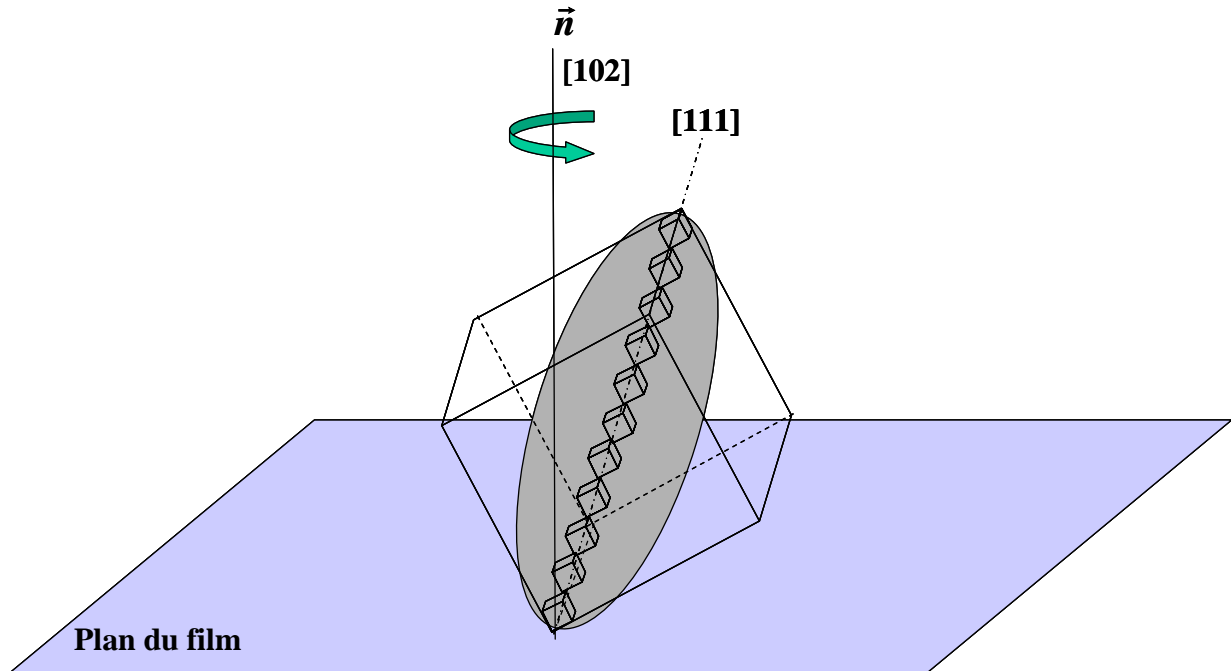


**Figure 16.** Représentation schématique de la croissance préférentielle des cristallites de forme ellipsoïdale avec les plans {111} inclinés de  $39^\circ$  par rapport à la direction de croissance du film ( $T_d = 600^\circ\text{C}$ ).

Cette inclinaison des plans {111} du 3C-SiC par rapport à  $\vec{n}$  a déjà été rapportée par Yasui et collaborateurs, mais avec un angle  $\alpha$  plus faible ( $15.8^\circ$ ), lorsque des fautes d'empilement apparaissent dans le 3C-SiC déposé par LPCVD. Le type de croissance observé dans nos films pourrait donc être caractéristique de la présence de nombreux défauts dans la croissance du 3C-SiC ce qui conforte l'hypothèse selon laquelle le pourcentage de 6H-SiC relativement élevé et nécessaire à l'affinement des spectres X, résulterait d'un grand nombre de fautes d'empilement dans le 3C-SiC.

Les observations en HRMET de nos films ont permis de corroborer cette hypothèse. En effet, sur les images HRMET, les grains observés dans le film déposé à  $T_d = 600^\circ\text{C}$  sont majoritairement de structure cubique ; cependant un certain nombre de grains présentent une structure zig-zag caractéristique de la phase hexagonale 6H-SiC (Figure 17 (a) et (b)). Un traitement numérique de cette image a permis de faire une étude fine de ces structures en

identifiant les séquences d'empilement des tétraèdres qui en fait ne peuvent pas correspondre à la séquence 6H-SiC mais s'apparentent plutôt à celle du 3C-SiC fortement fauté avec des parties multi-maclées (Figure 17 (c)). La mise en évidence de ces fautes d'empilement dans le 3C-SiC diminue lorsque  $T_d$  se rapproche de  $600^\circ\text{C}$  en parfaite cohérence avec ce qui a été observée par diffraction de rayons X. De plus, comme cela a été observé par diffraction des rayons X, les images en champ noir montrent que les grains de SiC sont allongés selon la direction  $\langle 111 \rangle$  et que les plans  $\{111\}$  sont inclinés par rapport à l'axe de croissance de la couche. Ce type de croissance colonnaire déjà observée dans les films de nc-Si, semble être fortement corrélée à la technique de dépôt employée.

Les caractéristiques structurales de ces films ont ensuite été corrélées aux propriétés optiques de nos films avec notamment l'étude du gap dit de  $T_{auc} E_0$ , du pseudo-gap  $E_{5,4}$  (énergie correspondant au coefficient d'absorption  $\alpha = 5 \times 10^{14} \text{ cm}^{-1}$ ) et de l'indice de réfraction  $n$ . Lorsque  $T_d$  augmente, les valeurs des deux gaps augmentent légèrement et l'indice  $n$  croît en se rapprochant de la valeur du SiC monocristallin. Cette évolution des propriétés optiques est vraisemblablement due à la désorption de l'hydrogène lorsque  $T_d$  augmente ce qui se traduit par une amélioration de la qualité cristalline (évolution d'un état quasi-amorphe à un état nanocristallisé) et de la compacité des couches.

Le dispositif réalisé à partir de couches de SiC (hétérojonction nc-SiC:H/c-SiC) déposées à  $600^\circ\text{C}$  présente d'excellentes performances (redressement de  $10^5$  à  $\pm 2\text{V}$ , courant de fuite en  $\mu\text{A.cm}^2$ ) avec un mécanisme de conduction en régime de faible injection qui se fait essentiellement par diffusion des porteurs comme le reflète la valeur du facteur d'idéalité proche de 1 (1.3). Le dispositif réalisé à  $300^\circ\text{C}$ , bien qu'il présente un redressement satisfaisant ( $10^3$  à  $\pm 2\text{V}$ ), est de moindre qualité comme prévisible du fait du caractère fortement hydrogéné de la diode responsable de la forte densité de défauts et de microcavités qui régissent la conduction par recombinaison (avec un facteur d'idéalité de 3.7). Le traitement de cette diode durant 30 minutes à une température de  $300^\circ\text{C}$  a permis de guérir une forte proportion de défauts avec une forte réduction du facteur d'idéalité de 3.7 à 1.5 rendant ainsi compétitif le mécanisme de conduction par diffusion par rapport à celui par recombinaison, tout en préservant le comportement redresseur.

Enfin, un recuit plus long (6 heures) continue à réduire ce facteur d'idéalité mais induit une augmentation du courant de fuite avec une légère détérioration du facteur de redressement jusqu'à une valeur qui reste cependant raisonnablement exploitable.

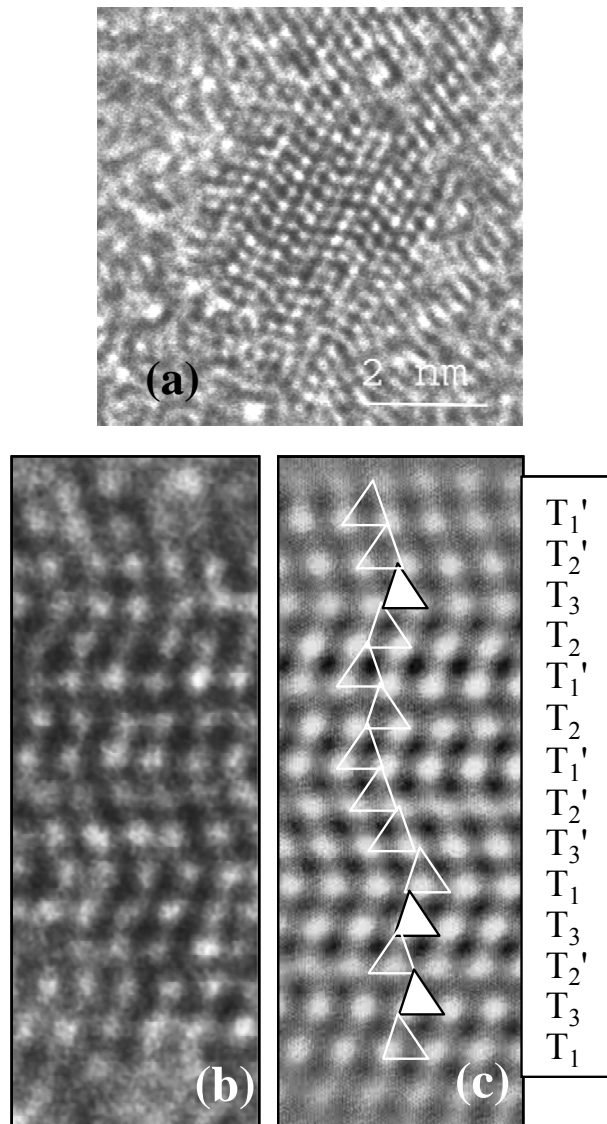


**Figure 17.** (a) Image HRMET d'un nanograin de SiC du film élaboré à  $T_d = 600^\circ\text{C}$ . Zoom d'une partie du nanograin (b) et image filtrée (c) avec la séquence correspondante des tétraèdres.

En conclusion, ce travail ouvre des perspectives prometteuses dans le domaine du carbure de silicium nanocristallin et la réalisation d'hétérojonctions. L'obtention d'un dispositif performant à  $300^\circ\text{C}$  suite à un simple recuit de 30 minutes constitue une avancée certaine pour le développement de dispositifs sur des substrats flexibles peu coûteux de type polymères. De plus, l'effet photovoltaïque mis en évidence lors de la caractérisation des diodes mérite un examen plus approfondi afin d'explorer la possibilité de réalisation de cellules solaires avec nos films de SiC nanocristallisés comme fenêtres d'entrée, ou de photodétecteurs.

### **3.5. Films minces composites $\text{Cr}^{2+}:\text{ZnSe}/\text{SiO}_2$ ou de $\text{Cr}^{2+}:\text{ZnSe}$ nanocristallisés pour la réalisation de micro-lasers émettant dans l'infrarouge moyen: Laboratoire SIFCOM – Stage de Master Recherche et thèse N. Vivet (soutenance prévue en octobre 2008)**

Parmi les lasers infrarouges à base de semi-conducteurs II-VI dopés avec des métaux de transition, les systèmes massifs à base de  $\text{Cr}^{2+}:\text{ZnSe}$  sont probablement ceux qui présentent les performances les plus spectaculaires de part leur grande section efficace d'excitation, leur rendement quantique élevé, leur bonne stabilité chimique et mécanique ainsi que leur excellente conductivité thermique permettant l'utilisation d'un fort flux de pompage. Dans ces matériaux, l'ion  $\text{Cr}^{2+}$  se substituant aux ions  $\text{Zn}^{2+}$  dans un environnement tétraédrique est responsable de l'émission laser dans l'infrarouge moyen à température ambiante, avec très peu de perte par absorption de l'état excité ou par des processus non radiatifs. Le domaine spectral d'émission de 2.3 à 3.4  $\mu\text{m}$  correspondant aux longueurs d'onde d'absorption de nombreuses molécules, est très important d'un point de vue technologique pour des applications dans le domaine de l'environnement avec la détection, l'identification et la localisation de traces de polluants atmosphériques, mais aussi du point de vue de la biologie, de la médecine et de la détection radar, à tel point que l'on qualifie de plus en plus le  $\text{Cr}^{2+}:\text{ZnSe}$  comme le nouveau système laser « Titane - Saphir de l'infrarouge moyen ».

Récemment, des développements spectaculaires ont été observés avec la mise en évidence dans le domaine de l'infrarouge moyen (i) d'un signal d'électroluminescence dans le matériau massif monocristallin, (ii) d'un effet laser à température ambiante en utilisant des nanopoudres de  $\text{ZnSe}$  dopées  $\text{Cr}^{2+}$  (avec des tailles de grains de 200 nm), et (iii) d'un signal de photoluminescence dans des films minces déposés par épitaxie par jet moléculaire (MBE). Ceci ouvre donc la voie au pompage électrique de ces structures en films minces à base de chrome et de  $\text{ZnSe}$ . Parmi les techniques d'élaboration de structures compactes sous forme de films minces, la pulvérisation magnétron radiofréquence présente de nombreux avantages par rapport à la MBE en particulier, avec une facile transposition à un niveau industriel et un plus faible coût. C'est pourquoi, dans le cadre de ce sujet débuté avec le stage de Master Recherche et la thèse de N. Vivet, nous nous sommes proposés d'élaborer en utilisant cette technique de dépôt des films minces  $\text{Cr}^{2+}:\text{ZnSe}$  nanocristallisés dans l'objectif de réaliser à partir de ces films un microlaser fonctionnant à température ambiante en pompage optique et/ou électrique. L'originalité de ce sujet consiste à tirer parti à la fois de la possibilité d'une excitation

électrique de ces structures dans un souci de compacité et d'intégrabilité croissant et des effets éventuels de confinement quantique liés à la taille des nanograins de ZnSe.

Etant donné que l'isolement individuel des nanograins de semiconducteurs par une matrice diélectrique offre un confinement quantique plus stable avec des modifications des états de surface qui augmentent l'efficacité du signal de luminescence, nous avons donc envisagé deux types de structures dopées  $\text{Cr}^{2+}$  : des films minces de ZnSe nanocristallisés ou des nanograins de ZnSe incorporés dans une matrice de  $\text{SiO}_2$ . L'étude de ces nanostructures devait permettre d'appréhender les mécanismes d'excitation, encore sujets à de nombreux débats dans le matériau massif, pour élaborer et optimiser dans un second temps des cavités laser résonantes qui seront étudiées sous pompage optique et électrique. L'excitation électrique constitue un des enjeux majeurs de ce sujet puisqu'une interaction efficace doit être obtenue entre les ions  $\text{Cr}^{2+}$  et les porteurs de charge.

#### **a) Détermination des conditions optimales de dépôt pour le dépôt de films minces composites de ZnSe/SiO<sub>2</sub>.**

Avant de doper nos films avec du  $\text{Cr}^{2+}$ , nous avons cherché dans un premier temps à déterminer les conditions optimales de dépôt pour synthétiser des films minces composites ZnSe/SiO<sub>2</sub> contenant une proportion maximale de ZnSe.



**Figure 18.** Photographie de la cible de  $\text{SiO}_2$  utilisée et recouverte de morceaux de ZnSe.

Pour cela, différents substrats monocristallins tels que [100]-Si et [100]-AsGa, et des substrats verres a- $\text{SiO}_2$  ont été utilisés et la cible de pulvérisation de  $\text{SiO}_2$  a été recouverte par des morceaux de ZnSe disposés uniformément avec un taux de recouvrement en surface du ZnSe sur le  $\text{SiO}_2$  de 30% (Figure 18). Différents paramètres de dépôt ont été explorés : la température des substrats  $T_d$  ( $20 \leq T_d \leq 385^\circ\text{C}$ ), la puissance radiofréquence ( $P_{\text{RF}} = 50\text{W}$ ,

100W, 150W), la pression d'Argon dans l'enceinte ( $P_{Ar} = 0.5 \text{ Pa}$  et  $2 \text{ Pa}$ ) et la distance cible-substrats ( $d = 7$  et  $10 \text{ cm}$ ).

Les corrélations existant entre la composition du plasma, la croissance, la structure, la microstructure et la composition des films déposés, ont été établies en utilisant différentes techniques de caractérisation :

- la spectroscopie d'émission optique in-situ qui a permis de suivre l'évolution des espèces Se, Zn, Si, O... présentes dans le plasma en fonction des différents paramètres de dépôt;
- la spectroscopie EDX donnant accès aux pourcentages en Si, Zn, Se et O constituant les films (avec une profondeur sondée d'environ  $1.3 \mu\text{m}$ );
- la réflectivité des rayons X pour obtenir des informations concernant l'épaisseur, la densité électronique et la proportion de ZnSe et de  $\text{SiO}_2$  (à partir des valeurs de  $q_c$ );
- la spectroscopie de rétrodiffusion Rutherford permettant d'accéder à la composition de la couche et au profil de distribution en profondeur du Zn et de Se;
- la diffraction des rayons X permettant d'accéder aux paramètres structuraux et microstructuraux via une analyse du film en volume;
- la microscopie électronique en transmission (MET) permettant d'accéder à la structure du film à une échelle très locale.

Il a été ainsi mis en évidence que l'espèce du plasma la plus sensible à la température de dépôt  $T_d$  est le Sélénium et que des  $T_d$  élevées favorisent sa désorption par évaporation des adatoms de Se à la surface du substrat, favorisant ainsi la formation de  $\text{SiO}_2$  dans nos films comme le prouvent les valeurs de  $q_c$  proches de celles du  $\text{SiO}_2$  pur. De plus, du fait du déficit en Se et de l'excès en Zn et O dans ces films, on observe sur les spectres Raman lorsque  $T_d > 215^\circ\text{C}$ , un changement de phase du ZnSe en ZnO. Les images HRMET des couches élaborées à  $P_{RF} = 50\text{W}$  et  $T_d \leq 215^\circ\text{C}$  mettent en évidence que ces couches sont constituées par une faible proportion de nanograins de ZnSe (36.4% au maximum) avec des tailles inférieures à  $1 \text{ nm}$ .

L'accroissement de  $P_{RF}$  de 50 à 100W et 150W favorise la croissance de films plus épais avec l'incorporation d'une plus grande quantité de Se et de Zn du fait de l'existence d'un meilleur équilibre entre les deux processus concurrentiels pour la croissance de ZnSe que sont la désorption par évaporation des adatoms de Se et le piégeage des ces derniers sur des sites de basse énergie. En effet, l'augmentation notable par rapport à  $P_{RF} = 50\text{W}$  de la vitesse de dépôt  $v_g$  d'un facteur 8 et 20 respectivement pour  $P_{RF} = 100$  et  $150\text{W}$  favorise la mobilité

en surface des adatoms de Zn et de Se (du fait de l'augmentation des collisions avec les autres adatoms), facilitant ainsi leur migration vers les sites de piégeage ce qui diminue l'opportunité de leur évaporation. Cependant, cet effet est nettement atténué lorsque  $T_d$  croît jusqu'à  $385^\circ\text{C}$  puisque la désorption devient alors à cette température plus efficace.

Afin d'étudier l'impact de  $P_{Ar}$  et de la distance substrat-cible  $d$  sur la composition des films résultants, nous avons donc choisi de travailler avec des  $T_d$  peu élevées ( $T_d \leq 215^\circ\text{C}$ ). L'augmentation de  $P_{Ar}$  de 0.5 à 2 Pa s'accompagne d'une augmentation de la probabilité de collisions des espèces dans le plasma diminuant ainsi leur énergie cinétique et donc leur probabilité d'atteindre le substrat, ce qui se traduit par une diminution de  $v_g$ . Cependant, les analyses EDX et la réflectivité des rayons X, avec des valeurs de  $q_c$  d'environ  $0.041 \text{ \AA}^{-1}$  pour  $P_{RF} > 50\text{W}$ , révèlent que plus de ZnSe a été incorporé. Cette diminution de  $v_g$  à  $P_{Ar} = 2 \text{ Pa}$  est compensée lorsqu'on diminue la distance substrat-cible ( $d = 7 \text{ cm}$ ) et des proportions plus importantes encore de ZnSe sont incorporées dans nos films ( $\approx 74\%$ ). Les vitesses de dépôts ainsi obtenues sont très élevées ( $v_g = 0.628 \text{ nm}\cdot\text{s}^{-1}$  au maximum) en comparaison de celles obtenues avec d'autres techniques pour le dépôt de ZnSe ( $v_g = 0.172 \text{ nm}\cdot\text{s}^{-1}$  et  $0.033 \text{ nm}\cdot\text{s}^{-1}$  respectivement par ablation laser et dépôt en phase vapeur) ce qui peut entraîner des inhomogénéités dans la croissance de la couche et se faire au détriment de sa qualité cristalline.

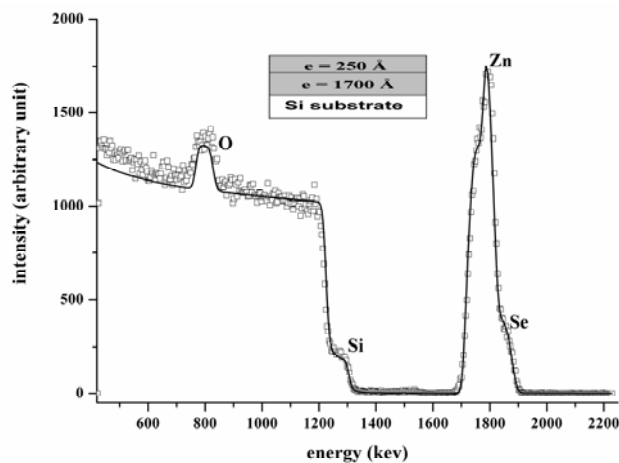


**Figure 19.** Spectres RBS expérimental (symboles carrés) et affiné avec le programme RUMP (ligne continue) pour un film déposé sur substrat de [100] - Si à  $P_{RF} = 50\text{W}$  et à  $T_d = 20^\circ\text{C}$ .

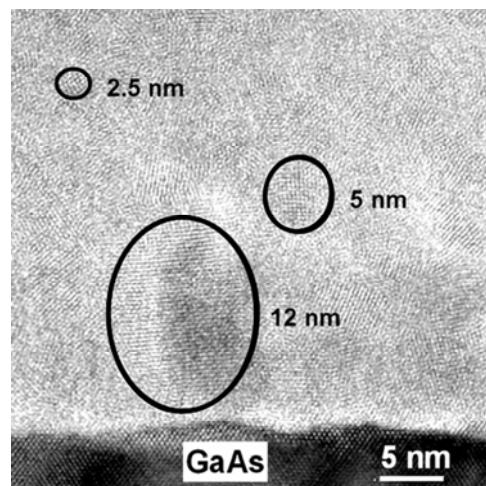


**Figure 20.** Image HRMET du film déposé sur substrat GaAs à  $P_{RF} = 150\text{W}$ ,  $d = 7 \text{ cm}$  pour  $P_{Ar} = 2 \text{ Pa}$  à  $T_d = 20^\circ\text{C}$  et présentant des grains de différentes tailles.

En effet, pour les affinements des spectres de RBS des films déposés avec  $P_{Ar} = 2$  Pa,  $d = 7$  cm et ce quels que soient  $P_{RF}$  et le substrat considéré, il a été nécessaire d'introduire 2 couches (Figure 19) : une couche en surface de faible épaisseur ( $2.5 \text{ nm} \leq e_2 \leq 9 \text{ nm}$ ) présentant des valeurs de  $q_c$  plus faibles que celles obtenues pour la couche plus épaisse à l'interface substrat-film ( $e_1 > 1440 \text{ nm}$ , épaisseurs non accessibles par réflectivité). Les rugosités de surface et d'interface correspondantes augmentent lorsque  $P_{RF}$  passe de 100 à 150W avec des valeurs maximales respectivement de 7.21 nm à  $T_d = 20^\circ\text{C}$  et de 1.37 nm à  $T_d = 215^\circ\text{C}$ . Lorsque  $T_d$  augmente on observe une diminution de 5 nm de cette rugosité de surface à  $P_{RF} = 150\text{W}$ , ce qui atteste que c'est bien la conjonction d'une vitesse de dépôt élevée, résultant de l'augmentation du nombre d'espèces pulvérisées à cette  $P_{RF}$ , et de la diminution de la distance  $d$  qui est responsable de l'inhomogénéité dans la composition des films et des importantes rugosités de surface observées.

Cette inhomogénéité de composition avec une couche plus dense à l'interface substrat-film a été confirmée par les observations MET et s'accompagne d'une inhomogénéité dans la distribution des tailles des nanograins de ZnSe, dans le domaine de 2.5 à 12 nm, d'autant plus marquée à  $P_{RF} = 150\text{W}$  (où  $v_g \times 3$  par rapport à 100W) et à  $T_d = 20^\circ\text{C}$  (Figure 20).

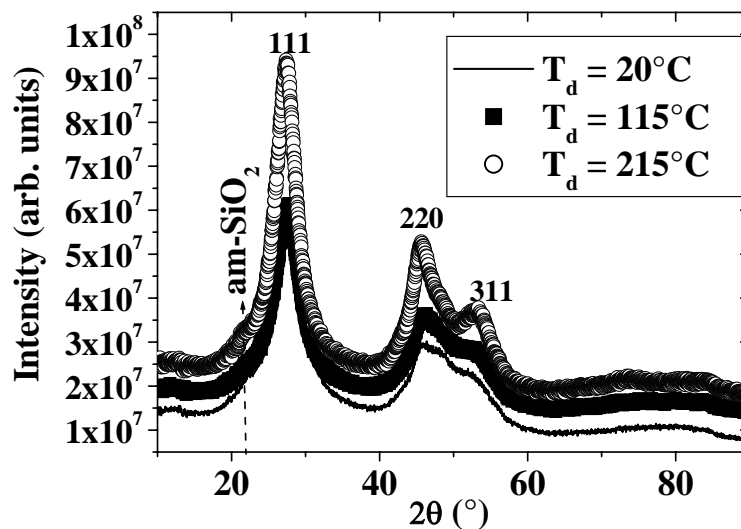


**Figure 21.** Diagrammes RX en configuration asymétrique  $\omega$ - $2\theta$  avec  $\omega = 13.65^\circ$  pour les films déposés sur substrat a-SiO<sub>2</sub> à  $P_{RF} = 150\text{W}$  et à différentes  $T_d$ .



Sur les spectres de diffraction des rayons X pour  $P_{RF} > 50W$  et  $P_{Ar} = 2 Pa$  à  $d = 7 cm$  et ce quel que soit le substrat utilisé, trois raies de diffraction sont clairement visibles (Figure 21). Les films obtenus ne sont pas texturés et les raies de diffraction peuvent s'indexer dans une structure cubique de ZnSe. Cependant, la largeur importante des raies de diffraction, caractéristique de la présence de nanocristallites, ne permet pas d'exclure la présence de ZnSe sous forme hexagonale. L'asymétrie de la raie 220 vers les angles  $2\theta$  plus grands (Figure 21), qui apparaît souvent plus marquée avec l'augmentation de  $T_d$ , ne peut en effet qu'être expliquée que par la présence d'une faible quantité de ZnSe sous forme hexagonale, comme cela a été observé par Rizzo et collaborateurs. La largeur à mi-hauteur de la raie 111 décroît lorsqu'on augmente  $T_d$  du fait de la compétition entre le processus de désorption des espèces Se et Zn dans le plasma et celui de croissance des grains de ZnSe, et est relativement indépendante du choix du substrat alors que ce n'est pas le cas avec d'autres techniques de dépôt. Il semble donc bien que l'incorporation des nanograins dans la matrice de  $SiO_2$  favorise la croissance de films dont la qualité cristalline est relativement indépendante du choix du substrat.

En conclusion, par un choix adéquat des différents paramètres de dépôt, la proportion  $SiO_2/ZnSe$  et la taille des cristallites de ZnSe peuvent être aisément contrôlées et ce quel que soit le substrat choisi. Cette étude a permis de cerner les conditions optimales de dépôt correspondant à des films non texturés avec une proportion maximale (73.5%) de nanograins de ZnSe de structure cubique et correspondant à  $d = 7 cm$ ,  $P_{Ar} = 2Pa$ ,  $T_d = 20^\circ C$  et  $P_{RF} = 150W$ .

### **b) Dopage des films de ZnSe avec du chrome et optimisation des propriétés de photoluminescence**

Pour l'incorporation du chrome dans ces films, nous avons choisi de co-pulvériser la cible de  $SiO_2$  précédente recouverte de morceaux de ZnSe en rajoutant des morceaux de chrome massif. Afin d'augmenter la proportion de grains de ZnSe dans nos films élaborés à température ambiante, nous avons choisi un taux de recouvrement en surface du ZnSe sur la cible de  $SiO_2$  de 60% et nous avons fait varier la quantité de chrome sur la cible  $M_{Cr}$  dans le domaine 0.02 - 0.8 g. Comme les études préliminaires sur la composition du plasma par spectroscopie d'émission optique ont révélé qu'une  $P_{RF}$  plus élevée favorise la pulvérisation du chrome, nous avons choisi de faire varier  $P_{RF}$  jusqu'à 250W alors que les autres paramètres de dépôt sont restés inchangés par rapport à précédemment.

L'épaisseur des films déposés a été déterminée dans le domaine 1.5-45  $\mu\text{m}$  par des mesures de profilométrie. L'augmentation du taux de recouvrement de la cible a conduit quel que soit le substrat utilisé à l'élaboration de films de ZnSe purs, très bien cristallisés dans la structure cubique zinc blende (Figure 22). Une très faible quantité de ZnSe sous forme hexagonale est néanmoins aussi présente dans ces films et est d'autant plus importante à  $P_{\text{RF}} = 200$  et 250W.

Ces films déposés à température ambiante sont très fortement texturés avec les plans  $\{111\}$  du ZnSe parallèles à la surface de l'échantillon (Figure 22) et ce que le substrat soit monocristallin ou amorphe.

De plus, les spectres de diffraction X correspondants ( $\omega-2\theta$ ) mettent en évidence pour les films déposés notamment à  $P_{\text{RF}} = 200$  et 250W la présence de tailles anisotropes pour les cristallites de structure ZnSe cubique ainsi que la présence de contraintes résiduelles. Une analyse combinée de ces spectres est donc nécessaire et est en cours.

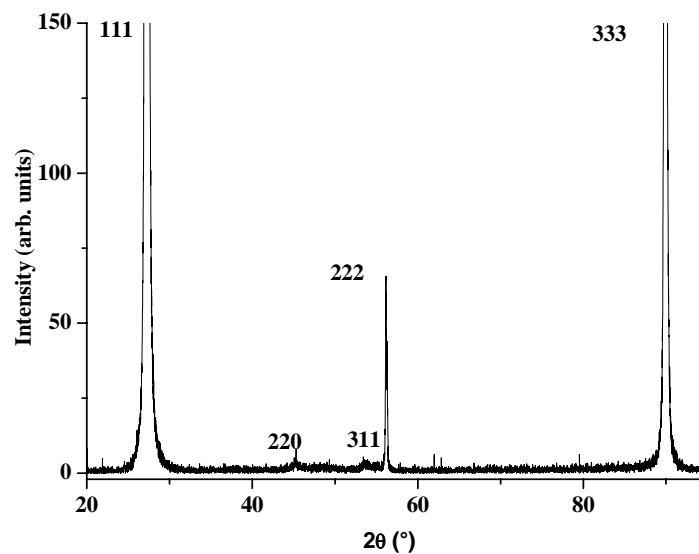


**Figure 22.** Diagramme RX  $\theta-2\theta$  d'un film  $\text{Cr}^{2+}:\text{ZnSe}$  déposé à  $P_{\text{RF}} = 200\text{W}$ .

Les observations en HRMET confirment cette composante majoritaire de texture selon la direction  $\langle 111 \rangle$  et mettent en évidence la présence d'une couche mince amorphe d'épaisseur environ 3 nm au début de la croissance (Figure 23). Ceci explique pourquoi quel que soit le substrat utilisé on observe dans nos films la même composante majoritaire de texture  $\langle 111 \rangle$ , correspondant à une direction de croissance selon les plans les plus compacts de la structure cubique faces centrées du ZnSe.

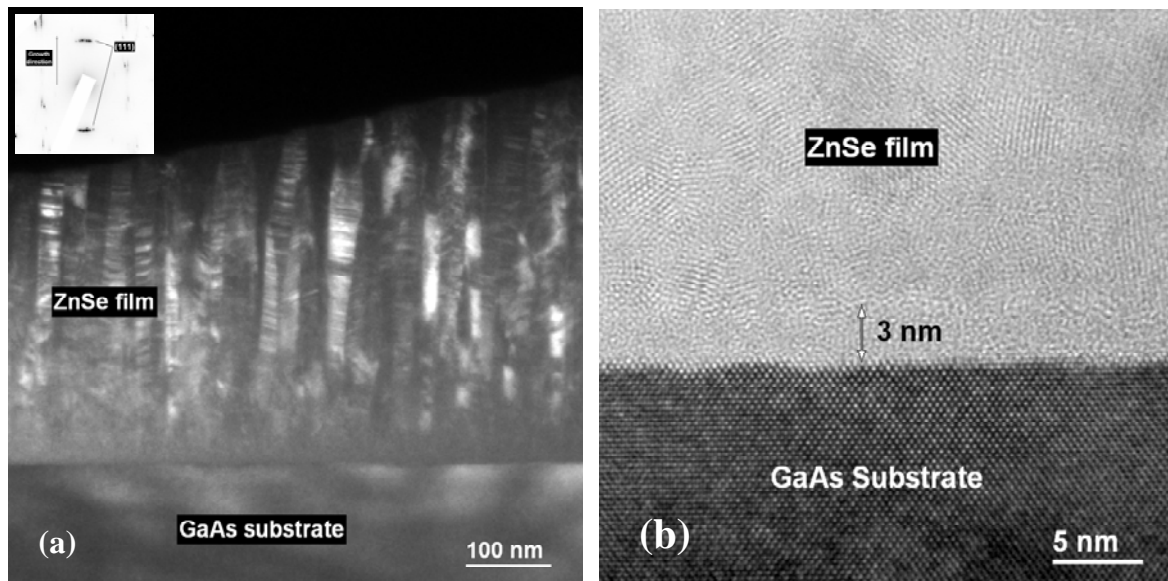


**Figure 23.** (a) Image MET en champ clair et son cliché de diffraction électronique correspondant mettant en évidence la croissance colonnaire du film déposé à  $P_{RF} = 200W$ , avec les plans  $\{111\}$  des cristallites parallèles à la surface du film. (b) Image HRMET du même film où est visible à l'interface du substrat de GaAs une couche amorphe.

Les spectres de photoluminescence (PL) obtenus par excitation directe (1850 nm) de ces films à température ambiante mettent en évidence comme dans l'échantillon monocristallin massif de référence une bande d'émission large centrée autour de 2200 nm. Cette bande d'émission est caractéristique de la transition inter-bande  $^5E \rightarrow ^5T_2$  de l'ion  $Cr^{2+}$  et prouve donc bien que le chrome a été incorporé en site tétraédrique par substitution du zinc dans le ZnSe. L'intensité des spectres de PL des films est toujours observée plus faible en comparaison avec celle de l'échantillon massif étant donné leurs épaisseurs très différentes mais la largeur de la bande d'émission est similaire.

Pour  $M_{Cr} = 0.17$  g, ce signal de PL n'est visible que lorsque  $P_{RF} > 100$  W et est maximum à  $P_{RF} = 250W$ . En accord avec les observations par spectroscopie d'émission optique, il semble donc bien que le Cr est plus facilement incorporé dans la structure en substitution des ions  $Zn^{2+}$  avec des  $P_{RF}$  plus élevées.

L'évolution du signal de PL à  $P_{RF} = 200$  et  $250W$  en fonction de  $M_{Cr}$  a été également étudiée. Il apparaît que ce signal de PL n'est visible que pour  $M_{Cr}$  dans le domaine 0.1-0.3 g avec un maximum de signal observé pour  $M_{Cr} = 0.17g$  (Figure 24). La décroissance du signal de PL pour  $M_{Cr} > 0.17$  g est certainement due, comme cela a déjà été observé dans le matériau

massif, au phénomène de "concentration quenching" et qui apparaît pour une concentration en  $\text{Cr}^{2+}$  supérieure à  $1.10^{19} \text{ at.cm}^{-3}$ .

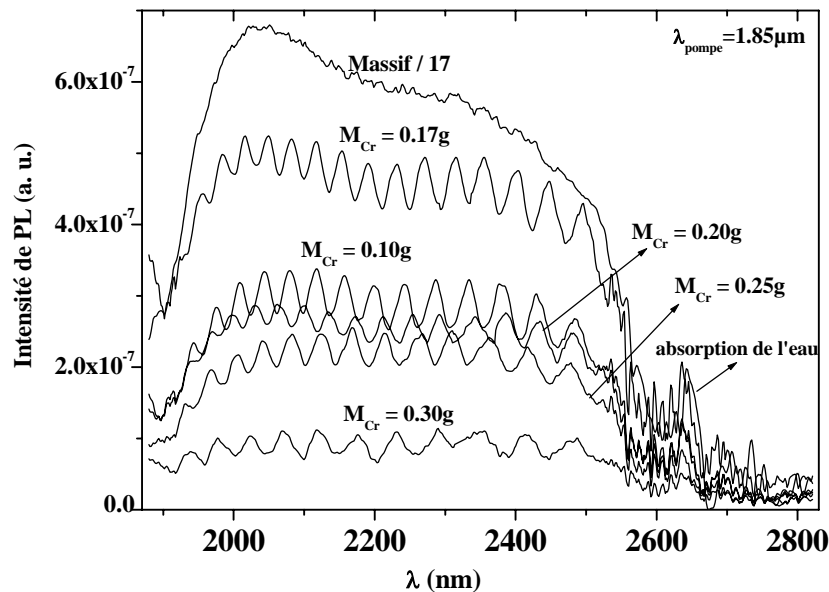


**Figure 24.** Spectres de PL à température ambiante de films minces déposés à  $P_{RF} = 250W$  avec différentes quantités de chrome  $M_{Cr}$  disposées sur la cible de  $\text{SiO}_2/\text{ZnSe}$ , et celui d'un échantillon massif de référence. Les oscillations observées sur les spectres de PL des films correspondent aux réflexions multiples sur les différentes faces du film.

Toutefois, du fait de leurs plus faibles épaisseurs, les valeurs des concentrations en  $\text{Cr}^{2+}$  ne sont pas accessibles dans nos films à partir des spectres de transmission optiques comme dans le massif. Celles-ci vont être déterminées en collaboration avec le laboratoire de Photonique et de Nanostructures (LPN - Paris) par des mesures de spectrométrie de photoélectrons X (XPS).

Cette étude montre donc que les conditions optimales de dépôt correspondant à un maximum d'intensité du signal de PL sont obtenues avec  $P_{RF} = 250 W$  et une quantité de Cr sur la cible  $M_{Cr} = 0.17g$ .

Des mesures de PL ont également été effectuées en excitant indirectement les ions  $\text{Cr}^{2+}$  via la bande de transfert de charge  $\text{Cr}^{2+}/\text{Cr}^{1+}$  grâce à un laser Argon (458 - 514 nm). Cette excitation indirecte donne également lieu à température ambiante à l'émission infrarouge des ions  $\text{Cr}^{2+}$  dans le ZnSe. Les mécanismes d'excitation indirecte mis en jeu

restent encore partiellement inexpliqués et sont en cours d'étude afin d'avancer vers la réalisation à partir de ces films de dispositifs pompés électriquement.

**PUBLICATIONS DU**

**CHAPITRE 2**



## X-ray Combined QTA using a CPS applied to a ferroelectric ultrastructure

M. Morales<sup>1</sup>, D. Chateigner<sup>2</sup>, L. Lutterotti<sup>3</sup>, J. Ricote<sup>4</sup>

<sup>1</sup>Lab. Physique de l'Etat Condensé, Univ. du Maine, BP 535, F-72085 Le Mans

<sup>2</sup>Lab. CRISallographie et sciences des MATériaux-ISMRA, F-14050 Caen

<sup>3</sup>Dipartimento di Ingegneria dei Materiali, Univ. Di Trento, I-38050 Trento

<sup>4</sup>Instituto de Ciencia de Materiales de Madrid, CSIC, Cantoblanco, S-28049 Madrid

**Keywords:** Texture; Structure; X-Ray diffraction combined approach; Ferroelectric thin films; Modified lead titanates;

**Abstract.** The new combined methodology for quantitative description of texture, structure and other microstructural parameters of thin layers using X-ray diffraction is presented and applied to the case of a ferroelectric thin film of  $\text{Pb}_{0.76}\text{Ca}_{0.24}\text{TiO}_3$  on a  $\text{Pt}/\text{TiO}_2/\text{SiO}_2/\text{Si}$  substrate. The approach allows the quantitative texture analysis of the ferroelectric thin film and the Pt electrode, refining simultaneously their structure, layers thickness, mean crystallite size and microstrain state. The layer thickness determination is estimated by the refinement of the thicknesses inserted in the absorption and volumic correction factors. The powerfulness of this methodology is discussed and compared with other approaches.

### Introduction

The microstructure of ferroelectric thin films is a determinant factor of their final properties, which are used in a wide range of technological applications [1,2]. Different techniques are used for this characterisation, and among them, X-ray diffraction has been routinely used as a non-destructive characterisation of texture, strain state, particle size, crystallographic structures, .... However, when applied to anisotropic polycrystalline samples, the classical diffraction approaches generally fail. For instance, a usual Bragg-Brentano diffraction diagram may not reveal all diffracted lines of a compound when it is strongly textured, making its structural determination impossible, and at the same time preventing any quantitative texture analysis. Also, strongly overlapping peaks often prevent any textural characterisation. This is usually the case of ferroelectric single thin films, and the situation becomes worth when bottom electrodes, anti-diffusion barrier or in general film stacking are used.

In this work, we have chosen the relatively recently developed approach [3], the so-called combined approach, which is able to determine all the parameters accessible by X-ray diffraction through the combination of adequate refinement procedures. We demonstrate that this approach allows the study of layered multiphase complex compounds. As an example, we apply it to a  $\text{Pb}_{0.76}\text{Ca}_{0.24}\text{TiO}_3/\text{Pt}/\text{TiO}_2/\text{SiO}_2/\text{Si}(100)$  ultrastructure.

### Materials and experimental procedure

A thin film of Ca-modified lead titanate of the nominal composition  $\text{Pb}_{0.76}\text{Ca}_{0.24}\text{TiO}_3$  (PTC), was obtained by spin-coating deposition of a sol-gel processed solution [4] on a  $\text{Pt}/\text{TiO}_2/\text{SiO}_2/\text{Si}(100)$



substrate previously treated at 650°C during 30 min. The 4 layers deposited were crystallised layer-by-layer by rapid thermal processing (heating rate  $\sim 30^\circ\text{C/s}$ ) at 650°C for 50 s. Once the film is crystallised, a further thermal treatment at 650°C during 1 hour is performed (heating rate  $10^\circ\text{C/min}$ ). The expected thickness of the PTC and Pt layers were approximately 400 nm and 50 nm respectively, as determined from the deposition parameters.

X-ray measurements were carried out with a Huber four-circle goniometer mounted on an X-ray generator equipped with a curved position sensitive detector (INEL CPS-120), as detailed elsewhere [5]. Spin-coated films usually exhibit fibre textures [5,6], which means that intensities are varying only with the tilt  $\chi$  of the goniometer. Therefore, we summed all diagrams in  $\phi$  for identical  $\chi$  angles (11 resulting diagrams), in order to first refine background,  $2\theta$  offset, instrumental broadenings and defocusing effects. All calibrations for instrumental contributions were operated on a KCl powder measured in the same conditions. The nominal composition for the PTC layer was used in the refinement, starting with bulk-like cell parameters. A first cycle applied to all the diagrams extracted the integrated intensities using the Le Bail algorithm [7]. These intensities are used for a first refinement of the orientation distribution (OD) by the WIMV [8] or the entropy modified WIMV (E-WIMV) [9] iterative methods. The OD obtained is then introduced in the cyclic Rietveld refinement of the diagrams. The new refined parameters are used for a new WIMV cycle to obtain a new OD, and so on. In this way, the OD refinement takes progressively account of the microstructural and structural reality, while the Rietveld analysis is corrected for texture in a physically sound manner. All the necessary calculations were carried out in the MAUD package [10] in which the layered model for ultrastructures measurements using a curved detector was implemented [11]. The refinement quality is assessed by the comparison of the experimental and recalculated diagrams and by the reliability factors: RP for OD refinement,  $R_w$  and  $R_{\text{Bragg}}$  for Rietveld refinement.

## Results and discussion

The experimental diagrams show a strong Pt preferred orientation with  $\{111\}$  parallel to the film plane (Fig. 1). The PTC film texture is difficult to analyse from  $\theta$ - $2\theta$  spectra, because of the overlap between peaks of the ferroelectric film and the underlying substrate. This difficulty is furthermore enhanced because of the overlaps of the peaks from the PTC structure itself. Indeed, the PTC structure is a tetragonal perovskite, but with only few distortions of the perovskite cell, making it pseudo-cubic in reality. Hence 100 and 001 lines are located approximately at the same Bragg angles in the diagrams. Unfortunately, polarisation vectors are located for the analysed phase along the c-axes of the structure only, and it becomes crucial to be able to separate 100 from 001 textural contributions quantitatively.

Up to now, the direct integration method used [5,6] extracts the texture information of the thin film only from those peaks not influenced by the underlying layers of the substrate, reducing considerably the input data used in the OD refinement. In this case, the structural data used for the OD calculations correspond to ceramic materials of equivalent compositions, with crystals not growing with substrate-imposed restrictions. Therefore, the correct quantitative texture analysis of both phases can only be calculated using the combination of the Rietveld and WIMV-like algorithms. Figure 1 shows two refinement results for the diagrams measured at  $\chi = 0^\circ$  using the WIMV and E-WIMV algorithms. For the Rietveld simulation we have chosen atomic positions and isotropic thermal parameters as the ones of the bulk materials. Trying to free atomic coordinates during the refinement of the texture and microstructure always gave divergence of the program, probably because of an insufficient number of experimental data compared to the number of fit parameters.

One can directly see the better refinement obtained using the E-WIMV approach, particularly for the very sharp peaks of Pt, which already denotes a strong texture, and of the ones corresponding to the Si single crystal. Note that we are able with this procedure to perform a reliable analysis of the Pt layer, which is covered by the ferroelectric thin film, thanks to the layer model implemented in the calculations. The layer model implemented for our calculations is based on the correction factors used to correct data for absorption and volume variations, for the PTC film [12]:

$$C_{\chi}^{\text{top film}} = g_1 (1 - \exp(-\mu T g_2 / \cos \chi)) / (1 - \exp(-2\mu T / \sin \omega \cos \chi)),$$

and the Pt electrode:

$$C_{\chi}^{\text{cov. layer}} = C_{\chi}^{\text{top film}} (\exp(-g_2 \sum \mu_i' T_i' / \cos \chi)) / (\exp(-2 \sum \mu_i' T_i' / \sin \omega \cos \chi))$$

in which equations  $\omega$  is the incidence angle of x-rays,  $\mu$  is the linear absorption coefficient of a film of thickness  $T$  which would be placed on the top of the stack,  $\mu_i'$  is the linear absorption coefficient of the films of thickness  $T_i'$  that would cover a bottom layer,  $g_1$  and  $g_2$  are geometrical factors taking account of the experimental set-up and of the peak position on the detector.

Figure 2 shows a selected series of diagrams measured at increasing tilt angles (every  $5^\circ$ ), with their corresponding refinements using the E-WIMV approach. All the diagrams are nicely reproduced, with reliability factors  $R_{\text{Bragg}}$  as low as 4.7 % (Tab. 1). The small observed discrepancies are due to strong substrate peak feet. From the refined orientation distribution we can recalculate the pole figures (Fig. 3), for the PTC and Pt layers.

The refinement was made on the 19 and 4 first available pole figures for PTC and Pt, respectively, but we present only the low-indices ones. In agreement with the diffraction diagrams, all the reliability factors indicated a better refinement using the E-WIMV approach (Tab. 1), which also indicated a stronger texture (higher texture indexes) both for PTC and Pt layers. This is due to the better ability of the E-WIMV algorithm to represent strong textures.

Texture indexes are  $2 \text{ mrd}^2$  for PTC and  $41 \text{ mrd}^2$  for Pt. While the Pt layer only shows preferential orientation along  $\langle 111 \rangle$ , the ferroelectric PTC film has also a small component along  $\langle 100 \rangle$  perpendicular to the film. Interestingly, no significant component along  $\langle 001 \rangle$  is observed (Fig. 3). The results of the microstructural parameters (Tab. 2) reveal the presence of larger microstrains in the PTC films than in the Pt layer, which presents the largest mean crystallite size. This is consistent with the fact that crystallites of the PTC film have sizes not larger than one tenth of the total layer thickness, while the Pt layer exhibits a mean crystallite size which extends to the full thickness of the layer. The values obtained for the Pt and PTC layers thickness are very close to the ones expected from the deposition conditions.

	Pt	PTC	Pt	PTC		
	Texture	Texture	RP <sub>0</sub>	RP <sub>0</sub>	Rw	R <sub>Bragg</sub>
	Index	Index	(%)	(%)	(%)	(%)
	(m.r.d. <sup>2</sup> )	(m.r.d. <sup>2</sup> )				
WIMV	48.1	1.3	18.4	11.4	12.4	7.7
E-WIMV	40.8	2	13.7	11.2	7	4.7

**Tab. 1:** Texture indexes and Reliability factors for the refinement of the PTC ultrastructure

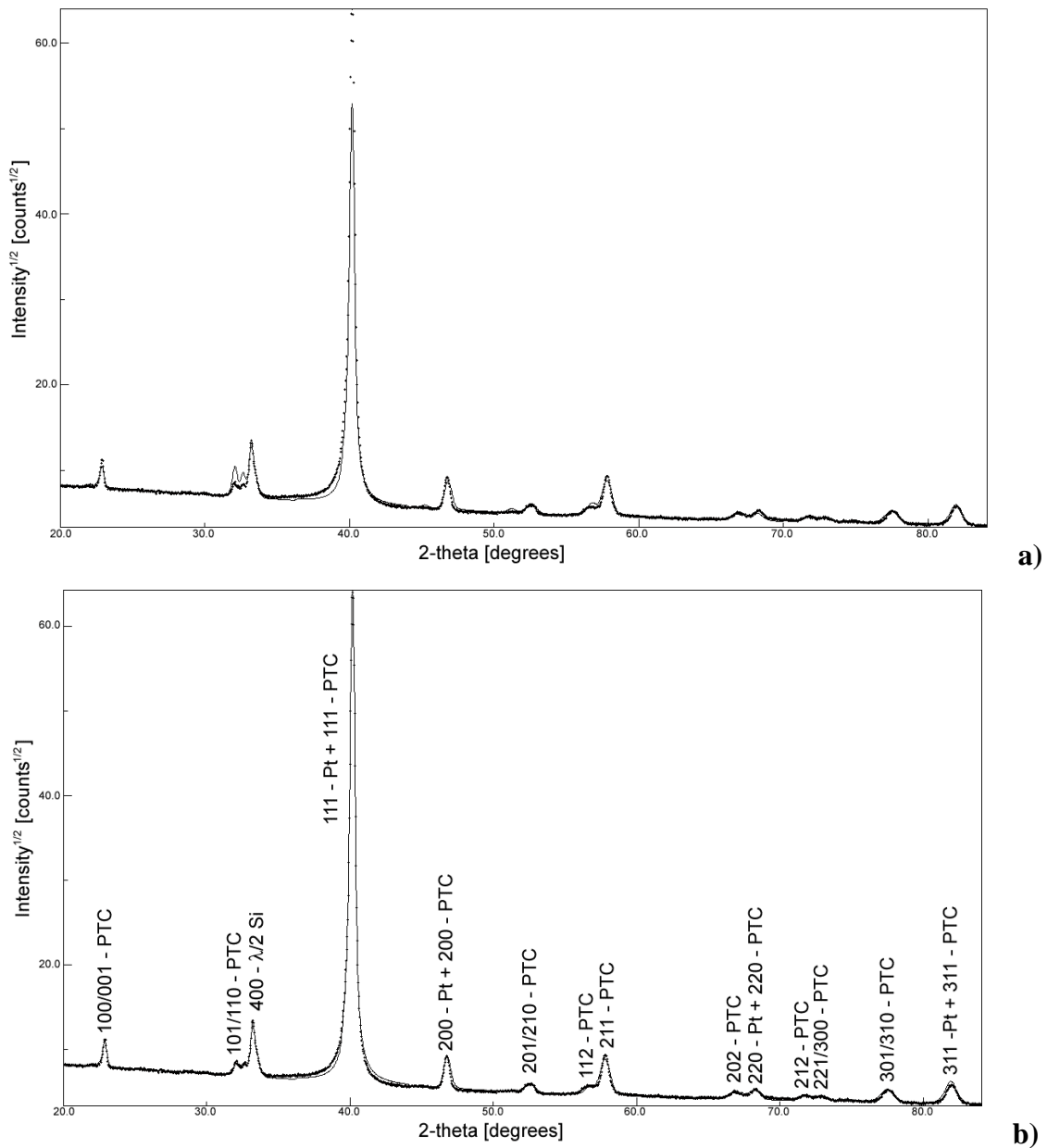


**Fig. 1:** Experimental (dotted line) and refined (solid line) diagrams for  $\chi = 0^\circ$ , using the WIMV (a) and E-WIMV (b) approaches.

	Cell parameters (Å)	Cryst. Size (Å)	$\mu$ strain param.	Layer thickness (Å)
Pt	3.955(1)	462(4)	0.0032(1)	458(3)
PTC	a=3.945(1) c=4.080(1)	390(7)	0.0067(1)	4080(1)

**Tab. 2:** Refined parameters for the PTC and Pt layers

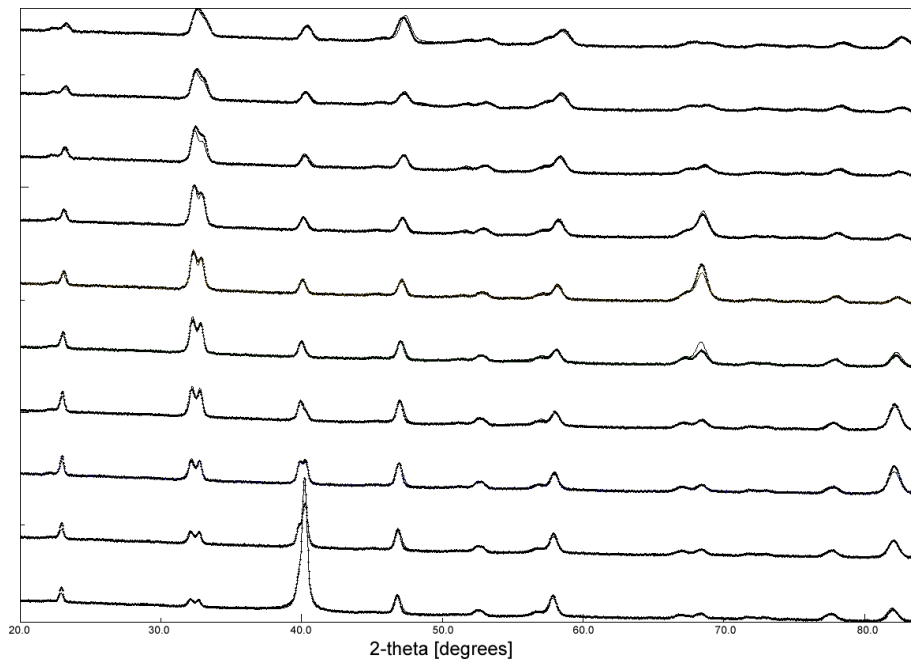


**Fig. 2:** Experimental (dotted line) and refined (solid line) diagrams from  $\chi = 5^\circ$  (bottom) to  $\chi = 45^\circ$  (top) step  $5^\circ$ , using E-WIMV combined with Rietveld analysis.

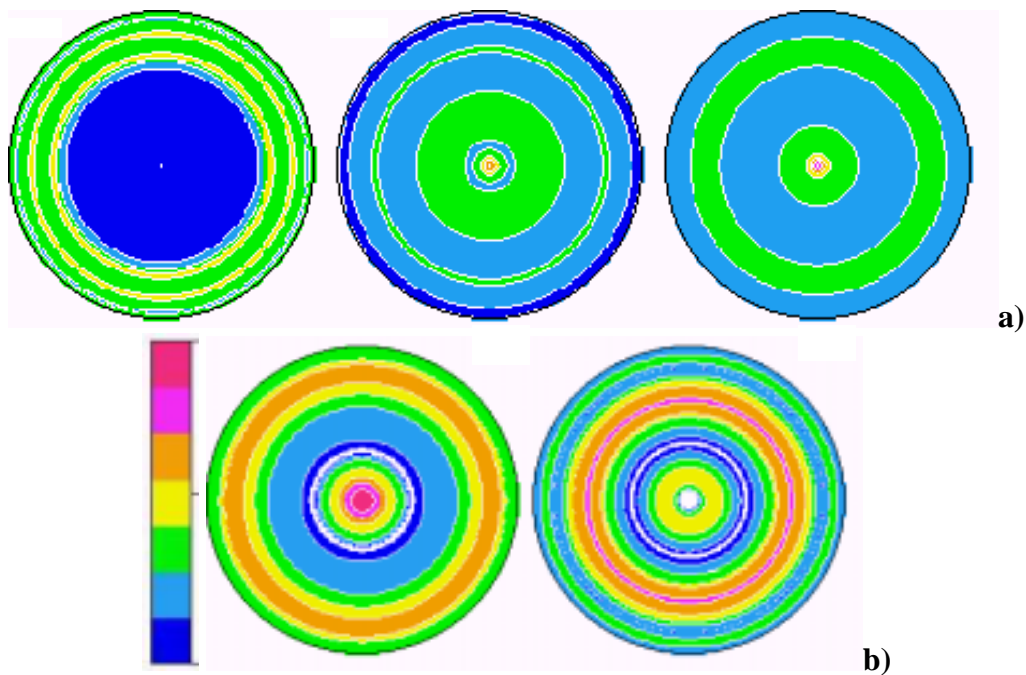


**Fig. 3:** Pole figures recalculated after E-WIMV refinement for **(a)** PTC: {001}, {100} and {111} pole figures from left to right (linear density scale, max = 3.8 m.r.d., min = 0.1 m.r.d.) and **(b)** Pt: {111} and {200} pole figures from left to right (logarithmic density scale, max = 63 m.r.d., min = 0) layers. Equal area projections.

Compared to previous studies [5,6], the approach appears to be much more powerful in extracting structural, microstructural and textural parameters in complex samples. Parameters divergence reveals to be astonishingly low, provided strongly dependent parameters were not released at the same time. This stability is very probably due to the high number of experimental pole figures taken into account in the refinements, allowing a decrease of the defocusing effect (large at high  $\chi$ -ranges) and a reduction of the number of OD solutions.

In summary, we present in this paper a new methodology for the analysis of X-ray diffraction data. Up to now, it has not been possible to obtain simultaneously reliable results of texture, structure and other microstructural parameters. This method also allows the study of other layers like the Pt bottom electrode. Applied to a ferroelectric thin ultrastructures, we extract important information for the optimisation of the material in view of its application in devices, which will be the focus of further work.

### **Acknowledgements**

This work has been funded by EU project GROWTH (G6RD-CT99-00169).

### **References**

- [1] J. F. Scott, *Ferroelectric Memories*, Springer Series in Advanced Microelectronics 3, Springer-Verlag Berlin Heidelberg 2000.
- [2] D.L. Polla and L.F. Francis, *MRS Bull.* **21**[7], 59-65 (1996).
- [3] M. Ferrari, L. Lutterotti, *J. Appl. Phys.* **76**(11), 7246-7255 (1994).
- [4] R. Sirera and M.L. Calzada, *Mat. Res. Bull.* **30**[1], 11-18 (1995).
- [5] J. Ricote, D. Chateigner *Bol. Soc. Esp. Cerám. y Vidrio*, **38**[6], 587-591 (1999).
- [6] J. Ricote, D. Chateigner, L. Pardo, M. Algueró, J. Mendiola and M.L. Calzada, *Ferroelectrics* **241**, 167-174 (2000).
- [7] A. Le Bail, H. Duroy, J.-L. Fourquet, *Mater. Res. Bull.* **23**, 447-452 (1988).
- [8] S. Matthies and G.W. Vinel, *Phys. Stat. Sol. B* **112**, K111-K120 (1982).
- [9] L. Yansheng, W. Fu, X. Jiazheng, L. Zhide, *J. Appl. Cryst.* **26**, 268-271 (1993).
- [10] L. Lutterotti, S. Matthies, H.-R. Wenk in "Textures of Materials" vol 2, NRC Research Press J.A. Szpunar Ed., 1599-1604 (1999).
- [11] A. Tizliouine, J. Bessières, J.-J. Heizmann, J.F. Bobo, *Mat. Sci. For.* **157**, 227-234 (1994).
- [12] J.-J. Heizmann, C. Laruelle, *J. of Appl. Cryst.* **19**, 1986, 467-472.

# Application of the X-ray combined analysis to the study of lead titanate based ferroelectric thin films

J. Ricote<sup>a,\*</sup>, D. Chateigner<sup>b</sup>, M. Morales<sup>c</sup>, M.L. Calzada<sup>a</sup>, C. Wiemer<sup>d</sup>

<sup>a</sup>*Instituto de Ciencia de Materiales de Madrid, CSIC, Cantoblanco, E-28049 Madrid, Spain*

<sup>b</sup>*Laboratoire de Cristallographie et Sciences des Matériaux-ENSICAEN, F-14050 Caen, France*

<sup>c</sup>*Laboratoire d'Etudes et Recherches sur les Matériaux-ENSICAEN, F-14050 Caen, France*

<sup>d</sup>*Materials and Devices for Microelectronics Laboratory, INFN, Via C. Olivetti 2, I-20041 Agrate Brianza, Milano, Italy*

## Abstract

Lead titanate based ferroelectric thin films are well known for their excellent piezo and pyroelectric properties. In order to obtain a complete characterisation of the structural, micro structural and texture parameters of these films, a recently developed combined analysis of the X-ray diffraction data is carried out. The advantages of this approach reside in the fact that we obtain simultaneously quantitative and more reliable information of these parameters than with more conventional methods. Results obtained for ferroelectric thin films are analysed and compared with those obtained with other methods of analysis. The conclusions show that the texture of the films obtained with the combined method is able to separate the contributions of close texture components, like  $\langle 100 \rangle$  and  $\langle 001 \rangle$ , or to study components with low contribution to the texture of the film.

© 2003 Elsevier B.V. All rights reserved.

**Keywords:** Quantitative texture analysis; Combined approach; Ferroelectric materials; Thin films

## 1. Introduction

Ferroelectric materials and specifically ferroelectric thin films, have attracted a great deal of attention recently due to their excellent polarisation, dielectric, piezoelectric, pyroelectric and optical properties, used in a wide range of technological applications, from ferroelectric random access memories (FeRAM) [1] to microelectromechanical systems [2]. The study of the crystallographic preferential orientation or texture plays a major role in these materials because the polar character of ferroelectrics characterised by a spontaneous electric polarisation, whose value greatly determines the performance of ferroelectrics in applications. Due to the interest of the texture analysis for the control and optimisation of ferroelectric thin film performance, a number of works using advanced X-ray diffraction analysis methods like the quantitative texture analysis (QTA) on ferroelectric thin films have been published recently [3–7]. However, the application of classical

diffraction approaches to anisotropic polycrystalline samples such as the ferroelectric thin films, may be problematic. For example a usual Bragg–Brentano diffraction diagram of a strongly textured film may not reveal all possible diffraction reflections, making its structural determination impossible, which in turn prevents any quantitative analysis. This can be solved with the relatively recently developed combined approach [8], which is now proved to be a viable tool [9], and has been successfully applied to ferroelectric thin films [10]. The advantage of this method, which consists in the combination of adequate refinement procedures, resides in the simultaneous and more accurate determination of the structure and texture of the films, which allows to obtain information not attainable by other means.

In this work we have applied successfully the combined method to the analysis of X-ray diffraction data of a series of ferroelectric lead titanate based thin films to show the advantages of the method over more traditional approaches. The separation of the contributions of the associated  $\langle 100 \rangle$  and  $\langle 001 \rangle$  texture components, or the study of the evolution of the structural and texture parameters of the deposited films with the

\*Corresponding author. Tel.: +34-91-334-89-87; fax: +34-91-372-06-23.

E-mail address: [jricote@icmm.csic.es](mailto:jricote@icmm.csic.es) (J. Ricote).

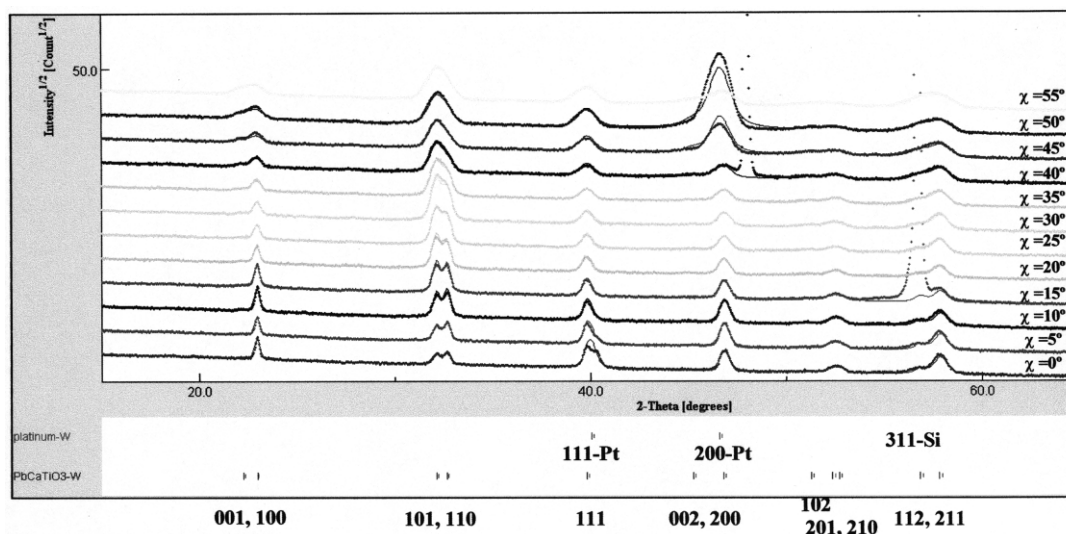


Fig. 1. Experimental (dotted line) and fitted (solid line) X-ray diffraction diagrams for  $\chi=0^\circ$  to  $\chi=55^\circ$  of a PCT film deposited on a platinumised Si based substrate. The refinement was carried combining Rietveld and E-WIMV analysis. (Reliability factors Rietveld:  $R_w=13\%$ ,  $R_B=12\%$ ,  $R_{exp}=22\%$ ; E-WIMV:  $R_w=5\%$ ,  $R_B=6\%$ ).

recrystallisation process, are two clear examples shown here of the large possibilities of analysis of this method.

## 2. Experimental procedure

### 2.1. Materials

Thin films of Ca-modified lead titanate (PCT) were obtained by spin-coating deposition of sol-gel processed solutions of  $\text{Pb}_{0.76}\text{Ca}_{0.24}\text{TiO}_3$  with 10% excess PbO [11] on substrates of Pt/TiO<sub>2</sub>/(100)Si (PCT-Si) and Pt/(100)MgO (PCT-Mg). Crystallisation was carried out at 700 °C for 50 s by rapid thermal processing (RTP), with a heating rate of  $\sim 30$  °C/s for all films. Film PCT-A<sub>0</sub> was prepared on a Pt/TiO<sub>2</sub>/(100)Si substrate without any previous treatment. All the rest of the films (PCT-B) were deposited on substrates that were previously annealed at 650 °C for 30 min (heating rate = 10 °C/min). A recrystallisation process at 650 °C (heating rate = 10 °C/min) has been applied to some of these films: PCT-B<sub>1</sub> for 1 h; PCT-B<sub>2</sub> for 2 h; and PCT-B<sub>3</sub> for 3 h. PCT-B<sub>0</sub> was left without recrystallisation for comparison.

### 2.2. X-Ray diffraction characterisation

Experimental pole figures were obtained using a Huber four-circle goniometer mounted on an X-ray generator at a fixed incident angle of 11°. A  $5 \times 5^\circ$  grid measurement was carried out to cover the whole pole figure. A position sensitive detector (INEL CPS-120), covering an angle of 120°, is used (angular resolution 0.03°). Pole figure data are normalised into distribution densities, and expressed as multiple of a random distri-

bution (m.r.d.), which is equivalent to volume percentage per 1% area. From the experimental pole figures we obtain by the WIMV (Williams-Imhof-Matthies-Vinel) iterative method [12], or the entropy modified WIMV (E-WIMV) [13], the orientation distribution (OD) of the sample. From the OD we can determine the texture index  $F^2$ , which is an indication of the degree of orientation of the material [4,7]. In this paper we describe the application of an alternative method of analysis of the X-ray diffraction data, the so-called combined approach [8]. In the case of chemical solution deposited films it has been shown that they present fibre textures, i.e. axial symmetry [4]. This means that intensities are varying effectively only with one rotation angle, allowing us to sum all X-ray diagrams corresponding to that angle, in order to refine first background,  $2\theta$  offset and defocusing effects. In the refinement we used the nominal compositions and the starting cell parameters were derived from equivalent bulk ceramics. A first cycle was applied to all the diagrams to extract the integrated intensities using the Le Bail algorithm [14]. These intensities were used for a first OD refinement. The OD is then introduced into the cyclic Rietveld refinement. The new refined parameters are used for a new OD refinement, and so on. Calculations were carried out with the Materials Analysis Using Diffraction package (MAUD) [15], in which the layered method [16] was implemented. This allows the analysis not only of the reflections coming from the ferroelectric thin film but also from the Pt layer beneath. An example of the application of the combined method on a ferroelectric PCT film deposited on a platinumised Si-based substrate can be seen in Fig. 1.

Table 1

Estimated values of the contribution of  $\langle 001 \rangle$  and  $\langle 100 \rangle$  texture components obtained by conventional quantitative texture analysis (QTA) and by the combined approach

Method of analysis	Film	Estimated contribution of texture components (%)	
		$\langle 001 \rangle$	$\langle 100 \rangle$
Conventional QTA	PCT-Si	62	38
	PCT-Mg	55	45
Combined approach	PCT-Si	7	93
	PCT-Mg	68	32

### 3. Results and discussion

#### 3.1. Separation of the contributions of texture components in PCT thin films

In tetragonal lead titanate based compositions, the polar axis is along the  $\langle 001 \rangle$  direction. Therefore, we ideally search for a preferential orientation along this axis perpendicular to the film surface. The problem is that, in chemical solution deposited films on substrates with un-related structures (without any obvious lattice match), orientation along this direction is always accompanied by an undesirable texture component along  $\langle 100 \rangle$  [7]. This results in a high number of crystals that do not contribute to the net polarisation of the film. The distribution of crystals along these two directions,  $\langle 001 \rangle$  and  $\langle 100 \rangle$ , seems to be directly related to the stress state present during the film processing [17]. As that stress state is mainly due to the different expansion coefficients of film and substrate, we can increase the contribution of the desired  $\langle 001 \rangle$  texture component by changing from a Si-based substrate (PCT-Si), which produces a tensile stress, to a MgO-based one (PCT-MgO), whose stress state is compressive. It has been reported that the use of MgO-based substrates results in a substantial improvement of the ferroelectric behaviour of the PCT films deposited on top [18].

However, the conventional quantitative texture analysis (QTA) of the X-ray pole figures gives similar estimated contributions for both directions regardless of the substrate used (see Table 1). A study of the evolution of the diffracted intensities of 100 and 001 reflections with the  $\chi$  angle concluded that these results did not reflect the real situation. The solution is the use of the combined method (Table 1), whose results are consistent with both the measured peak intensity evolution and the reported tendencies explained above.

Integration in the conventional QTA is carried out over the overlapped 001, 100 reflection, separating both contributions during the WIMV iterative process. This introduces a large ambiguity as the calculations are based on the orientation distribution coverage obtained

with the measurements, which is always limited due to the influence of reflections from the substrate, blind areas, and so on. In contrast to this 'integral approach', the combined method deconvolute first the 001, 100 peaks using the Rietveld refinement, improving greatly the number of constraints in the determination of the peak intensities. Then the WIMV process that follows is a second check for the coherency between intensities, resulting in an overall better evaluation of the texture and of the contributions of these two important texture components. The same would be applicable to any texture components of directions with close reflections: the combined method is the best approach to obtain reliable results.

#### 3.2. Effects of the processing parameters on the structure and texture of PCT thin films

In the search for methods to produce highly oriented thin films, the authors propose the annealing of the substrate previous to the film deposition. The increase of the surface roughness resulting of this process will disrupt the usual nucleation process of the deposited film on the substrate. As a result, it has been reported the inducement of preferential orientation along the  $\langle 111 \rangle$  direction, not observed in the non-treated substrate [6]. In order to increase the degree of orientation, we study the effect of the recrystallisation of the film, which in the case that the texture is growth controlled (oriented grains grow at the expense of the others) will produce an increase of the texture index [6].

The conventional QTA does not allow us to obtain information on the Pt layer of the substrate. With the use of the combined method, it is possible to compare the structural and texture characteristics of Pt before and after the different annealing process to which film and substrate are subjected to in this study. And we can refine the thickness and the lattice parameter of this layer, whose values do not vary significantly with the thermal treatments (see Table 2). Regarding the texture, we obtain a clear  $\langle 111 \rangle$  orientation, as the recalculated pole figures in Fig. 2 show. The annealing at 650 °C of the substrate produces a relatively important increase of the texture index, which is less affected by the recrystallisation for different times, although the highest value is achieved for the longest crystallisation time (Table 2). This may be a consequence of a preferential growth of the  $\langle 111 \rangle$  oriented crystals over the other.

The comparison of the PCT structural variations shows first the importance of the surface state of the substrate on which the deposition takes place. Both  $a$  and  $c$  values decrease when the film is deposited on a rougher Pt surface (annealed substrate) (Table 3). This may be a consequence of the increase of the stress present during the film formation on the rough Pt surface. The recrystallisation of the film seems to relax



Table 2  
Structural, microstructural and texture results of the Pt layer after different annealing treatments obtained by the X-ray combined analysis

Pt layer	$a$ (Å)	Thickness (nm)	Reliability factors (Rietveld analysis) (%)	Texture index- $F^2$ (m.r.d. <sup>2</sup> )	$R$ factors (Texture) (%)
<i>Non-treated substrate</i>					
Pt layer	3.9108 (1)	45.7 (3)	$R_w = 13$ $R_B = 12$ $R_{exp} = 22$	129	$R_w = 5$ $R_B = 6$
<i>Annealed substrate</i>					
Pt layer	3.9100 (4)	46.4 (3)	$R_w = 8$ $R_B = 14$ $R_{exp} = 21$	199	$R_w = 16$ $R_B = 18$
Pt (recryst. 1 h)	3.9114 (2)	47.8 (3)	$R_w = 9$ $R_B = 20$ $R_{exp} = 21$	199	$R_w = 20$ $R_B = 26$
Pt (recryst. 2 h)	3.9068 (1)	46.9 (3)	$R_w = 9$ $R_B = 14$ $R_{exp} = 22$	195	$R_w = 8$ $R_B = 9$
Pt (recryst. 3 h)	3.9141 (4)	47.5 (9)	$R_w = 27$ $R_B = 12$ $R_{exp} = 21$	222	$R_w = 14$ $R_B = 17$

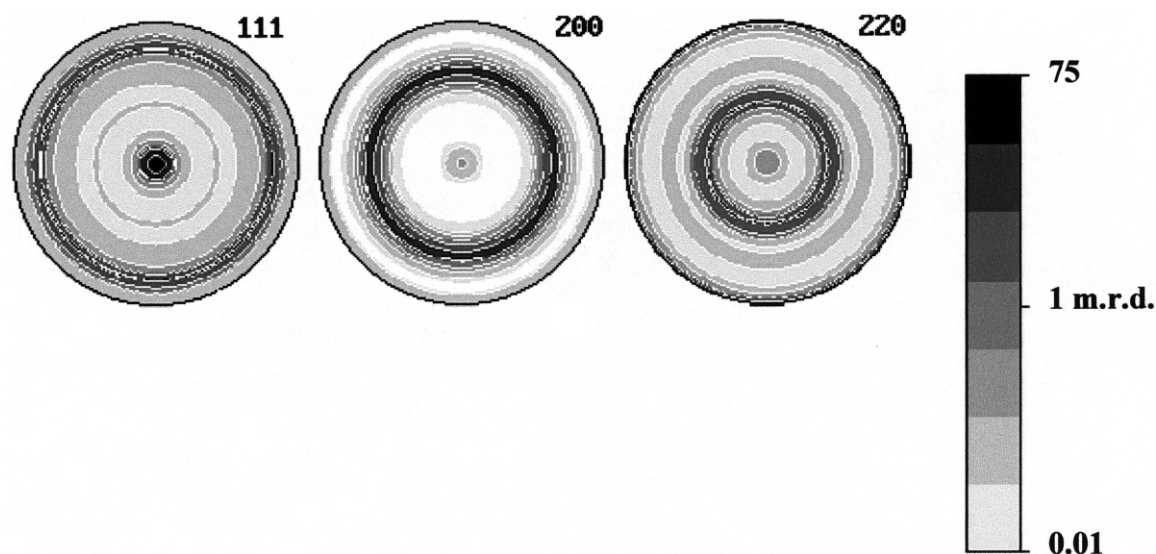


Fig. 2. Recalculated pole figures of the Pt layer from the orientation distribution (OD) obtained by the combined analysis. Equal area projection and logarithmic density scale.

Table 3  
Structural, microstructural and texture data of a series of PCT films deposited obtained by the X-ray combined analysis. (For reliability factors see Table 2)

Pt layer	$a$ (Å)	$c$ (Å)	Thickness (nm)	Texture index- $F^2$ (m.r.d. <sup>2</sup> )	Main texture component
<i>Non-treated substrate</i>					
PCT-A <sub>0</sub>	3.9156 (1)	4.0497 (6)	272.5 (13)	5.2	$\langle 100 \rangle$
<i>Annealed substrate</i>					
PCT-B <sub>0</sub>	3.8920 (6)	4.0187 (8)	279.0 (9)	2.1	$\langle 111 \rangle$
PCT-B <sub>1</sub> (recryst. 1 h)	3.8929 (2)	4.0230 (4)	266.1 (11)	2.1	$\langle 111 \rangle$
PCT-B <sub>2</sub> (recryst. 2 h)	3.8982 (2)	4.0227 (4)	258.4 (9)	2.5	$\langle 111 \rangle$
PCT-B <sub>3</sub> (recryst. 1 h)	3.9001 (4)	4.0228 (11)	253.6 (3)	2.5	$\langle 111 \rangle$

the stress present in the film, shown by a continuous increase of the lattice parameters with the annealing time, which is also reflected in a decrease of the film thickness (Table 3).

Fig. 3 shows the recalculated pole figures of two PCT films deposited on untreated and annealed substrates.

While the film on the untreated substrate has a texture dominated by an orientation along  $\langle 100 \rangle$ , the one formed on a previously annealed substrate has a strong texture component along the  $\langle 111 \rangle$  direction, accompanied by a decrease of the texture index (Table 3). This confirms previous results obtained with the conventional

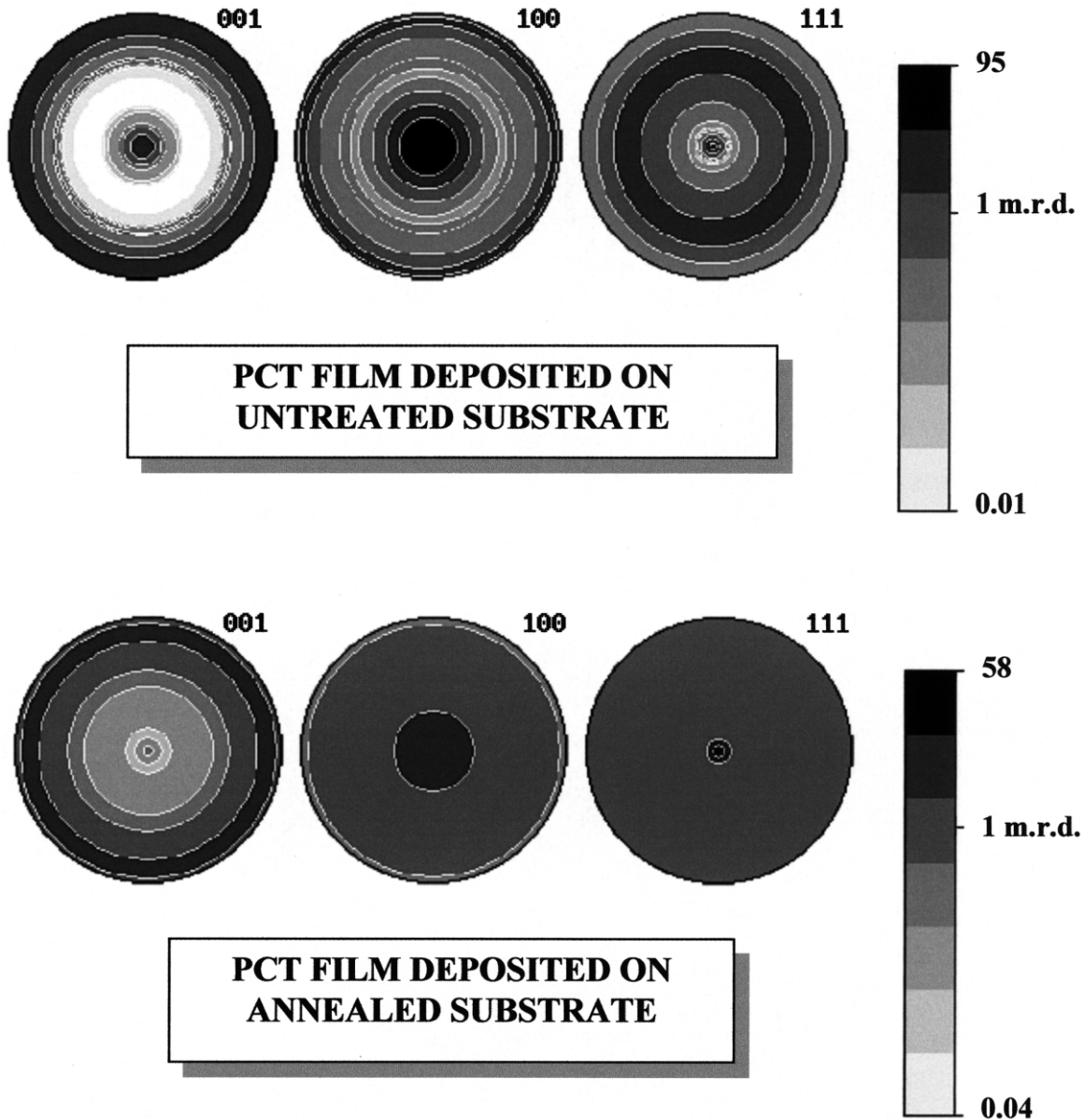


Fig. 3. Recalculated pole figures of the PCT films from the OD obtained by the combined analysis. Equal area projection and logarithmic density scale.

QTA [6]. However, while the tendencies obtained are equivalent, we can observe that, although in a very small quantity, the  $\langle 111 \rangle$  texture component is already present in the PCT film deposited on an ordinary substrate. Its small contribution, together with the fact that the 111 reflection of PCT is very close to the 111 of Pt, results in an underestimation of its contribution by conventional QTA, which makes that in fact this texture component has not been observed. This new information sheds light onto the origin of the  $\langle 111 \rangle$  texture component, which is therefore not induced by the rougher surface of the annealed substrate, as concluded before. Instead, it seems that  $\langle 111 \rangle$  becomes the

most important texture component as the main  $\langle 100 \rangle$  texture component does not appear in the annealed substrate. The decrease of the  $\langle 100 \rangle$  contribution to the texture results also in a decrease of the overall texture index. The reasons behind this change in the choice of texture components on the annealed substrate are not fully understood and it will be the focus of further work.

#### 4. Conclusions

The application of the combined method to ferroelectric calcium modified lead titanate thin films has proved to produce more accurate and reliable results than more

traditional X-ray diffraction analysis approaches. It also provides simultaneously information on the structure, microstructure and texture of both the deposited film and the substrate, revealing important characteristics of the Pt layer used in this study as bottom electrode.

An important aspect covered in this paper is the better resolution of the texture and, specifically of the contribution of the different texture components, obtained by the combined method. The separation of the contributions of two important texture components in the lead titanate based materials, as  $\langle 001 \rangle$  (containing the polar axis) and  $\langle 100 \rangle$ , has only been possible by the use of this method. The same is true for any other texture components derived from directions whose reflections are close, which results in an overall better quantitative determination of the texture of the films. Texture components that can be difficult to measure due to its low contribution and/or the overlap of their corresponding reflections with other from the substrate, like  $\langle 111 \rangle$  texture component of PCT, and that the conventional QTA is not able to treat, are also revealed with the combined method.

### Acknowledgments

Authors wish to thank Dr L. Lutterotti (University of Trento, Italy) for helpful discussions on the use of the combined method. This work has been funded by the European Union project GROWTH program (G6RD-CT99-00169 and MAT2000-1925CE) ESQUI ('X-ray Expert System for Electronic Films Quality Improvement') and the co-operation program CSIC-CNRS (2000FR0021).

### References

- [1] J.F. Scott, *Ferroelectric Memories*. Springer Series in Advanced Microelectronics, 3., Springer-Verlag, 2000.
- [2] D.L. Polla, L.F. Francis, *MRS Bull.* 21 (7) (1996) 59.
- [3] D. Chateigner, H.R. Wenk, A. Patel, M. Todd, D.J. Barber, *Integr. Ferroelectr.* 19 (1998) 121.
- [4] J. Ricote, D. Chateigner, *Bol. Soc. Esp. Cerám. Vidrio.* 38 (6) (1999) 587.
- [5] J. Ricote, D. Chateigner, L. Pardo, M. Alguero, J. Mendiola, M.L. Calzada, *Ferroelectrics* 241 (2000) 167.
- [6] J. Ricote, M. Morales, M.L. Calzada, *Mater. Sci. Forum* 408–412 (2002) 1543.
- [7] J. Ricote, R. Poyato, M. Alguero, L. Pardo, M.L. Calzada, D. Chateigner, *J. Am. Ceram. Soc.* 86 (2003) 1571.
- [8] H.R. Wenk, S. Matthies, L. Lutterotti, *Mater. Sci. Forum* 157–162 (1994) 473.
- [9] S. Matthies, L. Lutterotti, H.R. Wenk, *J. Appl. Cryst.* 30 (1997) 31.
- [10] L. Cont, D. Chateigner, L. Lutterotti, J. Ricote, M.L. Calzada, J. Mendiola, *Ferroelectrics* 267 (2002) 323.
- [11] R. Sirera, M.L. Calzada, *Mater. Res. Bull.* 30 (1) (1995) 11.
- [12] S. Matthies, G.W. Vinel, *Phys. Stat. Sol. B* 112 (1982) K111.
- [13] L. Yansheng, W. Fu, X. Jiazheng, L. Zhide, *J. Appl. Cryst.* 26 (1993) 268.
- [14] A. Le Bail, H. Duroy, J.L. Fourquet, *Mater. Res. Bull.* 23 (1998) 587.
- [15] L. Lutterotti, S. Matthies, H.R. Wenk, in: J.A. Szpunar (Ed.), *Textures of Materials*, 2, NRC Research Press, 1999, pp. 1599–1604.
- [16] A. Tizliouine, J. Bessières, J.J. Heizmann, J.F. Bobo, *Mater. Sci. Forum* 157 (1994) 227.
- [17] C.M. Foster, Z. Li, M. Buckett, D. Miller, P.M. Baldo, L.E. Rhen, et al., *J. Appl. Phys.* 78 (4) (1995) 2607.
- [18] R. Jiménez, M.L. Calzada, J. Mendiola in: E. Colla, D. Damjanovic, N. Setter (Eds.), *Proceedings of the Eleventh IEEE International Symposium on Applications of Ferroelectrics*, IEEE Catalog number 98CH36245, 1998, pp. 155–158.

# Structural and microstructural characterization of nanocrystalline silicon thin films obtained by radio-frequency magnetron sputtering

M. Morales,<sup>a)</sup> Y. Leconte, and R. Rizk

*Laboratoire Structure des Interfaces et Fonctionnalités des Couches Minces (SIFCOM)-Ensicaen,  
6 Bd. du Maréchal Juin, F-14050 Caen, France*

Daniel Chateigner

*Laboratoire de Cristallographie et Sciences des Matériaux (CRISMAT-Ensicaen,  
6 Bd. du Maréchal Juin, F-14050 Caen, France*

(Received 22 March 2004; accepted 3 November 2004; published online 14 January 2005)

Textured silicon thin films are deposited by reactive magnetron sputtering in hydrogen-rich plasma on (100)-Si and amorphous SiO<sub>2</sub> substrates. We quantitatively determine, combining x-ray texture analysis, x-ray reflectivity, transmission electron microscopy, atomic force microscopy measurements, and Raman and Fourier transform infrared spectroscopy analyses, the structure (cell parameter and mean electron density) and microstructure (crystalline fraction, preferred orientations, anisotropic crystallite sizes, thicknesses, etc.) of these films. For both kinds of substrates, no perfect  $\langle 111 \rangle$  orientation is observed whereas a systematic elongation of the anisotropic Si crystallites along one  $[111]$  direction is present. A small elongation of the Si cell parameter of the nanocrystals is found without internal stress. With the substrate to target distance, the crystalline fraction and mean electron density show an opposite behavior to that of the film porosity. The former increases and the latter decreases, and are correlated to the texture evolution. Preferred orientations are observed with texture strengths around two to three times a random distribution, with a tendency to achieve lower strengths for films grown on SiO<sub>2</sub> substrates. The texture components are evolving with the substrate to target distance, with  $\langle 110 \rangle$  and  $\langle h h \ell \rangle$  ( $\ell$  larger than 2) orientations favored for smaller and larger distances, respectively. All these microstructural properties are correlated with their optical properties and more particularly to their refractive index and their optical band gap. © 2004 American Institute of Physics. [DOI: 10.1063/1.1841461]

## I. INTRODUCTION

Nanocrystalline silicon thin films are promising structures for a wide range of applications in micro- and optoelectronics (flat panel display applications, solar cells, thin-film transistors, etc.).<sup>1</sup> Many studies have been carried out on films produced by vapor phase deposition techniques at moderate to relatively high temperature (600–750 °C), resulting in polycrystalline Si films with columnar growths. Such films exhibit texture components which vary with the deposition conditions and result in residual stresses, and are generally linked to the crystallite morphologies.<sup>2</sup> The lowering of the process temperature, to enable the use of low cost substrates such as common glasses and flexible polymers, is the main challenge to these large areas of microelectronic applications. The use of low temperatures leads generally to the growth of amorphous silicon films, but recently crystallized silicon layers have been achieved by synchrotron-radiation decomposition of disilane,<sup>3</sup> by plasma-enhanced chemical-vapor deposition<sup>4</sup> (PECVD), and also by our group using the reactive magnetron sputtering (RMS).<sup>5</sup> The interactions between the growing surface and the reactive hydride radicals present in the hydrogen-rich plasma originate films by PECVD and RMS techniques that are a mixture of amorphous and crystalline silicon. The growth and crystallization

mechanisms are still a matter of debate,<sup>6,7</sup> even though the key role of the highly reactive hydride species is now described by about three models.<sup>8,9</sup> Unfortunately, these mechanisms influence the resulting refractive indices via the crystallite sizes and crystalline phase amounts of the films (in general, layers with large grain size have a small refractive index). Although the growth mechanisms involved are of prime importance, key answers could be provided by a careful characterization of the films, in terms of structure and microstructure. Unfortunately, such a full investigation remains a hard task, for many reasons: (i) the films are composed of polycrystals exhibiting preferred orientations; (ii) the nanocrystals exhibit anisotropic shapes; (iii) they are mixed with amorphous silicon and porosity; and (iv) the films are deposited on various substrates.

We present in this work the results obtained using a recently developed x-ray technique, which is able to combine quantitatively the texture, structure, and anisotropic shape determinations. We complement the x-ray diffraction studies by x-ray reflectivity, Raman and infrared spectroscopies, and electron and atomic force microscopies in order to give access to other microstructural parameters such as porosity, crystalline fraction, etc. In this paper, all the structural and microstructural parameters of the films are correlated to their optical properties (refractive index and Tauc optical gap).

<sup>a)</sup>Author to whom correspondence should be addressed; electronic mail: magali.morales@ensicaen.fr

## II. SAMPLES AND EXPERIMENTAL DETAILS

Silicon thin films were grown by a radio-frequency magnetron sputtering technique in a plasma mixture of H<sub>2</sub> and Ar at 200 °C on amorphous SiO<sub>2</sub> (*a*-SiO<sub>2</sub>) and single-crystal (100)-Si substrates. The process used is detailed elsewhere<sup>10</sup> and the deposition conditions were the following: a power density of 2 W/cm<sup>2</sup>, a total pressure of 10<sup>-1</sup> Torr, and an 80% of hydrogen partial pressure. For both kinds of substrates we varied the target-substrate distance *d*. For *a*-SiO<sub>2</sub> substrates the *d* values were 4, 6, 7, 8, 10, and 12 cm corresponding to samples labeled A, B, C, D, E, and F, respectively, while on (100) Si two typical *d* values were chosen, *d*=6 and 12 cm (samples B' and F', respectively), aiming at a comparison of the substrate effect.

The structural and microstructural characteristics of the films were carefully characterized by the following techniques: conventional x-ray diffraction (XRD), quantitative x-ray texture analysis (QTA), specular x-ray reflectivity (XRR), Raman spectroscopy (RS), transmission electron microscopy (TEM), Fourier transform infrared (FTIR) spectroscopy, and atomic force microscopy (AFM).

For usual XRD and XRR experiments we used a Philips X-Pert MRD at the average Cu K $\alpha$  radiation ( $\lambda_{\text{Cu}} = 1.5418 \text{ \AA}$ ) equipped with a point scintillator detector. For the former, we measured the films with a step of 0.01° in a symmetric ( $\theta$ - $2\theta$ ) mode and then in an asymmetric mode using an incidence angle of  $\omega=0.5^\circ$ , while the latter scans were restricted to a maximum of 1° in  $\theta$  range due to the rapid decrease of the signal in our films. To refine the XRR data, we used the REFLEX<sup>11</sup> program using the Fresnel formalism and sample and beam size corrections with a  $q_z$  resolution of 0.0006  $\text{\AA}^{-1}$ . An off-specular reflectivity scan was performed in order to check that no any significant diffusion signal was present in the specular scan.

The conventional TEM observations were done on a Jeol 200 CX while the high-resolution TEM images were obtained on a Topcon 002B instrument with a 0.18-nm resolution using cross-sectional specimens. The TEM specimens were prepared using the standard ion-milling technique.

The crystalline volumes ( $f_c$ ) of the films deposited on *a*-SiO<sub>2</sub> were estimated by the deconvolution of Raman-scattering spectra as described in details elsewhere.<sup>12</sup> The argon laser beam used ( $\lambda=514.5 \text{ nm}$ ) had an estimated penetration depth in the silicon of 300 nm. In this approach the polycrystalline asymmetry of the Raman modes and the scattering yield of the amorphous and crystalline species are taken into account.

The FTIR experiments were done using a Nicolet Nexus FTIR spectrometer on thin films deposited on [100]-Si substrates in the 500–4000-cm<sup>-1</sup> range with a resolution of 2 cm<sup>-1</sup>. An incident angle of 65° was chosen, near the Brewster angle of the air/silicon interface, in order to reduce intensity losses. All the spectra have been normalized by the film thicknesses and the signal of the [100]-Si substrate has been subtracted.

The surface morphology of the film was studied by AFM on a Nanoscope III extended multimode instrument from

Digital Instrument using a tapping mode. We scanned over 10  $\mu\text{m}^2$  in surface within a 0.2-nm resolution.

In order to correlate the structure and microstructure with the optical properties of the films deposited on *a*-SiO<sub>2</sub> substrates, we have determined the refractive index of the films by optical transmission spectroscopy using a Perkin–Elmer Lambda 9 ultraviolet-visible spectroscopy (UV-VIS) spectrometer from 0.4 to 4.1 eV. Using the transmission and absorption,  $\alpha(\lambda)$ , coefficients of the thin films, we have deduced the values of the Tauc optical gap  $E_g$ .<sup>13</sup>

As the usual XRD patterns of the films exhibited preferred orientations and anisotropic line broadening, QTA was performed with a simultaneous Rietveld refinement including anisotropic line broadening and film thickness analyses. We used a Huber four-circle diffractometer and a curved position sensitive detector (INEL CPS 120), which spans a 120° range in  $2\theta$ , allowing the simultaneous recording of several pole figures and the full diffraction diagram.<sup>14</sup> These latter were measured by scanning the tilt angle of the goniometer,  $\chi$ , in the range of 0°–35° using 5° steps. We then acquired (for  $\chi=35^\circ$ ) diagrams for the azimuthal angle,  $\varphi$ , in the range of 0°–360° using 5° steps, in order to check for possible in-plane orientation. No significant diagram variation was observed during this latter scan, showing that the sample exhibits a fiber texture. We used an incident angle for the x-ray beam  $\omega=14.2^\circ$  corresponding to the Bragg angle of the 111 reflection of the cubic silicon.

For the quantitative analysis of these x-ray diffractograms, we used the material analysis using diffraction (MAUD) program<sup>15</sup> that combines the WIMV method,<sup>16</sup> used to solve the orientation distribution function (ODF), with a Rietveld analysis to extract the microstructural and structural parameters. The integrated intensities, extracted by the Le Bail method, are processed and corrected for the absorption, volume variations, and delocalization effects.<sup>17</sup> The instrumental resolution function has been determined by a full mapping (in  $\omega$ ,  $\chi$ , and  $2\theta$  ranges) of our diffractometer space using the NIST LaB<sub>6</sub> powder standard<sup>18</sup> used for the International Crystallographic round-robin. By the deconvolution of the instrumental broadening from the experimental profile in the Fourier space, using the Lorentzian and Gaussian parts<sup>19</sup> of the profile, the crystallite size and microstrains of the sample are calculated, respectively. The (*hkl*) dependence of diffraction line broadening is determined in the program by the use of the Popa rules based on the symmetrized spherical harmonics that allow the modeling of the mean crystallite shape.<sup>20</sup> The thin-film thicknesses are additional parameters fitted during the Rietveld refinement, implemented in the MAUD package via the necessary intensity corrections.<sup>21</sup> These thicknesses have been compared to those measured by profilometry, with a resolution of 10 nm, using a Dektak3 ST instrument. In the MAUD program, the errors on the refined parameters such as cell parameter, anisotropic sizes, and thicknesses, have been estimated as one estimated standard deviation given by the least-square fit. This corresponds to about 67% of the crystallites population for a normal distribution law for the size distribution.

The QTA provides pole figures, which are normalized, in order to be independent of porosity, crystal state, stresses,

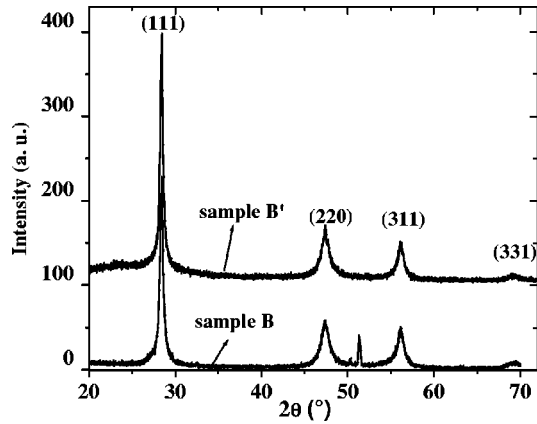


FIG. 1. Asymmetric XRD patterns measured at  $\omega=0.5^\circ$  for samples B and B' deposited, respectively, on (100)-Si and *a*-SiO<sub>2</sub> substrates. Note, for example, for sample B' the strong anisotropic line broadening as attested by the full width at half maximum values of 0.39° and 1.13°, respectively, for the (111) and (220) reflections. The narrow peak at 51.5° is the  $\lambda_{\text{Cu}}/2$  contribution of the Si single-crystal substrate (400) planes and illustrates the instrumental broadening around (220).

and thicknesses from film to film. This normalization is operated through the calculation of distribution densities that are expressed as multiples of a random distribution (mrd). The ODF allows then the recalculation of the experimental pole figures for comparison with the observed data and first reliability evaluation. The statistical ODF reliability is evaluated by the calculation of the  $RP_0$  factors<sup>22</sup> while the overall texture strength is estimated by  $F^2$ , the texture index value.<sup>23</sup> Since we determined that our film textures are axially symmetric around the normal to the film plane (fiber textures), the inverse pole figure calculated for this normal direction 001 is a complete representation of the ODF. We then chose to illustrate the exhibited textures using such inverse pole figures. Data reduction and calculations of the inverse pole figures were done using the GOMAN, POFINT,<sup>24</sup> and BEARTEX<sup>25</sup> packages, respectively.

### III. RESULTS AND DISCUSSION

#### A. XRD results

##### 1. X-ray diffraction pattern from single sample orientation

To gain some insight on the crystallization degree of our films we compare in Fig. 1 two typical XRD patterns recorded on samples B and B' deposited on two different substrates. The measurement carried out at a fixed low incident angle of  $0.5^\circ$  allowed to magnify the irradiated volume and avoided the long acquisition time necessary in the Bragg-Brentano geometry. The background observed for sample B is smoother than the one of sample B'. This latter exhibits diffuse scattering for angles lower than  $30^\circ$ , revealing the contribution of an amorphous part in the whole x-ray signal. Consequently, at first sight, the crystalline fraction of the film deposited on (100)-Si (sample B) appears higher than its counterpart for sample B' grown on *a*-SiO<sub>2</sub>. However, the spectrum of this latter would include the contribution part of the amorphous substrate, preventing any quantitative estimate of the crystalline fraction which would be determined

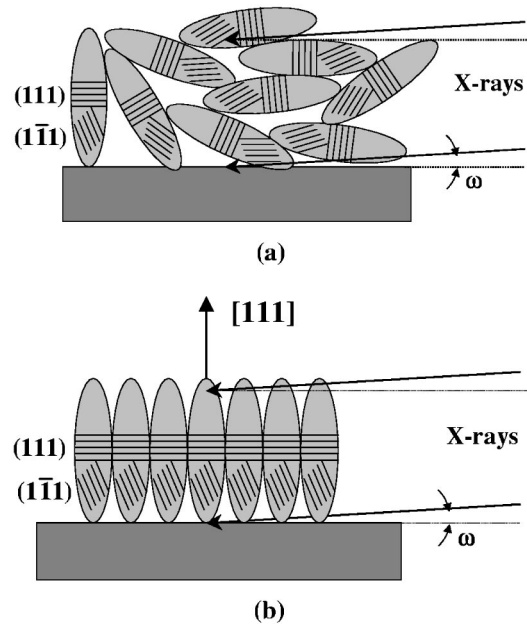


FIG. 2. Schematics of anisotropic crystallites having (a) a random orientation and (b) a texture with one [111] direction perpendicular to the film plane.

more appropriately further by RS. The diagram measured on sample B shows a narrow peak coming from the single-crystal substrate around  $2\theta=51.5^\circ$ , which corresponds to the  $\lambda_{\text{Cu}}/2$  contribution of the (400) planes. Compared to this latter peak, one can see that both patterns show strong line broadening for the silicon nanocrystal film. Also, preferred orientations of the crystallites are observed (the peak intensities are not the ones of a randomly oriented powder). The mean crystallite shape has been estimated in the first step from a Debye-Scherrer analysis of the  $\theta$ - $2\theta$  scans and taking into account in this formula the instrumental broadening correction in the same angular range.<sup>26</sup> We recall that the Debye-Scherrer formula is valid only in the symmetrical mode and assumes an isotropic shape of the coherent domains. With our experimental configuration, the upper and lower limits for size determination with this formula done by the step of our measurements ( $0.01^\circ$ ) and by the choice of the considered angular range around every  $hkl$  reflection ( $5^\circ$ ) are, respectively, 820 and 1.6 nm. The mean crystallites shape is found to be an ellipsoid with an elongation along the [111] direction, reaching a relatively large value of around 29 nm compared to the expected grain size.

However, in our case from a single measurement as the one shown in Fig. 1, the mean crystallite sizes determination is affected by peculiar artifacts. As a crystallographic texture is present, for one measured orientation of the sample, only some  $\{hkl\}$  planes are preferentially brought to diffraction, while the others are not detected. Consequently, crystallite sizes may be severely biased since they are only estimated from these diffracting planes. Figure 2 illustrates these aspects for a sample exhibiting anisotropic crystallite shapes with ellipsoids elongated along the [111] direction. In the case of crystallites randomly oriented in the sample [Fig. 2(a)], the mean crystallite size as deduced from the 111 line is an average over the 111 multiplicity. Since for a single

crystal of Si, the (111) plane is at  $70.53^\circ$  from  $(1\bar{1}1)$ ,  $(11\bar{1})$ , and  $(\bar{1}11)$ , the mean size along  $\langle 111 \rangle$  will take a value between the short and long axes of the ellipsoid. This approach remains valid for any  $hkl$  diffraction line, resulting in a systematic lowering of the shape anisotropy when calculated from a single diagram. For the case of a textured sample having (111) planes mostly parallel to the sample surface and  $[111]$  elongated crystallites perpendicular to it [see Fig. 2(b)], the long dimension of the crystallites is more favored than the short one, which has to be probed with other  $hkl$  lines. However, the long dimension is still underestimated if low  $\omega$  values are used, because this configuration does not ensure to probe the maximum of the distribution of the crystallites orientation. Such biased estimations are often encountered in works reporting silicon crystallite size determination using the Scherrer formalism, resulting in overestimated sizes with underestimate of shape anisotropy.<sup>27–30</sup> We prefer this approach to the integral width approach,<sup>31</sup> which Houben *et al.*<sup>32</sup> used, or even better the direct Fourier deconvolution of the signal from the x-ray profile<sup>17</sup> used in this work.

The cell parameter of the silicon structure may also be biased when determined from single pattern measurements. If structural strains are imposed by the substrate or the small crystal sizes, these ones will differ among differently oriented ( $hkl$ ) planes, resulting in peak shifts not corresponding to the mean shifts over all the orientations. In turn, a quantitative texture analysis will be difficult to perform without the exact determination of the crystal structure.

## 2. Combined x-ray diffraction analysis

To overcome the aforementioned problems, we performed measurements of the full diffraction diagrams for multiple orientations of the sample. This allows one to obtain a better estimate of the anisotropic shapes and cell parameter, weighted by the volumic ratio of material in a given orientation. This is achieved by the simultaneous analysis of the anisotropic shape and the quantitative textures through the so-called “combined refinement.”<sup>33,34</sup> Furthermore, the procedure enables to refine the film thickness (as probed by x rays).<sup>19</sup> A typical full texture analysis involves the measurements of a large number of diagrams, typically of the order of 1000 for a grid resolution of  $5^\circ$  used here (for as many sample orientation). However, due to the high crystal symmetry of Si, we only require  $\chi$  scans up to  $35^\circ$ , and taking into account that the texture is of fiber type only  $\chi$  scans can be used. This lowers the number of diagrams to be measured to eight corresponding to the  $\chi$  sample orientations. With such measurements, for a cubic unit cell, we calculated using the MIMA approach of BEARTEX<sup>23</sup> that a minimum value of four intersections of pole figure projection paths is obtained for all orientation cells (Fig. 3). This ensures a satisfactory determination of the ODF.<sup>35</sup> Consequently, the texture reliability factors  $RP_0$  (Ref. 20) as reported in Table I are generally around 1% and never exceed 3% hence attesting the good ODF definition. This reliability is also demonstrated by the comparison of experimental and simulated diffraction diagrams using the combined analysis (Fig. 4) with reliability factors  $R_B$ ,  $R_w$ , and  $R_{exp}$  around 5%.<sup>36</sup> Such reliabilities,

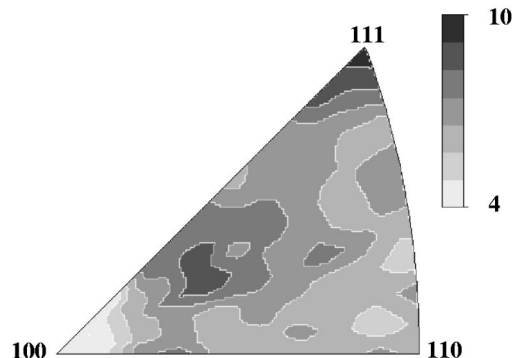


FIG. 3. Plot in cubic crystal reference frame with the evaluation of the orientation space coverage for the analyzed radial distributions. The levels are the numbers of observations per ODF cell. Notice that all the cells are determined by at least four observations whereas a minimum requirement of three is mandatory. Linear scale and equal area projection.

if they could be achieved by simple texture parameter fits such as those used in the March–Dollase<sup>37</sup> or Lotgering<sup>38</sup> approaches, would not correspond to a physically understandable model of the texture in our case, because of the fairly complex ODF of our samples, as will be seen in the next sections.

## 3. Stress-free crystal structure

Whatever the deposition conditions and the substrate considered (Table I), the film structure was found to be consistent with a regular diamond cubic structure of Si with a cell parameter  $a$  around  $5.44 \text{ \AA}$ . The observed values are always larger than those for bulk silicon and correspond to a mean lattice expansion of  $\Delta a/a = 0.07\% - 0.28\%$ . However, no peak shift was observed when tilting the samples in  $\chi$ , which indicates that the measured cell parameters correspond to the stress-free state of the silicon nanoparticles. This implies a thermodynamic origin of the larger cell parameters compared to the bulk, the surface energy taking a progressively larger influence as the crystallite size decreases. Such cell parameters are indeed larger than that reported in the literature for microcrystalline silicon films for similar film thicknesses.<sup>39</sup> However, the anisotropic expansion of the cell parameters reported in Ref. 39 when tilting the sample is interpreted as a tetragonalization of the unit cell. Such a unit-cell distortion is much more probably due in our opinion, to the effect of residual stresses stabilized in their films, and which are absent in our films (we did not observe any peak shift when tilting the samples). Faivre and Bellet<sup>40</sup> observed also a lower lattice expansion on porous silicon (PS) layers obtained by electrochemical etching of single-crystal silicon. In this case, the PS layer is nearly single crystalline and still under single-crystal stress, giving less deformation of the layer, while in our case the crystal size effect predominates on porosity effects.

## 4. Crystallographic texture

For a given substrate, if the overall texture strength of the films appears almost constant, the XRD characterizations show that the texture components are evolving as the  $d$  distances increase. Figure 5 illustrates this evolution of  $2\theta$  dia-

TABLE I. List of structural and microstructural parameters of the films resulting from the refinement and associated reliability factors  $R$  ( $R_w$ : weighted,  $R_B$ : Bragg,  $R_{exp}$ : experimental, and  $RP_0$ : ODF factor for all distribution densities). The texture index is  $F^2$ . Numbers in parentheses represent errors on the last digit as estimated by one standard deviation. The thicknesses measured by profilometry are with a resolution of 10 nm.

Sample	$d$ (cm)	$a$ (Å)	Measured thickness (nm)	RX thickness (nm)	Anisotropic sizes (Å)			Texture parameters			Reliability factors (%)			
					[111]	[220]	[311]	Maximum (mrd)	Minimum (mrd)	$F^2$ (mrd <sup>2</sup> )	$RP_0$	$R_w$	$R_B$	$R_{exp}$
A	4	5.4466 (3)	700	...	94 (3)	20 (1)	27 (1)	1.95	0.4	1.12	1.72	4.0	3.7	3.5
B	6	5.4439 (2)	1350	711 (50)	101 (3)	20 (1)	22 (1)	1.39	0.79	1.01	0.71	4.9	4.3	4.2
C	7	5.4346 (4)	1530	519 (60)	99 (3)	40 (1)	52 (2)	1.72	0.66	1.05	0.78	4.3	4.0	3.9
D	8	5.4461 (2)	1465	1447 (66)	100 (3)	22 (1)	33 (1)	1.57	0.63	1.04	0.90	5.5	4.6	4.5
E	10	5.4462 (2)	1470	1360 (80)	98 (3)	20 (1)	25 (1)	1.22	0.82	1.01	0.56	5.0	3.9	4.0
F	12	5.4452 (3)	1208	1110 (57)	85 (2)	22 (1)	26 (1)	1.59	0.45	1.05	1.08	4.2	3.5	3.7
B'	6	5.4387 (3)	1350	1307 (50)	89 (3)	22 (1)	28 (1)	1.84	0.71	1.01	1.57	5.2	4.7	4.2
F'	12	5.4434 (2)	1200	1214 (18)	88 (3)	22 (1)	24 (1)	2.77	0.50	1.12	2.97	5.0	4.5	4.3

grams recorded at  $\omega=14.2^\circ$  and  $\chi=0$ , for two films deposited on  $a$ -SiO<sub>2</sub> at interelectrode distances  $d=10$  cm and  $d=4$  cm. While a strong 111 peak is observed for  $d=10$  cm (sample E), this peak is strongly reduced at  $d=4$  cm (sample A). All the examined films are exhibiting fiber textures with multiple fiber components.<sup>20</sup> Figure 6 illustrates this multiple component fiber texture for sample E, using the five radial density profiles of the main pole figures recalculated from the ODF refined by the combined analysis on our XRD spectra. Two main components of orientation are observed with  $\langle 111 \rangle$  and  $\langle 400 \rangle$  directions aligned close to the film E normal (from  $\chi=0^\circ$ – $10^\circ$ ), as denoted by the density reinforcement of these two corresponding profiles [Figs. 6(a) and 6(b)]. However, other fiber components may exist in this film, which would not be detected using only these five radial distributions, because the available  $2\theta$  range of our instrument would not provide more measurable distributions in this system. The other potential components are included in all the measured profiles but are not easily seen from them since they are located at high  $\chi$  values and are overlapped

with others. A full representation of all fiber components is seen in inverse pole figures (Fig. 7). As evidenced on this figure, films deposited on  $a$ -SiO<sub>2</sub> substrates show a large texture dependence with the interelectrode distance. Although the overall texture strength of the films appears almost unaffected by the  $d$  variation [with  $F^2$  values around 1.2 mrd<sup>2</sup> at maximum and 001 inverse pole figure maxima not larger than 2 mrd (Table I)], the resulting texture components are strongly influenced. The closest distance (sample A) favors an orientation with  $\langle 110 \rangle$  directions aligned with the films normal as a major texture component (Fig. 7) whereas minor components are also observed with  $\langle 100 \rangle$  and  $\langle 124 \rangle$  directions of crystallites along the normal. The  $\langle 110 \rangle$  orientation is destabilized for distances larger than 4 cm and is no longer present for  $d=6$  cm (sample B). This  $\langle 110 \rangle$  component removal is accompanied by a slight tilt of the  $\langle 100 \rangle$  (which could correspond to a  $\langle h0\ell \rangle$  alignment with  $\ell$  around 11) and the appearance of a large component centered on  $\langle 221 \rangle$ -like orientation. Since this component is largely dis-

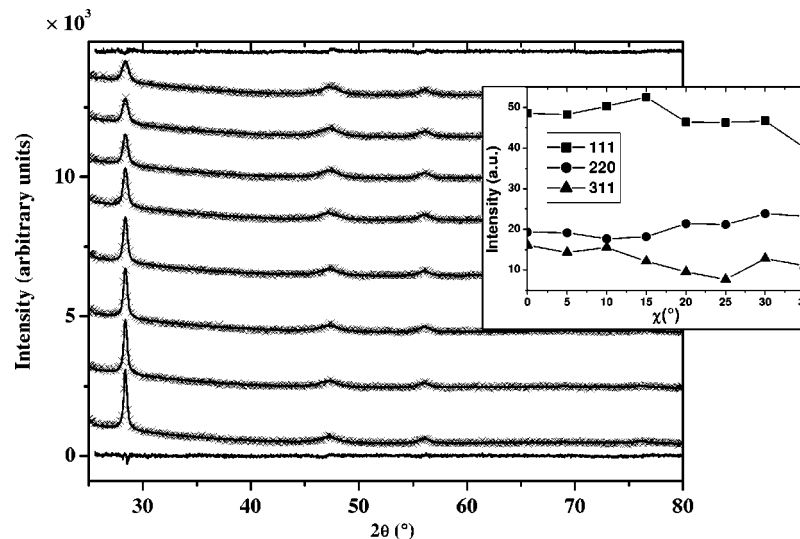


FIG. 4. Typical XRD diagram measured (crosses) on sample D ( $d=8$  cm) at different  $\chi$  positions ( $\chi=0^\circ$  at bottom and  $\chi=35^\circ$  at top) showing the broad and anisotropic-diffracted lines and the corresponding simulated spectra (solid line). The bottom and top diagrams correspond to the difference diagram (observed calculated) for, respectively,  $\chi=0^\circ$  and  $35^\circ$ . Inset shows the texture presence by the  $\chi$  scans of the three main integrated intensities (background is subtracted). Note the particularly high 311 intensity and the nonconstant variations of the lines with  $\chi$ . The diagrams have been shifted vertically for a better understanding.



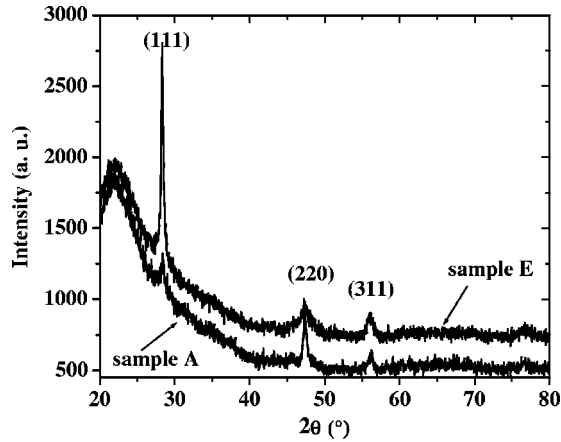


FIG. 5. Asymmetric XRD scans obtained with an incident angle  $\omega=14.2^\circ$ , corresponding to the Bragg angle of the (111) reflection, for  $\chi=0^\circ$ . Note the strong decrease of the 111 line for sample A ( $d=4$  cm) compared to sample E ( $d=10$  cm).

tributed, it corresponds to a set of closely oriented directions such as  $\langle 332 \rangle$ ,  $\langle 443 \rangle$ ,  $\langle 554 \rangle$ , ..., that can be present in this film, too. An interesting behavior is the progressive shift of this latter component towards a  $\langle 111 \rangle$  orientation for increasing  $d$  (samples B–F, see Fig. 7 at the bottom for checking indices). Comparing films B and E, one clearly sees the general trend starting in B from orientations around  $\langle 221 \rangle$  and reaching  $\langle 443 \rangle$  or  $\langle 553 \rangle$  in E. However, if the texture component would tend to coincide with a  $\langle 111 \rangle$  orientation for largest  $d$ 's (that is along the largest dimension of the crystallites), no pure  $\langle 111 \rangle$  orientation is observed that would correspond to a favored growth at the bulk state in the diamond structures.<sup>41</sup> Furthermore, for the largest distance (sample F) a  $\langle 112 \rangle$  orientation starts to appear. The  $\langle 100 \rangle$ -inclined orientation is fully removed for intermediate distances (samples C and D), then reappears for larger distances up to 12 cm.

Using (100)-Si single crystals as substrates strongly stabilizes the  $\langle 100 \rangle$  orientation (Fig. 7). Since in our elaboration conditions hydrogen species etch the native Si oxide layer of the substrate, this orientation may correspond to a heteroepitaxial component with [100] directions of the film aligned with the ones of the substrate. However, no heteroepitaxial but fiber texture is observed, implying that, if heteroepitaxy takes place at the interface with the substrate, it is rapidly removed through the thickness of the film. This would originate from island growing directly on the bare (100)-Si substrate, which stack into fiber textures along the [100] direction, a process helped by combining small crystals having large unit-cell parameters with partial crystallization of the films. This fiber texture precludes the columnar structure evidenced in Sec. III B by TEM and which is favored by the crystallization mechanism induced by the  $\text{SiH}_2$  species identified by FTIR as reported and discussed further (Sec. III C).

The minimum values of the ODF (Table I) are relatively high, from 0.4 to 0.82 mrd, indicating that 40%–82% of the volume of the material is randomly oriented (not textured). The texturation of the crystalline part of the film seems to be favored at low and high  $d$  values (typically lower than 6 cm and larger than 10 cm) whereas the textured volumic ratio is about 72% in average for  $6 \text{ cm} < d < 10 \text{ cm}$ . Comparing

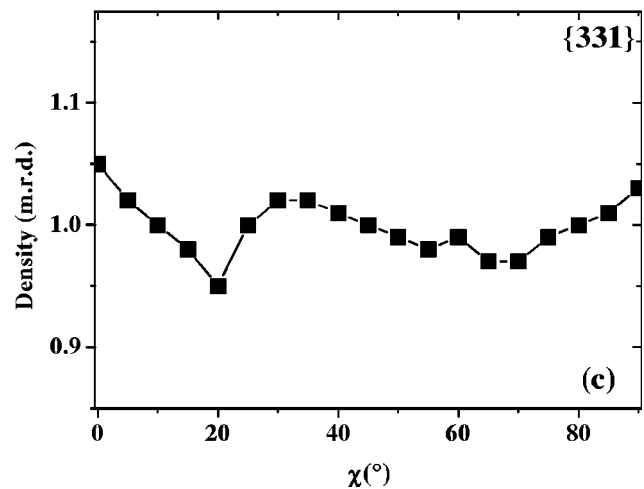
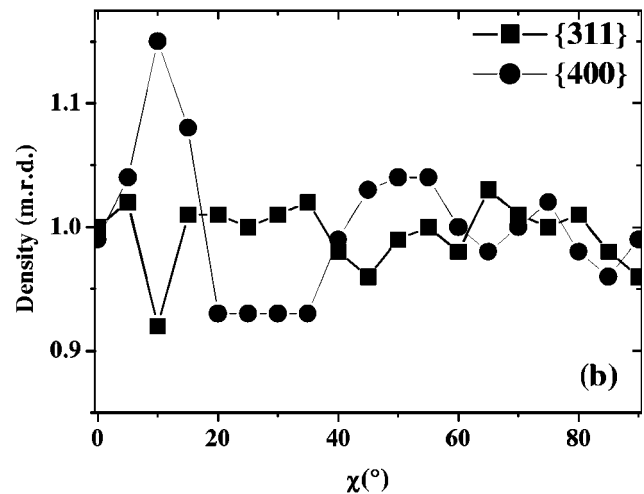
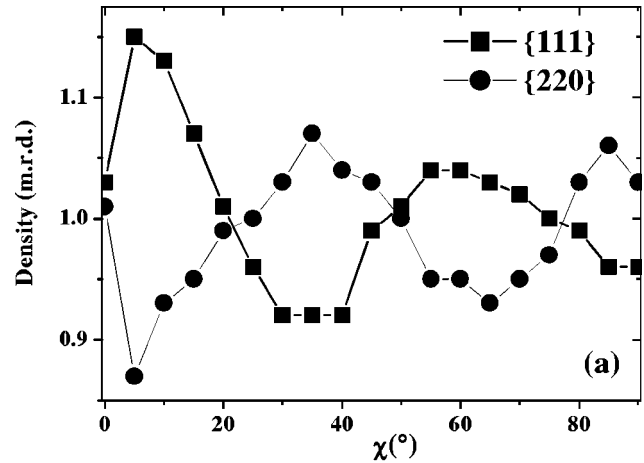


FIG. 6. Characteristic radial density profiles of the main pole figures recalculated from the ODF and refined in the combined analysis using the MAUD program for sample E: (a)  $\{111\}$  and  $\{200\}$ , (b)  $\{311\}$  and  $\{400\}$ , and (c)  $\{331\}$  distributions.

films B and F to B' and F', respectively, one can observe that this texturing effect at large distance is favored by the  $\alpha\text{-SiO}_2$  substrates, even though it does not correspond to the development of the same texture components. Due to the relatively high random component, any anisotropic property than one could observe on such materials will then be the

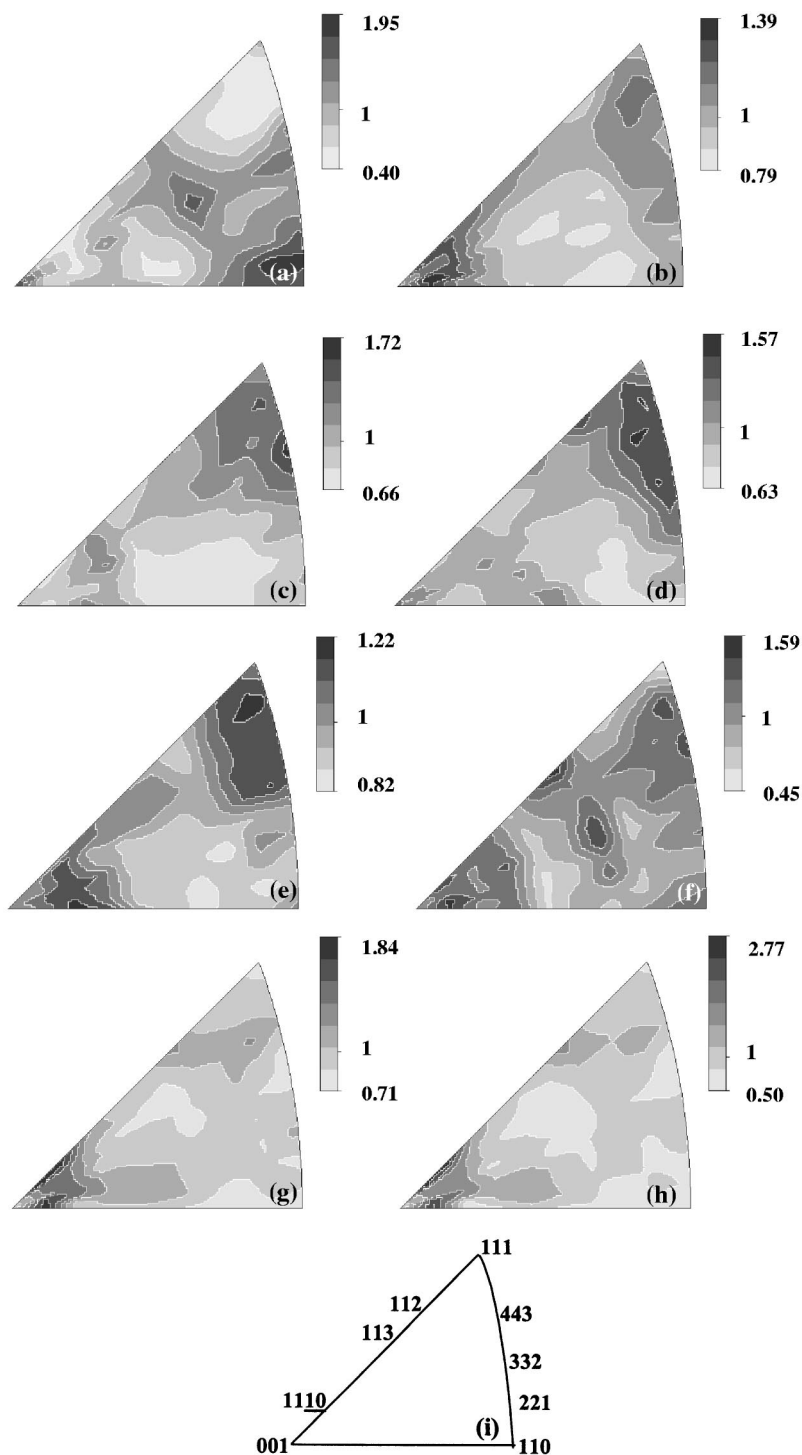


FIG. 7. (a)–(f) 001 inverse pole figures for samples deposited on  $\alpha$ -SiO<sub>2</sub> (samples A–F, respectively) and on (100) Si for (g) samples B' and (h) F'; (i) their corresponding pole locations are indicated by their Miller indices in the crystal frame. Equal area projections and linear distribution density scale.

consequence of only 60%–18% of the total volume, hereby considerably decreasing the probability of observation of such anisotropy.

Considering the numerous textural components present in the same film, a texture discussion from the simple diffracted intensity or intensity ratio, as often reported in the literature<sup>28,29,42–44</sup> is a very hazardous task. Authors generally find  $\langle 110 \rangle$  orientations coming from columnar growth at relatively high temperatures (typically in the range

of 600–700 °C), while our low-temperature process only produces this kind of orientation at small interelectrode distances,<sup>45,46</sup> and is interpreted by a fastest growth along  $\langle 110 \rangle$  directions. However,  $\langle 110 \rangle$ -preferred growth cannot by itself only explain the columnar microstructure since six crystallographically equivalent  $[110]$  directions would act, resulting in more isotropic growth shapes. Also, since  $[111]$ -elongated crystallites are found in this work whatever the texture, including  $\langle 110 \rangle$ -oriented films,  $[111]$  is probably the

largest growth speed at the conditions used for our films. This is coherent with observations by Yang *et al.*,<sup>47</sup> which revealed mixtures of  $\langle 111 \rangle$  and  $\langle 311 \rangle$  orientations at moderate temperatures in polycrystalline silicon. However, a direct comparison with polycrystalline films is not straightforward since our films are containing amorphous silicon in a non-negligible amount. Such an amorphous content can give rise to more homogeneous nucleation and may explain why we do not observe in our nanocrystalline films the same orientation dependency with thickness and temperature as other authors.<sup>45–50</sup> Also, since no stress could be observed, no stress-driven texture development model<sup>48</sup> can be applied.

### 5. Texture versus cell parameter

Concerning the correlation between the unit cell and the texture components, one can observe that when one of the major texture components (i.e.,  $\langle 100 \rangle$ ,  $\langle 110 \rangle$ , and the nearly  $\langle 111 \rangle$  orientation) is stabilized, the cell parameter tends to be larger for both kinds of substrates. For instance, comparing films A and B on  $\alpha$ -SiO<sub>2</sub>, in which the highest texture component is  $\langle 110 \rangle$ , the unit-cell parameter is  $5.4466 \pm 0.0003$  Å in film A which shows the largest texture strength (highest texture index), whereas the lesser textured film B exhibits a cell parameter  $a = 5.4439 \pm 0.0002$  Å. The same tendency occurs for films deposited on (100) Si (samples B' and F'), which exhibit both a stronger  $\langle 100 \rangle$  texture, the largest cell parameter being observed for the highest texture of film F'. In films C and D, the observed highest orientation near  $\langle 111 \rangle$  is concomitant to the largest cell parameter observed in our films whereas intermediate textures (films C and F) result in smaller unit cells. For similar texture strengths such as those for films A and B', the  $\langle 100 \rangle$  orientation seems to result in relatively lower cell parameter. Using high-resolution x-ray diffraction, Faivre and Bellet<sup>40</sup> observe a slight anisotropic deformation of the lattice, a less lattice expansion being observed for PS layers elaborated by etching (100) than (111) single-crystal silicon. They observe on individual crystals what we statistically observe via QTA information, but our nanocrystals are much expanded due to their small sizes.

### 6. Anisotropic mean crystallite sizes

The strong and anisotropic broadening of the diffracted lines observed in Fig. 1 is due to anisotropic shapes of individual crystallites. Thanks to the combined analysis, the mean crystallite shape was refined, corrected for texture effects. Whatever the deposition conditions and the substrate nature, the mean crystallite shape corresponds to an ellipsoid elongated along the [111] direction and almost isotropic in perpendicular directions (Table I). As schematically illustrated in Fig. 8, the average crystallite size along [111] is around 90 Å for sample D (which is around four times less than the value estimated by the Scherrer formula) and 20–40 Å in the perpendicular directions. The crystal shape anisotropy is therefore much larger than the one deduced from single pattern analysis.

In our films, we could not detect any significant Gaussian contribution in any of the peaks (no microstrains are present). This observation means on one hand that the

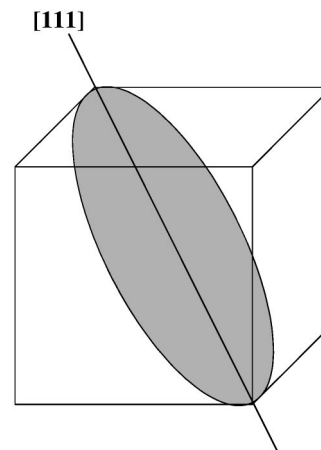


FIG. 8. Schematic mean crystallite shape for sample D represented in a cubic cell, as refined using the Popa approach and exhibiting a strong elongation along [111].

nanocrystals have nicely grown without internal  $d$ -spacing dispersion, and on the other hand that no dispersion of  $d$  spacing from crystal to crystal exists in a given film.

Whatever the substrate nature no pure  $\langle 111 \rangle$  texture could be observed, but a systematic elongation of the crystallites along this direction. This apparent absence of correlation between orientation and crystal shapes is the consequence of the growth interruption induced by the fabrication process, preventing more regular growth schemes from occurring such as in heteroepitaxial growing. However, looking closer at mean crystal sizes along  $\langle 111 \rangle$  and  $\langle 220 \rangle$  directions, one observes that films in which the  $\langle 100 \rangle$  orientation is present show a smaller crystal shape anisotropy. On (100)-Si substrates exhibiting a strong  $\langle 100 \rangle$  orientation, but also for film F on  $\alpha$ -SiO<sub>2</sub>, the  $\langle 111 \rangle$  mean dimension is around 85 Å, while that along  $\langle 220 \rangle$  is around 22 Å. Sample A exhibiting a major  $\langle 110 \rangle$  orientation but still a minor  $\langle 100 \rangle$  shows  $\langle 111 \rangle$  mean dimension around 94 Å, at least 5 Å less than films without the  $\langle 100 \rangle$  component (samples B, C, D, and E). Interestingly, Houben *et al.*<sup>32</sup> found similar crystallite sizes in nontextured and microstrain-free microcrystalline films; but with a reverse relationship of the shape anisotropy. Compared to our results on textured films, this definitely tends to demonstrate a textural relationship on anisotropic crystal shapes.

### 7. Profilometry and XRD thicknesses

According to profilometry measurements, the thicknesses of all films, except A, are around 1300 nm (Table II). The thicknesses refined by XRD and measured by profilometry are in good agreement for films deposited at larger distances on  $\alpha$ -SiO<sub>2</sub> and whatever the distance for films deposited on Si (films D–F'). For these films we observe, however, a systematically slightly smaller thickness by XRD. Thicknesses deduced by XRD for films (A–C) deposited at distances lower than 7 cm on  $\alpha$ -SiO<sub>2</sub> are showing large discrepancies with the ones measured by profilometry (approximately half the profilometry value for films B and C). For film A, the thickness is even not determinable by XRD (the refinement procedure diverges).

TABLE II. List of the refined parameters available using reflectivity analysis for samples B ( $d=6$  cm) and E ( $d=10$  cm) :  $q_c$  represents the critical wave vector,  $\beta$  the absorption coefficient,  $\sigma_{\text{rms}}$  the roughness, and  $P$  the porosity of the two layers used for the refinement. Numbers in parentheses represent errors on the last digit.

Distances $d$ (cm)	Layers	$q_c$ ( $\text{\AA}^{-1}$ )	$P$ (%)	$\sigma_{\text{rms}}$ ( $\text{\AA}$ )	$\beta(10^{-7})$	XRR thickness (nm)
10	Covered layer	0.02945(5)	13 (3)	12.9(2)	1.8 (2)	1200 (1)
	Top layer	0.0265 (7)	30 (4)	80 (1)	0.29(2)	16.7(9)
6	Covered layer	0.02724(5)	26 (3)	6.6(5)	1.8 (1)	1210 (2)
	Top layer	0.0245 (1)	40 (5)	69 (1)	0.31(6)	10.8(6)

Since the XRD-related thicknesses are refined from the diffracted intensity<sup>19</sup> (crystalline part of the films), these effects may be assigned to the presence of an amorphous silicon phase or to porosity. Since for the thinnest film (sample A) no XRD value could be obtained, a larger porosity or amorphous phase development is expected at the first growth stages, but none of the two techniques is able to discern between amorphous phase or porosity.

### 8. X-ray reflectivity

Although our films are too thick to allow the observation of oscillation in our x-ray reflectivity spectra, the critical angle value can provide a measurement of the mean electronic density of the layers. Figures 9(a) and 9(b) show typical specular reflectivity curves recorded for sample E ( $d=10$  cm) and sample B ( $d=6$  cm), respectively. In addition

to the absence of oscillation, as expected, the decrease of the curve in scattering wave-vector transfer  $q_z$  is very pronounced, indicating a roughness dominated phenomenon. We can observe two regimes in the curves: a first strong decrease after the total reflection regime which extends up to about  $0.03 \text{ \AA}^{-1}$  and a second regime between  $0.03$  and  $0.07 \text{ \AA}^{-1}$ , before the curves reach asymptotically the background. These two regimes prevent a correct refinement by a single layer model. A thin overlayer with a higher roughness has to be considered in the model in order to reproduce the high surface roughness as introduced, for instance, by Fujiwara *et al.*<sup>51</sup> In such a layer, thickness, absorption, roughness, and the critical scattering wave-vector transfer  $q_c$  are strongly correlated and only characterize the average electron density of a strongly rough and porous media. The XRR results for the two films are detailed in Table II. The strong decrease corresponds to a root-mean-square roughness  $\sigma_{\text{rms}}$  of  $80 \text{ \AA}$  for the top layer of sample E, as refined by a Fresnel formalism, giving a predominant contribution of the background for  $q$  larger than  $0.07 \text{ \AA}^{-1}$ . On the figure we indicate for comparison a  $1/q^4$  power-law decrease valid for a perfectly flat surface. The critical scattering wave-vector transfer  $q_c$  for the bulk of the film (deep layer) is  $0.02945 \text{ \AA}^{-1}$ , corresponding to a mean electron density of  $0.62 e^{-\text{\AA}^{-3}}$ . These values are lower than those for bulk silicon<sup>52</sup> ( $0.0316 \text{ \AA}^{-1}$  and  $0.708 e^{-\text{\AA}^{-3}}$ , respectively), which is a clear indication of the porosity of the films. From these analyses, the mean electron density increases with the distance  $d$  (in sample B it takes the value of  $0.02724 \text{ \AA}^{-1}$ ) for both top and covered layers, leading to a better understanding of the small XRD thickness refined for the thinner films (Table I). Due to a large roughness, the electron density of the material is considerably lower in the top layers as denoted by the difference in  $q_c$  values. The roughness of the films is not extended by more than  $170 \text{ \AA}$  in sample E with a mean value of  $80 \text{ \AA}$ .

XRR is a useful investigation method to probe the film porosities ( $P$ ). Buttard *et al.*<sup>53</sup> proposed an approach using the ratio between the measured critical angle ( $\theta_c$ ) and the theoretical bulk value for silicon ( $\theta_{c, \text{Si}}=0.222^\circ$ )

$$P = 1 - (\theta_c / \theta_{c, \text{Si}})^2. \quad (1)$$

For large distances (sample E,  $d=10$  cm) in our films we obtain porosities near 13% in the bulk of the material and 30% in the near-surface region, i. e., in a probed layer thickness of about 10 nm. However, such porosity reaches 26% and 40%, respectively, at smaller distances (sample B,  $d=6$  cm). Since our films are composed of mixed amorphous

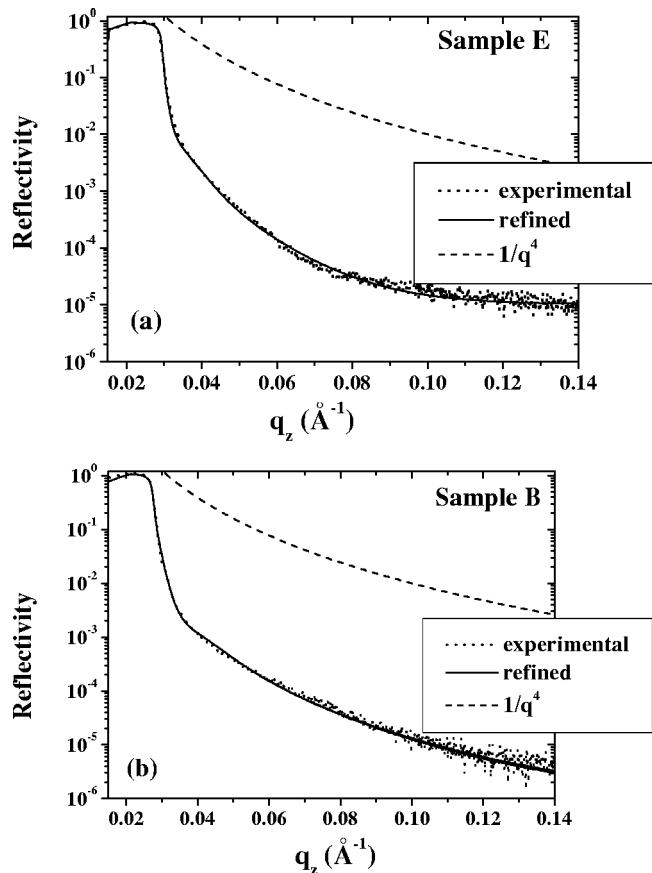


FIG. 9. Experimental and refined x-ray reflectivity curves (a) for sample E ( $d=10$  cm) and (b) sample B ( $d=6$  cm). The  $1/q^4$  curve illustrates at large  $q_z$ 's a sample without roughness.

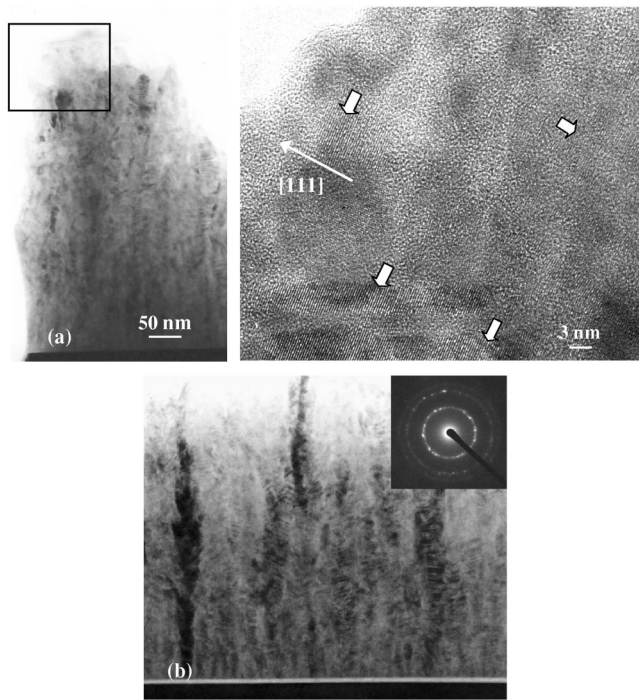


FIG. 10. Typical cross-section TEM images of samples deposited at (a)  $d = 6$  cm (sample B) and (b)  $d = 12$  cm (sample F), with in inset the corresponding selected area electron diffraction (SAED) pattern. The area limited on (a) by the rectangular frame is magnified on the right side and put in evidence the presence of nanograins (pointed out by white arrows) embedded in an amorphous environment.

and crystalline particles with different mean electron densities, such an approach results in a slightly biased estimation of the real porosity. However, it strongly underlines the porous character of the films.

## B. TEM

The discrepancy observed between the XRD and profilometry thicknesses is mainly attributed to the film porosity. Such a porosity is illustrated in Fig. 10 on cross-sectional TEM images of samples B and F for which Raman spectra analyses (reported below) indicate a crystalline ratio of 80% and 68%, respectively. These micrographs exhibit a highly columnar structure of silicon, similar to that observed by Vallat-Sauvain *et al.*<sup>29</sup> and Houben *et al.*,<sup>32</sup> with an average column width lower than 30 nm (sample F), within a highly porous and amorphous environment near the top of the layer<sup>10</sup> [inset of Fig. 10(a)]. In contrast, an almost complete crystallization with a relatively compact tissue is observed in the deep region. These observations provide strong support to the necessary introduction of two layers for the earlier-mentioned refinement of the XRR curves. Contrary to the observations reported in Refs. 29,32, the selected area diffraction diagram [see inset of Fig. 10(b)] does not show any amorphous contribution, but a polycrystalline powderlike pattern with strong reinforcements. These latter indicate the presence of larger crystallites in the probed volume. For the lower distances, the columns are shorter and unconnected along the depth of the film probably due to the accumulation of nanopowders, whereas the column contrast appears more

homogeneous for larger  $d$ 's. This is coherent with the increase of the compactness with  $d$  already shown by XRR.

The TEM observations are consistent with those reported by many authors<sup>29,51,54</sup> and also with our XRD analyses, providing coherent domain sizes lower than 10 nm on average. These domains are much smaller than the apparent crystal sizes probed by TEM, and porosity, resulting in small apparent XRD thicknesses. Indeed, there is no *a priori* relationship between coherent domain sizes as determined by diffraction and grains as seen in an image model by TEM. Some authors even report columnar growth of perfectly amorphous silicon.<sup>55</sup> For a direct comparison of XRD and TEM crystallite shapes and sizes, we report a high-resolution TEM image of the near-surface region of the film B in Fig. 10(a). It shows individual single crystallites embedded in a locally amorphous silicon matrix and approximately of the size and shape of XRD mean values. From the figure scale bar one can see the perfectly coherent results obtained by the two techniques.

Contrary to Houben *et al.*<sup>32</sup> no microtwinning could be observed in our films, as expected, since our films present a columnar growth resulting in fiber textures, i.e., without orientation relationship in the plane of the samples.

## C. Crystalline ratio and hydrogen content

RS studies have been carried out in order to determine the crystalline volume fraction  $f_c$ . In the particular case of silicon films with a mixed composition of amorphous and nanocrystalline phases, the Raman spectrum exhibits two main contributions for the transverse optical (TO) Si-Si Raman mode: a broad Gaussian-like component located around  $480 \text{ cm}^{-1}$  and a second Lorentzian one located at  $518 \text{ cm}^{-1}$ , both related, respectively, to the amorphous and the nanocrystalline phases. The  $f_c$  values are then obtained by the following relation:<sup>56</sup>

$$f_c = I_c / (I_c + \gamma I_a) \quad (2)$$

with  $I_a$  and  $I_c$  the deconvoluted intensities of the Si-Si TO components located, respectively, at  $480$  and  $518 \text{ cm}^{-1}$ . The term  $\gamma$  corresponds to the ratio of the relative Raman-scattering cross sections between the amorphous and crystalline Raman modes. The  $\gamma$  value depends both on form and size of the crystallites. We adopt for our work a  $\gamma$  value of 1.423 as suggested in Ref. 56. The assumption of equivalent signal efficiency for amorphous and crystalline phases<sup>54,57</sup> leads to an overestimate of  $f_c$ . The crystalline Raman Si-Si TO modes of concern exhibit a high local symmetry, which removes any textural effects from the crystalline part.

Figure 11 shows the evolution of  $f_c$  with  $d$  for the films deposited on  $a\text{-SiO}_2$ . Whatever the target-substrate spacing  $d$ ,  $f_c$  exceeds 60%. This is why we probably do not see any amorphous signal in the XRD diagrams, amorphous signals being broad and for such small volumes overlapped with the background, even on the nonamorphous Si substrates. Moreover, the lack of Raman shift for the Si-Si TO mode in the different analyzed films is consistent with the absence of residual stress as asserted from our XRD analyses. An abrupt increment of  $f_c$  (of around 30%) is observed for sample A

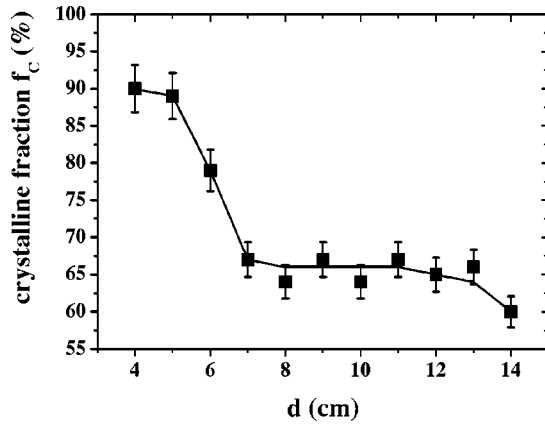


FIG. 11. Evolution of the crystalline fraction  $f_c$  vs the interelectrode distance  $d$  as deduced from Raman spectroscopy. Line is only a guide for eyes.

deposited at the closest distance ( $d=4$  cm) in comparison with sample E ( $d=14$  cm), that could be related to the collection of nanopowders formed in the near-cathode region for  $d \leq 7$  cm, as reported elsewhere.<sup>10</sup>

The high  $f_c$  values ( $>60\%$ ) are compatible with the low concentration of bonded hydrogen  $C_H$  (lower than 1 at. %), as calculated from the integrated intensity of the FTIR band around  $640\text{ cm}^{-1}$ .<sup>28,58</sup> The detection in FTIR spectra of the bending modes around  $880\text{--}890\text{ cm}^{-1}$  suggests the presence of the  $\text{SiH}_2$  species.<sup>59</sup> The decrease of the bending mode when  $d$  is lowered, is indicative of an important decrease of the  $\text{SiH}_2$  species for  $d \leq 7$  cm, region where a strong formation of Si nanopowder is observed.<sup>10</sup> This suggests that the formation of Si nanopowder for lower distances is due to the consumption of the highly sticking  $\text{SiH}_2$  radicals, which become, hence, less available for the columnar growth mechanism of silicon.<sup>60</sup> Furthermore, we recall that the insertion of this nanopowder formed near the target is responsible for the increment of  $f_c$  considering that the Raman probes the near-surface region.<sup>10,61</sup> Complementary studies by mass spectrometry and optical emission spectroscopy are necessary in order to check these hypotheses via a full characterization of the reactive plasma.

#### D. AFM

Figure 12 shows the AFM pattern for the film deposited

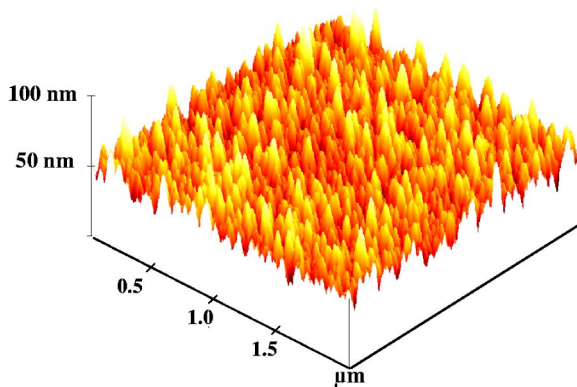


FIG. 12. Typical three-dimensional AFM micrograph for sample C ( $d=7$  cm).

at the edge distance limiting the region of powder production (sample C,  $d=7$  cm). Although the surface roughness has been shown to depend on the hydrogen partial pressure,<sup>61</sup> it remains relatively high for a degree of hydrogen-diluted argon percentage of 80% with a root-mean-square roughness  $r_{\text{msq}}$  estimated to 7 nm for this sample. This value is fully coherent with the corresponding one of 4 nm calculated from XRR curves, since porosity is located mainly at the top of the layer. Different  $r_{\text{msq}}$  values are reported in the literature: using low-pressure chemical-vapor deposition (LPCVD) and deposition temperatures around  $550\text{ }^\circ\text{C}$ . Modreanu *et al.*<sup>42</sup> obtain similar roughness (7–12 nm), while Fujiwara *et al.*<sup>51</sup> report values as high as 50 nm for PECVD samples deposited at temperatures comparable to ours. In this case, the PECVD seems to favor at  $220\text{ }^\circ\text{C}$  the growth of large crystals which induce larger roughness ranging from 18 to more than 100 nm.<sup>29,51</sup>

The use of radio-frequency PECVD by some authors<sup>29,51</sup> near  $220\text{ }^\circ\text{C}$  favored grain growth and then larger crystals than the ones we observed here, resulting in a considerably larger roughness, from 18 to more than 100 nm. However, the use of PECVD at  $360\text{ }^\circ\text{C}$  by Nakahata *et al.*<sup>43</sup> results in microcrystalline films exhibiting 5-nm roughness only, as determined by spectroscopic ellipsometry, for  $\langle 100 \rangle$ -textured samples. This would suggest some correlation between the  $\langle 100 \rangle$  orientations and the low roughness, useful for thin-film transistor applications whereas rough surface could be somehow required for solar cell devices.<sup>55</sup> However, the use of the reactive magnetron sputtering technique allowed us to achieve lower roughness in the low deposition temperature range ( $200\text{ }^\circ\text{C}$ ), which would make the films obtained by this technique suitable for field-effect thin-film transistor devices. The low roughness observed in our films seems to be independent of the texture of the films, mono- or multicomponents, even if the  $\langle 100 \rangle$  orientation would be more attractive for thin-film transistor (TFT) (due to the relatively smaller defect density induced at the oxide-silicon interface for these planes).

#### E. Optical properties

The detailed structural characteristics reported so far have been correlated to some physical features such as the optical properties of our layers. To this aim, optical absorption measurements have been performed and Fig. 13 compares the evolution with  $d$  of the refractive index,  $n$ , and of the Tauc *et al.*<sup>13</sup> gap,  $E_g$ , often used to estimate the optical band gap. The optical absorption coefficient  $\alpha$  follows the Tauc *et al.* relation<sup>13</sup> in the high absorption region ( $\alpha \approx 10^{-4}\text{ cm}^{-1}$ )

$$(\alpha E)^{1/2} = B(E - E_g), \quad (3)$$

where  $B$  is a constant and  $E$  is the incident photon energy. By plotting  $(\alpha E)^{1/2}$  vs  $E$ ,  $E_g$  can be obtained by the extrapolation of the linear part of the graph to the zero ordinate [ $(\alpha E)^{1/2} = 0$ ]. The refractive index  $n$  exhibits an abrupt increase with  $d$  before some tendency to saturate for larger  $d$  values. This behavior is strictly opposite to those of the speed deposition  $v_d$  (not illustrated here) and of  $E_g$ . When  $v_d$  is low, the spe-

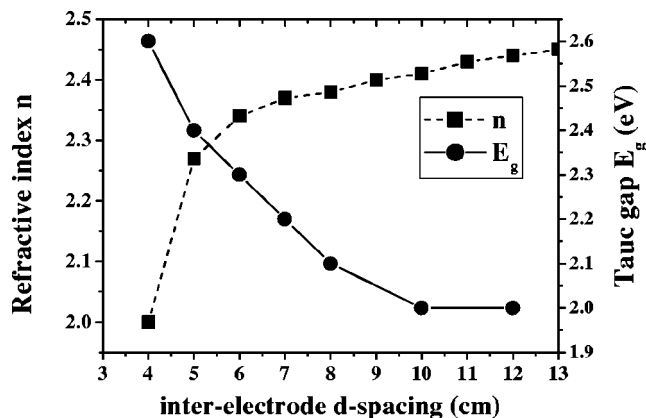


FIG. 13. Evolution of the refractive index  $n$  and of the optical gap  $E_g$  with the distance  $d$ . Lines are only guides for eyes.

cies sticking at the layer surface are more able to diffuse and contribute therefore to the relaxation of the structure. The inverse is also valid since a high  $v_d$  implies a strong rate of sticking species that hinders the diffusion at the surface and, consequently, the network relaxation. This would lead to the formation of microcavities which explains the low values of  $n$  for large  $d$  values compared to the case of close electrodes ( $d < 7$  cm) where the formed nanopowders are collected, hence accentuating the porosity, as observed by our x-ray analyses. In general, our  $n$  values reflecting the presence of some microcavity density are comparable to those reported elsewhere<sup>62,63</sup> and would be due to the desorption of volatile species upon crystallization.<sup>64</sup> Concerning the Tauc *et al.* gap  $E_g$ , the relatively high values observed (Fig. 13) cannot be uniquely explained by the usual recovery of the dangling bonds by hydrogen ( $C_H$  is lower than 1 at. % in our films). Comparable values have been reported by Furukawa and Miyasato<sup>65</sup> that suggest an origin lying in the quantum confinement effect, which widens the gap for their 2.5-nm Si grains. As already observed by TEM, some of the Si grains in our sputtered samples, and particularly collected in the nanopowder formed for the lower  $d$  values, are smaller than the critical value for quantum confinement (5 nm), leading to widen the band gap. However, the presence of significant density of microcavities is liable to induce similarly some widening of the band gap. Consequently, it is quite reasonable to consider that the high values of  $E_g$  are due to the combined effect of the nanosized scale of some grains and to a certain porosity.

#### IV. CONCLUSION

A precise characterization of thin nanocrystalline silicon films prepared by reactive sputtering has been carried out using a newly developed x-ray diffraction technique as well as scattering techniques (Raman and FTIR spectroscopies), electron microscopy, and AFM measurements. In given conditions, both the target to substrate distance and the substrate nature control the crystalline fraction of the films as well as their structural, textural, and microstructural features. The grown nanocrystals exhibit anisotropic shapes elongated along the [111] direction and embedded in a partially porous and amorphous medium, and the films exhibit larger porosi-

ties near the surface. The observed textures are fiberlike but with many components varying with the distance and never reaching the exact (111) orientation. The film structure is free of stress and microstrain, and the unit cell of the silicon nanopowders is always larger than the bulk silicon. Slight correlation between the stabilized textures and structures could be observed, so are with the anisotropic crystal shapes. The behaviors of both the refractive index  $n$  and optical gap  $E_g$  of the films are shown to be closely correlated to these structural features, and particularly to the crystal sizes and presence of microcavities.

#### ACKNOWLEDGMENTS

One of the authors (Y. L.) greatly acknowledges the French Ministère de la Recherche et de la Technologie for financial support and another author (D. C.) thanks the Délégation Régionale à la Recherche et à la Technologie-région Basse-Normandie for the x-ray experimentation financing.

- <sup>1</sup>Proceedings of the 19th International Conference on Amorphous and Microcrystalline Semiconductors, Nice, France, 27–31 August 2001 [J. Non-Cryst. Solids **299**, 2 (2002)].
- <sup>2</sup>U. F. Kocks, C. N. Tomé, and H.-R. Wenk, *Texture and Anisotropy: Preferred Orientations in Polycrystals and Their Effect on Materials Properties* (Cambridge University Press, New York, 1988), Vol. 1, Chap. 6, p. 272.
- <sup>3</sup>H. Akazawa, Phys. Rev. B **59**, 3184 (1999).
- <sup>4</sup>P. Roca and I. Cabarrocas, J. Non-Cryst. Solids **266–269**, 31 (2000).
- <sup>5</sup>Y. Leconte, R. Rizk, F. Gourbilleau, P. Voivenel, M. Lejeune, and C. Goncalves, Solid State Phenom. **80–81**, 65 (2001).
- <sup>6</sup>A. Matsuda and T. Goto, Mater. Res. Soc. Symp. Proc. **164**, 3 (1990).
- <sup>7</sup>A. Matsuda, Thin Solid Films **337**, 1 (1999).
- <sup>8</sup>S. Veprek, M. Heintze, F. A. Sarott, M. Jurcik-Rajman, and P. Willmott, Mater. Res. Soc. Symp. Proc. **118**, 3 (1988).
- <sup>9</sup>I. Shimizu, J. Hanna, and H. Shirai, Mater. Res. Soc. Symp. Proc. **164**, 195 (1990).
- <sup>10</sup>Y. Leconte, P. Marie, X. Portier, M. Lejeune, and R. Rizk, Mater. Sci. Eng., B **101**, 194 (2003).
- <sup>11</sup>G. Vignaud and A. Gibaud, computer code REFLEX (<http://ipc.univ-lemans.fr/reflex/reflex.htm>, 2000).
- <sup>12</sup>B. Garrido, A. Perez-Rodriguez, J. R. Morante, A. Achik, P. Gourbilleau, R. Madelon, and R. Rizk, J. Vac. Sci. Technol. B **16**, 1851 (1998).
- <sup>13</sup>J. Tauc, R. Grigorovici, and A. Vancu, Phys. Status Solidi **15**, 627 (1966).
- <sup>14</sup>J. Ricote and D. Chateigner, Bol. Soc. Esp. Ceram. Vidrio **38**, 587 (1999).
- <sup>15</sup>L. Lutterotti, H.-R. Wenk, and S. Matthies, in *Textures of Materials*, edited by J. A. Szpunar (NRC Research, Ottawa, 1999), Vol. 2, pp. 1599–1604.
- <sup>16</sup>S. Matthies and G. W. Vinel, Phys. Status Solidi B **112**, K111 (1982).
- <sup>17</sup>J. J. Heizmann and C. Laruelle, J. Appl. Crystallogr. **19**, 467 (1986).
- <sup>18</sup>[http://pcb4122.univ-lemans.fr/powdif/low\\_fw\\_hm\\_and\\_rp.html#4B](http://pcb4122.univ-lemans.fr/powdif/low_fw_hm_and_rp.html#4B)
- <sup>19</sup>D. Balzar, J. Appl. Crystallogr. **25**, 559 (1992).
- <sup>20</sup>N. C. Popa, J. Appl. Crystallogr. **31**, 176 (1998).
- <sup>21</sup>M. Morales, D. Chateigner, L. Lutterotti, and J. Ricote, Mater. Sci. Forum **408–412**, 113 (2002).
- <sup>22</sup>S. Matthies, G. W. Vinel, and K. Helming, *Standard Distributions in Texture Analysis* (Akademie, Berlin, 1987), Vol. 1, p. 449.
- <sup>23</sup>H.-J. Bunge, *Texture Analysis in Material Science* (Butterworths, London, 1982).
- <sup>24</sup>GOMAN, INEL France SA Licence 1997; POFINT: “Pole figure interpretation,” CNRS-INEL France SA Licence 2002.
- <sup>25</sup>H.-R. Wenk, S. Matthies, J. Donovan, and D. Chateigner, J. Appl. Crystallogr. **31**, 262 (1998).
- <sup>26</sup>A. Guinier, *Théorie et Techniques de la Radiocristallographie*, 3rd ed. (Dunod, Paris, 1964).
- <sup>27</sup>J. I. Lanford and D. Louer, J. Appl. Crystallogr. **15**, 20 (1982).
- <sup>28</sup>Y. Feng, M. Zhu, F. Liu, J. Liu, H. Han, and Y. Han, Thin Solid Films **395**, 213 (2001).
- <sup>29</sup>E. Vallat-Sauvain, U. Kroll, J. Meier, and A. Shah, J. Appl. Phys. **87**, 3137 (2000).
- <sup>30</sup>U. Kroll, J. Meier, P. Torres, J. Pohl, and A. Shah, J. Non-Cryst. Solids

- 227–230, 69 (1998).
- <sup>31</sup>D. Balzar and S. Popovic, J. Appl. Crystallogr. **29**, 16-23 (1996).
- <sup>32</sup>L. Houben, M. Luysberg, and R. Carius, Phys. Rev. B **67**, 045312 (2003).
- <sup>33</sup>L. Lutterotti, S. Matthies, H.-R. Wenk, A. S. Schultz, and J. W. Richardson Jr., J. Appl. Phys. **81**, 594 (1997).
- <sup>34</sup>D. Chateigner, in *Combined Analysis: Structure-Texture-Microstructure-Phase-Stresses Determination by X-ray and Neutron Diffraction* (2004); <http://www.ensicaen.ismra.fr/~chateign/texture/combined.pdf>
- <sup>35</sup>K. Helming, Textures Microstruct. **14–18**, 187 (1991).
- <sup>36</sup>R. J. Hill and R. X. Fisher, J. Appl. Phys. **23**, 462 (1990).
- <sup>37</sup>W. A. Dollase, J. Appl. Crystallogr. **19**, 267 (1986).
- <sup>38</sup>F. K. Lotgering, J. Inorg. Nucl. Chem. **9**, 113 (1959).
- <sup>39</sup>T. Kamiya, K. Nakahata, K. Ro, C. M. Fortmann, and I. Shimizu, Jpn. J. Appl. Phys., Part 1 **38**, 5750 (1999).
- <sup>40</sup>C. Faivre and D. Bellet, J. Appl. Crystallogr. **32**, 1134 (1999).
- <sup>41</sup>D. Chateigner, F. Brunet, A. Deneuve, P. Germi, M. Pernet, and P. Gonon, J. Cryst. Growth **148**, 110 (1995).
- <sup>42</sup>M. Modreanu, N. Tomozeiu, M. Gartner, and P. Cosmin, Thin Solid Films **383**, 254 (2001).
- <sup>43</sup>K. Nakahata, A. Miida, T. Kamiya, Y. Maeda, C. M. Fortmann, and I. Shimizu, Jpn. J. Appl. Phys., Part 2 **37**, L1026 (1998).
- <sup>44</sup>S.-I. Ishibara, D. He, M. Nakata, and I. Shimizu, Jpn. J. Appl. Phys., Part 1 **32**, 1539 (1993).
- <sup>45</sup>T. I. Kamins and T. R. Cass, Thin Solid Films **16**, 147 (1973).
- <sup>46</sup>T. I. Kamins, Sens. Actuators, A **21–23**, 817 (1990).
- <sup>47</sup>J. Yang, K. Kahn, A.-Q. He, S. M. Phillips, and A. H. Heuer, J. Microelectromech. Syst. **9**, 485 (2000).
- <sup>48</sup>M. Birkholz, B. Selle, E. Conrad, K. Lips, and W. Fuhs, J. Appl. Phys. **88**, 4376 (2000).
- <sup>49</sup>R. Bisaro, J. Maraino, N. Proust, and K. Zellama, J. Appl. Phys. **59**, 1167 (1986).
- <sup>50</sup>T. I. Kamins, *Polycrystalline Silicon for Integrated Circuit Applications* (Kluwer, Boston, 1988).
- <sup>51</sup>H. Fujiwara, M. Kondo, and A. Matsuda, Phys. Rev. B **63**, 115306 (2001).
- <sup>52</sup>J. Daillant, *X-ray and Neutron Reflectivity: Principles and Applications* (Springer, Berlin, 1999), p. 95.
- <sup>53</sup>D. Buttard, G. Dolino, D. Bellet, T. Baumbach, and F. Rieutord, Solid State Commun. **109**, 1 (1999).
- <sup>54</sup>S.-I. Ishibara, D. He, and I. Shimizu, Jpn. J. Appl. Phys., Part 1 **33**, 51 (1994).
- <sup>55</sup>T. Unagami, A. Lousa, and R. Messier, Jpn. J. Appl. Phys., Part 2 **36**, L737 (1997).
- <sup>56</sup>E. Bustaret, M. A. Hachicha, and M. Brunel, Appl. Phys. Lett. **52**, 1675 (1988).
- <sup>57</sup>F. Liu, M. Zhu, J. Liu, and L. Wang, Thin Solid Films **430**, 182 (2003).
- <sup>58</sup>A. Achiq, R. Rizk, F. Gourbilleau, and P. Voivenel, Thin Solid Films **348**, 74 (1999).
- <sup>59</sup>G. Lucovsky, R. J. Nemanich, and J. G. Knights, Phys. Rev. B **19**, 2074 (1979).
- <sup>60</sup>Y. Leconte, P. Marie, X. Portier, M. Lejeune, and R. Rizk, Thin Solid Films **427**, 252 (2003).
- <sup>61</sup>Y. Leconte, C. Dufour, B. Garrido, and R. Rizk, J. Non-Cryst. Solids **299–302**, 87 (2002).
- <sup>62</sup>G. N. Parsons, J. J. Bolland, and J. C. Tsang, Jpn. J. Appl. Phys., Part 1 **31**, 1943 (1992).
- <sup>63</sup>I. Shimizu, J. Non-Cryst. Solids **114**, 145 (1989).
- <sup>64</sup>T. Akasaka and I. Shimizu, Appl. Phys. Lett. **66**, 3441 (1995).
- <sup>65</sup>S. Furukawa and T. Miyasato, Phys. Rev. B **38**, 5726 (1988).





# Influence of substrate temperature on growth of nanocrystalline silicon carbide by reactive magnetron sputtering

H. Colder,<sup>a)</sup> R. Rizk, M. Morales, P. Marie, and J. Vicens

*Structure des Interfaces et Fonctionnalité des Couches Minces (SIFCOM), Unité Mixte de Recherche (UMR) 6176, Ecole Nationale Supérieure d'Ingénieurs de Caen (ENSICAEN), 6 Boulevard Maréchal Juin, 14050 Caen, France*

I. Vickridge

*Système d'Analyse par Faisceau d'Ions Rapides (SAFIR), GPS, Unité Mixte de Recherche (UMR) 7588, Campus Boucicaut, 140, Rue de Lourmel, 75015 Paris, France*

(Received 23 November 2004; accepted 1 June 2005; published online 26 July 2005)

Hydrogenated nanocrystalline silicon carbide were grown at various deposition temperatures  $T_d$  from 200 to 600 °C by means of reactive magnetron sputtering in a plasma of 80% H<sub>2</sub> and 20% Ar mixture. A detailed investigation of the structural, compositional, phase nature, and morphology was carried out by complementary sophisticated techniques, such as Fourier transform infrared spectroscopy, x-ray diffraction (XRD), Rutherford backscattering, nuclear reaction, and elastic recoil detection analysis techniques, in addition to conventional and high-resolution transmission electron microscopy (HRTEM) observations. A crystallization onset with a fraction of 35% was observed for  $T_d=300$  °C, which improved to 80% for  $T_d=600$  °C, reflected by an increasing density of the SiC nanocrystals which kept an average size of about 5 nm. The observed fiber textures present  $\langle 102 \rangle$  and  $\langle 11\ell \rangle$  texture components, with  $\ell$  larger than 2, while SiC nanocrystals elongated along the  $[111]$  direction are also evidenced. These latter are supported by the careful analyses of the HRTEM images which show evidence of faulted growing cubic SiC, as the origin of the very close hexagonal 6H-SiC structure taken into account in the XRD refinement. These various features were found quite consistent with the optical properties of the layers, and, in particular, the evolutions of both optical gap and static refractive index. © 2005 American Institute of Physics. [DOI: 10.1063/1.1985975]

## I. INTRODUCTION

In the past decade, relevant issues in material science have introduced numerous contributions in everybody's daily life, and particularly through original electronic inventions. This would correspond to some pressing needs and urgent demands for ever increasing cheapness, smallness, reliability, flexibility, durability, etc., of devices compatible with Si technology. Among these complementary metal-oxide-semiconductor (CMOS)-integrated semiconductors, silicon carbide is still the material of choice owing to its specific and outstanding features, such as wide band gap, chemical stability, and mechanical resistance, accounting for the great effort of research devoted to this material.<sup>1</sup> The additional characteristic of improved carrier mobility in crystalline silicon carbide has, on the other hand, motivated numerous works dealing with the growth of crystallized silicon carbide aiming at the development of a great variety of microelectronic and optoelectronic devices such as bipolar transistors,<sup>2</sup> photodetectors,<sup>3</sup> electroluminescent diodes,<sup>4</sup> and so on. These detectors, sensors, light emitters, and other SiC/Si heterojunctions gain by being processed at relatively low temperatures, as far as the use of flexible and low cost substrates is concerned. Such a possibility became quite effective for highly crystallized silicon obtained at tempera-

tures lower than 200 °C,<sup>5</sup> and its eventual extension to SiC allows one to overcome the problematic generation of lattice defects at the SiC/Si interface.<sup>1</sup> One can then proceed to a successive deposition of crystallized Si and SiC on a cheap and supple polymeric substrate, for example.

The low-temperature growth of high-quality crystallized SiC is, therefore, much in demand for the fabrication of SiC/Si heterostructures to take advantage of the wide-band-gap SiC with respect to Si aiming at reducing the leakage current. Relevant approaches have been reported these last years to crystallize SiC during deposition at relatively low temperature under a hydrogen-rich plasma by means of chemical-vapor deposition<sup>6,7</sup> (CVD) or magnetron sputtering<sup>8</sup> methods. Such a direct crystallization is ascribed to the highly reactive character of both Si-based<sup>9</sup> and C-based<sup>10</sup> radicals interacting with the growing surface. In addition to the detrimental generation of a substantial amount of plasma-induced defects and contaminant hydrocarbons,<sup>6,7</sup> the deposition temperature was still higher than 700 °C.<sup>8</sup> However, we have succeeded recently to reduce the direct crystallization temperature to a value as low as 300 °C using a reactive magnetron sputtering under a plasma of pure hydrogen.<sup>11</sup> The corresponding crystalline fraction was about 40% and improved to 60% for a deposition at 600 °C.<sup>11</sup> The good quality of the nanocrystalline silicon carbide (nc-SiC) obtained at 600 °C was attested by the high performance of nc-SiC/*c*-Si heterojunction diode.<sup>12</sup>

<sup>a)</sup> Author to whom correspondence should be addressed; electronic mail: heloise.taupin@ensicaen.fr

However, the achievement of such nc-SiC layers under pure hydrogen plasma is somehow thwarted by the noncompetitive relatively low growth rate of 0.5–0.8 nm min<sup>-1</sup>.

An interesting characteristic of silicon carbide is polytypism resulting from the formation of different stacking sequences of the Si–C double layers. Some 200 polytypes exist, having cubic, hexagonal, or rhombohedral, symmetry.

In this work we report detailed structural, morphological, and compositional studies of nc-SiC layers obtained with a relatively high growth rate through mixing the hydrogen of the plasma with 20% of argon. The relating features were subsequently connected to some optical properties. The influence of the deposition temperature on the degree of crystallization, the distribution and size of SiC nanocrystals, the nature of the polytypes formed, the generated lattice defects, the quality of the SiC/Si interface, the Si/C ratio, and the concentrations of total and bonded hydrogen, in relation with the optical behavior, was carefully examined by a set of complementary sophisticated techniques, described in Sec. II.

## II. EXPERIMENTAL DETAILS

The nc-SiC films investigated in this study were grown by reactive magnetron sputtering of a silicon target of 10 cm of diameter covered by a number of carbon chips. The carbon-to-silicon sputtered area ratio was maintained at about 30%, a value that exceeds the threshold required to incorporate a stoichiometry-related concentration of carbon for the samples previously obtained with a pure H<sub>2</sub> plasma.<sup>13</sup> The basic pressure in the sputtering chamber was lowered to a few 10<sup>-8</sup> Torr before the introduction of the precursor gas mixture (80% H<sub>2</sub>–20% Ar) up to 50 mTorr. The deposition temperature  $T_d$  was varied between 200 and 600 °C, while the power density was maintained constant at 2.5 W cm<sup>-2</sup>. The substrates used were quartz and single-crystal (100)-Si (*c*-Si), and the thickness of the deposited layers was in the 0.5–1.0 μm range.

The compositional, phase nature, structural, and physicochemical investigations were made by Fourier transform infrared (FTIR) absorption spectroscopy, x-ray diffraction (XRD), ion-beam analysis (IBA) that includes the Rutherford backscattering spectroscopy (RBS), the nuclear reaction analysis (NRA), and the elastic recoil detection analysis (ERDA) approaches, in addition to conventional and high-resolution transmission electron microscopy (CTEM and HRTEM) techniques. These investigations were complemented by the study of physical properties and notably the optical features by optical transmission (OT) spectroscopy. The choice between quartz and silicon substrates was made according to the characterization technique to be applied, with a silicon substrate used for all techniques except OT, where a transparent substrate was necessary.

The FTIR measurements were performed by a Nicolet 750-II spectrometer, while for the usual XRD experiments we used a Philips X-Pert MRD at the average Cu  $K\alpha$  radiation ( $\lambda_{Cu}=1.5418$ ) equipped with a point scintillation detector. The  $\theta$ - $2\theta$  XRD patterns of the films exhibited preferential orientations (the 200 reflection is not observed) and

anisotropic line broadening. Consequently, we performed quantitative texture analysis (QTA) with a simultaneous Rietveld refinement including anisotropic line broadening and film thickness analyses. We used a Huber four-circles diffractometer and a curved position-sensitive detector (INEL CPS 120), which spans a 120° range in  $2\theta$ , allowing the simultaneous recording of several pole figures and the full diffraction diagram.<sup>14</sup> These latter were measured by scanning the tilt angle of the goniometer  $\chi$  and the azimuthal angle  $\varphi$  in the 0°–35° and 0°–360° ranges, respectively, both using a 5° step with an incident x-ray beam  $\omega=17.1^\circ$  corresponding to the Bragg angle of the 111 reflection of the cubic silicon carbide.

For the quantitative analysis of these x-ray diffractograms, we used the material analysis using diffraction (MAUD) program<sup>15</sup> that combines the Williams-Imhof-Matties-Vinel method,<sup>16</sup> used to solve the orientation distribution function (ODF), with a Rietveld analysis to extract the microstructural (crystallite size, microstrains, etc.) and structural parameters (cell parameters, etc.), and the film thicknesses. The ( $hkl$ ) dependence of diffraction line broadening is determined in the program by the use of the Popa rules based on the symmetrized spherical harmonics that allow the modeling of the crystallite shape.<sup>17</sup> The refinement quality is assured by the comparison of the experimental and the recalculated diagrams and by the  $R_w$ ,  $R_{exp}$ , and  $R_B$  reliability factors for the Rietveld refinement:<sup>15</sup>

$$R_B = \frac{\sum_k |I_k - I_{ck}|}{\sum_k I_k},$$

$$R_w = \left[ \frac{\sum_i w_i (y_i - y_{ci})^2}{\sum_i w_i (y_{ci})^2} \right]^{1/2},$$

$$R_{exp} = \left[ \frac{N - P}{\sum_i w_i (y_i)^2} \right]^{1/2},$$

where  $I_k$  and  $I_{ck}$  are the observed and calculated intensities of the  $k$ th Bragg reflection,  $y_i$  and  $y_{ci}$  are the observed and calculated counts at the  $i$ th step,  $w_i$  is  $y_i^{-1}$ ,  $N$  the number of  $y_i$ , and  $P$  the number of adjusted parameters.

The composition of the films (Si, C, and H contents) was determined by NRA for carbon, by RBS for silicon, and by ERDA for hydrogen, with the ion-beam analysis system of the Groupe de Physique des Solides (SAFIR, University of Paris 6 et 7, France). RBS spectra were acquired with a 2-MeV incident beam of <sup>4</sup>He<sup>+</sup> ions for 5 μC of incident charge. The detector was positioned at 165° in the horizontal plane containing the beam axis, and the solid angle was determined using a Bi-implanted silicon reference sample. NRA spectra were acquired using a 1.1-MeV incident beam of D<sup>+</sup> to induce the C<sup>12</sup>( $d,p$ )C<sup>13</sup> nuclear reaction. The 300-mm<sup>2</sup> detector is fixed at a 150° detection angle in the horizontal plane containing the beam axis, and protected from elastically scattered particles by a 19-μm Mylar film. An anodic Ta<sub>2</sub>O<sub>5</sub> thin-film reference sample was used to determine the detector solid angle, assuming the cross sec-

tion for  $^{16}\text{O}(d,p_1)$  at  $150^\circ$  of shape given in Ref. 18, scaled by  $5.3/4.5=1.18$  to give a value of  $5.3 \text{ mb sr}^{-1}$  at  $857 \text{ keV}$ .<sup>19</sup> No reliable cross-section measurement exists at  $150^\circ$  for  $^{12}\text{C}(d,p_0)$ , leading to the use of the cross section at  $135^\circ$ .<sup>20</sup> This approach is partly justified by two facts: the mentioned cross section is actually in rather good agreement at  $968 \text{ keV}$  ( $30.5 \text{ mb sr}^{-1}$ ) with that of  $^{12}\text{C}(d,p_0)$  measured at  $150^\circ$  ( $29.5$ ),<sup>19</sup> and (ii) the  $^{12}\text{C}(d,p_0)$  cross sections at  $135^\circ$  and at  $165^\circ$  are rather similar, suggesting relatively flat angular distributions. ERDA spectra were acquired using a  $2\text{-MeV } ^4\text{He}^+$  beam with a current of  $10 \text{ nA}$ . The  $^4\text{He}^+$  beam was incident at  $15^\circ$  to the sample surface, with measurements made at a recoil angle of  $30^\circ$  with a  $10\text{-}\mu\text{m}$  Mylar foil in front of the detector to stop an elastically scattered primary beam. A high-density polyethylene thin film ( $\text{CH}_2$ ), as described in Ref. 19, was used as a reference sample.

The analysis of the IBA data proceeds by the determination, first, of the hydrogen content. The samples are “too thick” for the ERDA and the hydrogen content was therefore estimated from the height of the signal. The spectra are fitted using simulation and evaluation of nuclear reaction spectroscopy (SENRAS),<sup>21</sup> varying the hydrogen concentration while maintaining  $\text{Si:C}=1$ . Once the  $\text{Si:C}$  ratios had been determined using NRA and RBS, it was verified that the hydrogen content determined by ERDA was practically insensitive to the assumed value of  $\text{Si:C}$  used in the simulation, over the range of  $\text{Si:C}$  values found. The main source of error in the hydrogen determination is the energy calibration of the spectra, which could lead to systematic common errors of up to  $\pm 20\%$ . Relative errors are practically negligible. Next, the best simultaneous fits to the NRA and RBS spectra are sought via SIMNRA and RUMP, respectively, by varying  $\text{Si:C}$  and total film thickness and assuming the hydrogen content as determined by ERDA. For film thickness up to around  $10^{18} \text{ at. cm}^{-2}$ , the RBS spectrum contains thickness information in the position of the jump in Si signal corresponding to the underlying Si substrate, whereas the NRA spectrum contains only non-depth-resolved information. For films considered as too thick for RBS, the thickness information is contained in the shape of the  $^{12}\text{C}(d,p_0)$  peak of the NRA spectrum. In this paper the thickness found by ion-beam analysis is expressed as a product of density (expressed in  $\text{at./cm}^3$ ) by thickness (length unit) since this is what is actually measured by the ion-beam analysis methods. This could be expressed in units of length if the concentration was known; however, this is not the case here.

The CTEM and HRTEM observations were carried out on cross sections made on the films in a JEOL 200CX and a Topcon 002B microscope, respectively. The OT measurements were performed between  $0.4$  and  $4.1 \text{ eV}$  in a double-beam Perkin-Elmer ( $\lambda 9$ ) spectrophotometer, allowing the determination of the optical gaps and the refractive index  $n$ .

### III. RESULTS AND DISCUSSION

The dependence of the growth rate,  $\nu_g$ , against the deposition temperature  $T_d$  is shown on Fig. 1. A fair agreement can be noticed, within the experimental errors, between the data deduced from the different values of the layer thickness

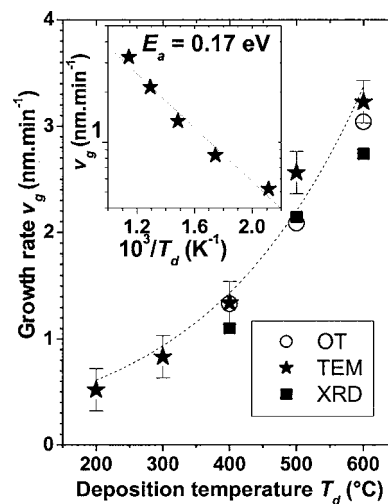


FIG. 1. Evolution of the growth rate  $\nu_g$  as function of the deposition temperature  $T_d$  as deduced from the film thicknesses obtained by different techniques [XRD, optical transmission (OT), and TEM observations]. The inset shows the corresponding Arrhenius plot.

deposited at a given  $T_d$ , as extracted from TEM, XRD, and OT analyses. Their evolutions show the same trend of  $\nu_g$  increase when  $T_d$  is raised, even though the  $\nu_g$  values corresponding to TEM observations would be the most reliable. The reactive character of our sputtering approach gives rise to two competing processes: on the one hand, the sticking and surface diffusion of highly reactive Si-based and C-based radicals and, on the other hand, the selective etching of weak or strained near-surface bonds. Apart from the resulting relaxation of the network towards the crystalline state, as discussed elsewhere,<sup>11,13</sup> the observed increase of  $\nu_g$  is indicative of the prevalence of both sticking and diffusion of the precursors, which appear more thermally activated than the concomitant etching process. Indeed, the sticking of H-based radicals was found to grow for increasing values of  $T_d$  (Refs. 22 and 23) and similar behavior is expected for C-based radicals. The evolution of  $\nu_g$  against  $T_d$  is reflected by the Arrhenius plot shown in the inset, bringing out an activation energy of  $0.17 \text{ eV}$  which should be understood as an effective one resulting from the already mentioned competing processes, sticking, surface diffusion, and selective etching. This energy seems to govern the growth kinetics that deserve to be carefully examined in a specific work not fitting with the present study.

Figure 2 shows the FTIR spectra recorded in the  $500\text{--}1200\text{-cm}^{-1}$  region and in the  $1800\text{--}3200\text{-cm}^{-1}$  range (see inset) on the films grown at the indicated  $T_d$  values. A main band is clearly recognized in all the spectra, which peaks at about  $800 \text{ cm}^{-1}$  and turns out to be shouldered by two structures at about  $900$  and  $1000 \text{ cm}^{-1}$ . The  $800\text{-cm}^{-1}$  peak is characteristic of the stretching modes of the Si-C bonds in crystalline SiC,<sup>24</sup> while the additional structures at  $900$  and  $1000 \text{ cm}^{-1}$  are most likely due to Si-H<sub>2</sub> bending and C-H wagging modes, respectively.<sup>25,26</sup> A contribution from Si-O bonds to the  $1000\text{-cm}^{-1}$  line can be excluded or at least neglected, since no signal from an O contaminant was detected by the ion-beam analyses (RBS and NRA) reported

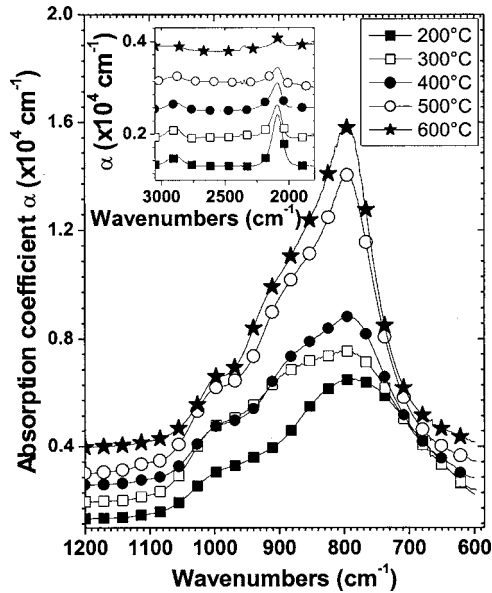


FIG. 2. FTIR spectra recorded in the 500–1200-cm<sup>-1</sup> region for the SiC layer obtained for different deposition temperatures,  $T_d$ . The inset shows the corresponding spectra in the 1800–3000-cm<sup>-1</sup> region.

below. On the contrary, the implication of H bonding is confirmed by the counterpart stretching modes at 2100 and 2900 cm<sup>-1</sup>.

On the other hand, the amplitude of the 800-cm<sup>-1</sup> peak is three to four times increased and its width is significantly lowered when  $T_d$  is raised from 200 to 600 °C. This is accompanied by a gradual evolution of its shape from a nearly Gaussian (200 °C) to a quasi-Lorentzian (600 °C), which reflects a concomitant progressive change of the distribution of the lengths and angles of the Si–C bonds, from highly dispersed, as for amorphous structure, to less and less distortion and dispersion characterizing a crystalline network. The 800-cm<sup>-1</sup> peak was deconvoluted into Gaussian and Lorentzian components in order to estimate, as already reported for identical samples<sup>12</sup> and comparable conditions,<sup>27</sup> the crystalline fraction  $f_C$  from the ratio  $L/(L+G)$ ,  $L$  and  $G$  being the areas of the Lorentzian and the Gaussian components. Additionally, the concentration of bonded hydrogen  $C_H$  and, in particular, the parts relating to its bonding with either silicon or carbon atoms have been evaluated from the integration of the stretching peaks around 2100 and 2900 cm<sup>-1</sup>, respectively. Figure 3 shows the evolutions of both  $f_C$  and  $C_H$  as function of  $T_d$ , as well as the histogram displaying the specific contributions of either Si–H and C–H bonds. It can be seen that  $f_C$  increases to 35% for  $T_d=300$  °C, doubles for  $T_d=500$  °C, and improves to a value as high as 80% when  $T_d$  reaches 600 °C. In parallel,  $C_H$  decreases from 30 at. % to less than 4 at. %, reflecting the well-known hydrogen desorption accompanying the crystallization induced by Si-based and C-based radicals encountered previously for silicon<sup>28</sup> and silicon carbide.<sup>29</sup> As mentioned above, the crystallization resulting from the selective etching of weak Si–H (320 kJ mol<sup>-1</sup>) and C–H (410 kJ mol<sup>-1</sup>) bonds and the subsequent formation of strong Si–C bonds (520 kJ mol<sup>-1</sup>) give rise to the observed desorption of hydrogen as volatile molecules. Figure 3 also shows that hydrogen is preferentially

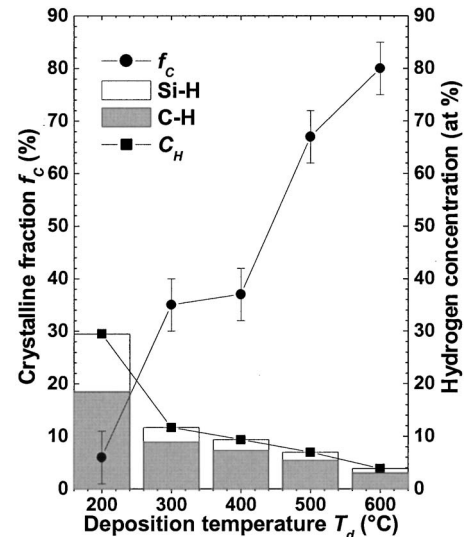


FIG. 3. Evolution as function of the deposition temperature  $T_d$ , of the crystalline fraction  $f_C$ , and of the hydrogen concentration bonded to silicon (Si–H) or carbon (C–H) atoms as deduced by FTIR. The total hydrogen concentration in the films as determined by ERDA has been also reported.

bonded to carbon with about 70% for  $T_d=200$  °C and 87% for  $T_d=600$  °C. Such a preferential bonding has been observed for hydrogenated amorphous SiC (Ref. 30) and is ascribed to the higher affinity of carbon towards hydrogen, compared to that of silicon. However, the evolution of the degree of this preferential bonding to C, from 70% to 87%, is rather connected with the ratio of C/Si which increases with  $T_d$ , as reported and commented hereafter.

ERDA, NRA, and RBS spectra from the thickest and thinnest films analyzed are shown, respectively, in Figs. 4(a)–4(c), while the film composition and the total hydrogen content are reported in Table I. The compositions are averaged over the film thicknesses since the RBS and ERDA spectra do not indicate, for any  $T_d$  value, significant compositional variations of the films as a function of the depth. No contaminants (Ar, O, and metals) were observed in any of the films. The film composition evolves from Si rich to near stoichiometric and the hydrogen content decreases with increasing deposition temperature (Table I). The total hydrogen content deduced by ERDA exceeds obviously everywhere the concentration of bonded hydrogen determined from FTIR spectra, as compared in Table I, even though the difference tends to be larger for higher  $T_d$  values. This difference is more than 10 at. % for  $T_d=600$  °C and might reflect some stability of the related configuration of hydrogen, such as molecular species located within microvoids and requiring an effusion temperature higher than 800 °C.<sup>31</sup> Concerning the Si/C ratio, its evolution could be connected to the conditions favoring the formation of SiC nanocrystals and, in particular,  $T_d$  which governs the crystalline fraction  $f_C$ . The trend of Si/C towards stoichiometry when  $f_C$  increases is quite compatible with earlier observations of the crystallization onset of Si<sub>1-x</sub>C<sub>x</sub> films when  $x$  reaches 0.5.<sup>32</sup> It is also supported by one of our earlier studies<sup>13</sup> reporting that carbon would be more easily retained (or incorporated) to form SiC nanocrystals rather than amorphous ones. On the other hand, the increase of C content with  $T_d$  (and  $f_C$ ) can clearly

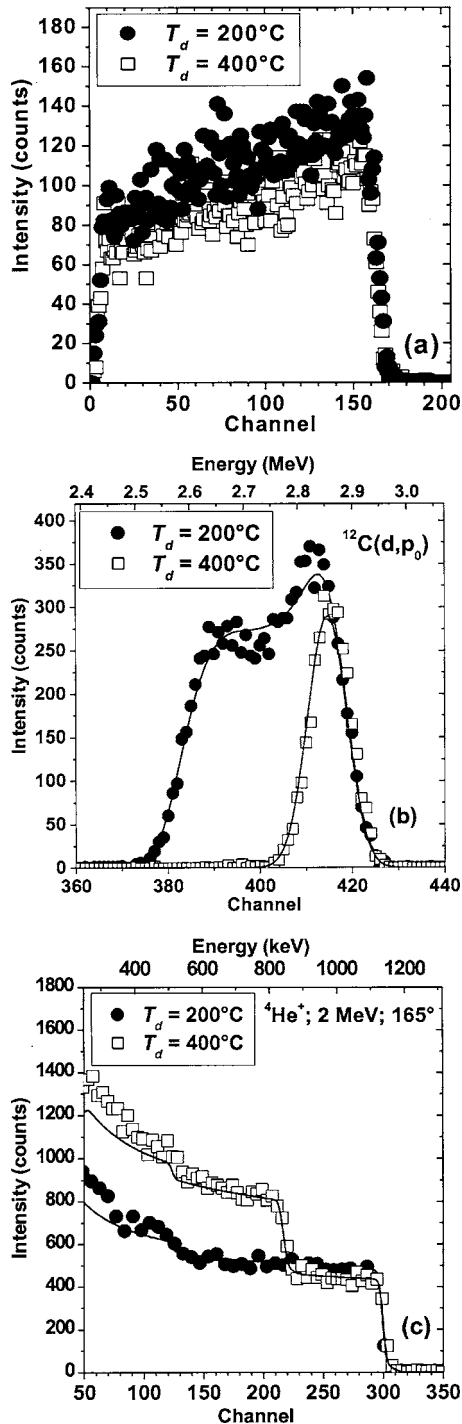


FIG. 4. (a) ERDA, (b) NRA, and (c) RBS spectra and associated fits for the thinnest ( $T_d=400^\circ\text{C}$ ) and the thickest ( $T_d=200^\circ\text{C}$ ) films analyzed.

explain the already reported enhancement of the C–H preferential bonding (see Fig. 3) since carbon becomes more and more available when  $T_d$  is increased.

As the films exhibit a fiber texture, the XRD spectra were summed over the whole range (0–360°) of the azimuthal angle  $\varphi$  for a given value of  $\chi$ , the goniometer tilt angle. Typical  $\omega$ -2 $\theta$  XRD patterns obtained for  $\chi=0^\circ$  are shown in Fig. 5 for films deposited in the temperature range of 200–600°C. They show some broadening of lines and preferred orientation of the crystallites, since the intensities of the peaks differ from those observed for a random powder

TABLE I. Composition of the elaborated SiC thin films at different deposition temperatures  $T_d$  as deduced from the RBS and NRA analyses.

$T_d$ (°C)	Si/C	Total H content (at. %)	Bounded H (at. %)
200	1.57	33.3	29.5
300	1.22	29.1	18.3
400	1	27.3	9.4
500	...	24.5	7.0
600	1.11	16.7	3.9

with notably the absence of the 200 reflection. The strong and anisotropic broadening of the diffracted lines is due to the anisotropic shape of the individual crystallites and the relatively large width of the lines is indicative of the presence of very small SiC crystallites. Upon decreasing  $T_d$ , the intensity of all these lines is lowered, indicating that the corresponding films are less and less crystallized or the growing crystallites are smaller and smaller. Three diffracted lines are clearly visible for  $T_d > 300^\circ\text{C}$  and can be indexed in an apparent cubic SiC unit cell named  $\beta$ -SiC ( $F\bar{4}3m$  space group). For  $T_d=200^\circ\text{C}$ , the weak signal observed could be due to some rare SiC crystallites, quite compatible with the low value of  $f_C$  ( $\sim 5\%$ ) reported above and deduced from FTIR analyses (Fig. 3). In a first step, for the refinement of these XRD spectra, we used only the  $\beta$ -SiC phase with preferential orientations and with anisotropic crystallite shapes. Discrepancies between the calculated and the experimental curves have been noticed after refinement when only  $\beta$ -SiC phase is considered. This has raised the question of the predominance of the  $\beta$ -SiC phase in our films and the possible formation of other polytypes. Among these latter, the 6H-SiC hexagonal phase ( $P6_3mc$  space group) is the most com-

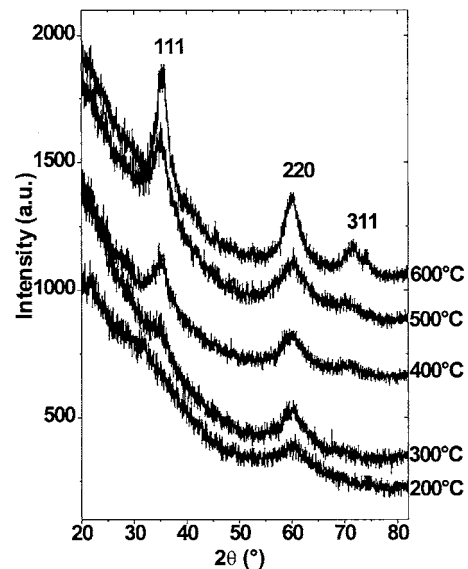


FIG. 5. Asymmetric XRD  $\omega$ -2 $\theta$  scans obtained for  $\chi=0^\circ$ , with an incident angle  $\omega=17.1^\circ$  corresponding to the Bragg angle of the 111 reflection of the 3C-SiC phase, and for thin films deposited in the temperature range of 200–600°C. The diffraction lines have been indexed using a  $\beta$ -SiC unit cell. Note, for example, for  $T_d=600^\circ\text{C}$  the anisotropic line broadening as attested by the full width at half maximum values of  $2.16^\circ$  and  $3.076^\circ$ , respectively, for the 111 and 220 reflections.

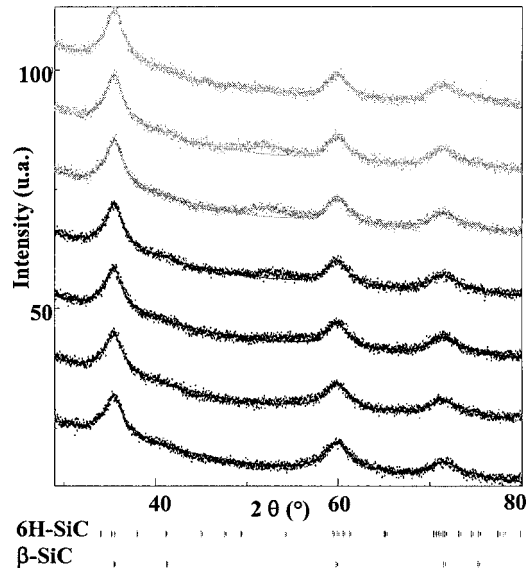


FIG. 6. Typical XRD diagram measured (dotted line) on the film deposited at  $T_d=600$  °C at different  $\chi$  positions ( $\chi=0^\circ$  at bottom and  $\chi=30^\circ$  at top,  $\Delta\chi=5^\circ$ ) showing the broad and anisotropic diffracted lines, and the corresponding simulated spectra (solid line).

monly observed and can derive from  $\beta$ -SiC via stacking faults occurring during the growth of the crystallites. The 6H-SiC polytype was, therefore, subsequently introduced with a proportion used as a refinement fitting parameter. For all samples, a good agreement between the experimental and the refined spectra can be clearly noticed in Fig. 6, as also asserted by reliability factors  $R_B$ ,  $R_w$ , and  $R_{exp}$  (Refs. 15 and 33) not exceeding 5.2% for specific proportions of 6H-SiC. For  $T_d=600$  °C, the best fitting was obtained with a proportion of 6H-SiC of about 33% and therefore a well understandable predominance of  $\beta$ -SiC. This situation is strangely inverted when  $T_d$  is decreased, since only 30% of  $\beta$ -SiC has allowed a good fitting for  $T_d=300$  °C. The relatively large proportions of 6H-SiC crystallites suggested by the XRD measurements are intriguing inasmuch as the growth of such fractions of 6H-SiC should occur at temperatures much higher than our  $T_d$  values,<sup>34</sup> unless it derives from faulted  $\beta$ -SiC as suggested above. The TEM and HRTEM observations described and commented in Sec. IV will provide more insight concerning this issue. They will also allow the comparison with the recently reported increase of the stacking faults (i.e., of the 6H-SiC refined proportion) when  $T_d$  is decreased.<sup>35</sup>

Whatever the  $T_d$  values, the  $a$  cell parameter is refined around 4.38 Å for  $\beta$ -SiC, while the  $a$  and  $c$  cell parameters for 6H-SiC were refined around 3.09 and 15.25 Å, respectively. These values are always larger than those for the counterparts bulk SiC polytypes and correspond to a mean lattice expansion of  $\Delta a/a=0.7\%$  for  $\beta$ -SiC. However, no peak shift was observed when tilting the samples in  $\chi$  (see Fig. 6), which indicates that the measured cell parameters correspond to the stress-free crystallized SiC layers. This contrasts with the stressed polycrystalline SiC layers grown at 900 °C by low-pressure CVD (LPCVD), as reported recently.<sup>36</sup> The difference would be due to the hydrogen-induced relaxation in our material, whereas the LPCVD layers are completely free from hydrogen.

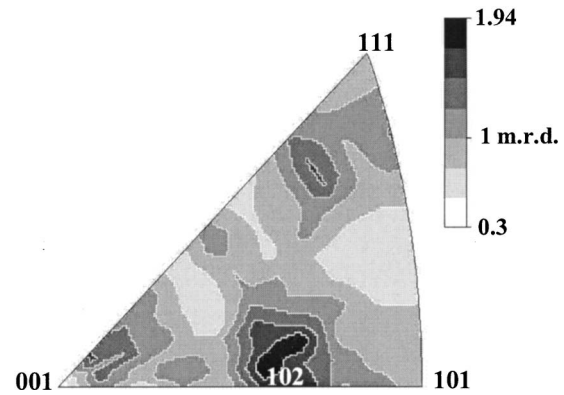


FIG. 7. 001 inverse pole figures for the film deposited at 600 °C on (100)-Si substrate. Pole locations are indicated by their Miller indices. Equal area projections, linear distribution density scale.

Thanks to the combined analysis, the mean crystallite shape for the two SiC phases was refined and corrected for texture effects. For all  $T_d$  values, the shape of the SiC crystallite corresponds to an ellipsoid elongated along the  $[111]$  direction and almost isotropic in the other directions. Such a shape has been recently evidenced by our group for a similar zinc-blende-like structure, namely, Si nanocrystals obtained by the same deposition reactive sputtering in H-rich plasma.<sup>37</sup> When the substrate temperature is increased from 300 to 600 °C, the grown SiC crystallites (6H or  $\beta$  phases) are slightly enlarged from 3 to 5 nm along the  $[111]$  direction, whereas the dimension in the perpendicular directions remains almost unchanged (mean size  $\sim 1.5$  nm).

Since we determined that the film textures are axially symmetric around the normal to the film plane (fibre textures), the inverse pole figure calculated for this normal direction 001 is a complete representation of the ODF. A typical inverse pole figure for the film deposited at 600 °C is shown in Fig. 7. A main contribution is observed around the  $\langle 102 \rangle$  texture components (reaching a  $\langle 1102 \rangle$  texture component with an orientation dispersion from  $14^\circ$  to  $20^\circ$ ). We observe also  $\langle 11\ell \rangle$  texture components with low and high  $\ell$  values (typically 2 and higher than 10, respectively). No  $\langle 111 \rangle$  and  $\langle 100 \rangle$  strong fiber textures were found as those usually observed in  $\beta$ -SiC columnar growth by CVD on (100)-Si substrate.<sup>38</sup> The observed texture strength is weak and evaluated at only four times a random powder distribution. The minimum values of the ODF are relatively high [for example, 0.3 multiples of a random distribution (mrd) at 600 °C and 0.7 mrd at 400 °C] indicating that 30%–70% of the volume of the film is randomly oriented (not textured), whereas for films deposited at higher temperatures ( $>1000$  °C), the relating values do not exceed 0.48 mrd.<sup>38</sup>

Figure 8 shows the cross-section micrographies of the films deposited at 200 (a), 300 (b), 400 (c), and 600 °C (d), while the insets display the corresponding electron-diffraction patterns (EDPs). For the lowest  $T_d$  value (200 °C) no crystallization was detected, whereas for all higher deposition temperatures ( $T_d \geq 300$  °C) numerous crystallized SiC grains can be observed. This is supported by the ring shown by the corresponding EDPs, which originates from the diffraction of the crystallized SiC, while the bright

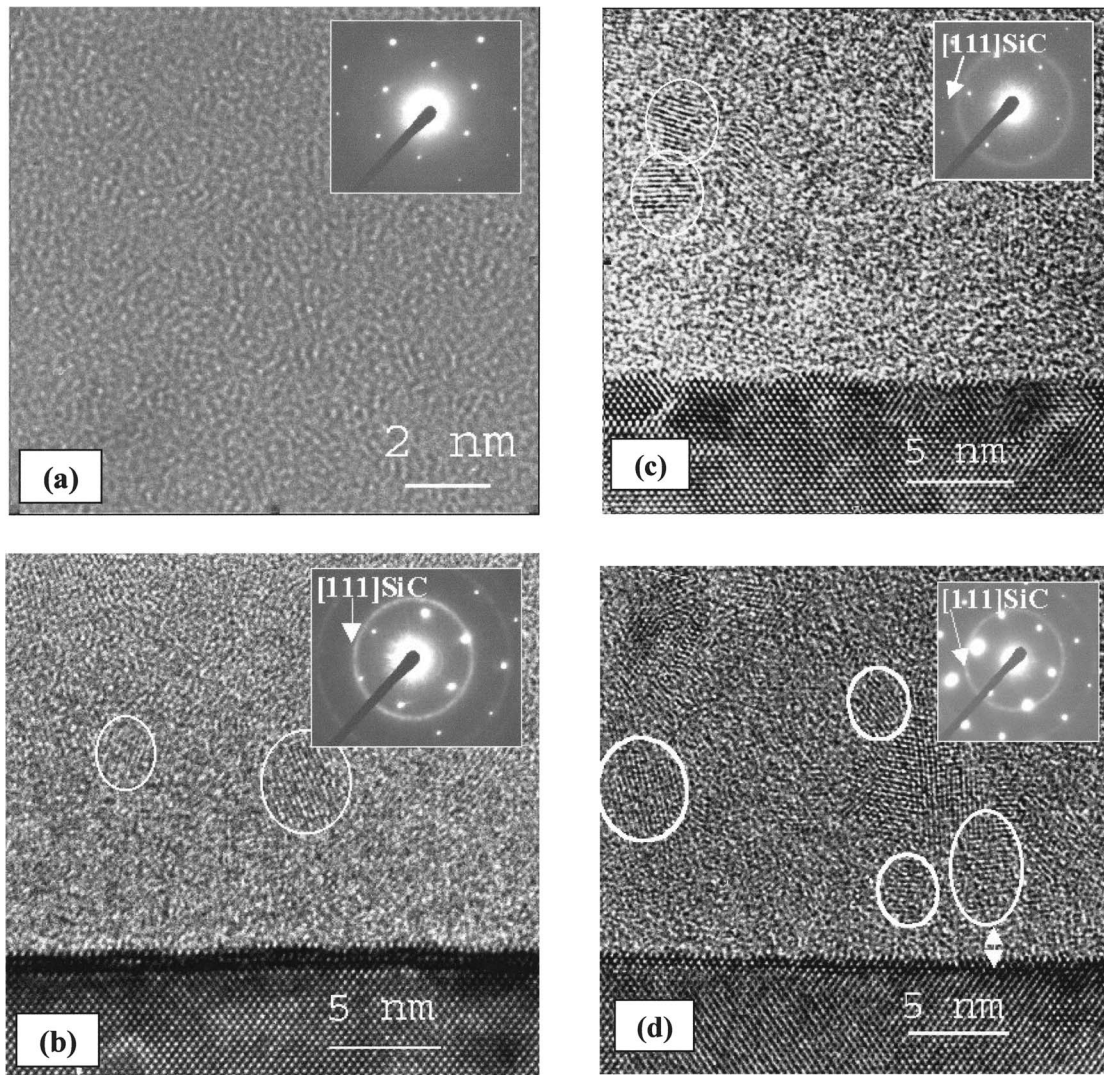


FIG. 8. Cross-sectional transmission electron micrographs for films deposited at (a)  $T_d=200$  °C, (b)  $T_d=300$  °C, (c)  $T_d=400$  °C, and at (d)  $T_d=600$  °C. In the inset, the corresponding selected area diffraction patterns.

spots are due to the electrons diffracted by the Si substrate. Most of the TEM images [Figs. 8(b)–8(d)] show the region of the film adjacent to the substrate, which is representative of the whole film since no microstructure change is observed all along the thickness. The increase with  $T_d$  of the (111) ring intensity in the EDPs is indicative of the increasing crystallization of the film between 300 and 600 °C, confirming the behavior of  $f_C$  against  $T_d$ , as described above (Fig. 3). The formation of nc-SiC is clearly evidenced by the observation of the reflecting planes for the well-oriented SiC grains. The mean grain size of the SiC nanocrystals is around 4 nm without a noticeable change with  $T_d$ , while their density increases with  $T_d$ . The substrate-film interface is flat, sharp, quite regular, and free from defects such as the cavities observed by Sun *et al.*<sup>8</sup> on similarly fabricated layers. Both nucleation and growth of nc-SiC take place at approximately 2-nm distance from the silicon substrate surface, as pointed out in Fig. 8(d) for the film deposited at 600 °C. This apparent 2-nm-thick buffer layer would represent the native oxide instead of an intermediate amorphous one as that observed for similarly deposited nanocrystalline silicon films.<sup>39</sup>

A careful observation of the HRTEM image [Fig. 8(d)] of the most crystallized film (600 °C) allows us to distinguish a columnar morphology of contiguous nc-SiC grains oriented in a direction close to the normal direction of the substrate. This columnar structure would result from the agglomeration of the [111] elongated nanograins, whose shape was evidenced by the analyses of the XRD spectra reported above. This is supported by the gradual extension of the columns with  $T_d$ , as being favored by the density rise of the grains. This is quite coherent with recent observations of highly pronounced columnar morphology for LPCVD polycrystalline SiC layers deposited at a temperature as high as 900 °C.<sup>36</sup> The most common polytypes are the  $\beta$  and 6H polytypes. In our films, the structure of the crystallized SiC can be determined by imaging the nc-SiC in  $\langle 110 \rangle$  or  $\langle 11\bar{2}0 \rangle$  orientations, depending on the cubic or hexagonal polytypes, respectively. The  $\beta$ -SiC phase with a cubic symmetry consists of the stacking of three sheets of tetrahedron along the  $\langle 111 \rangle$  direction. The stacking sequence can be denoted as  $\dots T_1 T_2 T_3 \dots$ , as illustrated by the simulated HRTEM image of a  $\beta$ -SiC crystal showing the projected atomic columns



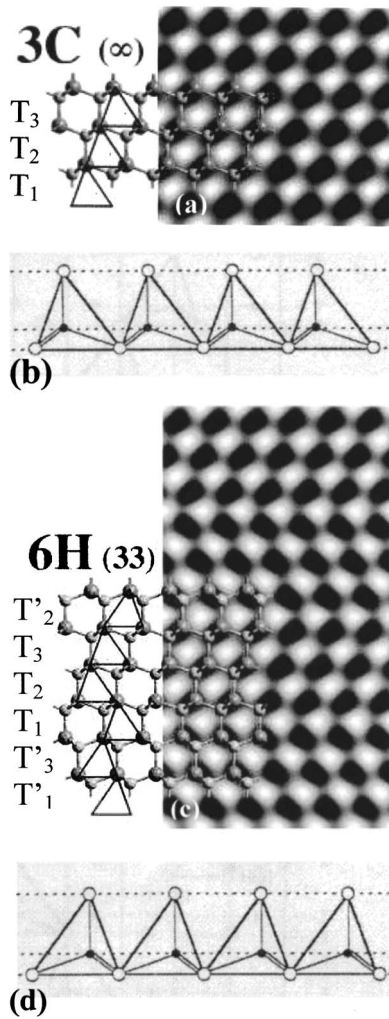


FIG. 9. HRTEM-treated images of the film elaborated at  $T_d=600^\circ\text{C}$  showing the two possible structures: (a)  $\beta$ -SiC and (c) 6H-SiC, and two sheets of tetrahedra: (b) in the  $T$  orientation and (d) in the  $T'$  orientation.

reproduced in Fig. 9(a). The crystal is observed along the  $\langle 110 \rangle$  direction. Figure 9(b) represents a sheet of tetrahedron in a  $T$  orientation following the notation introduced by Pirouz and Wang.<sup>40</sup> A similar simulated image of a 6H-SiC crystal showing the projected columns is reproduced in Fig. 9(c). Thus, in a twin orientation of  $\beta$ -SiC, the tetrahedron denoted  $T$  will be sheared in a  $T'$  orientation, as shown in Fig. 9(d). Consequently, the stacking sequence in a twinned  $\beta$ -SiC crystal can be described as

$$\dots T_1 T_2 T_3 T_1 T_2 T_3 T_2' T_1' T_3' T_2' T_1' T_3' \dots,$$

whereas the other common 6H polytype has a stacking sequence as

$$\dots T_1 T_2 T_3 T_2' T_1' T_3' \mathbf{T}_1 \mathbf{T}_2 \mathbf{T}_3 \mathbf{T}_2' \mathbf{T}_1' \mathbf{T}_3' T_1 T_2 T_3 T_2' T_1' T_3' \dots,$$

where the bold symbol of the 6H- stacking sequences represents the unit cell along the  $\langle 0001 \rangle$  direction.

From the careful observations of the HRTEM images for various  $T_d$  values, it appears clearly that, except the case of  $T_d=600^\circ\text{C}$ , the nc-SiC presents a  $\beta$ -SiC structure with the corresponding twinned variants along the  $(111)$  planes. The nanocrystal grown at  $T_d=600^\circ\text{C}$  [Fig. 10(a)] has been studied in more detail because the complexity of its stacking

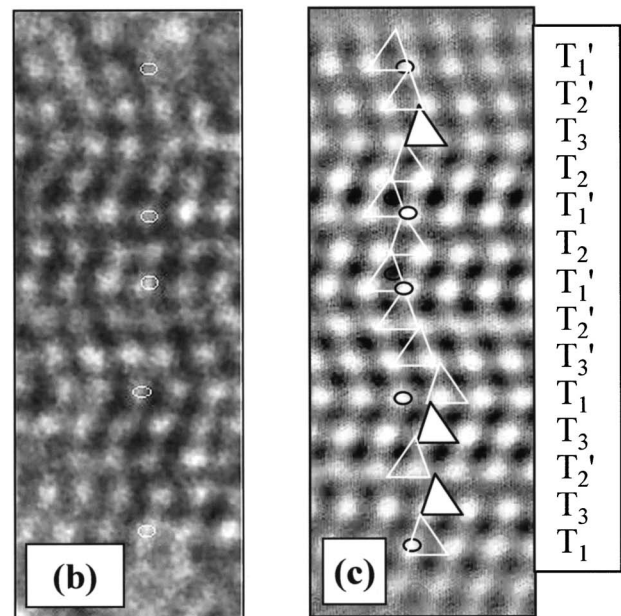
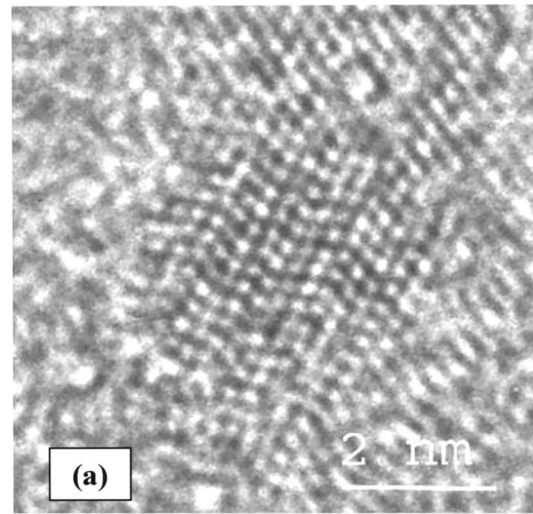


FIG. 10. (a) HRTEM image of a SiC nanograin in the film elaborated at  $600^\circ\text{C}$ , (b) with the corresponding enlarged part and (c) the filtered image and tetrahedron stacking.

sequence presents some similarity with a 6H stacking sequence. A filtered image of the experimental HRTEM observation shown in Fig. 10(b) [enlarged part of Fig. 10(a)] is reproduced in Fig. 10(c). This allowed the identification of the tetrahedron stacking sequence, as indicated in the drawing on Fig. 10(c). This sequence does not correspond to the 6H sequence but can be better understood as a highly faulted  $\beta$ -phase crystal (with twinned and multitwinned parts). Anyway, the growth of cubic SiC is not surprising since the deposition temperature did not exceed  $600^\circ\text{C}$ ,<sup>41</sup> i.e., well below the high temperature expected for the formation of other SiC polytypes.<sup>34</sup> For the earlier reported XRD refinement, it would have been interesting to introduce the faulted  $\beta$ -SiC model, instead of the used 6H phase, if such a procedure was available in the MAUD program. This point will be examined when possible.

To correlate the structural features described and commented so far to some physical properties, optical transmis-

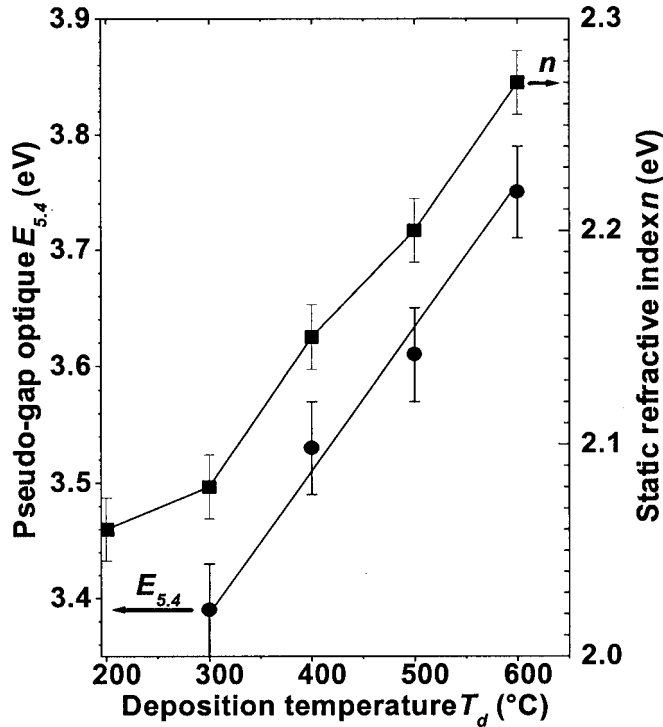


FIG. 11. Comparison of the evolution of the pseudogap  $E_{5.4}$ , deduced from the absorption coefficient spectra, and of the static refractive index,  $n$ , with the deposition temperature,  $T_d$ . The lines are only guide for the eyes.

sion measurements were carried out on our layers. From the absorption coefficients spectra  $\alpha(E)$  (not shown) we have deduced the pseudo-gap  $E_{5.4}$ , the energy at which  $\alpha=5 \times 10^4 \text{ cm}^{-1}$ , as well as the static refractive index  $n$ . We propose to examine the behavior of  $E_{5.4}$  values instead of the Tauc-gap values which could not be determined with enough reliability, owing to the extent of the valence- and conduction-band tails in the gap. Figure 11 displays the variations of both  $E_{5.4}$  and  $n$  as function of  $T_d$ . It can be seen that  $E_{5.4}$  shows a very slight increase against  $T_d$ , considering that the optical gap of hydrogenated silicon carbide is dependent of the Si/C ratio, the hydrogen content, and the crystallization degree. According to Solomon *et al.*,<sup>42</sup> the optical gap is governed, at first order, by the Si/C ratio whose variation with  $T_d$ , as reported in Table I, implies a change larger than that observed in Fig. 11. The widening of the band gap is expected to be even increasingly marked with the improvement for the layer crystallinity for  $T_d \geq 300$  °C. However, the decrease of the hydrogen content and the accompanying reduction of the microvoid density when  $T_d$  is increased should result in the shrinkage in the optical gap and might, therefore, explain the observed small changes of  $E_{5.4}$ . This counterbalancing effect of H desorption against that of Si/C is supported by the behavior of  $n$  vs  $T_d$  shown in Fig. 11. Although the increase with  $T_d$  of the density of SiC nanocrystals contributes to bring the  $n$  value closer to that of a nanocrystal, the major increase of  $n$  is mainly due to the drop of the hydrogen content, as reported earlier.<sup>11</sup> Such a drop by nearly an order of magnitude is clearly reflected by the substantial increase of  $n$  (Fig. 11) that probes somehow

the compactness of the material found to be increasingly improved by the gradual removal of the hydrogen-induced microvoids.

In principle, one can expect the quartz substrate used for OT measurements to induce some microstructural changes in the deposited film, in comparison with the layers grown on crystalline silicon. Nevertheless, the coherence between the evolution of the optical properties and the microstructural features suggests that there is a small effect related to the nature of the substrate, at least on the characteristics of the bulk part of the film, regardless of some differences on the thin buffer layer.

#### IV. CONCLUSION

This work provides a significant contribution to two main purposes: the achievement of low-temperature nanocrystalline silicon carbide layers with a competitive growth rate and the precise determination of their microstructural features by a combination of highly sophisticated and complementary techniques. Apart from the expected increasing crystallization with the deposition temperature  $T_d$ , its level was found generally improved by the significant enhancement of the growth rate, at least for high  $T_d$  values, in comparison with earlier works. The crystallization improvement with  $T_d$  was quasiexclusively reflected by an increasing density of the SiC nanocrystals whose average size remains almost constant around 4–5 nm, as attested by the various investigation techniques. Such a constancy in the nanocrystal size would be due to the multiple nucleation sites induced by the hydrides radicals interacting with the growing surface and giving, therefore, rise to some nanocrystallization. The [111] elongated SiC nanocrystals tend to agglomerate in a columnar growth structure, mainly along the  $\langle 102 \rangle$  direction for high  $T_d$  values without reaching the pure  $\langle 111 \rangle$  texture component generally observed for such a zinc-blende structure.

Finally, the intriguing question of the relatively important and non-negligible proportion of the 6H phase needed to satisfactorily simulate the x-ray diffraction data has been adequately addressed by detailed and careful analyses of the electron microscopy observations. It appeared that specific stacking faults have taken place during the growth of the SiC nanocrystals, leading to a structure which can be related to highly faulted  $\beta$ -SiC that would explain the proportion of noncubic SiC taken into account in the XRD refinement. The structure and phase modifications, in terms of crystallization degree, compactness, composition, etc., were found to be consistently correlated to the evolution of the optical properties, as reflected by the optical gap and refractive index.

<sup>1</sup>*Silicon Carbide and Related Materials*, Materials Science Forum Vols. 433–436, edited by P. Bergman and E. Jantzen (Trans Tech Publications, Switzerland, 2003).

<sup>2</sup>R. Alcubilla, D. Bardes, A. Orpella, J. Calerer, L. F. Marsal, J. Pallarès, and X. Correig, *Mater. Sci. Forum* **264–268**, 1455 (1996).

<sup>3</sup>C. Caputo, G. De Cesare, F. Irrerra, and F. Palma, *IEEE Trans. Electron Devices* **43**, 1351 (1996).

<sup>4</sup>Y.-A. Chen and C.-F. Chou, *IEEE Trans. Electron Devices* **44**, 1360 (1997).

<sup>5</sup>Y. Leconte, P. Marie, X. Portier, M. Lejeune, and R. Rizk, *Thin Solid Films* **427**, 252 (2003).

- <sup>6</sup>K. L. Cheng, H. C. Cheng, W. H. Lee, C. C. Liu, and T. R. Yew, *Appl. Phys. Lett.* **70**, 223 (1997).
- <sup>7</sup>J. Chaudhuri, X. Cheng, C. Yau, and A. J. Steckl, *Thin Solid Films* **292**, 1 (1997).
- <sup>8</sup>Y. Sun, T. Miyasato, J. K. Wigmore, N. Sonoda, and J. Watari, *J. Appl. Phys.* **82**, 2334 (1997).
- <sup>9</sup>D. G. Moon, B. H. Jung, J. N. Lee, B. T. Ahn, H. B. Im, K. S. Nam, and S. W. Kang, *J. Mater. Sci.: Mater. Electron.* **5**, 364 (1994).
- <sup>10</sup>S. Dasgupta, S. Gosh, S. T. Kshirsagar, and S. Ray, *Thin Solid Films* **295**, 37 (1997).
- <sup>11</sup>S. Kerdiles, A. Berthelot, F. Gourbilleau, and R. Rizk, *Appl. Phys. Lett.* **76**, 2373 (2000).
- <sup>12</sup>S. Kerdiles, A. Berthelot, R. Rizk, and L. Pichon, *Appl. Phys. Lett.* **80**, 3772 (2002).
- <sup>13</sup>S. Kerdiles, R. Rizk, A. Pérez-Rodríguez, B. Garrido, O. González-Varona, L. Calvo-Barío, and J. R. Morante, *Solid-State Electron.* **42**, 2315 (1998).
- <sup>14</sup>J. Ricote and D. Chateigner, *Bol. Soc. Esp. Ceram. Vidrio* **38**, 587 (1999).
- <sup>15</sup>L. Lutterotti, H.-R. Wenk, and S. Matthies, in *Textures of Materials*, edited by J. A. Szpunar (NRC Research, Ottawa, 1999), Vol. 2, p. 1599.
- <sup>16</sup>S. Matthies and G. W. Vinel, *Phys. Status Solidi B* **112**, K111 (1982).
- <sup>17</sup>N. C. Popa, *J. Appl. Crystallogr.* **31**, 176 (1999).
- <sup>18</sup>G. Amsel and D. Samuel, *Anal. Chem.* **39**, 1689 (1967).
- <sup>19</sup>V. Quillet, F. Abel, and M. Schott, *Nucl. Instrum. Methods Phys. Res. B* **83**, 47 (1993).
- <sup>20</sup>R. A. Jarjis, *Nucl. Instrum. Methods* **160**, 457 (1979).
- <sup>21</sup>G. Vizkelethy, *Nucl. Instrum. Methods Phys. Res. B* **45**, 1 (1990).
- <sup>22</sup>H. Rauscher, *Surf. Sci. Rep.* **42**, 207 (2001).
- <sup>23</sup>J.-H. Boo, S.-B. Lee, K.-S. Yu, M. M. Stung, and Y. Kim, *Surf. Coat. Technol.* **131**, 147 (2000).
- <sup>24</sup>G. Spitzer, D. A. Kleiman, and D. Walsh, *Phys. Rev.* **113**, 127 (1959).
- <sup>25</sup>M. H. Brodsky, M. Cardona, and J. J. Cuomo, *Phys. Rev. B* **16**, 3556 (1977).
- <sup>26</sup>P. I. Rovira and F. Alvarez, *Phys. Rev. B* **55**, 4426 (1997).
- <sup>27</sup>P. Musumeci, R. Reitano, L. Calcagno, F. Roccaforte, A. Mackhtari, and M. G. Grimaldi, *Philos. Mag. B* **76**, 323 (1997).
- <sup>28</sup>A. Achiq, R. Rizk, F. Gourbilleau, and P. Voivenel, *Thin Solid Films* **348**, 74 (1999).
- <sup>29</sup>S. Kerdiles and R. Rizk, *Philos. Mag. A* **82**, 601 (2002).
- <sup>30</sup>R. Dutta, P. K. Banerjee, and S. S. Mitra, *Phys. Status Solidi B* **113**, 277 (1982).
- <sup>31</sup>D. Ballutaud, P. de Mierry, J. C. Pesant, R. Rizk, A. Boutry-Forveille, and M. Aucoeur, *Mater. Sci. Forum* **83-87**, 45 (1992).
- <sup>32</sup>T. Takeshita, Y. Kurata, and S. Hasegawa, *J. Appl. Phys.* **71**, 5395 (1992).
- <sup>33</sup>R. J. Hill and R. X. Fisher, *J. Appl. Phys.* **23**, 462 (1990).
- <sup>34</sup>C. H. Carter *et al.*, *Mater. Sci. Forum* **353**, 3 (2001).
- <sup>35</sup>K. Yasui, M. Hashiba, and T. Akahane, *Appl. Surf. Sci.* **216**, 580 (2003).
- <sup>36</sup>X.-A. Fu, R. Jezeski, C. A. Zorman, and M. Mehregany, *Appl. Phys. Lett.* **84**, 341 (2004).
- <sup>37</sup>M. Morales, Y. Lecomte, R. Rizk, and D. Chateigner, *J. Appl. Phys.* **97**, 034307 (2005).
- <sup>38</sup>E. Hurtos and J. Rodríguez-Viejo, *J. Appl. Phys.* **87**, 1748 (2000).
- <sup>39</sup>F. Gourbilleau, A. Achiq, P. Voivenel, and R. Rizk, *Thin Solid Films* **337**, 74 (1999).
- <sup>40</sup>P. Pirouz and J. W. Wang, *Ultramicroscopy* **51**, 189 (1993).
- <sup>41</sup>T. Rajagopalan, X. Wang, B. Lahlouh, C. Ramkumar, P. Dutta, and S. Gangopadhyay, *Sci. Technol. Adv. Mater.* **3**, 113 (2003).
- <sup>42</sup>I. Solomon, M. P. Schmidt, and H. Tran-Quoc, *Phys. Rev. B* **38**, 9895 (1988).

# Optimization of ZnSe–SiO<sub>2</sub> nanostructures deposited by radio-frequency magnetron sputtering: Correlations between plasma species and thin film composition, structural and microstructural properties

M. Morales<sup>a,\*</sup>, N. Vivet<sup>a</sup>, M. Levalois<sup>a</sup>, J.F. Bardeau<sup>b</sup>

<sup>a</sup> Laboratoire Structure des Interfaces et Fonctionnalités des Couches Minces (SIFCOM)-ENSICAEN, 6 Bd. du Maréchal Juin, 14050 Caen, France

<sup>b</sup> Laboratoire de Physique de L'Etat Condensé, Av. O. Messiaen, 72085 Le Mans cedex 09, France

Received 21 April 2006; received in revised form 28 November 2006; accepted 5 January 2007

Available online 13 January 2007

## Abstract

ZnSe nanoparticle doped SiO<sub>2</sub> films have been grown on various substrates at different deposition temperatures, radio-frequency power, Argon pressures and substrate to target distances, by means of reactive magnetron sputtering. A detailed study of the correlations between plasma species and thin film composition, structure and morphology is investigated using X-ray reflectivity and diffraction, Raman and optical emission spectroscopies and Rutherford backscattering technique. It is evidenced that the most sensitive species in the plasma is the Selenium and that the optimal deposition parameters correspond to random stress-free films with a high content of quasi-stoichiometric ZnSe cubic nanocrystallites. A few amount of ZnSe in the hexagonal structure is also evidenced in these films. Using proper deposition parameters, the SiO<sub>2</sub>/ZnSe proportion in the films and the mean ZnSe particles size around 3 nm are easily monitored.

© 2007 Elsevier B.V. All rights reserved.

**Keywords:** Semiconductors; Nanostructures; Sputtering; Structural properties

## 1. Introduction

The synthesis of nanocrystalline (nc) or doped glass nc direct-gap semiconductors has presented in the last years a strong revival of research interest in particular for nonlinear optics and luminescent devices [1]. As the semiconductor crystal size approaches its exciton Bohr diameter, it exhibits optical properties different from those of the bulk material due to quantum size confinement [2]. It has been also shown that the isolation of the individual semiconductor nanocrystallites by a dielectric matrix offers larger and stable quantum confinement, with surface modifications that increase luminescence efficiency [3]. Among the II–VI compounds, zinc selenide (ZnSe) exhibits a large energy band gap at room temperature (about 2.7 eV) and is the most promising material for non linear optical and laser applications [4]. Indeed, doping this semiconducting structure with 3d impurities is of particular interest for laser

operation at room temperature in the 2–4 μm spectral range for biological and military applications [5].

Several deposition techniques, such as photochemical, chemical bath deposition, molecular beam epitaxy, pulsed laser and magnetron sputtering [6–13] have been used for the growth of ZnSe thin films. However, for the deposition of nc-ZnSe doped glass, the co-sputtering method offers wider parameter ranges to control the grain size, the composition, the amount and distribution of the semiconductor nanocrystals. A preliminary study by Hayashi and collaborators [14] using co-sputtering of ZnSe chips mounted on a SiO<sub>2</sub> target with an Ar pressure of 0.5 Pa, has shown that nc-ZnSe doped glass thin films can be achieved with nc-ZnSe particle sizes in the 0.4–4 nm range, depending on the chosen radio-frequency power and the substrate deposition temperature.

As many properties of interest are strongly correlated with the microstructure and texture developed during the growth process, the sputtering deposition parameters have to be optimized in order to achieve stoichiometric and uniform nc-ZnSe films, which, in a second step, will be doped 3d-impurities

\* Corresponding author. Tel.: +33 2 31 45 26 58; fax: +33 2 31 45 26 60.

E-mail address: [magali.morales@ensicaen.fr](mailto:magali.morales@ensicaen.fr) (M. Morales).

for laser applications. Consequently, in order to determine the optimal deposition parameters, we present in this paper an extensive study of the correlations between the plasma characteristics and the structure and composition of ZnSe/SiO<sub>2</sub> films deposited by magnetron sputtering. As the crystalline quality of the films (and consequently their optical properties) is strongly dependent also on the substrate selection (residual stress in the film is very important for their mechanical stability), we chose to deposit our films on different substrates such as monocrystalline [100]-GaAs for its low lattice mismatch with ZnSe (0.27%), monocrystalline [100]-Si and glass (a-SiO<sub>2</sub>) substrates.

## 2. Experimental details

The nc-ZnSe/SiO<sub>2</sub> films investigated in this study were grown using reactive magnetron sputtering of a SiO<sub>2</sub> target of 10 cm of diameter covered by ZnSe chips. The ZnSe-to-SiO<sub>2</sub> sputtered area ratio was maintained at about 30% and the substrate–target distances were fixed to 10 and 7 cm. The basic pressure of the sputtering chamber was lowered to a few 10<sup>-5</sup> Pa before introduction of the Ar gas. In order to determine the optimal deposition conditions, we firstly chose an Ar gas pressure ( $P_{Ar}$ ) of 0.5 Pa, with sputtering powers ( $P_{RF}$ ) varying in the 50–150 W range and deposition temperatures ( $T_d$ ) varying between the ambient temperature  $T_a=20$  °C to 385 °C. Secondly, the effect of  $P_{Ar}$  on the structural properties of the films has been investigated using a 4 times larger value of  $P_{Ar}$  ( $P_{Ar}=2$  Pa). During the deposition, an in-situ plasma phase characterization was performed using Optical Emission Spectroscopy (OES). The intensities of the emissive molecules and radicals in the plasma, measured in the 100–900 nm range with an accuracy of 1 nm, were collected by an optical fiber coupled to a multiple channel spectrometer.

The thickness of the deposited layers was measured by profilometry or by X-ray reflectivity (XRR) for the thinnest films deposited at  $P_{RF}=50$  W. They have been found in the 50–5000 nm range. For XRR, we used a Philips X-Pert MRD diffractometer at the average Cu K<sub>α</sub> radiation ( $\lambda_{Cu}=0.15418$  nm) equipped with a point scintillator detector. To refine the XRR data and extract in particular the critical wave vector  $q_c$  of the films, we used the Reflex program [15] using the Fresnel formalism and sample and beam size corrections, with a  $q_z$  resolution of 0.0006 Å<sup>-1</sup>. An off-specular reflectivity scan was performed in order to check that no any significant diffusion signal was present in the specular scan. With the used diffractometer, the theoretical thickness range accessible by the refinement of the XRR spectra (i.e. only taking into account the diffractometer angular resolution) is 2–314 nm. The corresponding refined thicknesses are with a resolution of 1 nm. By profilometry, the thicknesses are measured with a resolution of 10 nm for thicknesses higher than 100 nm (when the surface of the films exhibit low roughness) and good accuracy between these profilometry measured and XRR refined thicknesses in the 100–300 nm range has been found.

In order to correlate the film composition to the plasma species, a rapid control of the composition of the films de-

posited on Si and GaAs substrates has been operated by Energy Dispersive X-ray (EDX) analyses, accessing only the composition of the first 1.3 μm of the films. A more precise determination of the composition of these films was determined by Rutherford Back-Scattering analysis (RBS) using the Van de Graaf accelerator of the Groupe de Physique des Solides (University of Paris 6 and 7, France). RBS spectra were acquired with a 2 MeV incident beam of <sup>4</sup>He ions for 5 μC of incident charge. The detector was positioned at 165° in the horizontal plane containing the beam axis, and the solid angle was determined using a Bi-implanted silicon reference sample. These RBS spectra were fitted using the RUMP simulation program [16].

The structural and microstructural characterizations were made by Raman Spectroscopy and X-ray diffraction (XRD). The Raman spectra were recorded from 70 to 500 cm<sup>-1</sup> with a T64000 Jobin-Yvon multi-channel spectrometer with a triple subtractive configuration allowing a 0.7 cm<sup>-1</sup> resolution and equipped with a cooled CCD detector. An Argon–Krypton laser ( $\lambda_{Ar-Kr}=514.532$  nm) with about 20 mW power (on the sample) is used for the excitation. For the  $\omega$ -2 $\theta$  XRD experiments we used a Huber 4-circles diffractometer at the average Cu K<sub>α</sub> radiation ( $\lambda_{Cu}=0.15418$  nm) and a curved position sensitive detector (INEL CPS 120), which spans a 120° range in 2 $\theta$ . The incident X-ray beam was fixed to  $\omega=13.65^\circ$  corresponding to the Bragg angle of the 111 reflection of the cubic Zinc Selenide phase. In order to check if the films exhibit or not a texture, we measured XRD spectra by scanning, using 5° steps, the tilt angle of the goniometer,  $\chi$ , in the range 0–55° and the azimuthal angle,  $\varphi$ , in the range 0–360° [17].

## 3. Results and discussion

### 3.1. Determination of the optimal deposition parameters

In order to determine the optimal deposition parameters corresponding to thin films with a maximum proportion of stoichiometric nc-ZnSe doped SiO<sub>2</sub>, the correlations between the plasma and the resulting film composition as deduced by EDX analyses have been firstly studied. Table 1 summarizes the atomic lines and molecular bands that have been preferentially studied whatever the deposition conditions by OES, on the basis of the following criteria: intensities as high as possible and no interference with other lines, in particular with the strong Ar related lines. The literature values for these wavelengths have been taken from Ref. [18]. In Table 2 the composition of the deposited films as deduced from EDX analyses and the measured intensity in the plasma of chosen Zn and Se radical lines are given.

In order to optimize the substrate temperature  $T_d$ , the correlations between plasma characteristics and composition

Table 1  
Lines that have been preferentially observed for the OES observations

Species	Se	Zn	Se+Zn	SiO <sub>2</sub>	O	Si				
$\lambda$ (nm)	199	893	209	621	206	447	777	822	505	702

Table 2  
Evolution with the different probed deposition parameters of the Se and Zn optical emission lines and of the composition of the films deposited on Si and GaAs substrates, as deduced from EDX analyses

$P_{Ar}$	$d$	$P_{RF}$	$T_d$ (°C)	Substrate	EDX						OES lines (arb. units)			
					% Zn	% Se	% O	% Si	Si/O	Se/Zn	Se	Zn		
0.5 Pa	10 cm	50 W	$T_a$	Si	0.77	–	17.99	81.25	–	–	–	–		
				GaAs	4	–	15.63	80.47	0.19	–	–	–		
			100 W	115	Si	0.49	–	16.9	82.61	–	–	261	60	
					GaAs	3.8	–	14.25	81.95	0.17	–	–	–	
				215	GaAs	1.89	–	16.51	81.6	0.20	–	285	83	
					GaAs	1.85	–	15.02	83.13	0.18	–	309	97	
					GaAs	1.64	–	17.55	80.81	0.22	–	359	72	
					$T_a$	Si	21.32	9.92	49.23	19.525	–	0.47	–	–
						GaAs	27.94	12.63	59.42	11.59	0.20	0.45	–	–
						GaAs	24.42	16.58	44.03	14.96	0.34	0.68	338	118
		GaAs	12.73	9.27		63.88	14.11	0.22	0.73	386	126			
		150 W	315	GaAs	6.36	11.82	66.77	15.05	0.23	1.86	436	174		
				GaAs	3.57	1.91	76.03	18.49	0.24	0.54	430	171		
			$T_a$	Si	26.16	20.81	30.72	22.31	–	0.79	–	–		
				GaAs	25.18	24.72	34.5	15.2	0.44	0.98	–	–		
				Si	24.3	24.64	34.79	16.28	–	1.01	275	83		
				GaAs	32.45	24.64	31.4	10.7	0.34	0.76	–	–		
				Si	18.83	21.18	39.95	20.05	–	1.12	276	96		
				GaAs	19.73	22.11	39.27	18.88	0.48	1.12	–	–		
				Si	8	7.62	47.88	36.54	–	0.95	286	87		
GaAs	7.66			9.01	58.75	24.57	0.41	1.17	–	–				
Si	2.19	0.31	43.72	53.79	–	0.14	336	97						
GaAs	3.88	1.62	71.8	22.7	0.32	0.41	–	–						
2 Pa	10 cm	50 W	$T_a$	Si	1.16	0.66	15.67	82.61	–	0.57	269	97		
				GaAs	5.48	10.53	76.04	7.83	0.10	1.92	–	–		
			100 W	115	Si	0.49	–	12.42	87.09	–	–	443	174	
					GaAs	4.76	–	81.1	14.14	0.17	–	–	–	
				215	GaAs	4.5	–	80.23	15.23	0.19	–	472	172	
					Si	15.48	10.67	33.98	39.88	–	0.69	211	76	
					GaAs	22.11	20.17	50.64	7.08	0.14	0.91	–	–	
					Si	23.56	16.92	25.39	34.13	–	0.72	237	79	
					GaAs	30.61	27.79	34.56	7.03	0.20	0.91	–	–	
					Si	0.65	–	27.38	71.97	–	–	303	103	
		150 W	215	GaAs	29.94	18.54	43.92	7.59	0.17	0.62	–	–		
				Si	41.21	29.57	24.6	4.63	0.19	0.72	406	148		
			$T_a$	GaAs	40.85	30.18	24.28	4.7	0.19	0.74	–	–		
				Si	40.7	30.46	24.46	4.43	0.18	0.75	425	196		
				GaAs	41.95	30.62	22.76	4.66	0.20	0.73	–	–		
				Si	40.9	20.99	32.07	6.05	0.19	0.51	343	129		
				GaAs	43.32	22.67	28.82	5.2	0.18	0.52	–	–		
				115	Si	1.93	0.54	24.1	73.43	–	0.28	341	113	
					GaAs	7.69	7.29	74.84	10.18	0.14	0.95	–	–	
				100 W	115	Si	1.62	0.05	25.18	73.15	–	0.03	321	101
GaAs	6.51	2.29	81.28			9.92	0.12	0.35	–	–				
$T_a$	Si	1.1	0.03		19.82	79.05	–	0.02	288	92				
	GaAs	5.28	1.89		79.74	13.09	0.16	0.36	–	–				
	Si	44.77	36.38		16.7	2.15	0.13	0.81	342	109				
	GaAs	45	36.12		16.67	2.23	0.13	0.80	–	–				
	Si	43.78	30.34		23.08	2.8	0.12	0.69	360	111				
	GaAs	43.51	31.45		22.53	2.5	0.11	0.72	–	–				
	Si	43.44	21.8		30.9	3.86	0.12	0.50	298	75				
	GaAs	46.37	24.62		25.53	3.47	0.14	0.53	–	–				
150 W	$T_a$	Si	42.5	37	16.25	4.25	0.26	0.87	406	164				
		GaAs	42.06	36.59	17.32	4.03	0.23	0.87	–	–				
	115	Si	40.8	37.1	17.72	4.38	0.25	0.91	320	133				
		GaAs	41.65	37.21	16.85	4.30	0.26	0.89	–	–				
		Si	41.83	34.98	18.57	4.62	0.25	0.84	276	116				
		GaAs	43.27	35.81	17.49	4.42	0.25	0.83	–	–				

The film thicknesses probed with EDX are around 1.3  $\mu\text{m}$ . The errors on the EDX percentage and on the OES measured intensity lines are respectively at maximum of 0.06% and of 30 (arbitrary unit).

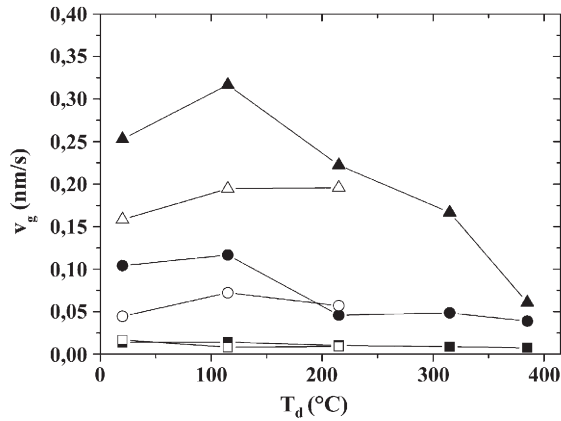


Fig. 1. Evolution of the growth rate  $v_g$  with the deposition temperature  $T_d$  in the  $T_a$ –385 °C and  $T_a$ –215 °C ranges for the films deposited at  $d=10$  cm with respectively  $P_{Ar}=0.5$  Pa (solid symbols) and 2 Pa (open symbols), and for various  $P_{RF}=50$  W (squares), 100 W (circles) and 150 W (triangles). Lines are only guide for the eyes.

and thicknesses of the films have been studied for films deposited firstly with  $P_{Ar}=0.5$  Pa,  $d=10$  cm and with  $T_d$  and  $P_{RF}$  varying respectively in the  $T_a$ –385 °C and 50–150 W ranges. The dependence of the growth rate  $v_g$  against the deposition temperature  $T_d$  is shown on Fig. 1. These  $v_g$  values have been deduced from the film thicknesses measured by profilometry with an accuracy of 10 nm for the thickest films deposited at  $P_{RF}=100$  and 150 W, and refined by reflectivity, with an accuracy of 1 nm, for the thinnest films deposited at  $P_{RF}=50$  W. Whatever  $P_{RF}$ ,  $v_g$  is maximum for  $T_d=115$  °C and for  $P_{RF}=50$  W the increase of the temperature between  $T_a$  to 385 °C leads to a  $v_g$  decrease by a factor 2. This trend is accentuated for  $P_{RF}=100$  W and 150 W for which  $v_g$  is divided by a factor 2.7 and 4 respectively. For  $P_{RF}=50$  W, the Se and O species of the plasma are maximum at  $T=385$  °C (Table 2) whereas for Si (not shown in Table 2) and Zn species it is respectively at  $T_a$  and 315 °C. The corresponding EDX analyses (Table 2) reveal that there is no Se and that few quantities of Zn (4% at maximum) are incorporated in the films. The increase of  $T_d$  leads also to a strong decrease of the Zn content in the films. Whatever  $T_d$ , the films are constituted by 80% of silicon. The Zn, Si and Se radicals of the plasma are maximum at  $T=385$  and 315 °C respectively for  $P_{RF}=100$  and 150 W, while for the O content (not shown in Table 2) it is at 315 °C and 215 °C respectively. With higher  $P_{RF}$ , the EDX analyses reveal that the Se and Zn species are better incorporated in the films. The

noticeable differences observed when  $P_{RF}$  is increased between 100 and 150 W concern the quantity of Se in the films, which is increased by a factor of 2 for instance at  $T_d=T_a$ . As observed for  $P_{RF}=50$  W, the  $T_d$  increase leads to a strong decrease of the Zn and Se contents in the films whereas the Si and O concentrations increase. This Se deficiency at temperatures larger than 250 °C has been also observed in ZnSe thin films grown by an evaporation technique [9]. In addition the deposited films in which the maximum values of the Se/Zn ratio are found, at about 1.86 and 1.17 respectively for  $T_d=315$  °C and  $P_{RF}=100$  and 150 W, exhibit small amounts of ZnSe (around 17%). The refined  $q_c$  values of the films (Table 3), as deduced by reflectivity, reached progressively with the increase of  $T_d$ , values that are closed to the one of a quasi-pure SiO<sub>2</sub> phase ( $q_c$  SiO<sub>2</sub>=0.0294 Å<sup>-1</sup>). According to the plasma species composition, it seems that higher  $T_d$  values favored the formation of a SiO<sub>2</sub> phase in our films.

It is well known that semiconductor films deposited by sputtering techniques at low substrate temperatures are characterized by high structural defect densities in comparison with films deposited at larger temperatures which exhibit a structure closer to the one of the bulk material target. However, the increase of the substrate temperature can lead to a lack in the film composition of some volatile constituents. For pressures of 0.1 Pa, the selenium and the zinc vapor temperatures are respectively 170 and 250 °C [19] and whatever the chosen  $P_{RF}$  values, these species are found maximum in the plasma for  $T \geq 315$  °C. As suggested by the temperature dependent growth rate  $v_g$ , we can consider a growth film mechanism via an adsorbed layer [20]: in this model, species from the plasma impinging onto the growing film surface are adsorbed and can either diffuse on the surface to find an open bond to be chemisorbed or can return to the gas phase via thermal desorption. In our case, it seems that for substrate temperatures higher than 115 °C and whatever  $P_{RF}$ , the Se and Zn thermal desorption is too rapid to let the species reach the chemisorption sites, leading to a growth rate decrease. The same trend has been observed with the growth of ZnSe by molecular beam epitaxy where Se and Zn desorption increase abruptly for thin films deposited with a GaAs substrate temperature of 350–400 °C [21,22]. The optimum growth temperature for ZnSe layers with this technique and by pulsed laser deposition [23] has been found respectively for substrate temperatures of 260–280 °C and 300 °C.

For  $T_d < 215$  °C, the increase of the radio-frequency power to 100 W and 150 W leads to  $v_g$  values increased by a factor 8 and

Table 3

Evolution with the different probed deposition parameters of the refined critical wave vector  $q_c$  as deduced from XRR refinement, for the films deposited onto a-SiO<sub>2</sub> substrates

$q_c$ (Å <sup>-1</sup> )	$P_{Ar}=0.5$ Pa and $d=10$ cm					$P_{Ar}=2$ Pa and $d=10$ cm			$P_{Ar}=2$ Pa and $d=7$ cm			
	$T_a$	115	215	315	385	$T_a$	115	215	$T_a$	115	215	
$P_{RF}$ (W)	50	0.0349 (2)	0.0338 (5)	0.0325 (2)	0.0322 (1)	0.0326 (5)	0.0372 (3)	0.0358 (2)	–	0.0384 (1)	0.0369 (4)	0.0363 (2)
	100	0.0394 (1)	0.038 (1)	0.0378 (4)	0.0373 (2)	0.030 (1)	0.0405*	0.0407 (2)	0.0426 (1)	0.0410*	0.04137*	0.04174 (2)
	150	0.0398 (2)	–	0.0375 (1)	–	0.0324*	–	–	0.0424 (1)	0.04051*	0.04207*	0.04121*

When the film is constituted by two layers with different thicknesses, the  $q_c$  values given in this table (marked by the \* symbol) are the corresponding level-headed average values. Numbers in parentheses represent errors on the last digit.

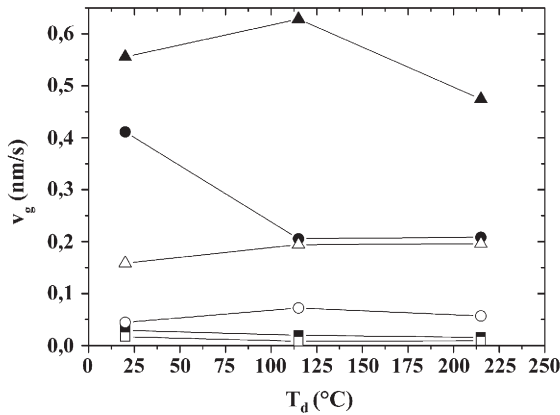


Fig. 2. Evolution of the growth rate  $v_g$  with the deposition temperature  $T_d$  in the  $T_a$ –215 °C range for films deposited at  $P_{Ar}$ =2 Pa for inter-electrode distances  $d$  of 10 cm (open symbols) and 7 cm (solid symbols) and for  $P_{RF}$ =50 W (squares), 100 W (circles) and 150 W (triangles). Lines are only guide for the eyes.

20 respectively and to higher Zn and Se percentage content in the corresponding films. Higher growth rates ( $v_g \times 90$ ) are achieved compared to the ones obtained for films deposited at ambient temperature by the same technique in the same conditions by other authors [13]. The EDX analyses reveal also that for  $T_d \leq 215$  °C the films are constituted of a maximum Zn and Se percentage with Se/Zn ratios around 1. The refined  $q_c$  values are higher than those determined for  $P_{RF}$ =50 W with intermediate

values between the ones of ZnSe ( $q_c$  ZnSe=0.0445 Å<sup>-1</sup>) and SiO<sub>2</sub> (Table 3). The increase in  $T_d$  leads to a decrease of the  $q_c$  values, which reach values close to the one of SiO<sub>2</sub> as also observed at  $P_{RF}$ =50 W (Table 3). The increase of  $P_{RF}$  leading to a higher ionization of the Ar gas is responsible of a higher number of ejected species from the target. The incident energy of these high energetic ions will contribute also to the surface migration precursors on the film surface towards the chemisorption site, limiting thus the Zn and Se species desorption previously observed for  $P_{RF}$ =50 W. For higher  $T_d$  values, this effect is attenuated as the thermal desorption becomes more efficient. As a consequence we observed smaller  $v_g$  and Se and Zn contents in the corresponding films, whereas the deposition of Si and O is favored as asserted by the decrease of the corresponding  $q_c$  values.

According to these results and in order to study the correlations between the plasma and the film composition at different  $P_{Ar}$  (0.5 and 2 Pa),  $P_{RF}$  (50, 100 and 150 W) and  $d$  (10 and 7 cm) values, we chose to limit  $T_d$  to values lower than 215 °C. For  $d$ =10 cm and with an argon pressure  $P_{Ar}$  multiplied by a factor 4,  $v_g$  is generally significantly decreased (Fig. 1) except for  $P_{RF}$ =50 W and  $T_d=T_a$ , and for  $P_{RF}$ =100 W and  $T_d$ =215 °C. During sputtering, the increase in working pressure  $P_{Ar}$  reduces the mean free path of the sputtered particles, due to the increase of their probability collision with the other species in the plasma. The resulting partial energy loss of these species

Table 4  
For the films deposited with  $P_{Ar}$ =2 Pa and  $d$ =7 cm, refined RBS compositions and average 111  $D$ -sizes as deduced by XRD experiments using the Debye–Scherrer formula for  $P_{RF}$ >50 W

$P_{RF}$	$T_d$ (°C)	Substrate	Layer	thickness (nm)	RBS					RX D size (nm)
					Composition					
					% Zn	% Se	% O	% Si	Se/Zn	
50 W	$T_a$	Si	Top	25	61.9	4.3	13.0	20.7	0.07	/
			bottom	170	23.2	5.3	58.0	13.5	0.23	/
		GaAs	top	48	11.9	16.7	59.5	11.9	1.4	/
			bottom	168	27.3	4.5	45.5	22.7	0.16	/
	115	Si	/	170	22	3.0	58	17	0.14	/
			GaAs	/	169	19	4.0	59.9	17.1	0.21
	215	Si	top	85	19	2.2	57.1	21.7	0.12	/
			bottom	62	19.6	6.4	53.8	20.2	0.33	/
	GaAs	top	17	14	15.9	46.7	23.4	1.13	/	
		bottom	130	17.3	3.2	53.0	26.5	0.18	/	
100 W	$T_a$	Si	/	/	44	41	/	/	0.93	2.36 (2)
		GaAs	/	/	45	39	/	/	0.87	2.19 (2)
		a-SiO <sub>2</sub>	/	/	–	–	/	/	–	1.98 (6)
	115	Si	/	/	44	33	/	/	0.75	1.68 (2)
		GaAs	/	/	45	33.5	/	/	0.74	1.59 (3)
	215	Si	/	/	46	28	/	/	0.61	1.62 (3)
GaAs		/	/	42	26	/	/	0.62	1.54 (3)	
150 W	$T_a$	Si	/	/	47	44	/	/	0.94	2.07 (2)
		GaAs	/	/	44	44	/	/	1	1.98 (2)
		a-SiO <sub>2</sub>	/	/	–	–	/	/	–	1.73 (1)
	115	Si	/	/	45	39	/	/	0.87	2.33 (4)
		GaAs	/	/	42.5	39	/	/	0.92	2.41 (2)
	215	a-SiO <sub>2</sub>	/	/	–	–	/	/	–	1.96 (2)
		Si	/	/	45	37	/	/	0.82	2.88 (3)
		GaAs	/	/	44.3	37.97	/	/	0.86	2.60 (3)
	a-SiO <sub>2</sub>	/	/	–	–	/	/	–	2.42 (2)	

Numbers in parentheses represent errors on the last digit.



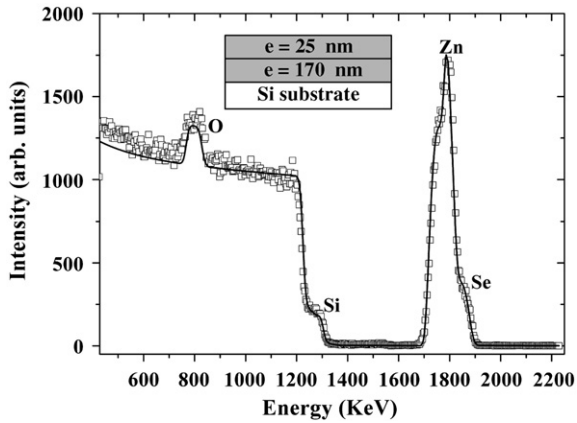


Fig. 3. RBS experimental spectrum (open squares) for the film deposited on Si substrate at  $P_{RF}=50$  W, at  $T_d=T_a$ , with  $d=7$  cm and the associated RUMP fit (solid line) exhibiting two layers of different compositions (done in Table 4).

decreases their ability to reach the substrate surface and reduces  $v_g$ . However, both EDX analyses (Table 2) and  $q_c$  values (Table 3) reveal that with increasing  $P_{Ar}$  more ZnSe is incorporated in the films. In the plasma, Zn and Se species are maximum for  $T_d=215$  °C with  $P_{RF}=50$  W and 100 W, and for  $T_d=115$  °C with  $P_{RF}=150$  W. The Zn content of the films is observed maximum at  $T_a$  for  $P_{RF}=50$  W, at 115 °C for  $P_{RF}=100$  W and remains almost constant in temperature for  $P_{RF}=150$  W. For the Se content, it is maximum for  $T_d=T_a$  at  $P_{RF}=50$  W and for  $T_d=115$  °C at  $P_{RF}=100$  and 150 W. Se is the most temperature sensitive species particularly for lower  $P_{RF}$  values. For  $P_{RF}=150$  W, as the Se species in the plasma are more energetic, the previously evidenced thermal desorption appears strongly reduced.

For the same  $P_{Ar}$  value of 2 Pa but with a substrate–target distance  $d=7$  cm, and whatever  $P_{RF}$ ,  $v_g$  is increased respectively by a factor of 2 for  $P_{RF}=50$  W and by a factor of 3 for  $P_{RF}=100$  and 150 W (Fig. 2) in comparison with  $d=10$  cm. Much higher growth rate can be achieved by magnetron sputtering ( $v_g=0.628$  nm  $s^{-1}$  at maximum) in comparison with other deposition technique in which  $v_g$  values of 0.172 nm  $s^{-1}$  and 0.033 nm  $s^{-1}$  have been found respectively by pulsed laser deposition [11] and by physical vapor technique [8]. We observed also for this closer distance that more Zn and Se are incorporated in the films as deduced by EDX and reflectivity analyses. With a lower  $d$  distance, there is in the plasma less probability for the sputtered atoms to collide with other species leading that more sputtered species with enough energy can reach the substrate, favoring the growth of the film. In the plasma, whatever  $P_{RF}$  the Zn and Se species are found maximum at ambient substrate temperature and the same trend is observed for the Se content of the corresponding films. The Zn content is also maximum at  $T_a$  for  $P_{RF}=50$  W whereas it remains almost constant with  $T_d$ , around 43%, at  $P_{RF}=100$  and 150 W.

According to these results, the best deposition conditions that lead to the highest Se and Zn contents, Se/Zn ratio, and  $q_c$  values in the corresponding SiO<sub>2</sub>/ZnSe films are  $P_{Ar}=2$  Pa and  $d=7$  cm.

### 3.2. Compositional and structural properties of the films deposited at $P_{Ar}=2$ Pa and $d=7$ cm for various $P_{RF}$ and $T_d$ values

The RBS analyses of the corresponding films (Table 4) show that, as previously observed, the most sensitive species to the temperature at  $d=7$  cm is the selenium. As the films deposited at  $P_{RF}=100$  and 150 W are too thick, we cannot access their Si and O contents. For  $P_{RF}\geq 100$  W the film exhibits a homogenous composition in thickness whereas for  $P_{RF}=50$  W, two layers are necessary for the fit of the RBS spectra (Table 4). As shown in Fig. 3 for the film deposited at  $P_{RF}=50$  W and  $T_a$  on Si substrate, the refined thinner top layer (around 25 nm) presents a large excess of Zn with a Se/Zn ratio four times lower compared to the one of the thicker layer at the interface of the substrate (Table 4). Quasi-stoichiometric ZnSe films can be achieved for  $P_{RF}\geq 100$  W and the  $q_c$  values around 0.042  $\text{\AA}^{-1}$  for the corresponding films deposited at  $d=7$  cm (Table 3), are close to the one of the bulk ZnSe ( $q_c=0.0445$   $\text{\AA}^{-1}$ ). If we consider that the films are constituted by a  $p$  percentage of ZnSe, the  $q_c$  values determined by reflectivity is a level-headed average between the  $q_c$  values of ZnSe and SiO<sub>2</sub>:  $q_c \text{ refined} = p q_c \text{ ZnSe} + (1-p) q_c \text{ SiO}_2$ . For  $P_{RF}=150$  W, whatever  $T_d$ , and 100 W for  $T_d>T_a$ , we found a SiO<sub>2</sub> percentage in the film in the 17–26% range.

However, for this closest distance ( $d=7$  cm), even for  $P_{RF}=100$  W and 150 W and whatever  $T_d$  (except for  $T_d=215$  °C at 100 W), our reflectivity refinements reveal that the films are constituted by 2 layers (Table 3). A thin layer on the top of the films is observed (in the 3–9 nm range) with lower  $q_c$  values in comparison with the one corresponding to the thickest layer at the interface with the substrate (Table 5). The corresponding surface and interface roughness are higher when  $P_{RF}$  is increased between 100 and 150 W, reaching a maximum value of 7.21 nm at  $T_d=T_a$  and 1.37 nm at  $T_d=215$  °C respectively (Table 5). The conjunction of the increase in sputtered species flux, resulting from the increase of  $P_{RF}$ , of the high deposition rate and the very close distance between the target and the substrates seems to be responsible for the inhomogeneity and the high surface roughness of the resulting

Table 5

Refined  $q_c$ , thickness and roughness values as deduced from XRR experiments for the inhomogeneous films deposited with  $P_{Ar}=2$  Pa and  $d=7$  cm on a-SiO<sub>2</sub> and [100]-Si substrates (for  $P_{RF}=100$  W only)

$P_{RF}$ (W)	Substrate	$T_d$ (°C)	$q_{c1}$ ( $\text{\AA}^{-1}$ )	$q_{c2}$ ( $\text{\AA}^{-1}$ )	$e_2$ (nm)	$r_{\text{interface}}$ (nm)	$r_{\text{surface}}$ (nm)
100	a-SiO <sub>2</sub>	115	0.04168 (2)	0.03705 (5)	4.0 (3)	0.21 (5)	1.27 (3)
	[100]-Si		0.04145 (5)	0.0377 (1)	9.9 (2)	0.41 (7)	1.39 (1)
150	a-SiO <sub>2</sub>	$T_a$	0.04051 (1)	0.03946 (6)	2.7 (2)	0.59 (1)	7.21 (2)
		115	0.04207 (1)	0.04143 (5)	8.7 (1)	0.89 (2)	4.06 (5)
		215	0.04122 (5)	0.03992 (2)	4.9 (2)	1.37 (5)	2.22 (7)

The thin top and the thick bottom layers on the substrate are named respectively 2 and 1. When 2 layers are present on the substrate,  $r_{\text{interface}}$  represents the interface roughness between these two layers. As the bottom layer of the deposited films are too thick (>1440 nm), this thickness and the substrate-bottom layer roughnesses are not accessible by XRR. Numbers in parentheses represent errors on the last digit.

films. However, the increase of the substrate temperature leads to a reduction at  $P_{RF}=150$  W to about 5 nm of the surface roughness, as it has been yet observed by atomic force microscopy for films deposited by brush plating technique [24].

Whatever the used substrates and with  $P_{RF}>50$  W, we find identical refined  $q_c$  values (Table 5), showing that the proportion of ZnSe incorporated in the film seems to be independent of the chosen substrate. Quasi-identical composition of the films deposited on GaAs or a-SiO<sub>2</sub> are found using RBS (Table 4). At  $P_{RF}=50$  W, the films deposited on GaAs exhibit higher Se/Zn values than the ones deposited on Si substrates and we observe a more pronounced tendency to a Zn excess in the formers.

Whatever the chosen substrate, the presence of a cubic ZnSe structure in the films deposited with  $P_{Ar}=2$  Pa and  $d=7$  cm has been asserted by Raman spectroscopy. The comparison of the micro-Raman spectra of the 50 W deposited thin film at  $T_a$  (Fig. 4) and a ZnSe reference powder allowed the identification of the ZnSe longitudinal optical (LO) phonon mode ( $255\text{ cm}^{-1}$ ) that coincides with the one of the ZnSe powder. No ZnSe transversal optical (TO) phonon mode ( $210\text{ cm}^{-1}$ ) is visible as also observed in vapor phase deposited polycrystalline ZnSe nanoparticles [25]. The ZnSe LO mode of the film deposited at  $T_a$  is asymmetrically broadened for the lower values of the Raman shift, which is a characteristic of the presence of small particle sizes [26,27]. Two extra Raman modes observed at  $305$  and  $432\text{ cm}^{-1}$  are also present (Fig. 4). According to the excess of Zn and O in this film found by RBS, these two modes can be attributed to the ZnO structure [28]. With an increase of the substrate temperature to  $215\text{ }^\circ\text{C}$  (Fig. 4), a change in the structure of the film with favored ZnO modes is observed with a strong vanishing of the ZnSe LO mode due to the lack of Se in the film. Whatever the chosen substrate, with higher  $P_{RF}$  values (100 and 150 W), these extra modes attributed to ZnO are not present (Fig. 5) and the four Raman modes observed at  $500.1\text{ cm}^{-1}$  (2LO),  $255.0\text{ cm}^{-1}$  (LO),  $212.6\text{ cm}^{-1}$  (TO),  $167.0\text{ cm}^{-1}$  (2 Transversal Acoustic (2TA)) are the signature of a ZnSe cubic structure [29]. The 2TA+TO at  $270\text{ cm}^{-1}$  is not

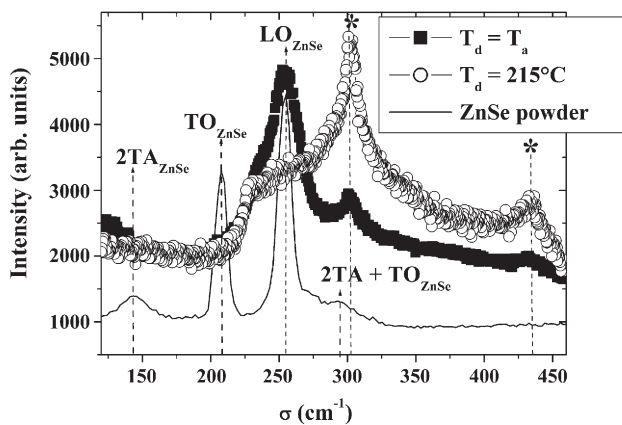


Fig. 4. Raman spectra of films deposited at  $P_{RF}=50$  W with  $d=7$  cm at  $T_d=T_a$  (solid squares) and at  $T_d=215\text{ }^\circ\text{C}$  (open circles) compared to the one of a ZnSe powder (solid line). The change of the ZnSe structure in a ZnO one is clearly visible for  $T_d>T_a$  and the \* symbol marks the position of the ZnO modes.

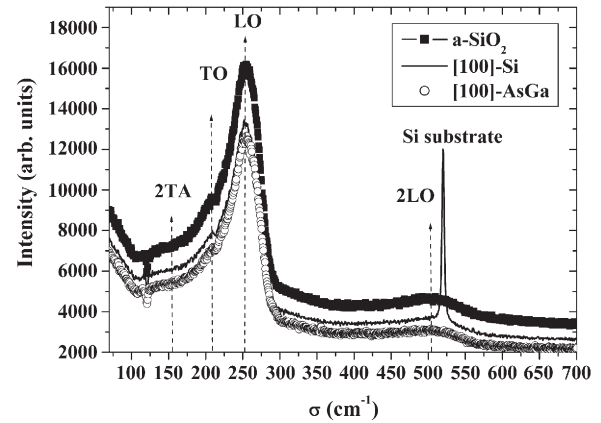


Fig. 5. Raman spectra of films deposited on various substrates (Si, GaAs and a-SiO<sub>2</sub>) at  $P_{RF}=150$  W with  $d=7$  cm at  $T_d=T_a$ .

visible but is probably present in the form of an unresolved shoulder at the right of the LO mode. These results for  $P_{RF}>50$  W are in agreement with the large amount of stoichiometric ZnSe as determined by XRR and RBS experiments.

A typical XRD diffraction pattern of the films deposited for  $P_{RF}>50$  W at  $d=7$  cm with  $P_{Ar}=2$  Pa is shown in Fig. 6 (for  $P_{RF}=50$  W only an amorphous contribution is evidenced in the diffraction patterns). Whatever  $P_{RF}$ ,  $T_d$  and substrates, there is no variation in the diffracted intensity lines with the  $\chi$  and  $\varphi$  angles variation. This fact asserts that no texture is present in our films contrarily to that observed by other authors for films deposited on [100]-Si using the same deposition technique [13] or for films deposited by laser ablation on [100]-GaAs and a-SiO<sub>2</sub> [30]. Three diffracted lines are clearly visible (Fig. 6) and can be indexed in an apparent cubic ZnSe structure with a-cell parameter around  $0.565\text{ nm}$  and  $0.561\text{ nm}$  for respectively  $P_{RF}=150$  and  $100$  W. The observed values are always smaller than those for bulk ZnSe ( $0.5667\text{ nm}$ ), and correspond to a mean

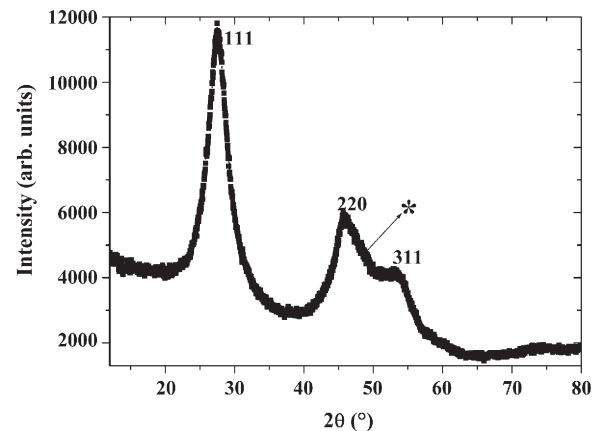


Fig. 6. Typical asymmetric  $\omega$ - $2\theta$  pattern obtained for films deposited at  $P_{RF}>50$  W with  $d=7$  cm and  $P_{Ar}=2$  Pa with  $\chi=0^\circ$  and with an incident angle  $\omega=13.65^\circ$  corresponding of the 111 reflection of the cubic ZnSe structure. All the observed diffraction lines have been indexed using a cubic ZnSe cell. The \* symbol at around  $2\theta=49.2^\circ$  that corresponds to the 103 hexagonal reflection, clearly indicates the presence of a few amount of the ZnSe hexagonal structure.

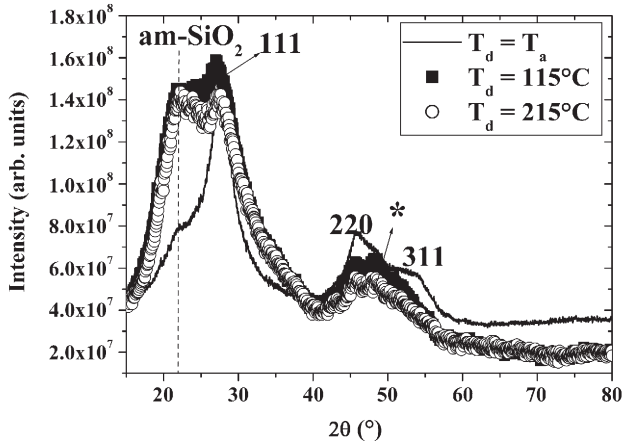


Fig. 7. Asymmetric XRD normalized patterns for the films deposited on a-SiO<sub>2</sub> substrates at  $P_{RF}=100$  W,  $d=7$  cm for substrate temperatures  $T_d$  in the  $T_a-215$  °C range. Note that the contribution of the amorphous substrate (am-SiO<sub>2</sub>) is more marked with the increase of  $T_d$ .

lattice shrinking of  $\frac{\Delta a}{a} = 0.3\%$  to 1.4%. However, whatever the substrate, no peak shift was observed when tilting the samples in  $\chi$ , indicating that the measured cell parameters correspond to the stress-free crystallized ZnSe layers contrarily to that observed for the deposition of pure ZnSe films onto Si substrates by the same technique [13]. The difference would be due to the presence of the a-SiO<sub>2</sub> matrix that induced relaxation in our material.

The relatively large width of these diffraction lines, that is indicative of the presence of ZnSe nanocrystallites, cannot exclude the presence of a ZnSe wurtzite type structure. The asymmetry on the right side of the 220 line which appears more marked with the increase of  $T_d$  for the a-SiO<sub>2</sub> substrate deposited films for example, can be only explained by the presence of a small amount of hexagonal ZnSe, as it has been observed by Rizzo and collaborators [13].

In order to compare the obtained XRD spectra for different  $P_{RF}$ ,  $T_d$  values and substrates, all the spectra have to be normalized by their thickness. With a CPS detector geometry, considering an angle  $\omega$  of incidence (in our case 13.6°), the

observed intensity  $y$  at the  $i^{th}$  point is corrected for absorption and volume by the relation  $y_i = \frac{G}{\mu \cdot \sin\theta_i} (1 - e^{-\mu \cdot T \cdot M(\omega, \theta_i)})$  where  $T$  is the thickness of the film,  $\mu$  the linear absorption coefficient of the film (value chosen in a first approximation equal to  $\mu_{ZnSe} = 0.292 \text{ cm}^{-1}$ ),  $M(\omega, \theta_i) = \frac{1}{\left(\sin\theta_i + \frac{1}{\sin(2\omega - \theta_i)}\right)}$ ,

and  $G$  a geometry dependent constant [31]. Consequently, we normalized for each film the measured intensities by the  $(1 - e^{-\mu \cdot T \cdot M(\omega, \theta_i)})$  term. For  $P_{RF}=100$  W and whatever the chosen substrate, the contribution of an amorphous SiO<sub>2</sub> (am-SiO<sub>2</sub>) phase is evidenced in the background of the corresponding XRD spectra with a more marked signature for the films deposited on a-SiO<sub>2</sub> substrates (Fig. 7). With the increase of  $T_d$  there is no significant variation of this am-SiO<sub>2</sub> contribution in the XRD spectra of the films deposited on the Si and GaAs substrates whereas this contribution appears predominant for the a-SiO<sub>2</sub> substrates. This latter is without ambiguity due to a more marked a-SiO<sub>2</sub> substrate contribution to the XRD signal as the film thickness has been found to decrease with  $T_d$ , as asserted also by the vanishing of this am-SiO<sub>2</sub> signal for thicker films deposited on the same substrate at  $P_{RF}=150$  W (Fig. 8).

The full width at half maximum ( $\beta$ ) of the 111 diffraction lines (which are in a symmetrical position) allow an estimate of the crystalline grain size  $D$  in our films [17] using the Debye–Scherrer formula:  $D = 0.9 \lambda_{Cu} / (\beta \cdot \cos \theta_{111})$ . The corresponding estimated sizes  $D$  are listed in Table 4 except for  $T=115$  °C and 215 °C at  $P_{RF}=100$  W on a-SiO<sub>2</sub> substrates where a small 111 contribution cannot allow an accurate  $D$  size determination. The obtained values are in the 2–3 nm range and are in agreement with those obtained for ZnSe/SiO<sub>2</sub> films deposited by magnetron sputtering ( $3.2 \leq D \leq 4.3$  nm) with  $P_{Ar}=0.5$  Pa [14]. Whatever  $P_{RF}$  and  $T_d$ , we have  $D_{Si} \geq D_{AsGa} \geq D_{a-SiO_2}$  showing that the films grown on a-SiO<sub>2</sub> have the smallest grain size as observed on films deposited by pulsed laser ablation [11]. However, the maximum difference observed on the  $D_{AsGa}$  and  $D_{a-SiO_2}$  sizes is only equal to 0.45 nm whereas by pulsed

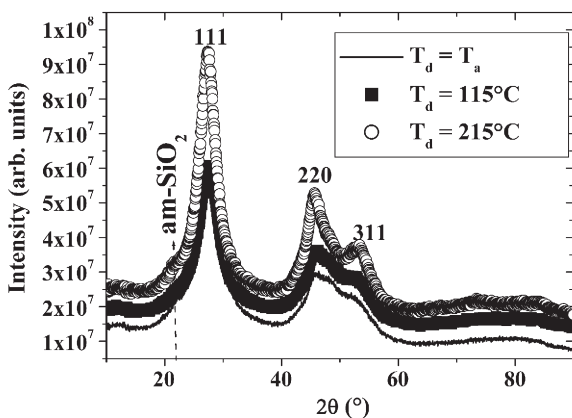


Fig. 8. Asymmetric XRD normalized patterns for the films deposited on a-SiO<sub>2</sub> substrates at  $P_{RF}=150$  W, with  $d=7$  cm for substrate temperatures  $T_d$  in the  $T_a-215$  °C range.

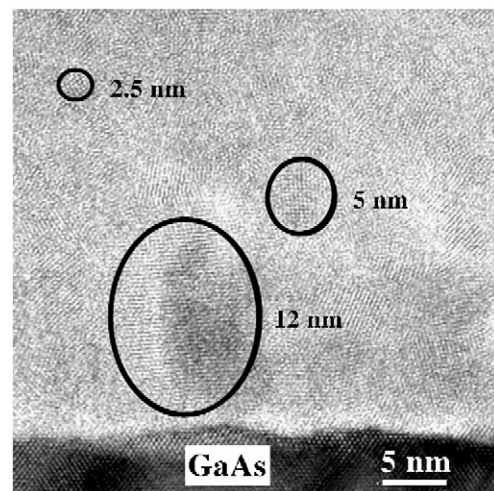


Fig. 9. HRTEM image of the film deposited on GaAs substrate at  $P_{RF}=150$  W,  $d=7$  cm for  $P_{Ar}=2$  Pa and  $T_d=T_a$ , showing inhomogeneous grain size distribution.

laser ablation, it was equal to 36 nm for pure ZnSe films grown with a substrate temperature of 400 °C. The incorporation of the ZnSe nanocrystals in a SiO<sub>2</sub> glass matrix allows the growth of thin films whose crystalline quality is almost independent on the substrate type. In addition, we can obtain controlled nanoparticles size sufficiently small (<10 nm) to induce quantum confinement effects that would lead to a subsequent increase of photoluminescence properties of such films.

With higher  $T_d$  values, at  $P_{RF}=100$  W (Fig. 7), the intensities of the three diffraction lines are strongly decreased with smaller  $D$  crystallite size of about 0.6 nm, whereas for  $P_{RF}=150$  W (Fig. 8), these  $hk\ell$  intensities are increased (with small differences between  $T_a$  and 115 °C) with a  $D$  size increase in the 0.62–0.81 nm range. With the increase of  $T_d$  a competition exists between desorption of the Zn and Se species of the plasma and the growth of ZnSe crystallites. At  $P_{RF}=150$  W, due to higher growth rates and a high number of ejected species from the target, the evaporation of ZnSe with an increase of  $T_d$  is strongly reduced in comparison with  $P_{RF}=100$  W, allowing the deposition of films with higher ZnSe content and the growth of larger crystallites for  $T_d > T_a$ .

At  $T_d = T_a$ , cross sectional Transmission Electron Microscopy (TEM) analyses of the deposited films reveal that there is an inhomogeneous crystallite size distribution, that is more marked at 150 W (certainly correlated to  $v_g$  values 3 times higher than at 100 W): in the typical High Resolution Transmission Electron Microscopy (HRTEM) image presented in Fig. 9, several grain sizes are clearly visible in the 2.5–12 nm range. This size distribution inhomogeneity at  $T_a$  and whatever  $P_{RF}$ , is due to the non constant substrate temperatures during the deposition due to the substrate heating by the plasma, leading to the growth to larger highly faulted ZnSe nanograins near the surface of the film. These temperatures reach at the end of the deposition values of 110 °C and 125 °C for respectively  $P_{RF}=100$  and 150 W. This aspect will be detailed and discussed, in correlation with a quantitative X-ray analysis of our films, in a forthcoming paper.

#### 4. Conclusion

ZnSe-nanocrystals doped SiO<sub>2</sub> glass thin films were deposited on [100]-Si, [100]-GaAs and a-SiO<sub>2</sub> substrates by reactive magnetron co-sputtering of a target of SiO<sub>2</sub> and chips of ZnSe with a relative ZnSe/SiO<sub>2</sub> surface area ratio of about 30%. The correlations between the composition, the structural film properties and the plasma characteristics have been explained to some extent by varying the different deposition parameters.

Se is without ambiguity the most sensitive species in the plasma to the substrate temperature and to the radio-frequency power values. The deposited films are stress-free and exhibit a random orientation and a cubic crystal structure with few quantities of ZnSe hexagonal phase. Whatever the used substrates, quasi-stoichiometric ZnSe films with a high proportion (73.5%) of ZnSe nanocrystals with an average particle size of 3 nm have been obtained for the following optimal deposition conditions: an Ar pressure of 2 Pa, a

substrate to target distance of 7 cm, an ambient substrate temperature and a sputtering power of 150 W. The size and the proportion of the ZnSe nanocrystals can be also easily monitored by the choice of the substrate temperature and of the sputtering power. Whatever the used substrate, the presence of the SiO<sub>2</sub> dielectric matrix favors the growth of ZnSe nanocrystallites with controlled sizes lower than 5 nm, of particular interest for future studies of quantum confinement effects. Moreover, a more precise determination of the nanocrystallite sizes and of the structure of these films using Raman, TEM and XRD quantitative analyses will be done in correlation with their optical properties in a forthcoming paper.

#### Acknowledgements

M. Morales thanks the Délégation Régionale à la Recherche et à la Technologie-région Basse Normandie for the sputtering and plasma diagnostic experimentation financing and, H. Cubero and P. Voivenel for the conception and the assembling of the sputtering chamber and Y. Vickridge for the helpful discussion for the RBS experiments.

#### References

- [1] G.P. Banfi, V. Degiorgio, D. Ricard, *Adv. Chem. Phys.* 47 (1998) 447.
- [2] T. Toyama, K. Yoshimura, M. Fujii, H. Haze, H. Okamoto, *Appl. Surf. Sci.* 244 (2005) 524.
- [3] B. Bhattacharjee, D. Ganguli, S. Chaudhuri, A.K. Pal, *Thin Solid Films* 422 (2002) 98.
- [4] H.R. Dobler, *Appl. Opt.* 28 (1989) 2698.
- [5] I.T. Sorokina, *Opt. Mater.* 26 (2004) 395.
- [6] R. Kumaresan, M. Ichimura, E. Arai, *Thin Solid Films* 414 (2002) 25.
- [7] R.B. Kale, C.D. Lokhande, *Appl. Surf. Sci.* 252 (2005) 929.
- [8] G.I. Rusu, M.E. Popa, G.G. Rusu, I. Salaoru, *Appl. Surf. Sci.* 218 (2002) 222.
- [9] Y. P Venkata Subbaiah, P. Prathap, M. Devika, K.T. Ramakrishna Reddy, *Phys.*, B 365 (2005) 240.
- [10] T. Takai, J.H. Chang, K. Godo, T. Hanada, T. Yao, *Phys. Status Solidi, B* 229 (2002) 381.
- [11] G. Perna, V. Capozzi, M.C. Planturama, A. Minafra, P.F. Biagi, S. Orlando, V. Marotta, A. Giardini, *Appl. Surf. Sci.* 186 (2002) 521.
- [12] S.K. Mandal, S. Chaudhuri, A.K. Pal, *Nanostruct. Mater.* 10 (1998) 607.
- [13] A. Rizzo, M.A. Tagliente, L. Caneve, S. Scaglione, *Thin Solid Films* 368 (2000) 8.
- [14] M. Hayashi, T. Iwano, H. Nasu, N. Sugimoto, K. Kamiya, K. Hirao, *J. Mater. Res.* 12 (1997) 2552.
- [15] G. Vignaud, A. Gibaud, computer code REFLEX (<http://pecdc.univ-lemans.fr/reflex/reflex.htm>, 2000). A. Gibaud, X-ray and neutron reflectivity: Principles and applications, in: J. Daillat, A. Gibaud (Eds.), Springer, Berlin, 1999.
- [16] L.R. Doolittle, *Nucl. Instrum. Methods Phys. Res., Sec. B* 9 (1985) 344.
- [17] M. Morales, Y. Leconte, R. Rizk, D. Chateigner, *J. Appl. Phys.* 97 (2004) 034307.
- [18] R.W.B. Pearse, A.G. Gaydon, *The identification of molecular spectra* 4th edition, Chapman and Hall, London, 1976.
- [19] A. Richardt, A.M. Durand, *La pratique du vide et des dépôts de couches minces*, Ed. In Fine, Paris, 1995, p. 351.
- [20] A. Von Keudell, *Plasma Sources Sci. Technol.* 9 (2000) 455.
- [21] K. Kojima, J.S. Song, K. Godo, D.C. Oh, J.H. Chang, M.W. Cho, T. Yao, *Mater. Sci. Semicond. Process.* 6 (2003) 511.
- [22] J. Riley, D. Wolframm, D. Westwood, A. Evans, *J. Cryst. Growth* 160 (1996) 193.
- [23] J.W. Mc Camy, M.J. Aziz, *Mater. Res. Soc. Symp. Proc.* 441 (1997) 621.

- [24] K.R. Murali, A. Austine, D.C. Trivedi, *Mater. Lett.* 59 (2005) 2621.
- [25] D. Sarigiannis, J.D. Peck, T.J. Mountziaris, G. Kioseoglou, A. Petrou, *Mater. Res. Soc. Symp. Proc.* 616 (2000) 41.
- [26] D. Sarigiannis, J.D. Peck, G. Kioseoglou, A. Petrou, T.J. Mountziaris, *Appl. Phys. Lett.* 80 (2002) 4024.
- [27] X. Fu, H. An, W. Du, *Mater. Lett.* 59 (2005) 1484.
- [28] B. Cao, W. Cai, Y. Li, F. Sun, L. Zhang, *Nanotechnology* 16 (2005) 1734.
- [29] B.K. Rai, R.S. Katiyar, K.T. Chan, A. Burger, *J. Appl. Phys.* 83 (1998) 6011.
- [30] G. Perna, V. Capozzi, M.C. Plantamura, A. Minafra, S. Orlando, V. Marotta, *Eur. Phys. J., B* 29 (2002) 541.
- [31] M. Morales, D. Chateigner, L. Lutterotti, J. Ricote, *Mater. Sci. Forum* 408–412 (2002) 113.

## Photoluminescence properties of Cr<sup>2+</sup>:ZnSe films deposited by radio frequency magnetron cosputtering

N. Vivet, M. Morales,<sup>a)</sup> and M. Levalois

*Laboratoire Structure des Interfaces et Fonctionnalités des Couches Minces (SIFCOM)-ENSICAEN, 6 Bd. du Maréchal Juin, 14050 Caen, France*

J. L. Doualan and R. Moncorgé

*Centre Interdisciplinaire de Recherche Ions Lasers (CIRIL)-ENSICAEN, 6 Bd. du Maréchal Juin, 14050 Caen, France*

(Received 23 January 2007; accepted 5 April 2007; published online 1 May 2007)

Cr<sup>2+</sup>:ZnSe films were grown at room temperature by the radio frequency magnetron cosputtering technique. The structural characterization of the films shows that the corresponding films are well crystallized mainly in the cubic zinc-blende structure with strong  $\langle 111 \rangle$  orientations. Using direct (1850 nm) and indirect (visible) excitations, photoluminescence experiments in the midinfrared spectral region reveal that Cr is incorporated in the optically active Cr<sup>2+</sup> state, and the shape of the spectra agrees with that reported for bulk materials. This study shows that magnetron cosputtering can provide viable structures for the realization of optically and electrically pumped midinfrared microlasers. © 2007 American Institute of Physics. [DOI: 10.1063/1.2735284]

Among the transition metal doped II-VI semiconductor compounds studied for room-temperature (RT) operated broadly tunable midinfrared (mid-IR) region (2000–4500 nm) laser sources, it has been pointed that Cr<sup>2+</sup> doped materials<sup>1,2</sup> seem to be the highly favorable systems.<sup>3,4</sup> In particular, in the case of Cr<sup>2+</sup>:ZnSe, pulsed,<sup>5</sup> continuous wave,<sup>6</sup> and mode locked<sup>7</sup> operations have been demonstrated. This laser has important potential applications in remote sensing, vibrational spectroscopy, trace detection, and medicine.<sup>8</sup> Moreover, the most exciting developments in Cr<sup>2+</sup>:ZnSe lasers were, on the one hand, the recent demonstration of a RT laser based on Cr<sup>2+</sup> ion doped ZnSe nanopowders (with 200 nm grain size) (Refs. 9 and 10) and, on the other hand, the report of electroluminescence in the mid-IR from Cr-doped bulk ZnSe.<sup>11,12</sup> Combined with the recent understanding of charge transfer processes, these allow us to consider as possible in the future the realization of simple electrically pumped active nanocrystalline lasers.

In ZnSe, Cr<sup>2+</sup> ions substitute for the Zn<sup>2+</sup> host and occupy tetrahedral sites leading to smaller crystalline field splitting of the free-ion energy levels, placing the dopant transitions into mid-IR.<sup>11</sup> The only intracenter transitions are expected between the levels <sup>5</sup>T<sub>2</sub> (ground state) and <sup>5</sup>E (first excited state) originated from the splitting of the free-ion ground state and give rise to an absorption band around 1750 nm and a double-peaked broadband emission between 2000 and 3000 nm. Recently, Cr<sup>2+</sup>:ZnSe thin films have been grown by molecular beam epitaxy at a temperature of 300 °C.<sup>13</sup> The RT emission spectra of the films in the mid-IR region were comparable to the bulk, showing that this technique provides optically active Cr<sup>2+</sup> in ZnSe. This result paves the way towards the fabrication of compact devices in the mid-IR at RT.

As an alternative technique, radio frequency (rf) magnetron sputtering, well established in industrial processing of various optical and photonic components, is versatile, is re-

producible, and presents various advantages such as low temperature (RT) film formation, good interfacial adhesion with the substrate, high packing density of the grown film, and compositions that can be easily adjusted. We reported in a previous paper<sup>14</sup> that ZnSe/SiO<sub>2</sub> films can be easily grown by rf magnetron cosputtering at RT of a SiO<sub>2</sub> target covered by a number of ZnSe chips. Stoichiometric and random ZnSe films with a high proportion (73.5%) of ZnSe nanocrystals with an average particle size of 3 nm have been obtained on different substrate types (monocrystalline [100]-AsGa and [100]-Si and glass substrate) with the following optimal deposition conditions: a ZnSe-to-SiO<sub>2</sub> sputtered area ratio (SAR) of about 30%, an Ar pressure of 2 Pa, a substrate to target distance of 7 cm and a sputtering power (SP) of 150 W. The Cr<sup>2+</sup>:ZnSe films investigated in this study were grown by the same method, but the SAR was fixed at about 60% (in order to increase the ZnSe nanocrystals content in the films) while adding various quantity of Cr in the range of 0.02–0.8 g among the ZnSe chips, and the SP was increased to 250 W to favor the incorporation of Cr in the films, as suggested by optical emission spectroscopy studies. The other deposition parameters remained unchanged. With this SAR value, no SiO<sub>2</sub> was incorporated in the corresponding films.

The structural and microstructural properties of the deposited films were investigated by Raman spectroscopy (T64000 Jobin-Yvon multichannel spectrometer,  $\lambda_{Ar-Kr}$  = 514.532 nm) (Ref. 14) and x-ray diffraction (XRD). As the usual  $\theta$ -2 $\theta$  XRD diagrams (Phillips XPERT diffractometer,  $\lambda_{Cu K\alpha}$  = 1.5418 Å) of the films exhibited a  $\langle 111 \rangle$  preferential orientation, quantitative texture analysis was also performed by using a Huber four circle diffractometer.<sup>14</sup>

Whatever the Cr quantity incorporated, the chosen substrates and the SP in the 150–250 W range, similar XRD and Raman patterns were observed. In both patterns, no extra peak corresponding to Cr or localized modes<sup>15</sup> of Cr<sub>Zn</sub>-Se, respectively, is evidenced, due to the small quantity of Cr incorporated in the films. These results were corroborated by the energy-dispersive x-ray analysis which indicates a large

<sup>a)</sup> Author to whom correspondence should be addressed; FAX: +33-2-31-45-26-60; electronic mail: magali.morales@ensicaen.fr

percentage of Zn and Se (57% and 43%, respectively), whereas Cr was under the detection limit. A typical  $\theta$ - $2\theta$  XRD pattern is shown in Fig. 1 where the first, second, and third order of the (111) reflection of the ZnSe cubic polytype ( $a \approx 5.67 \text{ \AA}$ ) is evidenced. The (220) and (311) reflections are also present but with very small intensity. As it has been previously reported for ZnSe thin films deposited on glass and silicon substrates,<sup>16–18</sup> the [111] axis of the ZnSe grains is predominantly oriented perpendicularly to the film substrate, as asserted by the inverse 001 pole figure represented on the bottom-right insert of Fig. 1. A few amount of ZnSe hexagonal polytype has been also evidenced although in a very disordered state. The crystallite sizes along the [111] direction, estimated by the use of the Scherrer formula, have been found in the 60–100 nm range. Contrary to that observed by pulsed laser ablation<sup>16</sup> for the deposition of pure ZnSe films, our Cr<sup>2+</sup>:ZnSe films deposited on [100]-GaAs substrate exhibit the same  $\langle 111 \rangle$  orientation and the ZnSe crystallite sizes are rather independent of the choice of the substrate. This is certainly correlated to the columnar growth of the films as asserted by transmission electron microscopy (not shown here). Moreover, the film orientation is observed quite independent of the chosen substrate because of the presence at the first growth stage of an amorphous ZnSe layer on the Si and GaAs substrates. The top insert of Fig. 1 shows a typical RT Raman spectrum of a Cr<sup>2+</sup>:ZnSe film deposited on glass substrate. It shows the two strong transversal optic (TO) and longitudinal optic (LO) phonon modes of cubic ZnSe (Ref. 15) at 216 and 257 cm<sup>-1</sup>, respectively, and the weak and broad transversal acoustic and longitudinal optic phonon modes at  $\sim 163$  and 505 cm<sup>-1</sup>, respectively. The relative width of LO (20 cm<sup>-1</sup>) and TO (36 cm<sup>-1</sup>) modes is found smaller than in our previous films<sup>14</sup> ( $>50 \text{ cm}^{-1}$ ) and no asymmetric broadening for the lower values of the Raman shift, indicating the presence of small particles of a few nanometers,<sup>19</sup> is visible for the LO peak. According to the XRD studies, this reveals that the increase of the SAR and of the SP has allowed the growth of more

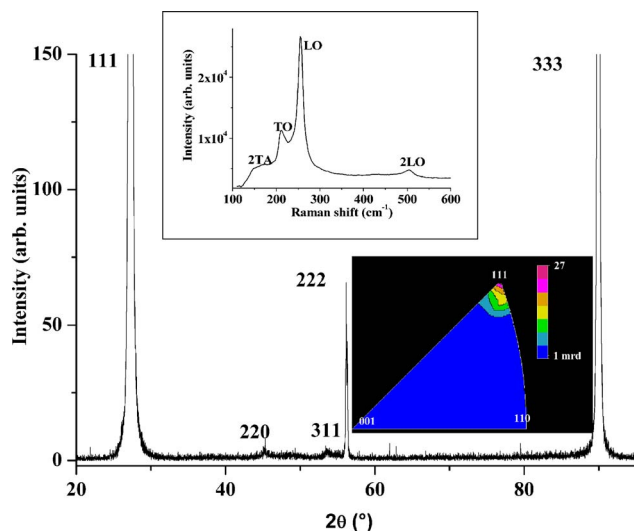


FIG. 1. (Color online) Typical  $\theta$ - $2\theta$  XRD pattern of a textured Cr<sup>2+</sup>:ZnSe film deposited on glass substrate and its corresponding 001 inverse pole figure (bottom-right insert) exhibiting a strong  $\langle 111 \rangle$  fiber texture (27 multiple of a random distribution). Pole locations are indicated by their Miller indices. Equal area projection and linear distribution density scale. RT Raman spectrum of Cr<sup>2+</sup>:ZnSe film deposited on glass substrate (top insert).

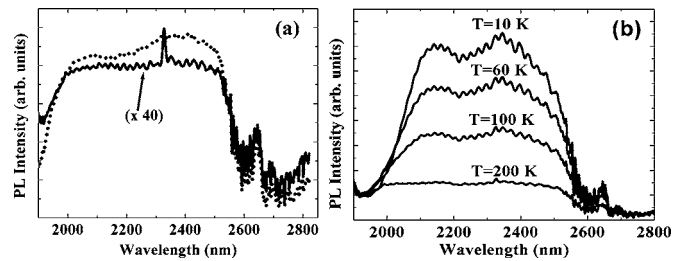


FIG. 2. (a) PL spectra of a Cr<sup>2+</sup>:ZnSe film deposited on glass substrate (solid line) and of a reference bulk crystal (dotted line) under a 1850 nm excitation at RT. (b) PL spectra of the same film at lower temperatures. The sharp emission line at about 2350 nm comes from the Ti:sapphire laser (third order of the monochromator grating) and the emission line at about 2650 nm is due to water vapor absorption.

crystallized films with higher crystallite sizes.<sup>14</sup>

The film thicknesses have been deduced from optical transmission spectroscopy studies<sup>20</sup> by using the value  $n = 2.44$  for the refractive index of ZnSe at RT in the 1–2  $\mu\text{m}$  spectral region.<sup>4</sup> They can be monitored in the 3–45  $\mu\text{m}$  range without any adhesive problem. Due to their small thicknesses, the Cr<sup>2+</sup> absorption band centered on 1750 nm (corresponding to the transition between the  $^5T_2$  and  $^5E$  states of the Cr<sup>2+</sup> ions<sup>1</sup>) is not detectable in our films and the Cr<sup>2+</sup> concentration cannot be determined as done in the bulk materials.<sup>4</sup>

Photoluminescence (PL) measurements were performed at different temperatures by fixing the sample on the cold finger of a cryogenerator. Direct pumping into the  $^5T_2 \rightarrow ^5E$  intracenter absorption of the Cr<sup>2+</sup> ion was reached using a *homemade* cw Tm<sup>3+</sup>:KY<sub>3</sub>F<sub>10</sub> laser<sup>21</sup> (1850 nm) pumped with a Ti:sapphire laser (780 nm). A liquid-nitrogen-cooled InSb detector followed by a fast preamplifier and lock-in amplifier was used for data acquisition. The RT measured PL spectra of both a reference bulk crystal (prepared by post-growth diffusion doping with a Cr<sup>2+</sup> concentration of about  $3.10^{18} \text{ cm}^{-3}$ ) and a Cr<sup>2+</sup>:ZnSe film are depicted in Fig. 2(a). The PL relative intensity of the Cr<sup>2+</sup>:ZnSe film is 40 times less than the bulk one but the shape of the two spectra is the same. Both samples exhibit the large emission band centered at about 2200 nm attributed<sup>1</sup> to the  $^5E \rightarrow ^5T_2$  intrashell transition of Cr<sup>2+</sup> ions. These spectra indicate that the Cr<sup>2+</sup> ions in our films have the same local atomic environment as in bulk material. The PL spectra of the Cr<sup>2+</sup>:ZnSe films exhibit oscillations which are due to multiple reflections on film surfaces, and from these oscillations we can determine the film thicknesses, which compare very well with the values obtained from optical transmission experiments [about 45  $\mu\text{m}$  for the film in Fig. 2(a)]. For the films deposited with less than 100 mg of Cr among the ZnSe chips, the Cr<sup>2+</sup> concentration is insufficient to observe the PL emission band. If the Cr mass on the target is larger than 400 mg, no PL emission band is observed. It could be due to concentration quenching. Indeed, for Cr<sup>2+</sup>:ZnSe bulk crystal<sup>22,23</sup> it was reported that for concentrations larger than  $10^{19} \text{ cm}^{-3}$  the lifetime decreases significantly, as a sign of Cr<sup>2+</sup> emission quenching. Consequently, for our films which exhibit a PL emission band, the Cr<sup>2+</sup> concentration must be less than  $10^{19} \text{ cm}^{-3}$ . Assuming an absorption cross section of  $1.15 \times 10^{-18} \text{ cm}^2$ ,<sup>24</sup> this will lead to a maximal decrease of the transmission coefficient at 1750 nm of only a few percent, not detectable in our optical transmission spectra, as reported above.

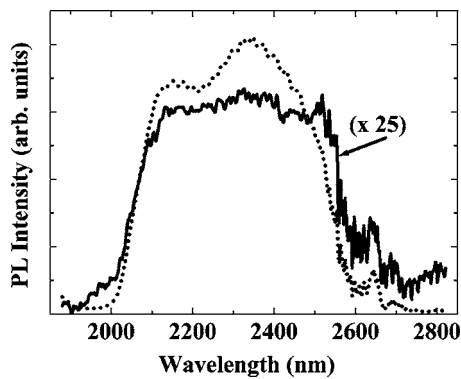


FIG. 3. PL spectra at 10 K of a  $\text{Cr}^{2+}$ :ZnSe film deposited on GaAs substrate under 1850 nm (dotted line) and multiline argon laser (solid line) excitation.

Figure 2(b) shows the  $\text{Cr}^{2+}$  emission of the same film at different temperatures under a 1850 nm excitation. These structured spectra display two peaks at low temperatures similar to those reported in bulk  $\text{Cr}^{2+}$ :ZnSe,<sup>2</sup> confirming that Cr has been incorporated in this film in the active  $\text{Cr}^{2+}$  state. The Cr radiative lifetime of a few microseconds and consequently the probability of the radiative transition is reported<sup>3,10</sup> to be nearly constant with temperature up to 300 K in bulk  $\text{Cr}^{2+}$ :ZnSe crystals. However, in our films the PL integrated intensity decreases when increasing sample temperature [Fig. 2(b)], while the PL linewidth is nearly constant. When the temperature increases, the absorption band is broadened and the maximum is reduced. As the pumping wavelength at 1850 nm is close to the absorption band maximum at 1750 nm, it induces a fluorescence decrease, but probably not enough to explain the PL intensity decrease, and other effects should be mentioned such as nonradiative processes by the interaction between the  $\text{Cr}^{2+}$  ions and impurities. Some temperature decay time fluorescence measurements are in progress in order to understand this specific behavior.

Pumping into the  $\text{Cr}^{2+}/\text{Cr}^+$  charge transfer band with a multiline argon laser (458–514 nm) was also investigated and gives rise to emission at low temperature (Fig. 3) as well as at RT in the same spectral range. Whatever the temperature, the PL intensity was smaller (divided by 25 at 10 K) under argon laser excitation than using the 1850 nm excitation. The comprehension of the physical mechanisms of  $\text{Cr}^{2+}$  ion optical interband excitation was subject to numerous investigations.<sup>10–12</sup> Generally, it was concluded that this excitation mechanism is a two-step process: an incident photon ionizes the  $\text{Cr}^{2+}$  ion to the  $\text{Cr}^+$  state by releasing a hole to the valence band. A second pump phonon ionizes the  $\text{Cr}^+$  ion to the excited state  $\text{Cr}^{2+*}$  putting an electron in the conduction band. The excited state relaxes to the  $^5E$  first excited energy level of  $\text{Cr}^{2+}$ , which radiative decay is finally accomplished by emission of mid-IR photon. So, pumping into the  $\text{Cr}^{2+}/\text{Cr}^+$  charge transfer band is less efficient than the direct internal excitation.

In summary, highly crystalline  $\langle 111 \rangle$  textured  $\text{Cr}^{2+}$ :ZnSe films were deposited at RT by rf magnetron cosputtering of a  $\text{SiO}_2$  target covered by ZnSe and Cr chips. The average Cr quantity incorporated in the films can be easily monitored by varying the Cr quantity on the target and the SP. The optical investigations have shown that this technique provides Cr-doped ZnSe films with chromium ions in the  $\text{Cr}^{2+}$  active state, leading to the mid-IR emission observed at RT at about 2200 nm under direct and indirect excitations. This study shows that rf magnetron sputtering is a viable technique for the fabrication of future optically or electrically pumped waveguides and/or laser microstructures broadly tunable in the mid-IR.

- <sup>1</sup>J. T. Vallin, G. A. Slack, S. Roberts, and A. E. Hughes, *Phys. Rev. B* **2**, 4313 (1970).
- <sup>2</sup>M. Kaminska, J. M. Baranowski, S. M. Uba, and J. T. Vallin, *J. Phys. C* **12**, 2197 (1979).
- <sup>3</sup>L. D. DeLoach, R. H. Page, G. D. Wilke, S. A. Payne, and W. F. Krupke, *IEEE J. Quantum Electron.* **32**, 885 (1996).
- <sup>4</sup>R. H. Page, K. I. Schaffers, L. D. DeLoach, G. D. Wilke, F. D. Patel, J. B. Tassano, S. A. Payne, W. F. Krupke, K. T. Chen, and A. Burger, *IEEE J. Quantum Electron.* **33**, 609 (1997).
- <sup>5</sup>A. V. Podlipensky, V. G. Shcherbitsky, N. V. Kuleshov, V. P. Mikhailov, V. I. Levchenko, V. N. Yakimovich, L. I. Postnova, and V. I. Konstantinov, *Opt. Commun.* **167**, 129 (1999).
- <sup>6</sup>G. J. Wagner, T. J. Carrig, R. H. Page, K. I. Schaffers, J.-O. Ndap, X. Ma, and A. Burger, *Opt. Lett.* **24**, 19 (1999).
- <sup>7</sup>T. J. Carrig, G. J. Wagner, A. Sennaroglu, J. Y. Jeong, and C. R. Pollock, *Opt. Lett.* **25**, 168 (2000).
- <sup>8</sup>R. W. Waynant, I. K. Ilev, and I. Gannot, *Philos. Trans. R. Soc. London, Ser. A* **359**, 635 (2001).
- <sup>9</sup>I. T. Sorokina, E. Sorokin, V. G. Shcherbitsky, N. V. Kuleshov, G. Zhu, A. Frantz, and M. A. Noginov, *Advanced Solid-State Photonics*, Santa Fe, NM, 2004 (unpublished), Paper No. WB14.
- <sup>10</sup>I. T. Sorokina, *Opt. Mater. (Amsterdam, Neth.)* **26**, 395 (2004).
- <sup>11</sup>V. V. Fedorov, A. Gallian, I. Moskalev, and S. B. Mirov, *J. Lumin.* **125**, 184 (2007).
- <sup>12</sup>J. Jaeck, R. Haidar, E. Rosencher, M. Caes, M. Tauvy, S. Collin, N. Bardou, J. L. Pelouard, F. Pardo, and P. Lemasson, *Opt. Lett.* **31**, 3501 (2006).
- <sup>13</sup>A. Gallian, V. V. Fedorov, J. Kernal, J. Allman, S. B. Mirov, E. M. Dianov, A. O. Zabezhaylov, and I. P. Kazakov, *Appl. Phys. Lett.* **86**, 091105 (2005).
- <sup>14</sup>M. Morales, N. Vivet, M. Levalois, and J. F. Bardeau, *Thin Solid Films* **515**, 5314 (2007).
- <sup>15</sup>B. K. Rai, R. S. Katiyar, K. T. Chen, and A. Burger, *J. Appl. Phys.* **83**, 6011 (1998).
- <sup>16</sup>G. Perna, V. Capozzi, M. C. Plantamura, A. Minafra, S. Orlando, and V. Marotta, *Eur. Phys. J. B* **29**, 541 (2002).
- <sup>17</sup>S. Venkatachalam, D. Mangalaraj, Sa. K. Narayandass, K. Kim, and J. Yi, *Physica B* **358**, 27 (2005).
- <sup>18</sup>A. Rizzo, M. A. Tagliente, L. Caneve, and S. Scaglione, *Thin Solid Films* **368**, 8 (2000).
- <sup>19</sup>X. Fu, H. An, and W. Du, *Mater. Lett.* **59**, 1484 (2005).
- <sup>20</sup>J. I. Pankov, *Optical Processes in Semiconductors* (Dover, New York, 1975), Chap. 4, p. 170.
- <sup>21</sup>A. Braud, P. Y. Tigréat, J. L. Doualan, and R. Moncorgé, *Am. J. Otolaryngol.* **72**, 909 (2001).
- <sup>22</sup>S. Bhaskar, P. S. Dobal, B. K. Rai, R. S. Katiyar, H. D. Bist, J.-O. Ndap, and A. Burger, *J. Appl. Phys.* **85**, 439 (1999).
- <sup>23</sup>U. Hommerich, I. K. Jones, E. E. Nyein, and S. B. Trivedi, *J. Cryst. Growth* **287**, 450 (2006).
- <sup>24</sup>A. Sennaroglu, U. Demirbas, A. Kurt, and M. Somer, *Opt. Mater. (Amsterdam, Neth.)* **29**, 703 (2007).





*CONCLUSION*

*ET PERSPECTIVES*



Faire le point dans ce manuscrit d'Habilitation à Diriger des Recherches sur les 8 années de recherche consécutives à ma thèse n'a pas été aisé étant donné que mon activité a connu des changements thématiques importants et comporté différents aspects qu'il n'a pas été possible de tous détailler.

Dans le cadre d'une diversification thématique, mes activités de recherche post-doctorales se sont orientées d'une part vers la caractérisation structurale de matériaux sous forme de films minces aux propriétés physiques variées (ferroélectriques, de conduction ionique, optiques,...), et d'autre part vers l'élaboration de films minces conducteurs ioniques en utilisant la technique de pulvérisation magnétron réactive (ATER 1999-2000). La compétence acquise dans cette technique d'élaboration a facilité d'ailleurs mon intégration (septembre 2002) au sein de l'équipe "NIMPH" (Nanostructures Intégrées pour la Microélectronique et la Photonique) du laboratoire SIFCOM. En effet, le laboratoire SIFCOM a développé une spécificité dans cette technique de dépôt, en utilisant le caractère réactif de l'hydrogène dans le plasma, pour la réalisation avec un contrôle compositionnel et dimensionnel unique de nanostructures compatibles avec la technologie CMOS. Cette expérience m'a permis de plus de co-encadrer au laboratoire la thèse de H. Colder ainsi que de développer et d'être responsable depuis février 2005 d'une nouvelle thématique avec les films minces semi-conducteurs  $\text{Cr}^{2+}:\text{ZnSe}$  (thèse N. Vivet).

Ces différentes thématiques de recherche visant à établir les corrélations existant entre la structure, la microstructure et les propriétés physiques des matériaux sous forme massive ou de films minces, m'ont permis néanmoins d'acquérir une compétence plus particulièrement dans la technique de diffraction, qu'elle soit aux rayons X, aux électrons ou aux neutrons. Cette compétence dans cette technique de caractérisation aux rayons X me permet de plus d'interagir fortement avec l'ensemble des thèmes de recherches développés dans mon laboratoire d'accueil par le biais de la réalisation de caractérisations structurales ponctuelles (diffraction et réflectivité des rayons X), et d'être le responsable scientifique du diffractomètre du laboratoire.

Ma démarche dans ces différentes thématiques visant à l'optimisation de matériaux anisotropes massifs ou sous forme de films minces, il apparaît que dans cet objectif l'analyse quantitative des orientations préférentielles (QTA) par diffraction des rayons X, méthode d'investigation non destructive, est un outil de choix incontournable. De plus, l'ajout des informations de QTA a permis de repousser certaines limites avec notamment l'analyse dite combinée "structure / microstructure / texture / contraintes", au développement de laquelle j'ai

participé lors de mon activité post-doctorale. C'est pourquoi, j'ai choisi de centrer l'ensemble des travaux présentés dans ce manuscrit autour des différentes applications possibles de cette méthode d'analyse QTA par diffraction des rayons X soit via une approche dite classique et faisant l'objet du Chapitre 1, soit via une approche avec l'analyse combinée (Chapitre 2), et ce dans l'objectif de l'optimisation des différents matériaux que j'ai étudiés.

L'analyse QTA classique a permis notamment l'optimisation des matériaux massifs ferromagnétiques texturés sous champ magnétique de ma thèse mais aussi celle de films minces conducteurs ioniques (Li,La)TiO<sub>3</sub> que j'ai élaborés par pulvérisation magnétron réactive (ATER à l'université du Maine), et de films minces semi-conducteurs d'InN étudiés au Laboratoire SIFCOM.

Dans le cadre des matériaux composites ferromagnétiques, la détermination de la fonction de distribution des orientations cristallines (FDOC) via cette analyse QTA a permis notamment la simulation des courbes d'aimantation anisotropes expérimentales M(H), ouvrant ainsi la voie à une éventuelle détermination de texture magnétique.

L'utilisation de l'analyse QTA s'est avérée également indispensable pour l'optimisation des films minces texturés conducteurs ioniques (Li,La)TiO<sub>3</sub> et semi-conducteurs d'InN. En effet, rappelons que les intensités diffractées dépendent de la porosité, de l'état cristallin, de l'épaisseur, du pourcentage de phases... de l'échantillon étudié et que donc pour pouvoir comparer différents échantillons entre eux d'un point de vue uniquement de l'orientation, les figures de pôles expérimentales doivent être normalisées. De plus, n'oublions pas que les figures de pôles expérimentales sont souvent incomplètes du fait de problèmes pratiques liés à la défocalisation du faisceau RX lorsque l'on tourne en  $\chi$ , d'où la nécessité d'utiliser une méthode d'affinement de la FDOC (par exemple la méthode WIMV), permettant de recalculer les figures de pôles afin de vérifier leur cohérence avec celles expérimentales mais aussi de compléter les zones aveugles et non mesurées. Enfin, pour les films présentant une texture de fibre (cas notamment des films (Li,La)TiO<sub>3</sub>) l'accès aux figures de pôles inverses à partir de la FDOC permet d'avoir une représentation plus aisée et plus complète des différentes composantes de texture.

Il apparaît dans ce manuscrit également que l'analyse QTA classique est très rapidement limitée lorsque les hétérostructures texturées sous forme de films minces présentent des recouvrements de pics inter- ou intra-phases, des microstructures particulières (microdéformations ou tailles de cristallites anisotropes) et la présence de contraintes résiduelles. C'est pourquoi, l'analyse globale du profil des spectres de diffraction X, développée dans le programme MAUD (en collaboration avec L. Lutterotti), est un outil

indispensable et fiable pour déterminer à la fois la structure, la microstructure, la texture, le pourcentage de phases et les contraintes de films minces notamment, problématique qui jusqu'à présent ne pouvait être résolue par aucun programme de traitement de données X (ou neutrons).

L'expertise acquise dans l'utilisation du programme MAUD m'a d'autre part permis de participer comme intervenant à deux actions de formation CNRS, régionale (en juin 2005) et nationale (en juin 2006), et intitulées "Analyse combinée par diffraction des rayons X et neutrons".

L'optimisation et la démonstration de la pertinence de cette analyse globale du profil des spectres de diffraction X a été réalisée durant mon stage post-doctoral à l'université du Maine sur la base de deux exemples types de films minces texturés (films minces ferroélectriques (Pb,Ca)TiO<sub>3</sub> et films de TiC et de TiN) présentant des recouvrements importants de pics intra- et inter-phases.

Pour ce qui est des films minces nanostructurés de Si (participation à la thèse de Y. Leconte) et de SiC déposés au laboratoire SIFCOM, l'utilisation de l'analyse combinée a permis pour la première fois la détermination de tailles anisotropes de cristallites dans ces échantillons texturés. Notamment, il a été mis en évidence que bien que la forme de ces nanocristallites soit ellipsoïdale, allongée selon la direction  $\langle 111 \rangle$ , cette direction d'allongement ne correspond pas forcément à l'axe de développement de la texture dans ces films. De plus, l'analyse combinée des données de rayons X couplée à la microscopie électronique en transmission pour une caractérisation à une échelle très locale des films minces nanostructurés sont des outils complémentaires et de choix, particulièrement bien adaptés aux couches minces semi-conductrices étudiées au laboratoire SIFCOM. Dans ces films, nous avons mis également en évidence que l'évolution de leurs propriétés optiques (gap et indice de réfraction) en fonction des différents paramètres de dépôt (distance substrat – cible pour le Si et température de dépôt pour le SiC) est corrélée avec leur structure, microstructure et les pourcentages de phases.

En ce qui concerne les films de Cr<sup>2+</sup>:ZnSe texturés, une analyse combinée des spectres de diffraction X est nécessaire du fait de la présence dans ces films de tailles anisotropes, de contraintes résiduelles et de la coexistence des phases hexagonale et cubique du ZnSe. Cette analyse globale du profil n'a pas pu être encore finalisée de manière satisfaisante. La difficulté rencontrée dans la reproduction de l'intensité du pic très fin 111 (indexation dans la maille ZnSe cubique) suggère de plus la présence de fautes d'empilements qu'il va falloir donc

essayer de prendre en compte, ce qui augmente encore la difficulté de résolution de cette problématique.

*Dans* le cadre du nouveau sujet de recherche que je développe ces dernières années au laboratoire SIFCOM et visant à la réalisation de microlasers sous forme de films minces à base de semi-conducteurs  $\text{Cr}^{2+}:\text{ZnSe}$  et émettant autour de  $2.4 \mu\text{m}$  à température ambiante (en collaboration avec le laboratoire CIRIL–Ensicaen), les perspectives à court et moyen termes sont nombreuses. En effet, cette région du moyen infrarouge ( $2\text{-}4.5 \mu\text{m}$ ), caractéristique de modes de vibration d'un grand nombre de molécules, est particulièrement intéressante pour des applications dans le domaine de l'environnement (détection de traces de polluants), de la médecine (source médicale laser pour des diagnostics non invasifs) et de la défense (détection Lidar). L'excitation électrique de ces microstructures sous forme de films constitue un des enjeux majeurs de ce projet (en collaboration avec l'Onera). Dans cet objectif, la compréhension des différents mécanismes d'excitation de l'ion  $\text{Cr}^{2+}$ , encore sujette à de nombreux débats dans le matériau massif, est la première étape pour l'élaboration et l'optimisation d'une cavité laser résonante, qui sera étudiée sous excitation optique (au laboratoire CIRIL–Ensicaen) et sous excitation électrique. Afin d'obtenir une interaction efficace entre les ions  $\text{Cr}^{2+}$  et les porteurs de charge, le contrôle de la quantité de dopant ( $\text{Cr}^{2+}$ ) ainsi que l'optimisation de la composition, de la structure de la couche active  $\text{Cr}^{2+}:\text{ZnSe}$  et du design de la cavité seront donc requis.

En tenant compte des résultats déjà obtenus sur les dispositifs électroluminescents dans le domaine visible à base de films minces nanostructurés de ZnS dopés par des ions métaux de transition ou de terres rares, il semble que le confinement optique associé au confinement quantique lié à une éventuelle nanostructuration des films de  $\text{Cr}^{2+}:\text{ZnSe}$  devrait ouvrir de nouvelles perspectives en nanophotonique. Cet aspect devra donc être également exploré puisque le rendement de luminescence des films de ZnS dopés  $\text{Mn}^{2+}$  ou  $\text{Tb}^{3+}$  a été nettement amélioré suite à leur nanostructuration. Un des verrous majeurs qu'il faudra sans doute lever concerne la taille des nanograins de ZnSe; en effet, il a été mis en évidence dans les nanostructures  $\text{Mn}^{2+}:\text{ZnS}$  que pour des tailles de grains de ZnS inférieures à  $2 \text{ nm}$  le dopant Mn ne pouvait plus être incorporé dans la structure. Enfin, à plus long terme, le dopage ou le co-dopage de ces films avec d'autres ions tels que  $\text{Co}^{2+}$ ,  $\text{Ni}^{2+}$  ou  $\text{Fe}^{2+}$  pourra être envisagé.

**D**ans la communauté de synthèse de couches minces, l'étude des caractéristiques des plasmas revêt une importance capitale de par la sophistication et la complexité des structures développées, nécessitant de plus des outils de contrôle et de caractérisation in-situ non perturbateurs, non destructifs et d'une grande sensibilité. Dans cet objectif, il apparaît que les techniques de spectroscopie de masse et d'émission optique sont des méthodes complémentaires particulièrement bien adaptées au diagnostic précis du plasma. En effet, la spectroscopie de masse permet notamment d'identifier la nature des espèces neutres pulvérisées, d'apporter des informations sur l'énergie des espèces ionisées dans le plasma alors que la spectroscopie d'émission optique permet une détermination précise de la composition du plasma ainsi que la mise en évidence des processus d'excitation de toutes les espèces en fonction des différents paramètres de dépôt envisagés.

Dans le but d'identifier et de quantifier (en terme de nature, d'énergie, de densité des espèces ...) le plasma élément vecteur de la technique de dépôt et dans un souci de maîtriser la reproductibilité et la qualité des dépôts, le laboratoire SIFCOM s'est équipé récemment de ces deux dispositifs de caractérisation in-situ du plasma. Avec la thèse de H. Colder que j'ai co-encadrée, j'ai initié au laboratoire le développement de la spectroscopie d'émission optique in-situ avec un diagnostic qualitatif du plasma (identification des espèces du plasma et évolution de ces dernières en fonction des différents paramètres de dépôt). Dans les films nanocristallisés de SiC, il a été mis ainsi en évidence l'importance des radicaux hydrures du plasma dans les mécanismes de cristallisation du carbure de silicium.

L'utilisation de la spectroscopie d'émission optique nous a permis également dans le cadre de la thèse que je co-encadre de N. Vivet, de cerner très rapidement les conditions optimales de dépôt des films composites non dopés de ZnSe/SiO<sub>2</sub>, d'appréhender les mécanismes intervenant dans la croissance de ces films, puis de déterminer la puissance radiofréquence optimale pour l'incorporation du chrome dans ces structures.

Ce diagnostic qualitatif in-situ du plasma par spectroscopie d'émission optique doit être maintenant complété à moyen terme par un diagnostic quantitatif de l'ensemble des espèces présentes dans le plasma pour maîtriser la structure (taux de cristallinité, composition...), la microstructure (défauts, taille des particules...) des couches minces en vue de l'optimisation de leurs propriétés optiques pour leurs applications potentielles. Cet aspect que j'envisage de développer afin de maîtriser dans un premier temps la reproductibilité des dépôts de Cr<sup>2+</sup>:ZnSe, devra bien entendu être accompagné d'un travail de modélisation et de simulation numérique des plasmas réactifs ou non, souvent nécessaire à l'interprétation des



diagnostics expérimentaux. Pour cela j'envisage de collaborer avec des équipes possédant une expertise dans ce domaine telles que celles du Laboratoire de Physique des Gaz et des Plasmas (LPGP) - Orsay, SupElec ou du Groupe de Recherche sur l'Energétique des Milieux Ionisés (GREMI) – Orléans. Enfin, le couplage de cette technique de caractérisation du plasma avec la spectrométrie de masse et des caractérisations à l'aide d'une sonde de Langmuir devra être également développé à plus long terme.

*Les analyses par faisceaux d'ions (IBA) regroupent des techniques qui utilisent un faisceau de particules légères et chargées de quelques MeV ( $^4\text{He}^+$ ,  $^2\text{H}^+$ ...) telles que la spectroscopie de rétrodiffusion Rutherford (RBS) pour la détection des éléments lourds ( $Z > 15$ ) et l'analyse par réaction nucléaire (NRA) ou par détection des ions de recul élastique (ERDA) pour la détection des éléments légers (H, Li, C...). Ces dernières sont des outils de choix pour mettre en évidence la présence d'éventuels contaminants, pour accéder à la composition de films (d'épaisseurs inférieures à  $1\ \mu\text{m}$ ) ainsi qu'aux profils de concentration en profondeur des différents éléments les constituant (avec une sensibilité d'environ  $10^{13}\ \text{at}/\text{cm}^2$  pour la RBS), et ce avec une altération très faible de la qualité des couches.*

Toutefois, ces dernières années, face à la nécessité de détecter de plus en plus finement des traces de contaminants dans les films de l'industrie microélectronique, une nouvelle technique d'analyse de rétrodiffusion basée sur un procédé analogue à la RBS mais utilisant des ions lourds de quelques centaines de KeV, dite HIBS (pour Heavy Ions Backscattering Spectrometry), a été développée. Notamment, une équipe américaine a montré qu'en utilisant cette technique de HIBS (faisceau de  $^{12}\text{C}^+$  de 200 à 400 KeV) la sensibilité de la détection d'éléments lourds par rapport à la technique RBS pouvait être augmentée de plus d'un facteur 1000, ce qui dans un souci permanent d'optimisation de la qualité des couches élaborées au laboratoire SIFCOM ouvre de nouvelles perspectives. En effet, au sein du laboratoire SIFCOM (thèses de H. Colder et de N. Vivet) j'ai pu faire bénéficier de mon expérience dans l'analyse par faisceaux d'ions ainsi que de ma collaboration avec l'Institut des Nanosciences (Paris 6 et 7) pour l'utilisation de l'équipement SAFIR. Ces analyses IBA couplées à celles in-situ du plasma ont d'ailleurs permis d'appréhender les mécanismes de croissances des couches minces de SiC et de  $\text{Cr}^{2+}:\text{ZnSe}$ .

Dans le contexte de la fusion prochaine (prévue en janvier 2008) du laboratoire SIFCOM avec le laboratoire CIRIL, dont l'activité est par ailleurs étroitement liée à celle du grand accélérateur National d'Ions Lourds (GANIL), il apparaît donc qu'à long terme le développement et l'optimisation de cette nouvelle technique de HIBS sur le site caennais

pourrait être envisagée. Pour cela, les possibilités offertes par la ligne IRRSUD du GANIL pourront être utilisées (en collaboration avec I. Monnet), en consacrant une partie du temps de faisceau aux analyses HIBS, analyses qui devraient nous permettre de détecter des éléments de  $Z > 12$  avec une excellente sensibilité.